Characterization of the thermomechanical behaviour of metals for high strain-rates, using ultra-high speed imaging cameras

Adrien Vinel

DOCTORAT BRETAGNE SCIENCES LOIRE POUR L'INGENIEUR

CENTRALE NANTES

THÈSE DE DOCTORAT DE

L'ÉCOLE CENTRALE DE NANTES

ÉCOLE DOCTORALE N° 602
Sciences pour l'Ingénieur
Spécialité : *Mécanique des solides, des matériaux, des structures et des surfaces*

Par
Adrien Vinel

Caractérisation thermomécanique du comportement dynamique de métaux via mesures de champs ultra-rapides

Thèse présentée et soutenue à Nantes, le 24 Janvier 2022
Unité de recherche : Institut de Recherche en Génie Civil et Mécanique (GeM)

Rapporteurs avant soutenance :

Patricia Verleysen — Professeure, University of Ghent
Fabrice Pierron — Professeur, University of Southampton

Composition du Jury :

Examinateurs :	Patricia Verleysen	Professeure, University of Ghent
	Fabrice Pierron	Professeur, University of Southampton
	Dirk Mohr	Professeur, ETH Zurich
	Bertrand Wattrisse	Professeur, Polytech Montpellier
	Dominique Saletti	Maître de conférence, Université Grenoble Alpes
Dir. de thèse :	Julien Réthoré	Directeur de Recherche CNRS, GeM
Co-encadrants :	Rian Seghir	Chargé de Recherche CNRS, GeM
	Julien Berthe	Responsable d'unité de recherche ONERA, ONERA Lille
	Gérald Portemont	Chargé de recherche ONERA, ONERA Lille

Table of Contents

Chapter 1

General Introduction

Aeronautical structures are often exposed to extreme loadings during bird-strike or lightning for example: particularly in terms of temperatures and strain-rates. When exposed to these loadings, multi-physical phenomena, especially thermomechanical ones can happen and thus considerably change the behaviour of the structure, sometimes leading to its ruin. In order to deepen our understanding of such events, the development of experimental procedures is needed. Such procedures should enable the *in situ* observation of these coupled events. These observations will either be used to enrich existing models or lead to the elaboration of new models.

The characterization of a metal's behaviour requires, in the general case, to have access to the stress distribution. Obtaining such an un-observable quantity is an ill-posed mechanical problem. However, several strategies have been developed to close the problem. Classically, one way to close the problem is by performing statically determined tests *e.g.* Kolky's bar for high strain-rates. This test constitutes the gold standard for rate-dependent material characterization. However, these tests rely heavily on scalar measurements (through the use of gauges). Furthermore, the conditions needed (*e.g.* for Kolky's bar) — 1D, quasi-static equilibrium — still limit heavily quantitative measurements under real case scenario. As a result heterogeneous transient phenomena naturally induced by dynamic loadings cannot be thoroughly characterized and understood. Another route consists in using constitutive laws to close the problem. The problem then changes from obtaining stress distribution to the inverse identification of constitutive parameters. This strategy assumes that the constitutive laws, usually constructed and calibrated on statically determined tests, can be extrapolated for complex loadings. Nevertheless, it allows to retrieve stress fields during heterogeneous tests that lead to loadings closer to real life scenario.

Besides the fundamental question of stress distribution evaluation, experimentally characterizing dynamic behaviours of metals face several difficulties:

- the observation and characterization of heterogeneous transient phenomena require measurements with both spatial and temporal high resolutions. This is still, to this day, a challenge,
- the intrinsic multi-physical aspect of the dynamic processes requires finding alter-

natives to the mono-parametric approaches. Particularly, thermo-coupled analysis are, in that context, helpful.

In the last few years, these difficulties has been partially tackled. Indeed, the progress in ultra high-speed imaging paired with digital image correlation made possible measurements at precise resolutions (a few µm and µs) [Moulart *et al.*, 2011, Malchow *et al.*, 2019]. This opened the way to the realization of heterogeneous tests and enables the identification of dynamic constitutive parameters [Kajberg and Wikman, 2007, Peirs *et al.*, 2011]. However, since constitutive laws are established using statically determined tests, their ability to accurately capture the behaviour of metals submitted to complex loadings (*e.g.* heterogeneous, multi-axial and coupled) is questionable.

Would it be possible to observe the heterogeneous dynamic stress response of materials without modelling *a priori* ?

In the recent years strategies have been developed to retrieve stress fields without having to rely on constitutive laws. For instance, the measurement of acceleration fields during 1D dynamic experiments allows now the direct estimation of stress-strain relations [Pierron *et al.*, 2014, Koohbor *et al.*, 2016, Seghir and Pierron, 2018, Forquin and Lukić, 2018]. Recently, an attempt to extend these approaches to 2D case [Seghir *et al.*, 2019] has been proposed through the resolution of an inverse problem. Similarly, the recent development of Data-Driven approaches applied to mechanics [Kirchdoerfer and Ortiz, 2016, Leygue *et al.*, 2018, Leygue *et al.*, 2019] allows the estimation of heterogeneous stress distributions, in a regularized but non-parametric way, from heterogeneous kinematic fields, both in quasi-static and dynamic. Regarding the thermodynamical side of the problem, the recent improvement in infrared thermography enables high-speed coupled measurements during experiments [Seidt *et al.*, 2017]. Thus, in principle, the thermodynamical quantities needed for a behaviour model elaboration can now all be measured experimentally.

Nevertheless, combining thermo-coupled measurements with high spatial and temporal resolutions and non-parametric stress estimation approaches is still a scientific and technological challenge, which is yet to be overcome. This PhD thesis is part of a collaboration between the GeM and the Materials and Structures Department (DMAS) of ONERA, one of whose missions is the characterization of structures' dynamic behaviour during a crash or an impact. The objective of this PhD thesis is to develop such tests and the analysis methodology associated. The aim of this work is to pave the way for a new material characterization strategy for high strain-rate and heterogeneous experiments, by combining the use of state-of-the-art cameras with unparalleled spatio-temporal samplings and the use of innovative stress estimation methods.

After an introduction about material behaviour modelling, the work proposed in this manuscript is divided in three main parts. First, both the ultra high-speed and InfraRed cameras will be presented. A particular focus is done on the methodologies used to extract

kinematic and thermal fields and their accuracies. Then, an inertial impact test is performed on a PMMA sample for validation purposes. The following part is dedicated to the design of a dynamic tensile test and its realization. Using Finite Element simulations, a sample design is chosen. Then, synthetic images as well as virtual deformation processes are used to ensure that the resulting kinematic fields can be retrieved experimentally with the presented methodologies. A test campaign is then performed on an XES steel from ONERA and both kinematic and temperature fields are retrieved. Finally, the last part focuses on the exploitation of the thermomechanical fields obtained. In this part, a non-parametric approach is investigated to characterize the material's behaviour. First the proposed methodology is applied on a numerical test case. Then it is applied to the experimental data. The results of the proposed approach is compared to, first the simulations predictions. And then, the comparison with a constitutive model traditionally used to model the material of this study will be discussed. Since non-parametric approaches are a very recent open subject, this work is of a seminal nature and aims to explore and discuss the possibilities offered by non-parametric approaches. Obviously, many questions remain open and a long journey remains before thinking of substituting methodologies that have been established over decades by the investigated one.

Chapter 2

Material behaviour modelling and characterization

2.1 A brief recall of the mechanical problems

In this section, definition of some problems in continuum mechanics will be recalled [Pierron and Grédiac, 2012], especially the so called direct and inverse problem. In what follows, the small strain formalism is assumed.

To this effect let us consider a continuous deformable body Ω (see Fig. 2.1). This body is submitted to imposed displacements $\mathbf{u}_D$ on the boundary Γ_D, and to a load distribution $\mathbf{t}_N$ on the boundary Γ_N. Note that when neither a displacement nor a load is imposed one can consider that a 0 load is imposed, as a result the boundary where nothing is applied (in the schematic the black boundary for instance) can be considered as a part of Γ_N. In addition, this solid is subjected to a distributed body force $\mathbf{f}$, defined per unit of volume.

Usually, when boundary conditions are known, the mechanical problem is to find the displacement field $\mathbf{u}$ and the stress field $\boldsymbol{\sigma}$ that verify:

- $\boldsymbol{\varepsilon} = \frac{1}{2}\left(\nabla\mathbf{u} + \nabla^T\mathbf{u}\right)$ (strain compatibility),
- $\boldsymbol{\sigma}^T = \boldsymbol{\sigma}$ (for Cauchy medium).
- $\mathbf{u} = \mathbf{u}_D$ on Γ_D,
- $\boldsymbol{\sigma} \cdot \mathbf{n} = \mathbf{t}_N$ on Γ_N,
- $\mathrm{div}(\boldsymbol{\sigma}) + \mathbf{f} = \rho\mathbf{a}$.

This problem is ill-posed since the number of equations, *e.g.* 9 in 3D, is lower than the number of unknowns, *e.g.* 15 in 3D. As a result, the solution is not unique.

In practice, experimentally knowing $\mathbf{u}(\mathbf{X})$ (from DIC) and $\int_{\Gamma_N} \boldsymbol{\sigma}(\mathbf{X}) \cdot \mathbf{n} d\Omega$ (from load-cell) is not sufficient to get $\boldsymbol{\sigma}(\mathbf{X})$ in the general case. Historically, one of the first way to solve this problem is to perform statically determined tests (see Section 2.2), *i.e.* by considering particular geometries and loadings the number of unknowns of the problem can be reduced which allows to close the problem. Alternatively, the assumption of a constitutive law that links the primary variables (*e.g.* strains and its time derivatives,

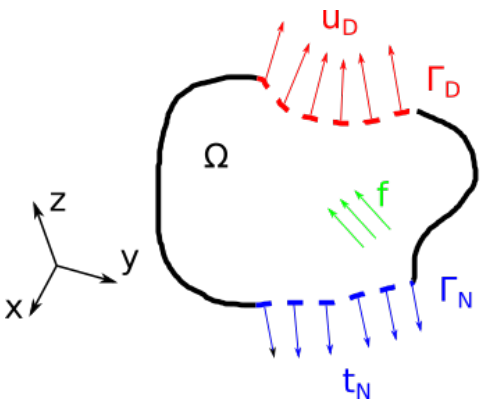

Figure 2.1: Schematic of a mechanical problem in the deformed configuration.

temperature) to constitutive variables (*e.g.* stresses) closes the problem. Through the use of a constitutive law, two mechanical problems can be defined:

- The so called direct problem. For this problem, the geometry and boundary conditions are known. Furthermore, a constitutive law is chosen and its parameters are supposed known. Then, the problem consists in finding $\mathbf{u}$ and $\boldsymbol{\sigma}$. This is typically the problem solved by Finite Element solvers.

- The so called inverse problem. For this problem, the applied load as well as the displacement fields are supposed known. As a result, the problem consists in finding $\boldsymbol{\sigma}$ and either identify parameterized a constitutive law or its parameters.

It follows that, for complex and statistically undetermined tests, constitutive laws are considered as a mandatory brick for simulations and material characterization. To model the wide variety of materials and specific responses to specific loading conditions, a large quantity of constitutive laws have been developed. These constitutive laws result generally from models that are motivated by either theoretical background (*e.g.* the Klepaczko model [Klepaczko and Chiem, 1986] or the Gao-Zhang model [Gao and Zhang, 2010] that are based on dislocation mechanics), or heuristic considerations (such as the Johnson-Cook model [Johnson and Cook, 1983]). The parameters involved in constitutive laws are often considered as material parameters. Despite the freedom that is allowed for the creation of constitutive laws let us note that four main physical principles must be verified:

- physical admissibility: the constitutive variables respect conservation laws as well as the second law of thermodynamics,

- determinism: constitutive variables at time $t = t_i$ are only determined by primary variables at previous times ($t \leq t_i$),

- locality: constitutive variables at the point X are dependent of the primary variables in the vicinity of X,

- objectivity: constitutive laws are invariant with respect to a rigid body motion of the spatial frame of reference. This induces that constitutive laws depend on strain tensor rather than the displacement.

Both strategies, statically determined tests or complex tests combined with the use of *a priori* modelled behaviours, have some limitations:

- Statically determined tests assume that complex responses can be characterized through the sum of various "simple tests". One of the consequence is that it requires a multitude of experiments in order to characterize a material response for a wide range of strain-rates, temperatures and multi-axiality ratio.

- Inverse identification of material parameters heavily relies on the assumption that the constitutive laws, that are constructed and calibrated on statically determined tests, can be extrapolated for complex loadings (*e.g.* heterogeneous, multi-axial, subjected to strong gradients of all sorts). This assumption is undermined by the fact that parameters identified for a material during heterogeneous tests often differ from the one identified for the same material using statically determined tests. Moreover, even though the use of constitutive laws allows to close the problem, its resolution requires the use of complex identification methods (see Section 2.3.1). At last but not least, such strategy denotes a change of paradigm: rather than trying to measure the material response, one focuses on parameter optimizations which may limit our ability to truly characterize new materials.

In the following sections, the principle of statically determined test will be first presented as well as the measurements methods. Then, statically undetermined tests will be discussed. In particular, different strategies to solve the closed mechanical inverse problem will be presented, as well as full-field measurement methods allowing to fully take advantage of such approaches. The main interest of the two sections to come (Section 2.2 and 2.3) is to provide a series of information, test configurations and basic concepts that will implicitly be used in the rest of the document.

At last, since 2016 a new strategy to close and solve the mechanical problem is developed. It consists in assuming the existence of a constitutive space in which the material behaviour can be described as a manifold. This strategy, relies on the availability of a significant database in order to estimate stresses. The use of such an approach could potentially allow to build constitutive equations from local full-field imaging only, in a bottom-up approach rather than in the classically used top-down approach. This would allow the constitutive law to naturally take into account all the richness of the material (*e.g.* thermomechanical couplings, influence of the multi-axiality...). This innovative and original strategy will be presented and discussed in depth in Chapter 8.

2.2 Statically determined tests

2.2.1 Principle

The first way to solve the ill-posed problem described above is to perform statically determined tests. These tests (and in particular the geometry used) are designed so that the stress distribution can be computed analytically using the loads measured. This strategy relies mainly on the assumption that the quantities of interest remain homogeneous in the region of interest (the gauge length) during the whole duration of the test.

Ensuring the homogeneity of the fields in the gauge length can be challenging, especially when one wants to characterize a material under extreme conditions (very high or low temperatures, dynamic loadings...). Furthermore, an additional condition when characterizing a material at high strain-rate, is that the strain-rate has to remain constant during the duration of the experiment in the whole gauge length. As a result, the specimen geometry and the loading paths have to be carefully chosen with respect to the material and the domain of characterization investigated. To this effect, multiple standardized tests have been developed (ASTM, ISO, EN...). These norms help to ensure the respect of the conditions needed to perform a statically determined test by fixing the specimen geometry, the boundary conditions as well as the possible loading paths. Hence, the test design space is strongly constrained.

Let us note that the statically determined tests presented can also lead to the identification of the parameters of a constitutive law. It is done by minimizing a cost function in the least-square sense, generally defined as:

$$\phi(\underline{P}) = \sum_{k=1}^{N} \|\sigma_{\text{exp}}(k) - \sigma_{\text{law}}(k, \underline{P})\|^2, \tag{2.1}$$

where N is the number of experimental points, $\|\|$ is a chosen norm (usually the Von-Mises norm), σ_{exp} are the experimental stresses, σ_{law} are the stresses obtained using the constitutive law considered and $\underline{P}$ the parameters of the constitutive law that are sought.

2.2.2 Measurement methods

For statically determined tests, since a homogeneous state of the fields of interest is assumed in the gauge length, loads, displacements, strains and temperatures can be obtained directly using punctual measurement techniques such as load cells, extensometers, strain gauges and thermocouple.

2.2.3 Examples

2.2.3.1 Uniaxial tensile test

Uniaxial tensile test is one of the most used experimental technique for the characterization of a material. It consists in the application of an uniaxial tension to a specimen (see Fig. 2.2 for an example of the apparatus). The specimen geometry is chosen so that the dimension in the tensile direction is preponderant versus the other two. When the fields are homogeneous in the gauge length (*i.e.* before the necking of the specimen), the engineering strain and the engineering stress are computed as follows:

$$\begin{aligned} \varepsilon_{\text{eng}}(t) &= \frac{\Delta L(t)}{L_0}, \\ \sigma_{\text{eng}}(t) &= \frac{F(t)}{S_0}, \end{aligned} \tag{2.2}$$

where L_0 is the initial gauge length, $\Delta L(t)$ is the elongation of the gauge length at the time t, S_0 is the initial cross-section and $F(t)$ is the measured load at t. The true strain and stresses, that represent the true material behaviour are obtained using the following relations:

$$\begin{aligned} \varepsilon_{\text{true}}(t) &= \int_{L_0}^{L(t)} \frac{\Delta L}{L} = \ln(1 + \varepsilon_{\text{eng}}(t)), \\ \sigma_{\text{true}}(t) &= \frac{F(t)}{S(t)}. \end{aligned} \tag{2.3}$$

In the case of an incompressible and isotropic material, Eq. 2.3 can be further simplified into $\sigma_{\text{true}} = \frac{F(t)}{S_0}\ln(1 + \varepsilon_{\text{eng}}(t))$.

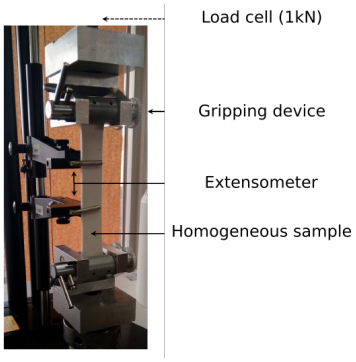

Figure 2.2: Example of a uniaxial tensile test apparatus for elastomers. From [Dalemat, 2019], the caption were translated in english.

2.2.3.2 Split Hopkinson Pressure Bar tests

Another fundamental statically determined test that is extensively used to characterize materials at high-strain rates is the Split Hopkinson Pressure Bar test [Gray III, 2000,

Gama *et al.*, 2004]. The experimental apparatus usually consists in a striker bar, an input and an output bar. The two bars (input and output) are instrumented with strain gauges and the specimen is usually sandwiched between these two bars (see Fig. 2.3 for a schematic of a SHPB apparatus). Furthermore, the two bars have a uniform cross section, and their length to diameter ratio is often taken between 20 and 100. The input and output bars are usually in the same material. The properties of the bar material as well as the specimen dimension are supposed to be known. Then, using 1D stress wave analysis in the bars [Gray III, 2000], the strains and stresses in the specimen can be analytically computed using the strains and stresses in the bars:

$$\begin{aligned} \sigma(t) &= \frac{A_\mathrm{b} E_\mathrm{b} \varepsilon_T(t)}{A_\mathrm{s}}, \\ \dot{\varepsilon}(t) &= -\frac{2 c_\mathrm{b} \varepsilon_R(t)}{L_\mathrm{s}}, \\ \varepsilon(t) &= \int_0^t \dot{\varepsilon}(\tau) d\tau, \end{aligned} \tag{2.4}$$

where, A_b, E_b, c_b are respectively the cross-section, the Young modulus and the wave speed of the bars, A_s, L_s are the initial cross-section and initial length of the specimen and ε_R, ε_T are respectively the axial strain of the reflected wave in the input bar and the axial strain of the transmitted wave in the output bar.

However, the use of such tests relies on several assumptions [Gama *et al.*, 2004]:

- The stress wave propagation in the bar is 1D. This is usually ensured if the bar material is homogeneous and isotropic, and that the bars remain in their linear elasticity domain during the experiments. Furthermore, in order to guarantee that the stress distribution is uniform in the entire cross section of the bars, the length to diameter ratio has to be higher than 20.

- The interfaces between the bars and the specimen remain plane during the experiment.

- The effect of inertia in the sample is negligible. It classically means waiting 3 to 4 wave rebounds within the material until it reaches static equilibrium $F_\mathrm{in} = F_\mathrm{out}$. This makes the accurate characterization of brittle material or of the elasto-plastic transition very difficult.

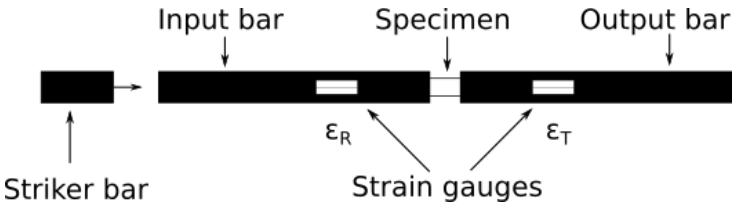

Figure 2.3: Schematic of a classical Split Hopkinson Pressure Bar test apparatus.

- The stress fields in the sample are homogeneous. This condition is usually considered true when static equilibrium is reached.

To summarize, by taking advantage of the a priori knowledge of analytical solutions thanks to carefully chosen simple geometries, the statically determined tests can be used to identify the behaviour of a material without the use of a constitutive law and by only measuring loads and strains. However, this identification only yields a sparse sampling of the material's response. To bypass this drawback, these experimental techniques can also be used to fit the parameters of a constitutive law modelling the material. Yet, this often leads to an important number of tests, since the more complex the material the more parameters have to be identified. Furthermore, the complex couplings that appears during high strain-rate experiments with localization phenomena will never be captured.

2.3 Statically undetermined tests using a constitutive law

The recent developments in optical sensors as well as in full-field measurements techniques enable the quantitative measurement of kinematic and temperature fields during an experiment. Hence, statically undetermined tests leading to heterogeneous fields – and thus potentially larger spectra of strain, strain-rate and temperature during a single experiment – can be considered. Furthermore, since heterogeneous fields are influenced by a higher number of parameters than homogeneous ones, these tests also potentially lead to the identification of a greater number of parameters at the same time [Pierron and Grédiac, 2012]. In what follows, non exhaustive different methodologies allowing to identify material parameters using statically undetermined tests will be presented. These descriptions are based on literature reviews [Avril *et al.*, 2008], the reader may refer to this article for further information.

2.3.1 Principle of different identification methods

2.3.1.1 The Finite Element Model Updating (FEMU) method

The FEMU method is one of the most commonly used and most intuitive method. It was first introduced by [Cottin *et al.*, 1984] and relies on the use of a Finite Element solver. By using a FE model of the experiment, the method consists in finding a set of parameters $\underline{P}$ which minimizes the discrepancy between the measured and predicted forces (FEMU-F) or displacement fields (FEMU-U):

- FEMU-U: This method consists in comparing measured displacement fields U_m to the one obtained after a FE simulation using a set of parameters $\underline{P}$ and known

boundary conditions w, $U_s(\underline{P}, w)$. The cost function used takes the form of:

$$\phi_U(\underline{P}, w) = \frac{1}{2}(U_m - U_s(\underline{P}, w))^T W_U (U_m - U_s(\underline{P}, w)), \tag{2.5}$$

where W_U is a symmetric, positive definite weighting matrix. This method is iterative and thus several FE simulations have to be conducted. As a result, this method can be costly in term of computation times.

- FEMU-F: This method consists in comparing the measured loads R_m and the one obtained for the FE model R_s. Let us note that FE simulations are not needed to compute R_s, however this method needs the availability of the displacements fields for every node as well as the prescribed loads. The cost function is usually written as:

$$\phi_F(\underline{P}) = \frac{1}{2}(R_m - R_s(\underline{P}))^T W_F (R_m - R_s(\underline{P})), \tag{2.6}$$

where W_F is a symmetric, positive definite weighting matrix.

Many variations of these two proposed methods exist, one can for instance combine ϕ_U and ϕ_F and performed FEMU-F-U. This identification method have been used to identify constitutive parameters for a broad range of materials as well as models. For instance, it has been applied to identify viscoplastic parameters for high strain-rate tests on steels [Kajberg and Wikman, 2007], or the Johnson-Cook parameters for an aluminium alloy using a method derived from FEMU [Peirs *et al.*, 2011]. More recently, this methodology has been used to identify Johnson-Cook damage model parameters [Verleysen and Peirs, 2017]. The FEMU method has also been applied for hyperelastic parameters identification [Giton *et al.*, 2006]. Note that even more recently, the temperature has been introduced to identify thermomechanical properties, giving birth to the FEMU-T [Herb *et al.*, 2019, Archer *et al.*, 2020].

One of the notable drawback of such a method is its heavy dependency on the FE modelling of the experiment. Indeed, it is especially important to have a good knowledge of the boundary conditions during the experiment in order to have access to relevant predictions of either displacements or loads.

2.3.1.2 The Virtual Fields Method (VFM)

This method is usable when the strain field $\boldsymbol{\varepsilon}$ is measured in the volume Ω or simply computed within the volume from surface measurements (2D extruded, bending shell theory...). The Virtual Fields Method is based on the use of the Principle of Virtual Work [Grediac, 1989]:

$$-\int_\Omega \boldsymbol{\sigma}(\underline{P}) : \boldsymbol{\varepsilon}^* dV + \int_{\partial\Omega} \mathbf{T} \cdot \mathbf{u}^* dS + \int_\Omega \mathbf{f} \cdot \mathbf{u}^* dV = \int_\Omega \rho \mathbf{a} \cdot \mathbf{u}^* dV, \tag{2.7}$$

where $\mathbf{u}^*$ denotes a virtual displacement field, $\boldsymbol{\varepsilon}^*$ its associated virtual strain field, $\mathbf{t}$ the stress vector acting on the boundary $\partial\Omega$ and $\mathbf{f}$ the body load. ρ is the density of the material, $\mathbf{a}$ is the acceleration fields obtained through full-field measurement methods and $\boldsymbol{\sigma}(\underline{P})$ the stress tensor computed from the constitutive law and the experimental strains $\boldsymbol{\varepsilon}$. The methodology relies on the choice of relevant virtual fields. Each virtual field chosen combined with Eq. 2.7 leads to a scalar equation, as a result a number of virtual field equal to the material parameters sought is needed. The virtual fields are usually chosen case by case, however some authors developed methods to automatically choose the virtual fields for elastic cases [Grédiac *et al.*, 2002], then for plastic cases [Marek *et al.*, 2017].

This method has been extensively used for quasi-static loadings to characterize various materials as well as models. For a thorough review of the VFM applications the reader can refer to [Grédiac *et al.*, 2008]. More recently, the VFM has been applied to identify the dynamic tensile strength of concrete [Forquin and Lukić, 2018], or hyperelastic parameters [Tayeb *et al.*, 2021]. In addition, it has recently been extended to dynamics by using the acceleration as a load cell [Pierron *et al.*, 2014] and applied to identify Johnson-Cook strain-rate parameters for titanium alloys [Fourest *et al.*, 2020].

The main drawbacks of such a method can be summarized as follows [Grediac, 1989]. First and foremost, in order to use this method the strains in the volume must be directly related to the surface strains (as a result it is difficult to use it to study 3D composite for example). As a result, this method is usually applied to 2D geometries and loadings. Furthermore, the choice of the virtual fields, even if it can be automatic, requires an expertise of the user of the method.

The two methods presented in this section heavily rely on the ability to retrieve full-field measurements during experiments. This has been rendered possible with the development of full-field measurement techniques as well as the recent advances in optical sensors. As a result in the following paragraphs, such measurement methods will be presented.

2.3.2 Full-field measurement methods

The recent advance in optical sensors as well as full-field measurement methods have opened the way to quantitative kinematic and temperature measurements during complex experiments. Several methods of contactless full-field measurement exist. A small selection of them will be presented in this section.

2.3.2.1 Interferometry

Interferometric methods are one of the oldest non-destructive method to capture full-field displacement fields and have been extensively studied [Rastogi, 2000]. These methods use a monochromatic light source to simultaneously illuminate directly a CCD sensor and the

specimen (see Figure. 2.4). Because of the difference of optical path, the illumination on the CCD sensor will create fringe patterns. By comparing fringe patterns obtained with the specimen unloaded and then loaded, one can retrieve the displacement fields. Among these interferometric methods speckle interferometry and Moiré interferometry are the most popular and widely used.

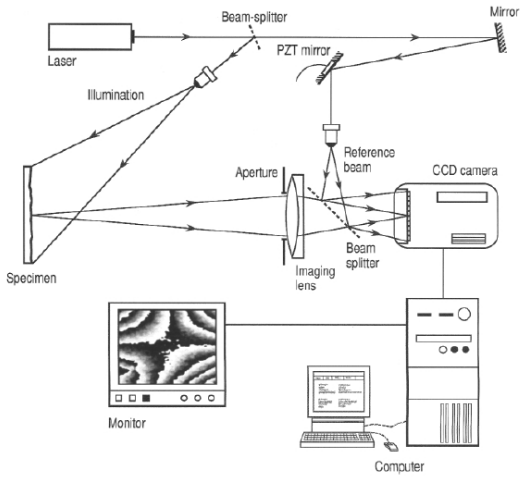

Figure 2.4: Schematic of a speckle-pattern interferometer, figure from [Rastogi, 2000].

For speckle interferometry, the specimen surface is used to generate a speckle pattern, which when compared to a reference one leads to interference patterns. For this method to work, the specimen has to be able to diffuse the illumination light. Furthermore, this method is especially relevant to track small displacements. Moiré interferometry relies on the comparison between an underformed reference grid and one transferred on the specimen. The overlapping of this two grids will lead to Moiré fringes. As a result, in plane displacements fields can be retrieved.

While interferometric methods are very efficient, especially for small displacements, their implementation in practice is quite difficult. Indeed, it requires a complex optical apparatus which is especially sensible to external vibration.

2.3.2.2 White light methods

Grid method The grid method is an in-plane full-field kinematic measurement method which has been thoroughly reviewed in [Grédiac *et al.*, 2016]. This method relies on the use of a known regular pattern: a grid that is transferred onto the specimen. This grid main property, namely its pitch which can range from the µm to the mm, is chosen accordingly with the imaging setup and the magnitude of the strain that needs to be measured. Several techniques exist to create and then transfer such a grid on the test specimen (film bonding, high resolution printing, lithography, laser etching).

The procedure to extract displacements from experimental images is presented in details in [Grédiac *et al.*, 2016]. To this effect, the light intensity is considered quasi-

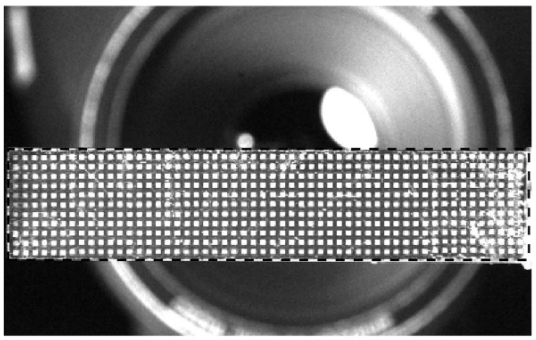

Figure 2.5: Example of a grid used for an ultrasonic experiment in [Seghir *et al.*, 2019].

periodic and is described by the following relation:

$$s(x,y) = \frac{A}{2}(2 + \gamma \text{frng}(2\pi f x + \phi_x(x,y)) + \gamma \text{frng}(2\pi f y + \phi_y(x,y)), \tag{2.8}$$

where $s(x,y)$ is the light intensity at the point (x, y), A is the average global field illumination, γ the contrast of the pattern between 0 and 1, f is the grid frequency, frng is a 2π periodic function with an amplitude of 1 and an average value of 0, ϕ_x and ϕ_y denote the phase modulations. The phase modulations of the grid are caused by displacements and the following relation can be demonstrated:

$$\mathbf{u}(\mathbf{x}) = -\frac{1}{2\pi f}\left(\boldsymbol{\phi}^d(\mathbf{x} + \mathbf{u}(\mathbf{x})) - \boldsymbol{\phi}^r(\mathbf{x})\right), \tag{2.9}$$

where $\mathbf{u}(\mathbf{x})$ is the displacement vector at the point $\mathbf{x} = (x,y)$, $\boldsymbol{\phi}^r$ and $\boldsymbol{\phi}^d$ are respectively the modulations in the reference image and in the deformed image. This relation is obtained by assuming the conservation of the optical flux. The displacements are then retrieved by either linearizing this relation or by using an iterative computation method. As a result, to measure displacements the phase modulation have to be extracted from images. This is usually done through the use of methods based on Fourier Transform. As the phase modulation hence extracted is known modulo 2π spatially and temporally, *unwrapping* techniques are then employed to cancel phase jumps.

The main advantages of this technique are the simplicity of the algorithms, the reproducibility (since it relies on perfect grids) and the high metrological performance of phase-shift techniques. Nevertheless, the main constraint resides in the use of regular pattern, since the transfer of the grid onto the specimen may not be trivial. In addition, actual technologies still limit spatial grid resolutions to 100 µm per period at best, while airbrush paint patterns can go down to a few microns, potentially leading to resolutions of tens of micron with DIC.

Digital Image Correlation The Digital Image Correlation (DIC) is also a kinematic measurement method [Sutton *et al.*, 1983, Chu *et al.*, 1985, Schreier *et al.*, 2009]. It con-

sists in finding the displacement and deformation between two images based on the grey level variation. To this effect, a random speckle pattern is classically used: it is usually obtained by using black and white paint, but sometime the natural material texture may be sufficient [El Bartali *et al.*, 2008].

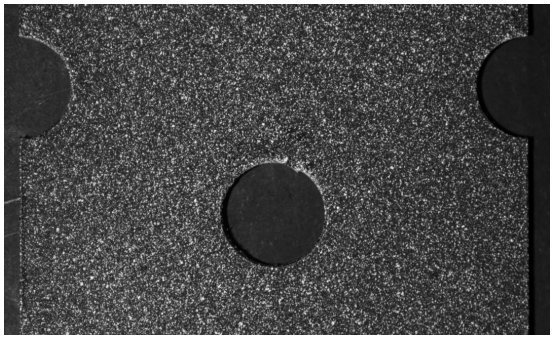

Figure 2.6: Example of a black and white painted speckle pattern.

The objective is to find the displacement between the reference image f and a deformed image g. Using the conservation of the grey level, the following equation is obtained:

$$f(\underline{X}) = g(\underline{X} + \underline{u}(\underline{X})), \tag{2.10}$$

where $\underline{u}(\underline{X})$ is the sought displacement at the position $\underline{X}$, *i.e.* in the reference configuration. Since the problem is ill-posed and in order to be robust to the acquisition noise, the problem is usually transformed into a minimization problem of a chosen criterion over a subset of the image. Several criteria can be used [Pan *et al.*, 2009] for the correlation problem. They are mainly based on the sum of square differences. One notable used metric is the Zero-normalized sum of squared differences (ZNSSD) which is robust to noise and mitigate the impact of change of lightning between two images. In addition, two main different strategies can be distinguished for the consideration of the subset. One strategy consists in considering each subset independently, which lead to the so called local DIC [Hild and Roux, 2012]. Another strategy consists in considering all the subset at the same time, named global DIC [Sun *et al.*, 2005, Besnard *et al.*, 2006].

2.3.2.3 Infrared thermography

Infrared thermography is based on Planck's law, which states that a perfect blackbody, *i.e.* a body whose emitted radiation depends solely on its temperature, with a temperature superior to 0 K will be the source of electromagnetic radiations following the relation:

$$I(\lambda, T) = \frac{2\pi hc}{\lambda^5} \frac{1}{e^{\frac{hc}{\lambda kT}} - 1}, \tag{2.11}$$

where $I(\lambda, T)$ is the spectral radiance of a blackbody for the wavelength λ at T. h denotes Planck's constant, c the speed of light and k the Boltzmann constant. The derivation of

this relation with regard to the wavelength leads to Wien's law that states that for a given temperature, the spectral radiance of a blackbody will reach a maximum for a particular wavelength. As a result, blackbodies with a temperature superior to room temperature and inferior to 1500 K have a peak of emission between 2 µm and 10 µm, which are in the infrared wavelengths. Cameras, similar to the ones used for visible wavelengths, but with photo-sites based on material sensitive to IR wavelengths (*e.g.* indium antimonide (InSb)) and dedicated cooling systems can be used to capture such infrared emissions. In practice, since the material recorded are not perfect blackbody, the relation has to be adapted. In particular, materials usually absorb only partially the incident radiations $a(\lambda)$, reflect partially other radiations $r(\lambda)$, transmit $t(\lambda)$ radiations and emits $\epsilon(\lambda)$. The thermodynamic equilibrium leads to these relations:

$$\begin{aligned} a(\lambda) &= \epsilon(\lambda), \\ \epsilon(\lambda) + r(\lambda) + t(\lambda) &= 1. \end{aligned} \tag{2.12}$$

Furthermore, for opaque materials $t(\lambda) = 0$. It follows that opaque materials emit radiations and reflect as well radiations from their environment. A typical thermal scene is depicted in Figure 2.7, the IR camera records the radiations emitted and reflected by the specimen that passes through the atmosphere, as well as the radiations emitted by the atmosphere itself. At the end, the user has access to digital levels. As a result, in order to retrieve the temperature fields a proper calibration procedure as to be used, and attention has to be given to the sample's emissivity and the test environment. This last point is usually tackled by spraying a very thin coating of black paint which leads to an emissivity close to 1.

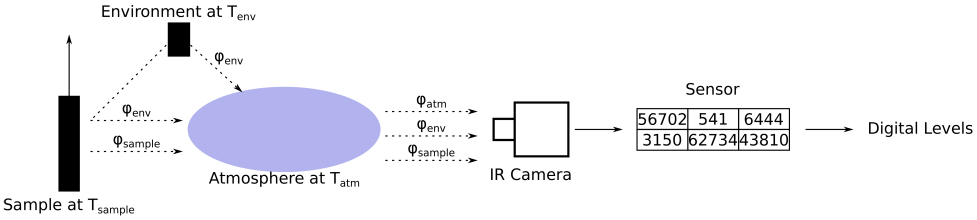

Figure 2.7: Schematic of a thermal scene recorded by an IR camera.

2.3.2.4 Coupled measurements

At last, the strategies used to have access to both temperature and kinematic fields during a single experiment will be briefly introduced here. Three main techniques can be mentioned:

One shot measurement This strategy consists in using a single camera to capture both kinematic and temperature fields during an experiment. This allows to have both

fields in the same configuration and with the same spatio-temporal sampling. This can be achieved by using an InfraRed camera [Maynadier *et al.*, 2012]. In this case, the method relies on the heterogeneity of the sample's emissivity using a special coating to perform DIC to extract displacement fields. However, since the grey level recorded by the camera evolve with the temperature, the optical flow conservation used for DIC is no longer verified. As a result, calibrations procedure have to be performed for each specimen. However, the main drawback of such a method lies in the fact that spatial resolution of IR sensors is far inferior to those of CCD sensors or CMOS sensors (it can be 10 time lower when compared to the best existing CCD sensors). Another method is proposed in [Orteu *et al.*, 2008], which uses CCD cameras that are able to capture near-infrared range radiations. In their work, the authors were able to measure kinematic fields as well as the apparent temperature of the object. In order to retrieve quantitative temperature fields, the evaluation of the emissivity of the specimen is required. The main drawback of the proposed method is that only temperatures above 300 °C can be measured since the CCD camera captures only near-infrared radiations. Hence, this technique cannot be applied for the study of metals at room temperature.

Simultaneous recording on the same face This strategy consists in recording the same face of the sample simultaneously using both visible and infrared cameras. When using one CCD camera to retrieve in-plane kinematic fields, Bodelot and her collaborators [Bodelot *et al.*, 2011] proposed a setup that enables the recording of the specimen surface while ensuring that the cameras optical axis are perpendicular to it. The setup uses a dichroic mirror in front of the sample (see Fig. 2.8). This mirror transmits the infrared radiations of the sample directly to the IR camera, while the visible radiations are reflected into the CCD camera. However, in order to be able to use such methods, the specimen preparation requires proper care. Indeed, temperature measurements require a homogeneous coating with high emissivity, while kinematic measurements require heterogeneous and contrasted coating. One solution proposed by Bodelot *et al.* [Bodelot *et al.*, 2011] is to use a specific coating, made of different oxide powders, that appears uniform in the IR range and heterogeneous in the visible spectrum due to intrinsic coating properties and camera resolutions.

Simultaneous recording on the two faces This strategy may be considered as the most intuitive. Since the temperature measurements require a homogeneous coating and the kinematic measurements require a heterogeneous one, each camera records a different face of the specimen. This setup is possible only if the temperature and the kinematic fields are constant through the thickness. This reduces the application range of this setup to thin specimens. Furthermore, in order to retrieve both information in the same configuration, a spatial matching of the two different fields is needed. This can be done by

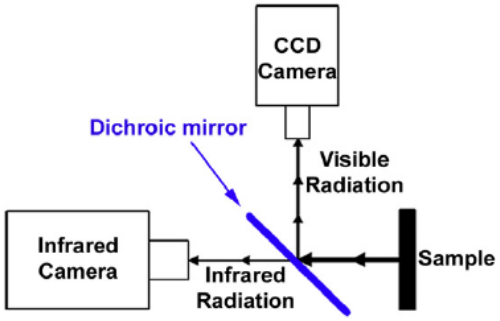

Figure 2.8: Schematic of the experimental setup used to simultaneously measure displacement and temperature fields. The figure is from [Bodelot *et al.*, 2011].

either using a calibration procedure with a calibration target [Wang *et al.*, 2016a] or by using specific points in the sample's geometry [Toussaint *et al.*, 2012].

To summarize, by taking advantage of the recent advance in optics and in full-field measurements methods, it is now possible to have access to both kinematic and temperature fields in the same configuration during an experiment. In addition, complex stress distribution can now be estimated. This strongly widen the mechanical test design space, opening the way to the development of statically undetermined tests leading to heterogeneous and complex fields.

In the last 6 years, very recent development of different strategies to estimate stress fields during experiments without using constitutive laws have been developed [Pierron *et al.*, 2014, Kirchdoerfer and Ortiz, 2016, Leygue *et al.*, 2018, Liu, 2021, Cameron and Tasan, 2021]. In particular, the strategy devised in [Leygue *et al.*, 2018] allows to take advantage of the high spatio-temporal resolutions of available cameras to estimate stress fields during statically undetermined tests without the use of a constitutive law. These innovative methodologies will be presented and explored more in depth in the last part of this work.

Part I

Measurements techniques and metrological assessment

Chapter 3

Kinematic fields measurement: methodology and metrology

Content

3.1 Introduction

The measurement of strains is fundamental when studying the mechanical behaviour of a material. In conjunction with load force measurement, it allows constitutive equations to be established, which is the mandatory brick for material and structure behaviour simulations and safety predictions. Since the 80s and the emergence of contactless full-field measurement techniques, strain fields can nowadays be quantitatively captured within more and more complex experimental and loading configurations. Nevertheless, they remain challenging when studying transient phenomena in opaque materials subjected to heterogeneous loadings, for instance: wave and crack propagation, adiabatic shear band instabilities, shock-induced damage, microstructure transformations and/or phase transition. Such phenomena require, to be captured and understood, both high temporal and high spatial samplings. Recent developments of full-field measurement methods, combined with the development of time and space-resolved ultra-high speed cameras, opened the way to the study of such dynamic phenomena during high strain-rate tests.

Figure 3.1 is a chart that represents the majority of the high speed cameras available on the market. The rectangle area denotes the image size of the camera and the circular pie represents the shutter time as a fraction of the interframe time. High speed cameras are in the top left corner of the chart. Due to limited memory transfer times between the camera and a computer, a trade-off has to be made between the temporal and the spatial sampling. This is highlighted by the fact that the areas decrease when the number of

fps increases. Ultra high speed cameras (located in the bottom side of the chart) propose technologies that allow to bypass such limitations. To do so several strategies are adopted. For example, some cameras (*e.g.* Kirana, Shimadzu) store the data on their chip. This enables these cameras to have a constant spatial sampling for the range of fps available. However, due to the in-situ storage, their spatial sampling is quite low (400 × 250 pixels for the Shimadzu HPV-X) as depicted by the red and blue square areas. Another strategy is to rely on multi-sensor technologies (Gated intensified cameras or cameras with a rotating mirror). These technologies are the only one that allow to record images at ultra-high speed with spatial samplings higher than 1 mega-pixel. Nevertheless, ultra-high speed technologies remain limited regarding the number of frames they can record (*e.g.* 78 for the Cordin-580, 128 for the Shimadzu HPV-X2, 180 for the Kirana).

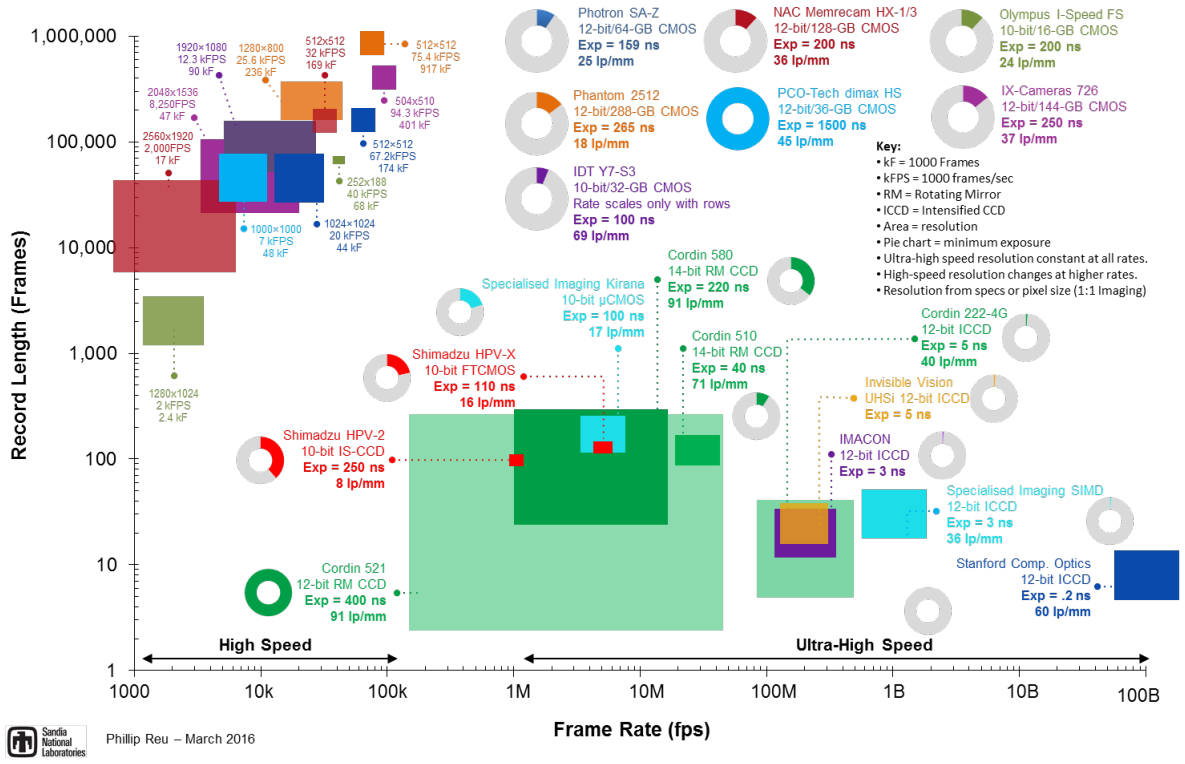

Figure 3.1: High speed camera chart from [Reu and Nissen, 2014]. The rectangle area denotes the image size while the circular pie represents the shutter time as a fraction of the interframe time.

In that technological context, dynamic processes observation and characterization have been developed over the past years. For instance, in 2007, Kajberg *et al.* [Kajberg and Wikman, 2007] imaged impact tests with with 15 frames of 166 × 192 pixels at 125,000 frames per second (fps) with a high speed camera. Using a speckle pattern and Digital Image Correlation (DIC), the authors were able to retrieve the displacement and strain fields with random errors of 0.1 pixel and 15 mm/m, respectively. In 2015, Gao *et al.* [Gao *et al.*, 2015] studied brittle fracture mechanisms considering a notched semi-circular specimen

made of concrete subjected to dynamic three-point bending. By taking 24 photographs of 1082 × 974 pixels at a speed of 180k fps and with the use of both DIC and elastic fracture mechanics theory, the authors were able to extract the crack-tip position, its speed and the dynamic fracture initiation toughness of the material for different loading rates. In 2018, Forquin *et al.* [Forquin and Lukić, 2018], studied the tensile response of concrete when exposed to high strain-rates. Using the grid method, the authors extracted the displacement and the strain fields from 102 images of 312 × 260 pixels taken at 1 million fps. Furthermore, experimentally computing acceleration fields and using the Virtual Fields Method (VFM), the mean stress and Young modulus were identified. Results were consistent with the data obtained using numerical simulations and a PRM Damage model. These works demonstrate the ability to measure mechanical values of interest during a high strain-rate experiment. However, the presented works highlight the actual systematic trade-off to find between the number of frames used to sample the event, the temporal sampling and its spatial counterpart, when using a mono-sensor camera.

On the other hand, multi-sensor technologies provide two ways of recording at high and ultra-high frame rates while maintaining an image resolution higher than 1 mega-pixel. Gated Intensified CCD cameras split the beam into the number of captured frames (usually less than 16). The resulting low intensity beams have to be amplified. This technology allows the user to record few frames at ultra-high speed with an image resolution above 1 mega-pixel. This technology has been successfully used for dynamic experiments [Tiwari *et al.*, 2007, Pierron *et al.*, 2011a, Pierron *et al.*, 2011b, Le Louëdec *et al.*, 2015]. However, these works highlight a high level of noise [Pierron *et al.*, 2011b]. According to the authors, this noise, spatially correlated, is attributed to a "leakage" of the photons from an amplifier to the pixels surrounding it. It creates, in practice, significant blurring of the images, compromising the quality of strain measurements. In 2019, Rubino *et al.* [Rubino *et al.*, 2019] delivered an interesting comparison of DIC fields obtained from gated-intensified and mono-sensor technologies, emphasizing such a strong increase of measurement uncertainty. Moreover, as only few frames can be recorded for practical consideration, a trade-off has to be made anyway between the acquisition speed and the duration of the event recorded. The second technology is, to the authors' knowledge, *the only one* that allows a significant number of frames to be recorded with an image resolution higher than 1 mega-pixel (see Fig 3.1). It relies on a rotating mirror and multiple sensors. Haboussa *et al.* [Haboussa *et al.*, 2011] studied in 2011 the effect of a hole or a pre-crack on the propagation of a dynamic crack. The authors recorded the dynamic crack propagation in a PMMA sample at 200k fps using a rotating mirror camera Cordin-550. They were able to extract the crack tip position, which was in good agreement with the results of X-FEM simulations. Using the rotating mirror camera Cordin-550, Jajam *et al.* [Jajam and Tippur, 2011] studied in 2011 the dynamic crack propagation through a glass inclusion in an epoxy pre-notched sample. By recording the events at 300k fps, with 32 images of

1000 × 1000 pixels, Jajam *et al.* were able to extract the crack tip position, its speed and the stress intensity factors (SIFs). They could observe the influence of the bond between the inclusion and the matrix as well as the influence of the inclusion's position on the crack growth and the SIFs. Similarly, Lee *et al.* [Lee *et al.*, 2012] studied the dynamic fracture of unidirectional graphite/epoxy composite. A Cordin-550 was used to record the events between 100k fps and 250k fps. Using DIC, the authors were able to extract the SIFs values for different samples.

While a series of works has used such technology to observe in details dynamic processes and even extract some fracture mechanics parameters, only a couple have achieved quantitative measurements and performed a metrological analysis of such cameras, where important measurement bias can arise due to the multiplicity of the optical paths [Kirugulige *et al.*, 2007, Pierron *et al.*, 2011a, Moulart *et al.*, 2011]. Moreover, in these few valuable works, displacement and strain noise floors were evaluated using a route that may be questionable. Indeed, the methodology, which will be referred to as sensor-to-sensor approach, consists in using two sets of successive and independent image sequences of static samples, and in evaluating kinematic errors by comparing the images taken by the same sensor. Hence, displacement fields are computed for each image in a different and distorted configuration due to complex optical path. This has to be opposed to the classical Lagragian approach in mechanics where the whole kinematic history has to be expressed in a single undistorted reference configuration. Such a procedure is a way to bypass the issue of evaluating individual sensor distortions by assuming that they are sensor-dependent but small and constant from one shot to another. In the present work, it will be demonstrated that these assumptions are not necessarily fulfilled. Furthermore, it will be shown that the use of these assumptions may lead to significant errors on the displacement and strain fields. In that context, the various authors only obtained lower bounds of displacement and strain random errors, in the order of 0.1 pixels and 1 mm/m, respectively. Kirugulige *et al.* [Kirugulige *et al.*, 2007] went one step further by identifying an affine distortion correction for each sensor, in order to mitigate the impact of the distortions induced by the optical apparatus.

In this PhD work, we will focus on a camera using a rotating mirror as well as multiple sensors. While a proper metrological assessment has yet to be done before using this kind of camera to perform proper DIC, the technology has now achieved an unprecedented combined spatio-temporal sampling and length of recording, compared to the other available technologies. This spatio-temporal sampling will allow, for instance, to take fully advantage of statically undetermined tests at high strain-rates leading to heterogeneous fields, in order to characterize materials. This also potentially opens the way to the characterization of materials during transient and localization phenomena. In that context, the present chapter proposes a new, potentially more robust, calibration procedure ded-

icated to such a multi-sensor ultra-high-speed camera. The displacement field measured is a composition between the effective displacement field and the distortions induced by the camera. Thus, the dedicated calibration procedure for the ultra-high-speed camera Cordin-580 that enables the retrieval of the effective displacement field is presented first. Hence, particular attention is given to the distortions induced by the complex optical apparatus and the chosen way to model them. The metrological issues raised by the camera will also be discussed and the performances obtained analysed.

Notice that the majority of the information in this chapter can be found in [Vinel *et al.*, 2021].

3.2 Digital Image Correlation

The methodology relies on Digital Image Correlation (DIC) at two stages. First for the estimation of the total displacement and also for the distortion model calibration. In this section, the principle of DIC is presented, as well as some details about its implementation in the open source software Ufreckles [Réthoré, 2018]. DIC is based on the optical flow equation which stands for the conservation of brightness between one reference image f and a deformed image g. This fundamental principle is

$$f(\underline{X}) = g(\underline{X} + \underline{u}(\underline{X})), \tag{3.1}$$

where $\underline{u}(\underline{X})$ is the sought displacement vector at the position $\underline{X}$ in the frame of the reference image. Note that this non-linear inverse problem is ill-posed, since two components are sought for the displacement but only one equation can be written for the grey level conservation. Images are discrete by nature, since they are acquired by a sensor composed of a matrix of photosites where photons are collected. The grey level is thus known at the integer pixel position $\underline{X}_p$. In the following, F is a vector with as many rows as pixels considered in the region of interest (ROI), which collects the value of f at the pixel location $\underline{X}_p$. In this same spirit, $\bar{G}$ collects the value of the advected deformed image $g(\underline{X}_p + \underline{u}(\underline{X}_p))$. To reduce the number of unknowns in the problem, a finite-element description of the displacement fields is adopted. A mesh conforming to the ROI is thus created. It might be a regular mesh of square elements [Besnard *et al.*, 2006] or, as in finite element simulation, a mesh of arbitrary shaped finite elements of different types. Only linear elements are considered in the following; they can be either quadrangles or triangles. A generic form for the displacement field is

$$\underline{u}(\underline{X}) = \sum_{n \in \mathcal{N}_n} N_n(\underline{X}) \underline{U}_n. \tag{3.2}$$

Note that $\underline{U}_n$ is the nodal displacement at the node n, which has two components. In the same manner as for the image, $\boldsymbol{N}$ will collect the value of the finite-element shape functions N_n at each pixel of the reference image. $\boldsymbol{N}$ is thus a matrix with a number of rows equal to the number of pixels, and the number of columns is the number of nodes $\mathcal{N}_n$. If $\underline{U}$ is the vector collecting the nodal displacement vector, then the vector collecting the displacement vector at all the pixels of the ROI is:

$$\underline{U}_p = \boldsymbol{N}\underline{U}. \tag{3.3}$$

The resolution of the optical flow equation, even in its discrete format, is a non-linear problem that will be solved following an iterative process. Given an initial vector of nodal displacement $\underline{U}^i$, a solution increment $\underline{dU}$ is sought. After a linearisation of the deformed image advected by this new solution, the problem is written in a matrix format for all the pixels within the ROI:

$$F = \bar{G} + \nabla_X \bar{G}. * \boldsymbol{N} dU_X + \nabla_Y \bar{G}. * \boldsymbol{N} dU_Y. \tag{3.4}$$

In this equation, $\nabla_X \bar{G}, \nabla_Y \bar{G}$ are vectors collecting the value of the two components of the advected image gradient, dU_X, dU_Y vectors collecting the components of the vector nodal displacement increment $\underline{dU}$ and $.*$ stands for the element-wise multiplication of the vector/matrix element along the line index. After some manipulations, one obtains the following linear system of equations:

$$[\ \nabla_X F. * \boldsymbol{N} \qquad \nabla_Y F. * \boldsymbol{N}] \begin{bmatrix} dU_X \\ dU_Y \end{bmatrix} = F - \bar{G}. \tag{3.5}$$

In this system of equations, the gradient of the advected image has been replaced by the gradient of the reference image. This generally affects the convergence speed, but it allows for this gradient to be computed once. This over-determined system is solved in a least-squares sense by assembling the usual operator of the Sum of Squared Difference (SSD) criterion in DIC:

$$\boldsymbol{M} \begin{bmatrix} dU_X \\ dU_Y \end{bmatrix} = b, \tag{3.6}$$

with

$$\boldsymbol{M} = \begin{bmatrix} (\nabla_X F. * \boldsymbol{N})^T \nabla_X F. * \boldsymbol{N} & (\nabla_X F. * \boldsymbol{N})^T \nabla_Y F. * \boldsymbol{N} \\ (\nabla_Y F. * \boldsymbol{N})^T \nabla_X F. * \boldsymbol{N} & (\nabla_Y F. * \boldsymbol{N})^T \nabla_Y F. * \boldsymbol{N} \end{bmatrix} \tag{3.7}$$

and

$$b = \begin{bmatrix} (\nabla_X F. * \boldsymbol{N})^T (F - \bar{G}) \\ (\nabla_Y F. * \boldsymbol{N})^T (F - \bar{G}) \end{bmatrix}. \tag{3.8}$$

Moreover, a penalty term is usually added to this least-square problem in order to filter-out spatial noise and thus prevent any issue that may arise from a bad conditioning of $\boldsymbol{M}$. In the present work, a Tikhonov regularization is used [Poggio *et al.*, 1988, Witz *et al.*, 2017b], so Eq. 3.6 becomes:

$$(\boldsymbol{M} + \omega \boldsymbol{R}) \begin{bmatrix} dU_X \\ dU_Y \end{bmatrix} = b - \omega \boldsymbol{R} \begin{bmatrix} U_X^i \\ U_Y^i \end{bmatrix}, \tag{3.9}$$

with

$$\boldsymbol{R} = \begin{bmatrix} (\nabla_X \boldsymbol{N})^T \nabla_X \boldsymbol{N} & (\nabla_X \boldsymbol{N})^T \nabla_Y \boldsymbol{N} \\ (\nabla_Y \boldsymbol{N})^T \nabla_X \boldsymbol{N} & (\nabla_Y \boldsymbol{N})^T \nabla_Y \boldsymbol{N} \end{bmatrix}, \tag{3.10}$$

and where ω sets the cut-off wave length of the induced smearing of the displacement variation. This regularization acts like a low-pass filter on the displacement fields.

In the following, this DIC formulation is used in order to obtain the total displacements (ensuing from the effective mechanical fields and the distortions from the camera). As we will see later on, no camera image is free of distortions so none can be considered as a reference. In this case, the reference image f is a synthetic image of a tailored pattern. This pattern is then used to engrave the surface of the sample (either the target for calibration or the experimental sample). The images acquired by the camera are considered as deformed images g.

3.3 Distortion modelling, calibration and correction

3.3.1 Distortion model

In this study, the distortions are considered continuous and bounded. It is then reasonable to approximate them with polynomials. Therefore, the distortion field is written as:

$$\underline{u_d}(\underline{X}, P) = \sum_k P_k Q_k(\underline{X}), \tag{3.11}$$

where $\{Q_k\}$ is the family of polynomials used to approximate the distortion field and $\{P_k\}$ is the corresponding coefficients. In the present case, Zernike's polynomials are considered. These polynomials are generally used in ophthalmology [Thibos *et al.*, 2002] to describe the retina's deformation and aberration. They are defined on the unit circle, and thus rely on polar coordinates: $\theta \in [0; 2\pi]$ and $\rho \in [0; 1]$. The polynomials are defined as follows [Lakshminarayanan and Fleck, 2011]:

$$\begin{aligned} Z_j^i(\rho, \theta) &= R_j^i(\rho)\cos(i\theta), \\ Z_j^{-i}(\rho, \theta) &= R_j^i(\rho)\sin(i\theta), \end{aligned} \tag{3.12}$$

where j is the order of the model, $j \geq i \geq 0$, and R_j^i are radial polynomials defined as:

$$R_j^i(\rho) = \begin{cases} 0, \text{ if j-i is odd,} \\ \sum_{k=0}^{\frac{j-i}{2}} \frac{(-1)^k (j-k)!}{k!(\frac{i+j}{2}-k)!(\frac{j-i}{2}-k)!} \rho^{j-2k}, \text{ else.} \end{cases} \tag{3.13}$$

Figure 3.2 displays the various polynomials involved in a 5^{th} order model. Using this basis gives a physical meaning to the modes: for instance Z_1^{-1} and Z_1^1 are the stretch and rotation components when Z_3^{-1} and Z_3^1 describe a barrel effect.

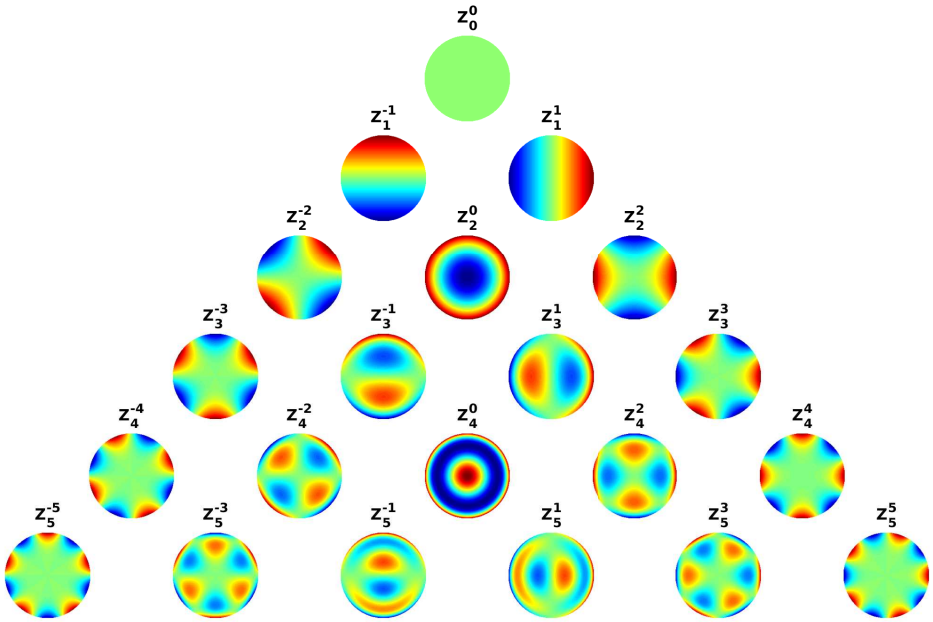

Figure 3.2: Zernike modes up to the 5^{th} order.

3.3.2 Calibration of the distortion model

To calibrate the distortion model, *i.e.* to obtain its parameters from a set of images, a FE-DIC problem is solved on a reduced basis. This reduced basis is the finite-element approximation of the Zernike polynomials of order j. Hence, the component in the X direction of the sought displacement has the following form:

$$u_d^X(\underline{X}) = \sum_k \sum_{n \in \mathcal{N}_n} N_n(\underline{X}) P_k^X Q_k(\underline{X}_n), \tag{3.14}$$

where $\underline{X}_n$ are the nodal positions. Using the notation introduced in Section 3.2, this description of the displacement field is recast as:

$$\underline{U}_d^X = \boldsymbol{N}\boldsymbol{Q}\underline{P}^X, \tag{3.15}$$

where, in the same spirit as in Section 3.2, $\boldsymbol{Q}$ collects the value of the selected Zernike polynomials at the nodal positions and $\underline{P}^X$ collects the amplitude of the polynomials for the X component of the displacement. Using this reduced description of the displacement fields, the DIC problem is rewritten as:

$$\underline{\boldsymbol{Q}}^T \, \boldsymbol{M} \underline{\boldsymbol{Q}} \begin{bmatrix} dP_X \\ dP_Y \end{bmatrix} = \underline{\boldsymbol{Q}}^T \, b, \tag{3.16}$$

where $\underline{\boldsymbol{Q}}$ is a block diagonal matrix filled with two $\boldsymbol{Q}$ matrices. The incremental correction of the Zernike amplitudes for the two components of the distortion field are thus obtained directly from the images of a dedicated target obtained by the camera (used as deformed images) and a synthetic image of the target (used as a reference image).

3.3.3 Computation of the effective displacements

Once the distortion model is calibrated, the effective displacements $\underline{u}_r$ have to be retrieved from the total displacements $\underline{u}_T$ obtained by DIC. However, its computation is not straightforward since it results, in the general case, from the composition of the distortion and the sample deformation as presented in Fig. 3.3. This leads to the following non-linear equation:

$$\underline{u}_T(\underline{X}) = \underline{u}_r(\underline{X}) + \underline{u}_{di}\left(\underline{X} + \underline{u}_r(\underline{X})\right), \tag{3.17}$$

where $\underline{u}_{di}$ is the distortion field during the recording. Contrary to the DIC problem presented above, this non-linear inverse problem is well-posed. There is thus no need to solve it *in average* in a least-squares sense. Hence, the resolution is performed point-wise. From an initial estimate of $\underline{u}_r = \underline{u}_T\left(\underline{X}\right) - \underline{u}_{di}\left(\underline{X}\right)$, an incremental correction $\underline{dU}_r$ to the current nodal displacement $\underline{U}_r$ is sought. Equation (3.17) is linearized assuming that the correction is small and the following linear system is solved at each node of the finite-element mesh used for estimating $\underline{u}_r$:

$$\underline{\underline{\nabla}} \, \underline{u}_{di}\left(\underline{X}_n + \underline{U}_r\right) \underline{dU}_r = \underline{U}_T - \underline{U}_r - \underline{u}_{di}\left(\underline{X}_n + \underline{U}_r\right). \tag{3.18}$$

After solving this linear system at each node, the effective displacement $\underline{U}_r$ is updated using the estimated correction $\underline{dU}_r$. Note that the distortion field $\underline{u}_{di}$ is defined by polynomials whose gradient can be estimated analytically. The convergence of this non-linear iterative process is thus extremely fast, robust and accurate. Convergence to a numerically zero correction is usually obtained after 2 to 3 iterations. Notice that the initial guess suggested above corresponds to an additive composition of the distortions and the effective sample transformation, which in practice is closely related to the solution obtained when using a sensor-to-sensor approach. A correction to this first (rough) estimate is accessed through the proposed procedure.

Fig. 3.3 summarizes the various transformations occurring when recording a static sample (in blue) or a moving sample (in red). $\underline{X}$, $\underline{X}_d$, $\underline{x}$ and $\underline{x}_d$ denote, respectively, the reference configuration, the reference configuration but distorted, the deformed configuration and the deformed configuration but distorted. In addition, $\underline{u}_{d1}$ and $\underline{u}_{d2}$ denote, respectively, the distortion fields when recording a static (moving) sample. Indeed, we will see in Section. 3.4.3 that a non-negligible level of variability can be observed on camera distortions from one shot to another, which must be taken into account when attempting to compare series of images. Finally, $\underline{u}_{ss}$ denotes the displacements obtained when using a sensor-to-sensor approach (*e.g.* [Moulart *et al.*, 2011]). From this figure, the following relation can be deduced:

$$\underline{u}_{ss}(\underline{X}_d) = \underline{u}_r(\underline{X}) + \underline{u}_{d2}(\underline{X} + \underline{u}_r(\underline{X})) - \underline{u}_{d1}(\underline{X}). \tag{3.19}$$

It follows that the first order error, ϵ, when using a sensor-to-sensor strategy can be computed as follows:

$$\epsilon \approx -\underline{\underline{\nabla}}\, \underline{u}_{d2}(\underline{X}) \cdot \underline{u}_r(\underline{X}) + \underline{u}_{d1}(\underline{X}) - \underline{u}_{d2}(\underline{X}). \tag{3.20}$$

In this relation, three terms appear: the gradient of the experiment's distortions, the effective displacement and the difference between the calibration's distortions, and those of the experiment. Hence, for this error to be negligible, three conditions have to be met: the displacements must be small enough during the experiment, the distortions must be small and constant enough from one shot to another. It will be shown that these conditions are not fulfilled when using a Cordin-580. An estimation of the error introduced when using a sensor-to-sensor (or additive) approach in comparison with a true composition approach, in terms of resulting displacement and strain fields, will be discussed in Sections 3.4.5 and 5.2.

3.3.4 Target design and manufacturing artefacts

Usually, DIC is performed between two images taken by the same camera. In the present case, as distortions are induced by the camera, a true reference is needed. In order to have an undistorted image of reference, a highly spatially resolved (*e.g.* 50M pix) image of a black and white sprayed paint speckle can be taken or a synthetic one can be created. Both options will be used in this work, but only a synthetic reference image will be used within this metrological chapter. Several kinds of targets are proposed in the literature for optical calibration. Usually, dot patterns [Kirugulige *et al.*, 2007] or grids [Pierron *et al.*, 2011a] are used. However, in this study, a speckle pattern will be used. It will provide information all over the sensor, for all distortion spatial frequencies, and will fall into a single DIC framework. Several articles have been published tackling the issue of generating optimized

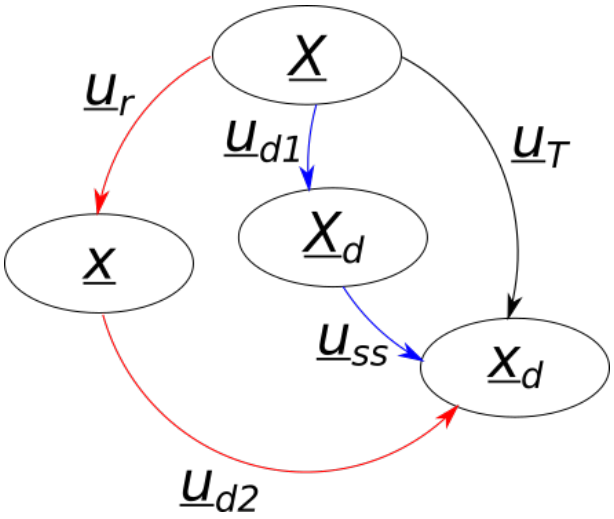

Figure 3.3: Schematic diagram of the transformations for a static sample (in blue) and for a moving sample (in red). This Figure emphasizes the fact that the distortions can differ from one shot to another. $\underline{u}_r$ is the effective displacement, while $\underline{u}_{ss}$ denotes the displacement obtained using a sensor-to-sensor approach.

speckle patterns for DIC [Kirkpatrick *et al.*, 2007, Song *et al.*, 2016]. This is usually done by working in Fourier's space then applying an inverse transformation [Bossuyt, 2013]. In the present methodology, an image twice the size of the sensor's size is generated, in order to avoid any boundary effects. A ring is constructed in Fourier's space, in which the amplitude and the phase are randomly attributed following a Gaussian law between -1 and 1. The radius of the ring defines the size of the pattern, the thickness defines the pattern's variation and the random values define the pattern intensity's variation. The speckle pattern is obtained using an Inverse Fast Fourier Transform (IFFT). It is then cropped to the sensor's size (Fig. 3.4a). The obtained pattern is then dynamically renormalized in 16 bits so that the whole range of grey level is used (Fig. 3.4b).

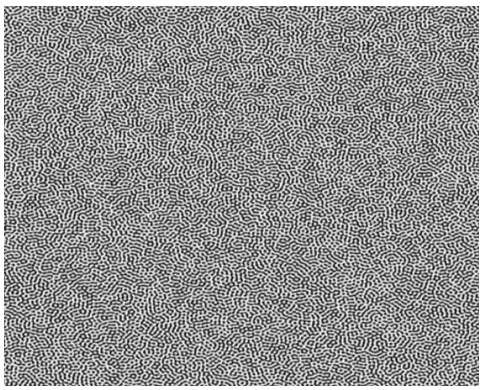

(a) Portion of the speckle pattern generated.

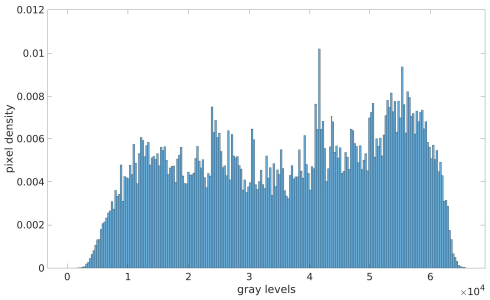

(b) Histogram of the speckle pattern.

Figure 3.4: Generation of a speckle pattern.

Several techniques have been tried to transfer this synthetic speckle pattern to a physical target: using a standard printer, using a professional printer on a dibond plate, and

using a laser-etching machine. All of these induced some specific artefacts. Here, only the artefacts induced by the laser-etching machine will be discussed, since this is the technology used in the rest of the metrological analysis of the Cordin-580. The laser-etching machine used for this work produces a beam with a size of approximately 200 µm. By controlling the intensity of the beam and its speed, the speckle can be printed on a PMMA sample with an approximate etching depth of 50 µm. Due to the beam size of this machine, the manufacturing of patterns smaller than 600 µm to 800 µm cannot be achieved. As a result, for small specimen, the reference image will be created using a highly spatially resolved image of a black and white sprayed paint speckle (see Chapter 7). The effective displacement u_{raw} obtained (after deconvolution, see Eq. 3.18) when performing DIC between the synthetic speckle pattern and the first frame taken by the camera is depicted in Fig. 3.5a. Vertical and horizontal (not shown) bands with a magnitude of approximately 1 pixel are detected. To study the evolution of these bands over time, a pixel line orthogonal to the bands (depicted by the black dashes in Fig. 3.5a) is plotted for all the frames (Fig. 3.5b). This highlights the fact that these bands are stationary. Hence, it is thought that these bands are induced by the printing method (for instance by the screws controlling the displacement of the beam-head). Considering the very low amplitude of such systematic bias induced by the printing technology, and in order to cancel-out contribution, in the rest of this work the effective displacements will systematically be corrected, in an additive manner, as follows:

$$\underline{u}^i_{\text{corr}} = \underline{u}^i_{\text{raw}} - \underline{u}^1_{\text{raw}}, \tag{3.21}$$

where i is the frame number. Notice that this procedure implies that the first frame taken, during the experiment, is an image of the sample at rest. In this case, it only encloses such a stationary printing bias.

3.3.5 Error definition

The indicator classically used in DIC to quantify the quality of the measurement is the mean value and the standard deviation of displacement fields computed using a series of images of a static sample. The first one refers to the systematic error (bias), while the second assesses the random error; *i.e.* the uncertainty. However, since the camera used in this work relies on multiple sensors, systematic error can be different from one frame to another; thus, the global standard deviation, over a series of images, may include both systematic and random errors. To avoid any confusion, systematic error is simply obtained from the mean error over field and sensors, while the global camera random error indicator is obtained from the square root of the average of the sensor variances ($\bar{V^s}$ see Eq. 3.22), noted as σ_{cam}. In comparison, single-sensor random error (see, *e.g.,* in Section 3.4.2) is simply noted as $\sigma\,(s)$.

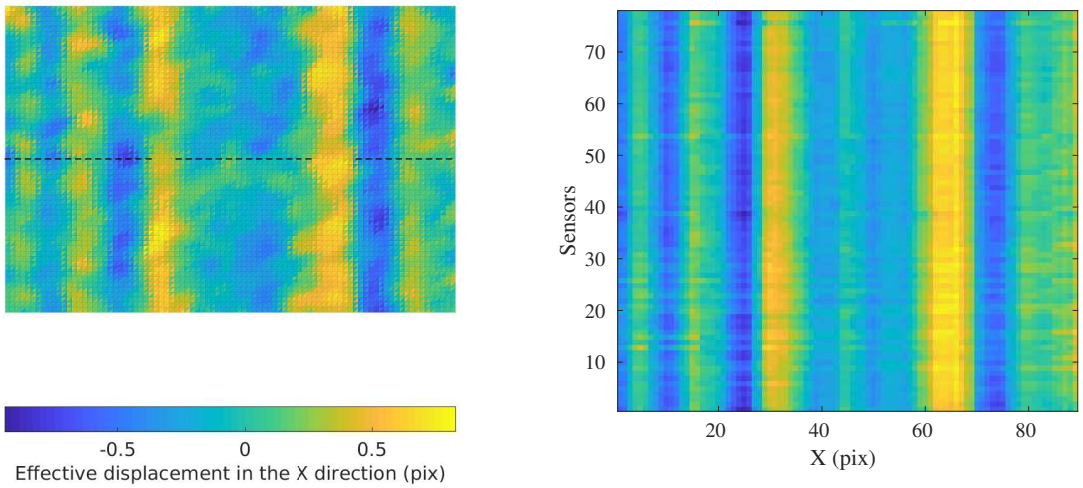

(a) artefacts induced in the X direction on Frame 1,

(b) Evolution of the artefacts along all of the sensors,

Figure 3.5: Example of the artefacts induced by the printing and their evolution on the sensors.

$$
\begin{aligned}
V^s &= \frac{1}{\mathcal{N}_n} \sum_n (\underline{U}_n^s - \overline{\underline{U}^s})^2, \\
\sigma(s) &= (V^s)^{\frac{1}{2}}, \\
\sigma_{\text{cam}} &= (\overline{V^s})^{\frac{1}{2}},
\end{aligned}
\tag{3.22}
$$

where $\underline{U}^s$ denotes the displacement field obtained for the sensor s.

Notice that such definition of the systematic error and the random error is totally fair as long as we deal with displacement, strain and strain-rates, which is the objective of this chapter. Nevertheless, it does not clearly highlight the error arising when differentiating displacement from one frame to another; *i.e.* dealing with speed and acceleration. Indeed, in that case, an additional indicator capturing the systematic error jump from one frame to another would need to be defined. It may be computed, for instance, as the standard deviation over a series of images of the mean displacement value per sensor.

3.4 Application to the Cordin-580

3.4.1 Presentation of the Cordin-580

As introduced above, the camera used in this work is a Cordin-580. This camera is a rotating mirror camera that is able to capture 78 images with a resolution of 2472 × 3296

pixels (*i.e.,* 8 mega-pixels), up to a speed of 4 millions fps. For speeds below 500k fps, an electric turbine is used for mirror rotation. Between 500k fps and 700k fps, a dedicated gas turbine is fed with compressed air. Finally, above 700k fps, both the gas turbine and the camera must be fed with helium to increase the rotation speed and mitigate friction. Within the framework of this PhD thesis only the electric drive will be used, so we will focus on speeds lower than 500k fps. Nevertheless, the proposed methodology is not turbine dependent.

The optical apparatus used in the camera is depicted in Fig. 3.6a. The light-beam, depicted by the black arrows, enters the camera through the objective. It then encounters a cube beam-splitter, that will either transmit the light or reflect it with an angle of 45°. The light is then reflected on mirrors until it reaches a lens. After this lens, another mirror reflects the light beam onto a 3-faced rotating mirror. Finally, the light goes through a lens, used to mitigate the bias induced by the mirror rotation over individual sensor exposure time, and eventually reaches the sensor. Additionally, some specificities of the camera's geometry are worth mentioning. First, in order to let the light beams pass, Sensors 40 and 80 do not exist, thus black images are given for these theoretical sensors. Furthermore, due to their positioning, Sensors 21 to 60 are always the ones hit by the beam reflected by the beam-splitter. For the same geometrical reasons, Sensors 1, 39, 41 and 79 are illuminated when the rotating mirror is nearly perpendicular to the light beam. On the contrary, Sensors 20, 21, 60 and 61 are illuminated when the rotating mirror is hit by the beam with a shallow angle. This is illustrated in Fig. 3.6b.

Since each optical element (mirror, lens) may have an influence on the final distortion field, it is in practice impossible to determine the contribution of each one. Therefore, a phenomenological model has been chosen (see Section 3.3.1). However, it is possible to identify some physical dependencies of the distortion field. Indeed, given that the beam is split, the distortion field may depend on whether the light has been transmitted or reflected by the beam-splitter. In addition, since the rotating mirror has three faces with their own defects, the distortion field may also depend on which face reflected the light. Furthermore, since there are 78 independent lens – mirror – sensor combinations, the field may differ from one sensor to another. At last, as the mirror can rotate at a speed up to 16,000 rotations per second (RPS), inertial forces may deform the mirror making the distortion field speed dependent.

The objective of the following sections is to identify the minimal bricks and parameters that we need in order to statistically capture camera-induced intrinsic distortions.

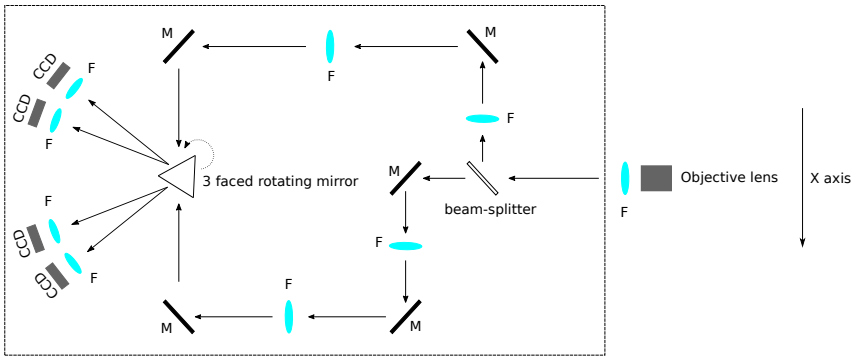

(a) Schematic diagram of the Cordin-580 and its components: M, mirrors; F, lens; CCD, CCD sensors.

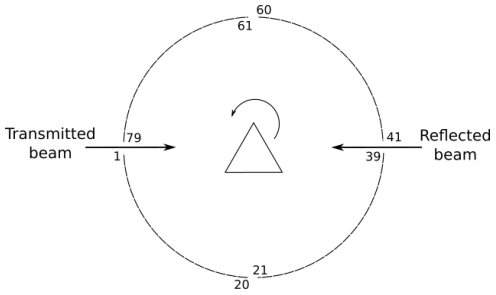

(b) Schematic diagram of the sensor layout.

Figure 3.6: Schematic diagram of the Cordin-580.

3.4.2 Single shot model

Capturing high-order distortions requires a high number of polynomials, which thus decreases the robustness of the identification, especially with respect to noise. To enhance the robustness while maintaining an accurate identification, one can reduce the order of the basis used. In order to find the optimal order of Zernike polynomials, several orders (from 2 to 7) are used to perform a calibration on a particular frame. Indeed, since each sensor has its own focusing system, a relatively significant variation of the focus can be observed from one sensor to another — thus the sharpest image, using the criterion from [De and Masilamani, 2013], is used to identify the model parameters. Once the order is chosen, a calibration is performed on all the frames to ascertain its relevance and see how it behaves as a function of image sharpness.

Frame 12 is first used to perform different calibrations using a different order of the Zernike basis (from 2 to 7). Fig. 3.7 depicts $\sigma(12)$ obtained versus the basis' order for both directions X and Y. As expected, the higher the order, the lower the projection error. From this figure, a 6^{th} order basis is chosen since no significant improvement is achieved with higher orders. This 6^{th} order basis leads to 28 sought parameters per direction. To evaluate this choice and underline relative image sharpness influence, a calibration is performed on a whole image set taken at 480k fps. Fig. 3.8 depicts the random error obtained for each frame in both directions. Notice that the higher the sharpness, the lower the errors. The influence of the sharpness on the projection error is clearly visible — minimizing the

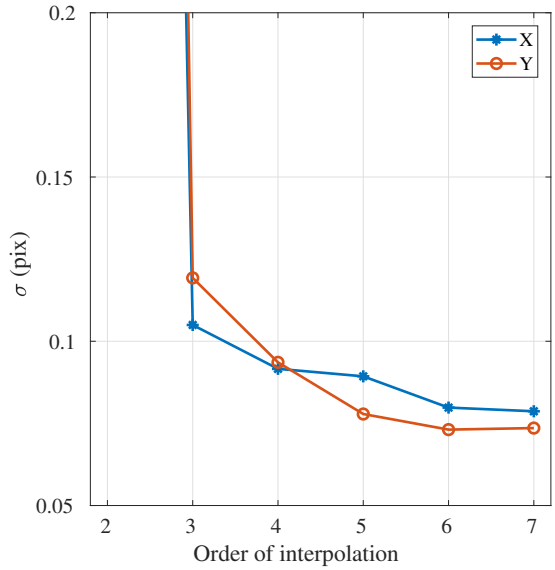

Figure 3.7: $\sigma(12)$ versus the polynomial order.

issue of focus variation from one sensor to another is thus a necessity however it has not been tackled in this PhD thesis. In the end, a calibration with a 6^{th} order basis leads, on average, to a displacement random error, noted as σ_{cam}, of 0.084 and 0.078 pixels in the X and Y directions, respectively. It is interesting to notice that, in practice, the observed variability of the displacement random error from one frame to another is not random over time. This point can be observed in Fig. 3.9, where random errors are displayed, not as a function of sharpness, but rather as a function of sensor number; *i.e.* in the order they appear within the recording time sequence. The relative sharpness variability is still underlined through the use of a linear colour scale. The two dashed lines delineate the sensors hit by the reflected beam from those illuminated by the transmitted beam. Let us recall that Sensors 40 and 80 are non-existent and are replaced by dark images. Hence, their random errors are equal to zero. In Fig. 3.9, two particular signals are obtained: for the X direction (see Fig. 3.9a) random errors have a square-like signal, whereas for the other direction (see Fig. 3.9b) they have a triangular-like signal. It has been verified that these signals are obtained for all the speeds tested. In the X direction, the random error is higher for sensors in the centre of the timeline, meaning when light beams are reflected by the beam-splitter (Fig. 3.6a), from Sensor 21 to 60. Hence, the reflection by the beam-splitter seems to increase the noise obtained on the concerned sensors. On the other side, the triangular signal obtained on Y direction seems to be related to the angle between the mirror face and the incident light beam. Indeed, the random errors are minimal when the light beam hits the mirror face perpendicularly; *i.e.,* close to Sensors 1, 39, 41 and 79, and increase when the angle of reflection becomes more and more shallow (up to Sensor 20 and 60). Notice that, in practice, sharpness issues (see Fig. 3.8) and incident beam angle issues (see Fig. 3.9b) are closely related. Indeed, shallow angles increase the image

blurring. Therefore, such a random error pattern over time is somewhat inherent to the technology.

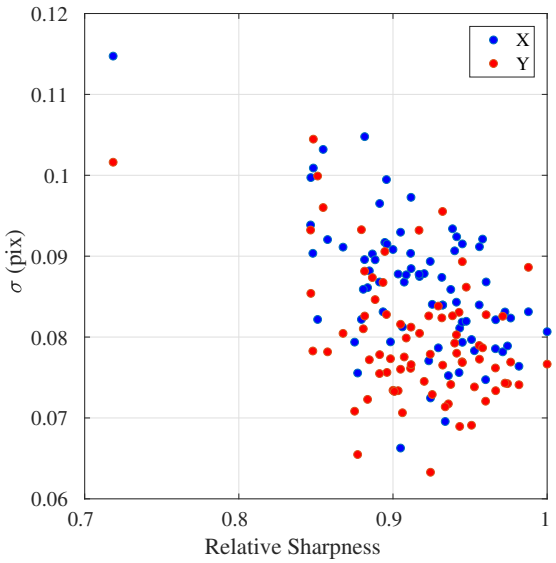

Figure 3.8: Random errors obtained for all frames of a shot taken at 480k fps, with a full 6^{th} order basis.

[h!]

Finally, Fig. 3.10 depicts distortion fields for both directions identified on a particular frame. It highlights the complexity of the distortion fields. Furthermore, let us note that the amplitude of the distortion identified is about 40 pixels, which is non-negligible compared to the effective displacement that we wish to capture during real experiments. This further justifies the need to properly model these distortions.

It is observed, in this section, that a 6^{th} order Zernike polynomial basis and sensor-dependent optimized parameters can capture the complex distortion pattern induced by the camera apparatus for a single shot reasonably well. While the random error is mainly kept below 10^{-1} pixels, it clearly remains sensor-dependent at least for two connected reasons: relative sharpness variation and relative sensor position within the rotation sequence. Such variabilities can potentially be slightly mitigated by finely tuning the individual focus ring but cannot be eliminated.

3.4.3 Camera model

The purpose of the camera model is to deal with potential parameter variation from one shot to another. As introduced earlier, many parts of the apparatus can affect the ultimate distortion perceived by each sensor. Some bias can be systematic, some probabilistic like the impact of the mirror face, and some random like vibrations. The final objective is to have a unique model that is statistically representative of the distortions induced by the

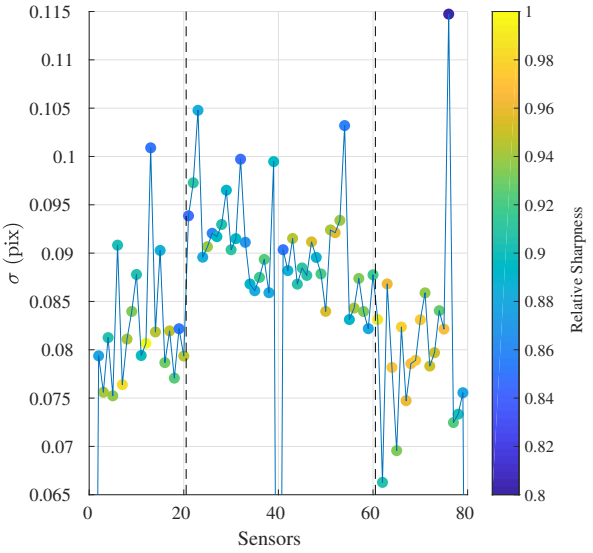

(a) Random errors obtained in the X direction (pix),

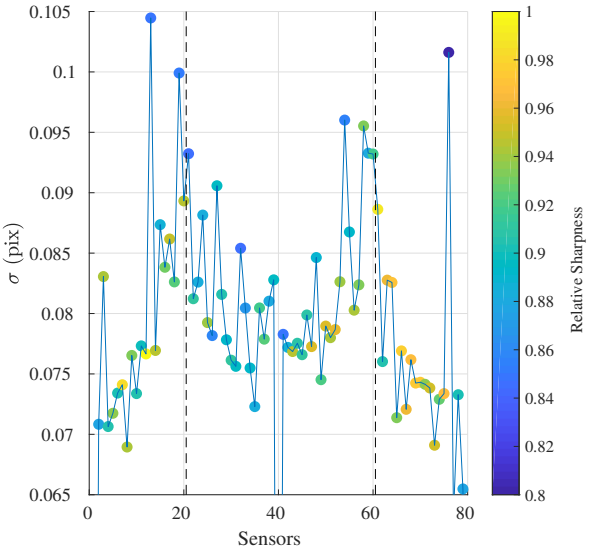

(b) Random errors obtained in the Y direction (pix),

Figure 3.9: Example of the random errors obtained with a shot at 480k fps, in both directions.

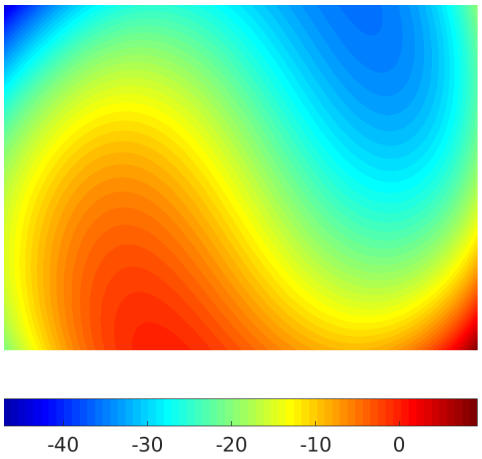

(a) Distortion field in the X direction (pix),

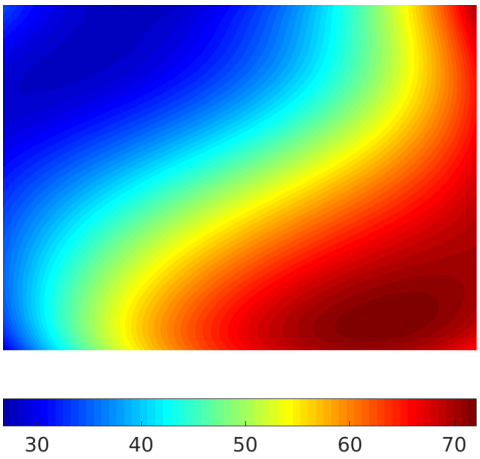

(b) Distortion field in the Y direction (pix),

Figure 3.10: Example of distortion field obtained on a particular frame of a shot at 480k fps, using a 90 mm Tamron objective lens at a working distance of approximatly 50 cm.

camera and calibrated once for all. To do so, the parameters' dependencies are investigated over a large set of recording sequences. To study the possible impact of the rotation speed, shots have been taken for different speeds. In order to statistically have each sensor illuminated by each face of the mirror, several shots have been taken for each speed. Then, using the optimal order polynomial basis found previously, the distortion parameters can be identified for each frame and for each recording shot. Finally, a global camera model is constructed by averaging the parameters associated with the same sensor, the same

mirror face permutation (1 over 3) and rotation speed. That is to say that, for a given speed and a given sensor, the model will have three possible values for each parameter, depending on the mirror face that illuminated the sensor. In the end, the camera distortion model is parameterized by 28 × 2 (directions) × 3 (faces) × 78 (sensors) parameters per acquisition speed; *i.e.,* a total of 13,104 parameters.

In order to carry out the construction of the model, the mirror face illuminating each sensor has to be determined. Since the mirror is rotating, and since the sensors' layout is known, only the mirror face illuminating one of the sensors has actually to be determined. Using optics considerations and the fact that the mirror is not a perfect equilateral triangle, the mirror face can be determined using the parameter corresponding to the rigid-body motion in the Y direction. Indeed, when plotting the value of this parameter for all the shots, three distinctive clusters can easily be identified by means of the k-means clustering algorithm (see Fig. 3.11, each cluster is depicted by a colour). In addition, several typical parameter variabilities can also be underlined. It is observed, in Fig. 3.11, that depending on the mirror position when triggering (1 possibility among three permutations) a rigid-body motion variation of up to 12 pixels can be obtained from one shot to another. It particularly calls into question the classical methodology, which consists in using a previous recording sequence as a reference to cancel-out distortion bias. Furthermore, parameter variation from one rotation speed to another can also be observed on the plot. It induces about 5 pixels of variation over the studied range. Finally, let us note that, at a given rotation speed, there is a spread of about 2 pixels even between the shots from the same cluster. This trend illustrates the variability of the parameters, which is attributed to the vibrations induced by the system. Notice that 2 pixels means a rigid-body motion of 11 µm (with the current experimental settings), which is minor when considering an electric drive rotating at 2,000 RPS. It is obvious at that stage that averaging parameters over a large series of calibration shots will increase the robustness of the model but it is also clear that the residual ±1 pixel variation within individual clusters cannot be eliminated and will lead to a slight increase in the measurement errors obtained, in the previous section, on a single shot.

Once the camera model has been built, it can be re-applied to the calibration shots. The random errors can then be computed and compared to the one obtained previously, where a model was specifically identified for every single shot. In Tab. 3.1 the random errors obtained using the single shot model are compared to those obtained from the camera model, for the shots taken at 480k fps. The systematic error increases by an order of magnitude but remain reasonably low; see for example the systematic Y displacement error, which is 0.15 pixels. Nevertheless, random errors remain in the same order; *i.e.* kept below 0.1 pixels. Note that the levels of strain error are similar to those obtained using a single shot model with a negligible systematic error lower than 40 µm/m combined with a random error lower than 2 mm/m.

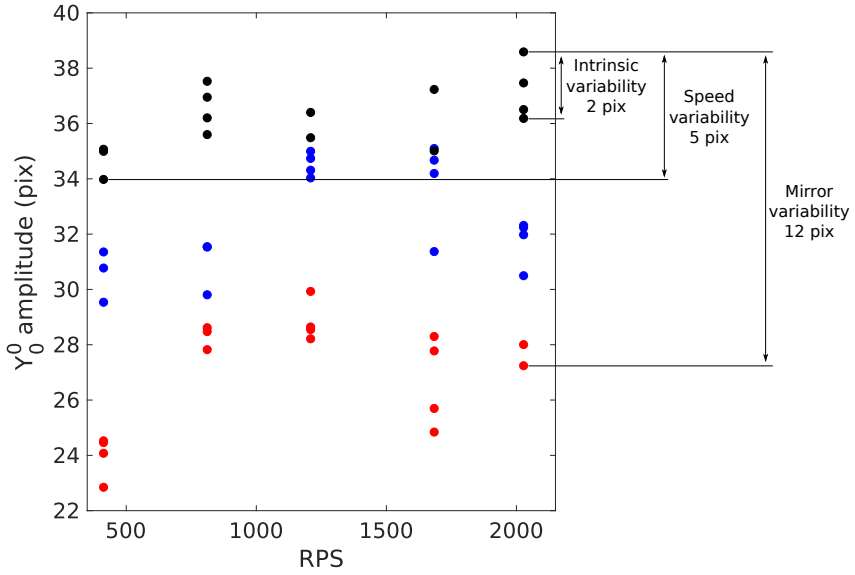

Figure 3.11: Amplitude of Y_0^0 versus the mirror's rotating speed, for each shot taken, for one frame.

Let us note that the pairing between the sensors and the mirror faces illuminating them is *a priori* unknown during an acquisition. Hence, it is necessary to apply the three possible permutations of the global camera model to the experimental data. For the same reasons as explained earlier, the use of the wrong permutation will introduce non-physical displacements in the Y direction, for example a displacement jump of 12 pixels (see Fig. 3.11), from Sensor 20 to 21 and from Sensor 60 to 61. As a consequence, in what follows the correct permutation; *i.e.* appropriate model parameters, are identified manually using, as a figure of merit, the time variation of the displacement field obtained in the Y direction. However, recent developments from the constructor now allow to automatically know the absolute permutation index, thus allowing to skip the metrological step described in this last paragraph.

	Shot-dependent model		Camera model	
	Mean	σ_{cam}	Mean	σ_{cam}
u^x_{corr}	0.003 pix	0.08 pix	-0.020 pix	0.09 pix
u^y_{corr}	0.026 pix	0.08 pix	0.152 pix	0.09 pix
ε_{xx}	$-13.0\,\mu\varepsilon$	$1.6\,m\varepsilon$	$-11.3\,\mu\varepsilon$	$1.6\,m\varepsilon$
ε_{xy}	$36.3\,\mu\varepsilon$	$2.0\,m\varepsilon$	$32.9\,\mu\varepsilon$	$2.0\,m\varepsilon$
ε_{yy}	$-27.2\,\mu\varepsilon$	$1.4\,m\varepsilon$	$-29.6\,\mu\varepsilon$	$1.4\,m\varepsilon$

Table 3.1: Errors obtained for all of the shots taken at 480k fps, using a 6^{th} order Zernike basis and both single-shot and global camera model.

3.4.4 Extrinsic parameters

As explained earlier, the final objective is to have a unique camera model calibrated once for all. However, since the experimental conditions between the calibration procedure and a true experiment may differ, the evaluation of extrinsic parameters has to be addressed.

Since the positioning of the sample, during calibration and/or real experiment, relative to the camera sensor is done manually, measurement fields may differ by an affine transformation. Hence, a correction to the camera model's parameters has to be found and applied, in order to account for the change of these extrinsic parameters. The difficulty here lies in the fact that the sought affine transformation is composed with all the distortions produced along each individual optical path. Therefore, this does not necessarily produce the same effect on each sensor, especially from one side to another of the beam-splitter. Since our camera model is both phenomenological and statistical, a proper deconvolution is complex. In that context, we propose a sensor-dependent evaluation of the apparent change of extrinsic parameters through the acquisition of a set of images prior to the experiment. These images must be taken in the same configuration as for the experiment and the sample has to be static.

Once the pairing is identified, the camera model can be applied to obtain displacements from the images of this static shot. An apparent change of extrinsic parameters can then be evaluated from these fields. In practice, for each sensor, the parameters are obtained from a simple least-squares projection of these displacement fields onto a 6^{th} order Zernike polynomial basis. The camera model parameters are then updated in an additive manner using the parameters obtained from this projection. Let us remark that this correction methodology relies on the assumption that the displacements, captured on a static sequence, are solely induced by the change of *physically* extrinsic parameters (the respective position between the camera and the sample) and that the change actually induced on the images is more complex (to be captured with the full 6^{th} order Zernike polynomial basis).

3.4.5 Validation of the model: Imposed translation

In order to validate the model constructed previously, controlled translations along the X direction have been imposed to the sample using positioning stages (see Fig. 3.12). The controlled translations have been imposed along the X axis from $-2.5\,\text{mm}$ to $2.5\,\text{mm}$ with a step of $0.5\,\text{mm}$. Since the positioning stages have a $10\,\mu\text{m}$ graduation, the systematic error on the imposed displacement is estimated to be $5\,\mu\text{m}$. Furthermore, the alignment between the focal plane and the sample has been ensured using a laser setup. Using this setup, the misalignment error is estimated to be about $0.1°$. The images were acquired with the camera at 100k fps. In addition, a set of images were taken with no displacement

imposed. These images are used in order to correct the change of the extrinsic parameters, as explained previously. Once the correct permutation of the model is identified, the displacement and strain fields can be recovered, as well as the resulting errors (Tab. 3.2). Given that only translations are imposed on the sample, the strains should be zero. The strains obtained remain of the same order of magnitude of those obtained previously (see Section 3.4.3). Focusing on displacement and applying the appropriate pixel to millimetre ratio, here 33.7 µm/pixel, imposed displacements are recovered on average within 8.3 µm (or 0.25 pixels), with a random error of 4.8 µm (or about 0.11 pixels) in the X direction, and -15.6 µm (or -0.47 pixels), with a random error of 4.0 µm (or about 0.12 pixels) in the Y direction. While the random error is close to that obtained previously on stationary images, the systematic error increased slightly. While a significant part of the errors (at least along the X direction) can be explained by the uncertainty of the stage positioning (5 µm), the origin of the systematic error in the Y direction remains unclear. A tiny play within the 3-angle rotation stage composing the experimental setup (see Fig. 3.12) may explain part of the result, but no obvious clue has been found.

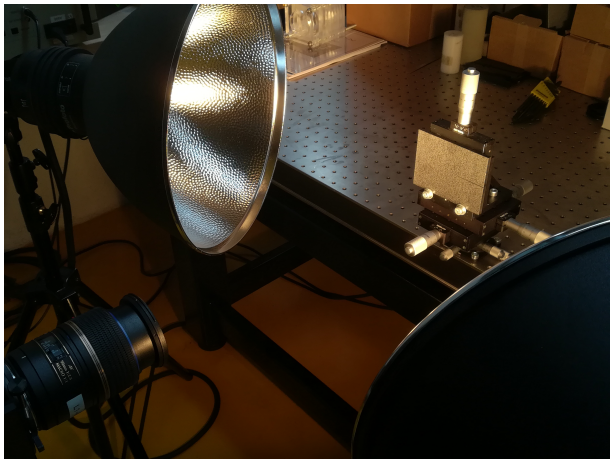

Figure 3.12: Setup for the imposed translation experiment.

While errors obtained following the proposed methodology are apparently close to those obtained in the literature [Moulart *et al.*, 2011] it is interesting to look at the hidden error implicitly induced in previous works when assuming an additive composition of the distortion and the effective displacement. In this work, the composition equation is solved to recover the effective displacement from the knowledge of the distortion and the total displacement (Eq. 3.17). Using Fig. 3.3 and Eq. 3.20, the difference between the two methodologies can be quantitatively assessed. As an illustration, Fig. 3.13 depicts an example of displacement fields and the resulting strain fields obtained using either a composition scheme or an additive scheme, noted respectively as $\underline{u}_r$ and $\underline{u}_{ss}$, for an imposed displacement of 2500 µm. First, let us remark that the use of an additive scheme leads to heterogeneous displacement fields, with amplitude of about 5 pixels. Furthermore, since the displacement fields obtained using an additive scheme are heterogeneous over the

u_{imp}	$u_{\text{corr}} - u_{\text{imp}}$								ε_{xx}		ε_{xy}		ε_{yy}	
	Mean				σ_{cam}									
X	X		Y		X		Y		Mean	σ_{cam}	Mean	σ_{cam}	Mean	σ_{cam}
µm ± 5	µm	pixel	µm	pixel	µm	pixel	µm	pixel	µε	mε	µε	mε	µε	mε
500	11.1	0.33	-40.3	-1.20	5.0	0.15	3.7	0.11	30.3	1.7	-72.3	2.0	31.1	1.5
1000	7.1	0.21	-47.5	-1.41	4.8	0.14	4.5	0.13	7.7	1.7	-34.3	2.0	102.6	1.5
1500	16.0	0.48	-24.1	-0.72	4.6	0.14	3.9	0.12	34.3	1.5	-42.8	1.7	23.0	1.3
2000	29.6	0.88	-25.7	-0.76	4.9	0.15	3.9	0.12	43.0	1.6	-123.3	1.8	-2.4	1.4
2500	19.1	0.57	-32.6	-0.97	4.6	0.14	3.8	0.11	-8.8	1.7	-48.5	1.9	15.4	1.5
-500	9.1	0.27	-15.9	-0.47	4.6	0.14	4.1	0.12	61.7	1.6	-30.7	1.9	-49.1	1.4
-1000	5.1	0.15	-1.3	-0.04	4.4	0.13	3.9	0.12	96.4	1.5	7.1	1.7	-15.7	1.3
-1500	-6.2	-0.18	5.7	0.17	4.9	0.14	3.7	0.11	76.2	1.8	-7.2	2.1	33.7	1.5
-2000	-5.7	-0.17	9.8	0.29	4.9	0.14	4.0	0.12	158.4	1.6	74.4	1.8	29.4	1.3
-2500	-2.5	-0.07	15.5	0.46	5.4	0.16	4.8	0.14	177.7	1.9	83.3	2.0	69.2	1.3
Overall average														
	8.3	0.25	-15.6	-0.47	4.8	0.14	4.0	0.12	98.6	1.7	-19.4	1.9	23.7	1.4

Table 3.2: Systematic errors and random errors obtained for the imposed translations with the model identified at 100k fps.

sensor, they will lead to errors in the strain fields. For example, this lead to errors of about 10 mm/m (or 1 %) on the axial strain, which is 5 times higher than the random error discussed in the previous section. Even more critical, such strain field errors committed when assuming an additive composition are not systematic errors, but are heterogeneous over the sensors, which could strongly affect the analysis of the data. This demonstrates the relevance of the composition assumption in order to obtain the effective displacement and correct strain fields. The importance of this step will be further demonstrated in Section 5.2, where the transformation applied to the sample is no longer homogeneous.

It is important to underline here that the impact of the two additive steps introduced within our methodology to account for extrinsic parameters and printing bias has not been evaluated. Nevertheless, both are associated with tiny displacement fields compared to the camera distortion itself (see Fig. 3.10); thus, it will introduce minor errors.

In the end, a global model has been constructed that is able to model the distortions for a given speed, a given sensor and for a given mirror permutation. By recording a reference sequence prior to the test in its configuration, the change of extrinsic parameters can be accounted for with a correction. The measurement random error obtained with this methodology, for imposed translations, is about 0.2 pixels for the displacement, and 2.0 mm/m for the strain. The global procedure and the errors obtained at each step are summarized in Fig. 3.14. These values are rather high compared to standards in DIC using mono-sensor technologies: 10^{-3} pixels for the displacement and 0.1 mm/m for the strain when using a Shimadzu HPV-X [Fletcher *et al.*, 2019]. However, these results are promising, since the imaging technology used allows images with unparalleled image resolution (8 mega-pixels) to be recorded at ultra-high-speeds.

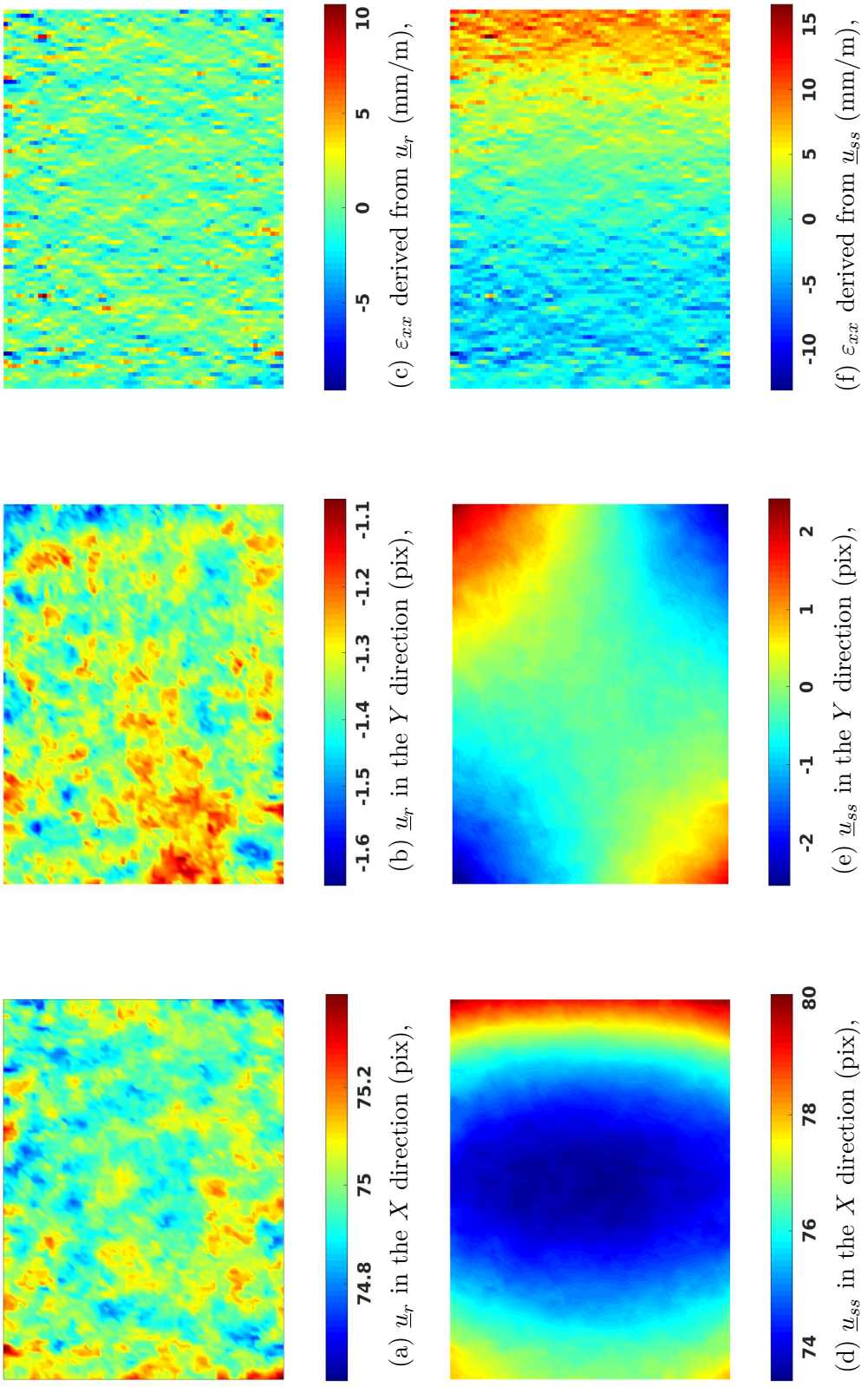

(a) $\underline{u}_r$ in the X direction (pix), (b) $\underline{u}_r$ in the Y direction (pix), (c) ε_{xx} derived from $\underline{u}_r$ (mm/m),

(d) $\underline{u}_{ss}$ in the X direction (pix), (e) $\underline{u}_{ss}$ in the Y direction (pix), (f) ε_{xx} derived from $\underline{u}_{ss}$ (mm/m),

Figure 3.13: Comparison of the displacement fields obtained using a compositional approach ($\underline{u}_r$) or an additive approach ($\underline{u}_{ss}$) and their corresponding strain fields obtained for an imposed displacement of 2500 µm (74.18 pixels) for a given sensor.

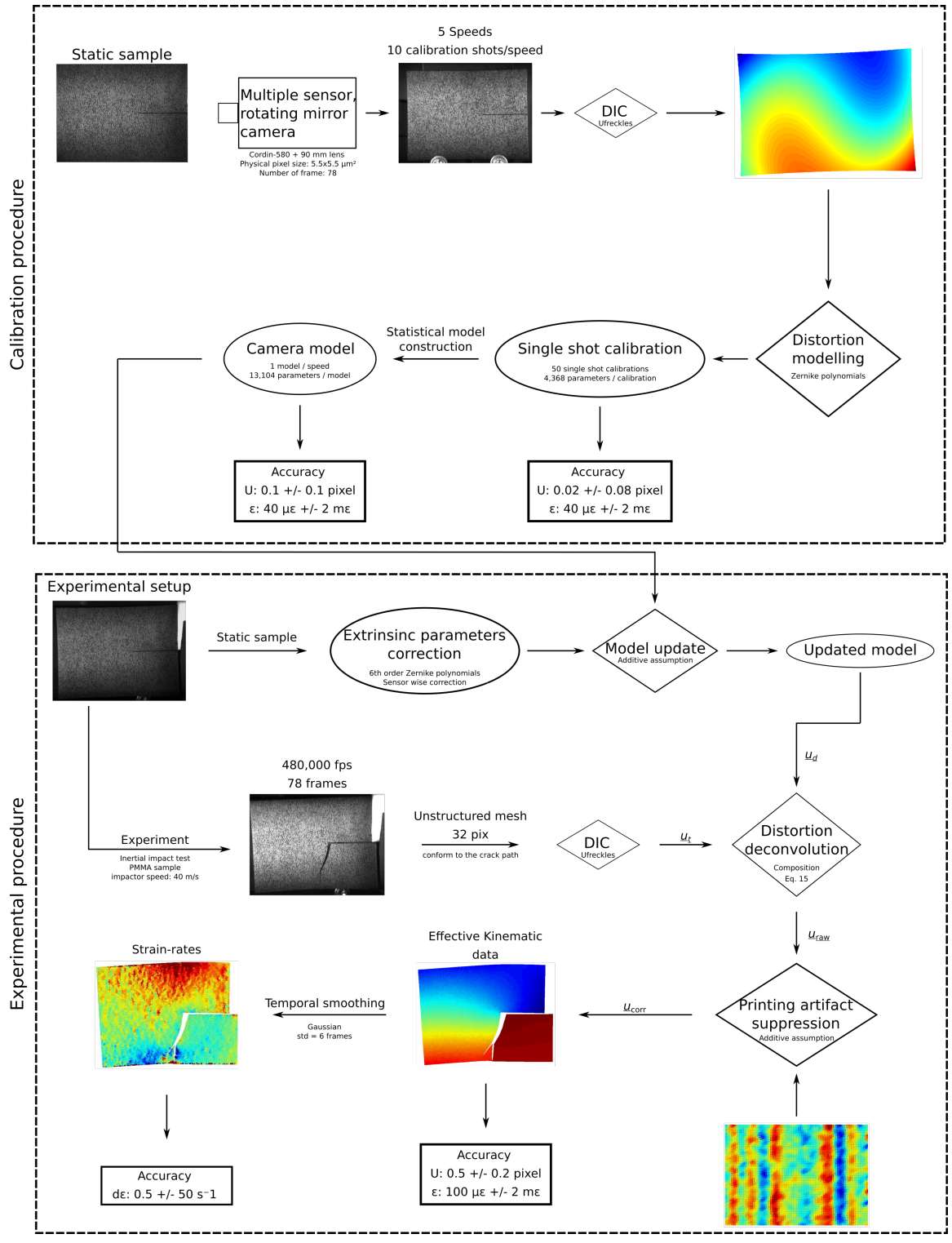

Figure 3.14: Schematic representation of the calibration and experimental procedures used to obtain quantitative kinematic data using a Cordin-580.

3.5 Outstanding issues and scope of the method

Although the feasibility of a very high spatial and temporal sampling DIC measurement based on the multi-sensor and rotating mirror technology has clearly been evidenced within this chapter, it is important to understand the limitations and outstanding issues of the proposed methodology. A few points need to be raised.

Even if this work attempts to propose a general camera model that could be built once for all in the laboratory and then probably occasionally checked and adjusted to take into account any camera behaviour variation over time, the present work has focused on a specific lens and field of view. However, the lens is part of the distortion chain and no attempt to deconvolve its contribution from the camera contribution has been done. A series of measurements for different magnifications has been performed (not presented here) and results evidence a variation of the camera model parameters. Nevertheless, integrating a lens parametrization would probably require a deviation from a simple phenomenological and polynomial camera model to a physical one introducing ray tracing, which is beyond the scope of the present work. In that context, the present methodology requires, in practice, the realization of the calibration under experimental conditions (speed, field of view, lens), thus doing it every time the set-up configuration changes.

In line with the previous point, the impact of the mirror rotation speed has been evidenced, but no obvious parametrization has emerged from the data. The progressive deformation of the mirror when increasing speed, due to centrifugal effects, would have logically mainly implied an increasing vertical compression of the image, but the data shows much more complex variations with a clear trend transition beyond 300k fps. This transition seems to be related to PID parameters. Indeed, PID parameters affect the speed ramp which in turn affect distortions, but in a manner which still remain not fully understood. In that context, the present camera model does not allow for extrapolating parameters over acquisition speeds. Only calibrated speeds, in our case 100, 200, 300, 400 and 480k fps, can be used for material testing. This point is critical, since the short term main goal is to perform tests beyond a million frames per second. However, at that speed, the helium drive is required and only 5 to 6 shots can be run with a 50 L bottle. This implies that at least 2 bottles have to be used to run a test, one and a half for calibration, plus one or two tests. This introduces significant additional cost, but more importantly, requires long camera run times at very high speed which has strong impact on the mirror-bearing lifetime. A way of mitigating that would be to avoid changing the setup configuration. In that case, this material and supply over-cost would be reduced to a single calibration campaign.

All the results presented in this chapter are based on a single, non-optimized, speckle pattern. The characteristic period of the pattern, 32 pixels, has been chosen to account for the weak sharpness of the images, which are blurred over about 20 pixels. Such blurring

is partly due to the camera itself, where the light reaches each sensor with a different reflected angle up to very shallow ones. Secondly, each sensor has its own focusing system which is tuned manually in factory. If a significant sharpness improvement can be achieved, a finer DIC mesh could be used and better performances could be reached. Thus, it is important to notice that the results provided here are speckle-dependent.

3.6 Conclusion

In this chapter, a dedicated calibration methodology for a multi-sensor rotating mirror ultra-high-speed camera is presented. The accuracy of the method has been assessed using images from a static sample, then using images after an imposed translation. The main conclusions are as follows:

- Since complex and non-negligible distortions are induced by the optical apparatus of the multi-sensor rotating mirror camera, they need to be modelled and corrected. These distortions are modelled with Zernike polynomials and identified using DIC and a synthetic speckle pattern.

- The error usually made when using a sensor-to-sensor approach is given, in a first order approximation, by the following equation: $\epsilon \approx -\underline{\underline{\nabla}}\, \underline{u}_{d2}(\underline{X}) \cdot \underline{u}_r(\underline{X}) + \underline{u}_{d1}(\underline{X}) - \underline{u}_{d2}(\underline{X})$. Hence, three requirements are needed to use this strategy: the distortions have to be constant from one shot to another and small; the effective displacements also have to be small. When using a Cordin-580, the first two conditions are not met. Furthermore, during an actual experiment, the last condition is not necessarily fulfilled either. It follows that the use of such an approach would lead to a displacement error proportional to the displacement of the sample and the distortion gradient. For example, for a translation of 2.5 mm (74.2 pixels) an error of nearly 0.2 mm (6 pixels) is obtained on the displacement, which induces strain errors of about 15 mm/m. This highlights the great interest of using the proposed methodology.

- The proposed methodology achieved statistical accuracy, over shots, of 0.15 ± 0.09 pixels for the displacements and $40\,\mu m/m \pm 2\,mm/m$ for the strains. Applying this dedicated calibration, on a moving sample, using imposed micrometer displacements, an ultimate accuracy of about 0.5 ± 0.2 pixels and $100\,\mu m/m \pm 2\,mm/m$ for the strains was eventually achieved. These errors include algorithmic, camera variability and experimental bias.

- These kinematic fields obtained have a better spatial sampling than what can traditionally be obtained with classically used high-speed cameras, at the price of higher strain random errors.

Chapter 4

Thermal field measurement: methodology and metrology

Content

4.1 Introduction

Constitutive models are mandatory in order to perform material and structure behaviour simulations. It stands for reason that the choice of the material parameters is crucial in these simulations, since it can drastically affect the results of such simulations. It is thus essential to be able to accurately identify the material parameters experimentally, and thus one need to be able to accurately capture both kinematic and thermal fields. Since the 80s and the development made in electronics, IR cameras now allow to have access to full-field temperature measurements. Furthermore, methodologies are now well-established to retrieve heat sources during quasi-static experiments, from macro to micro scale [Chrysochoos *et al.*, 2010, Seghir *et al.*, 2013, Wang *et al.*, 2016b]. For instance, in 2016 Wang and its collaborators [Wang *et al.*, 2016b] performed tensile tests on aluminium oligocrystals at an axial strain rate of $1.20 \times 10^{-2}\,\mathrm{s}^{-1}$. Through the use of an infrared camera and visible-light one, they were able to study the plastic deformation at grain scale.

Up until recently, the thermomechanical behaviour of a material was often characterized by realizing several experiments with different sample temperatures. However, these approaches are not sufficient to accurately model what happens to the material when couplings play an important role, as in adiabatic shear bands or during high strain-rate and heterogeneous experiments for example. Hence the need to be able to couple both

thermal and kinematic fields. In 2014, Martinez *et al.* [Samaca Martinez *et al.*, 2015] realized coupled measurement to observe the crack tip of filled rubber during quasi-static cyclic loadings. By recording the events at 50 fps with both an infrared and a visible-light camera, the authors were able to observe the events taking place at the crack tip of filled rubber, during cyclic loadings. They demonstrated that the crack tip is a zone that always produces heat during these tests, and that the heat production decreases with the number of cycles. Let us note that in this example, the kinematic data is mainly used in order to transfer the eulerian temperature field into the lagrangian configuration. Very recently, Rose and Menzel [Rose and Menzel, 2021] went one step further and fully coupled both kinematic and thermal fields in order to perform inverse identification of material parameters. The authors developed a methodology which, similarly to FEMU, allows the identification of parameters for thermomechanicaly coupled material models. By performing quasi-static tensile test on an aluminium alloy and recording it with both visible-light and infrared cameras, they were able to identify parameters for thermomechanical models.

Furthermore, the improvement of electronics and infrared cameras' technologies have rendered these applications possible for experiment involving intermediate to high strain-rates. To this effect, Guzman and his collaborators performed dynamic compressive tests on different alloys [Guzmán *et al.*, 2009]. By using an infrared camera during compressive tests performed on a split Hopkinson bar, they were able to measure the temperature rise due to the plastic deformation. In 2017, Seidt *et al.* [Seidt *et al.*, 2017] performed synchronous full-field strain and temperature measurement for tensile tests on steel at intermediate and high strain-rates. The authors collected thermomechanical data by recording the events at up to 30,000 fps for the temperatures and 90,000 fps for the visible-light camera.

These recent works demonstrate that it is now possible to collect thermomechanical data during high strain-rate experiments. Furthermore, these coupled data can now be used to identify the parameters of fully coupled thermomechanical constitutive models. In that context, this PhD thesis proposes to take advantage of the spatio-temporal sampling possible with one of the most recent high speed IR camera available on the market. However, the accurate measurement of intermediate temperature increase ($\leq 100\,^{\circ}\mathrm{C}$) at room temperature and high speed requires a dedicated calibration procedure, which is the focus of this chapter. Hence, the calibration procedure used to retrieve the temperatures will be presented first. Then its accuracy will be measured and discussed. At last, since the goal is to collect thermomechanical data during an experiment, a methodology to transfer the eulerian temperatures into the same configuration as the kinematic fields is proposed.

4.2 Calibration methodology

Several issues have to be tackled in order to be able to extract the temperature of a material point during an experiment. First and foremost, the infrared (IR) camera measures radiative fluxes and returns digital levels (DL) which is a non-physical unit. The relationship between the fluxes and the temperature depends on the material surface's properties such as emissivity. Moreover, the fluxes recorded by the camera may be altered by the presence of heat sources, such as flashes, in the thermal scene or other elements in its vicinity. In addition, each pixel of an IR camera sensor has its own dynamic and noise which induces a spatially and dynamically non-uniform behaviour of the sensor. Pixels that exhibit singular behaviour compared to the majority of the pixels have to be handled.

Hence, a calibration methodology has to be implemented in order to be able to retrieve the eulerian temperature fields from the DL recorded by the IR camera, while minimizing the errors at the different steps. The methodology presented in this section is similar to the one employed in [Berthel, 2007, Bodelot, 2008, Seghir, 2012], but the handling of singular pixels is done slightly differently.

Let us first introduce some notations that will be used in the sequel. For this purpose, let us consider a function ψ of N variables $\{V_k\}_{k\in[1:N]}$. For a given set of values of these variables, the average and the standard deviation of ψ over the k$^{\text{th}}$ variable will be denoted as:

$$\overline{\psi}_{|Vk}(\{Vi\}_{|i\neq k}) = \frac{1}{N_{Vk}}\sum_{Vk}\psi(\{Vi\}), \tag{4.1}$$

$$\sigma_{|Vk}[\psi](\{Vi\}_{|i\neq k}) = \sqrt{\frac{1}{N_{Vk}}\sum_{Vk}(\psi(\{Vi\}) - \overline{\psi}_{|Vk}(\{Vi\}_{|i\neq k}))^2}. \tag{4.2}$$

4.2.1 Radiometric, pixel-wise calibration

Since an infrared camera converts fluxes into DLs, a calibration is necessary to convert these DLs back into fluxes. Obviously, every IR camera is delivered with a built-in calibration done to match as much as possible different settings and experimental configurations (integration time, temperature...). Nevertheless, a finer precision can always be achieved when conducting a dedicated calibration for a given temperature range that will be investigated experimentally and for given parameters (IT, window size...). A comparison will be presented in Section 4.4. The calibration is done pixel-wise in order to address the issue of spatially non-uniform response as well as dynamically non-uniform behaviour (the DL range may vary from one pixel to another). Some explanations about the origin of the non-uniformities may be found in [Marcotte *et al.*, 2013, Tremblay *et al.*, 2010]. In addition, the calibration is performed for a given integration time (IT).

4.2.1.1 From fluxes to temperatures

Let us first consider the origin of the flux received by a pixel. Figure 4.1 depicts a thermal scene during an experiment. The fluxes recorded by an IR camera have various sources: they can come from the radiation emitted by the sample or by elements in the thermal scene's environment (*e.g.* flashes), the sample also reflects the fluxes emitted by some elements in the environment. Finally, the atmosphere can also (humidity, temperature of the room) affect these fluxes. Thus, the flux received by a pixel is usually written as [Berthel, 2007]:

$$\begin{aligned}\phi_p = \tau_{\text{atm}} \left[\epsilon_s \phi_s(T_s) + (1-\epsilon_s)\phi_{\text{env}}(T_{\text{env}}) + \epsilon_{\text{env}}\phi_{\text{env}}(T_{\text{env}})\right] \\ + (1-\tau_{\text{atm}})\phi_{\text{atm}}(T_{\text{atm}}).\end{aligned} \tag{4.3}$$

With ϕ_p, ϕ_s, ϕ_{env} and ϕ_{atm} being respectively the flux received by the pixel p considered, the one emitted by the sample, the environment or the atmosphere. τ_{atm} is the transmission factor of the atmosphere and ϵ_s, ϵ_{env} respectively the emissivity of the sample or the environment. In the present case, the emissivity and the transmission are assumed high enough and the environment well controlled enough so that the surrounding's perturbations can be neglected. Furthermore, the Stefan-Boltzmann's model for a grey body is considered to model the sample. This leads to the following simplified equation of the radiated flux:

$$\phi_p(T_s) = \epsilon_s \sigma T_s^4. \tag{4.4}$$

4.2.1.2 From DL to fluxes

A pixel-wise polynomial expansion is chosen in order to convert the DLs into fluxes. Using a blackbody (BB) at different given temperatures T_{BB}, one can construct an abacus curve for each pixel of the sensor. Moreover, in order to make it robust to the sensor's noise, the DLs of each pixel are averaged over 500 frames for every given temperatures. Thus, the expansion's parameters α_k are identified for each pixel p by solving the following problem

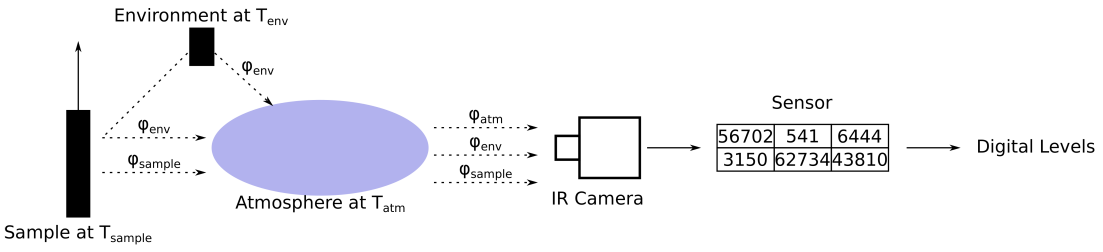

Figure 4.1: Schematic of a real thermal scene captured with an IR camera.

in a least square sense:

$$\forall\, T_{\mathrm{BB}} :\ \phi_p(T_{\mathrm{BB}}) \approx \sum_{k=0}^{N} \alpha_k (\overline{\mathrm{DL}}_{|t}(p, T_{\mathrm{BB}}))^k, \tag{4.5}$$

where T_{BB} are the given temperatures of the blackbody, N is the expansion's order and $\overline{\mathrm{DL}}_{|t}(p, T_{\mathrm{BB}})$ is the averaged DL over 500 frames for a given pixel and temperature. The choice of these temperatures will be discussed in Section 4.7.

The order of the polynomial expansion has been determined by looking at the systematic and random errors for orders ranging from 5 to 9. Here, the so called systematic error is the error averaged over every pixel of the sensor and all the frames for a given T_{BB}, whereas the random error is its standard deviation. For the sake of simplicity, only the results for an IT of 22.31 µs are presented in Figure 4.2. First let us note that the random error seldom changes with the polynomial expansion's order. Its values range from 0.12 °C at low temperature to 0.065 °C at high temperature. For the systematic error however, two different behaviours appear. With a 5^{th} order expansion, the systematic error ranges from −0.06 °C to 0.05 °C. When updating the expansion's order to 6, the systematic error's range decreases in order to be between −0.04 °C and 0.03 °C. The systematic error remains stable beyond the order 6 and no significant change is visible. The same level of systematic error can be found in the literature, *e.g.* [Bodelot, 2008]. Thus, a 6^{th} order expansion is considered sufficient and will be used in the rest of the work.

4.2.2 Outlier pixel detection

The pixel-wise calibration presented previously addresses the issue of the spatially and dynamically non-uniform behaviour of the camera's sensor. However, even after this procedure, some pixels still exhibit singular behaviour compared to the majority. These pixels are considered as "bad" pixels and will be ignored for the analysis. This step is essential in order to have accurate measurements at high speeds since only a few pixels are available (*e.g.* 4 × 64 pixels at 100k fps). Different kinds of behaviour can be observed, hence three criteria have been implemented to detect and exclude these pixels.

4.2.2.1 Criterion 1: temperature dependence

A pixel is considered defective if its response is almost independent of the temperature's variation. In this case, this is a dead pixel. This can be induced by manufacturing issue, especially with the less developed semiconductors used in IR cameras, or ageing. The criterion hence takes the following form:

$$\forall\, T_{\mathrm{BB}} :\ |\overline{\mathrm{DL}}_{|t}(p, T_{\mathrm{BB}}) - \overline{\mathrm{DL}}_{|t,p}(T_{\mathrm{BB}})| < 4\sigma_{|p}[\overline{\mathrm{DL}}_{|t}](T_{\mathrm{BB}}). \tag{4.6}$$

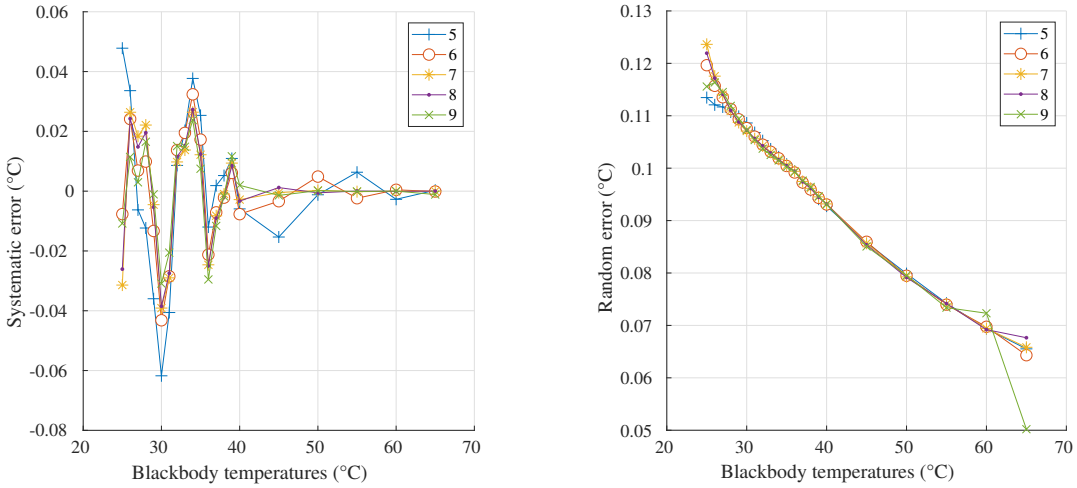

(a) Order's influence on the systematic error, (b) Order's influence on the random error,

Figure 4.2: Polynomial's order influence, for an IT=22.31 µs between 25 and 65 °C.

In Figure 4.3, all the curves are tightly packed and no monotonous curve is observed. This shows that there is no dead pixel on the sensor of the IR camera.

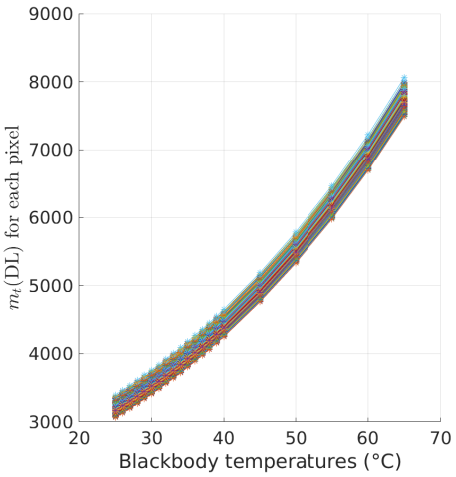

Figure 4.3: $\overline{\mathrm{DL}}_{|t}$ for each pixel versus the BB's temperature, IT = 20 µs.

4.2.2.2 Criterion 2: time dependence

A pixel is considered defective if its temporal response is significantly unstable compared to the rest of the pixels. This step tackles noise issues. The criterion takes the following form:

$$\forall\, T_{\mathrm{BB}} \;:\; |\sigma_{|t}[\mathrm{DL}](p, T_{\mathrm{BB}}) - \overline{\sigma_{|t}[\mathrm{DL}]}_{|p}(T_{\mathrm{BB}})| < 3\sigma_{|p}[\sigma_{|t}[\mathrm{DL}]](T_{\mathrm{BB}}). \tag{4.7}$$

However, enforcing this criterion for all the temperatures may be too restrictive, as some experimentally induced errors might have to be accounted for. Hence, this criterion is relaxed so that a pixel is considered defective if the last criterion is verified for a majority

of temperatures, *i.e.* if:

$$\text{Size}(T_{\text{BB}} \text{ verifying Eq. (4.7)}) > \frac{\text{Size}(T_{\text{BB}})}{2} \tag{4.8}$$

Figure 4.4 shows for all the pixels, the temporal standard deviation of the DL as a function of the blackbody's temperature. The pixels considered defective using Eq. 4.8 are depicted in red stars. For this particular case of an IT of 20 µs in 32 × 64 windowed mode, 0.49% of the pixels are removed.

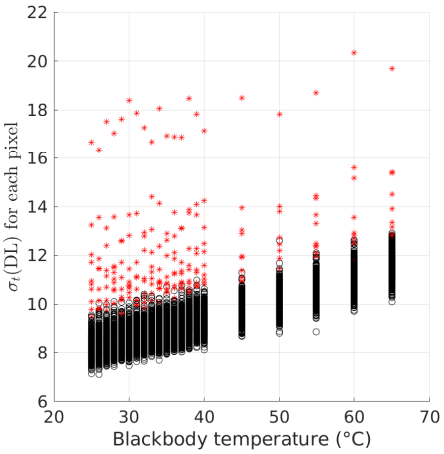

Figure 4.4: $\sigma_{|t}[\text{DL}]$ as a function of T_{BB} for all the pixels, IT = 20 µs.

4.2.2.3 Criterion 3: spatial dependence

A pixel is considered as defective if its response is significantly different from the rest of the sensor. This results mainly from vignetting effect. Compared to the 2 previous criteria, this criterion requires the temperature T and not the raw DL as the pixel-wise radiometric model tackles the spatial non-uniformity of the sensor's response. The criterion proposed here is inspired from [Bodelot, 2008].

This criterion is divided in two steps. First, if a pixel's temperature varies too greatly from the average response of the sensor it is considered defective. This translates into the following criterion, where δT is a given threshold:

$$\forall\, T_{\text{BB}} \;:\; |\overline{T}_{|t}(p, T_{\text{BB}}) - \overline{T}_{|t,p}(T_{\text{BB}})| < \delta T \tag{4.9}$$

Once these defective pixels singled out, the previous quantities are recomputed ignoring the bad pixels. Then, in the same spirit of the previous step, if a pixel's temperature is too different from the average response of the sensor, it is considered as a bad pixel. However, for this step, the threshold used is quite specific:

$$\forall\, T_{\text{BB}} \;:\; |\overline{T}_{|t}(p, T_{\text{BB}}) - \overline{T}_{|t,p}(T_{\text{BB}})| < k\alpha, \tag{4.10}$$

where α can be interpreted as the overall variation of the sensor's response:

$$\alpha = \overline{\sigma_{|p}[\overline{T}_{|t}]}_{|T_{\mathrm{BB}}}. \tag{4.11}$$

In this methodology, k is an integer that has to be determined specifically. Figure 4.5 shows the evolution of the number of bad pixels identified using Eq. (4.10), as a function of k, for an IT of 20 µs. The progression is logical: the higher k is, the less restrictive the criterion is and thus less bad pixels are detected. Heuristically, it appears that the number of bad pixel reaches a plateau (which is here depicted in black). This indicates that the remaining bad pixels detected on this plateau are truly defective. Indeed, no matter how loose the restrictions are, they are still having an abnormal response. Hence, these pixels are considered as defective and are singled-out. The number k chosen for the criterion is then the first integer corresponding to the plateau.

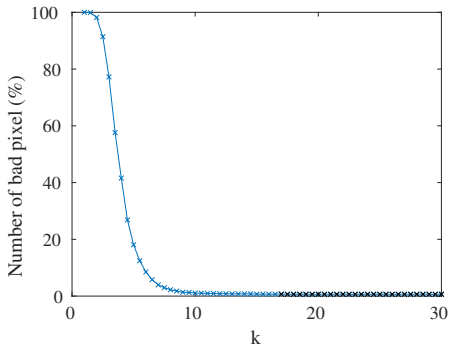

Figure 4.5: Number of bad pixels as a function of k using Eq. (4.10).

4.2.2.4 Singular pixels' cartographies and analysis

After implementing the presented methodology, bad pixels cartographies have been obtained for several IT (see Section 4.3 for further details). For all the IT considered (IT $\in$ [5.02 – 22.31 µs]), the bad pixels are consistent despite the different windowing used. This highlights the robustness of the bad pixels' detection method.

Figure 4.6 presents different bad pixels' cartographies, the bad pixels are depicted with black dots. The first is the one obtained in this study and the following two are cartographies that can be found in the literature. The bad pixels' repartition seems to be random over the sensor, which is coherent with what is found in the literature. In addition, the number of bad pixels obtained after the use of each criterion is summarized in Table 4.1. The percentages represent the number of the bad pixels relatively to the windows' size. Let us note that the increase of these percentages observed after windowing is biased as the windowing is always done in the centre, which may not be representative of the whole sensor. These values can be compared to the literature, *e.g.* Bodelot found 0.5% [Bodelot, 2008] and Honorat found 0.29% [Honorat *et al.*, 2005] (see Fig. 4.6).

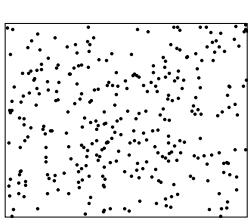

(a) Telops M3K
IT = 22.31 µs,

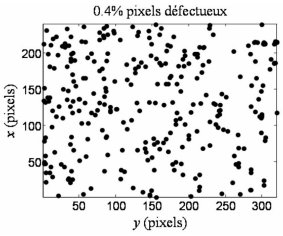

(b) [Berthel, 2007], Jade 3
at 50 FPS,

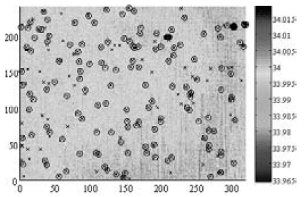

(c) [Honorat *et al.*, 2005],
Jade
IT = 2 ms,

Figure 4.6: Bad pixels' cartographies obtained in this work and by other authors.

Moreover, it is to be noted that the number of bad pixels does not significantly change between the second and last criteria of the identification process. By doing a pixel-wise calibration, one tries to guarantee a spatial uniformity. But the temporal variations are not taken into account when doing the calibration. This may explain why the temporal variation criterion is able to detect most of the bad pixels.

4.3 Thermal scene setup

4.3.1 Calibration setup

As explained in Section 4.2, the calibration methodology requires reference data. This is usually done by recording with the IR camera a calibrated blackbody, which is set to a predetermined set of temperatures. The following section describes the equipment and the setting used for the acquisition of these data. They have been chosen in order to match the future experimental conditions.

In this work, a M3K Telops camera is used with a lens from Janos Technology (ASIOS SERIES 55 mm F/2.3 MWIR). The camera recorded the DCN1000 H4 blackbody from HGH Infrared. The blackbody's emissivity is 0.98 ± 0.02 [HGH-Infrared, nd]. The camera was set approximately 50 cm from the BB, and it was tilted with a small angle in order to minimize the sensor's reflection on the BB (Fig. 4.7). Four different couples of integration times and frame rates have been investigated while keeping the other parameters identical. Notice that the selected IT are the longest integration times allowed for the selected frame

Table 4.1: Number of bad pixel identified at different steps for the different IT, for a calibration between 25 and 65 °C with 6^{th} order polynomials.

Number of bad pixels / FPS	after criterion 1	after criterion 2	after criterion 3
3,000 (256 pix × 320 pix)	0	290 (0.35 %)	316 (0.39 %)
25,000 (32 pix × 64 pix)	0	10 (0.49 %)	10 (0.49 %))
50,000 (16 pix × 64 pix)	0	4 (0.39 %)	4 (0.39 %)
95,000 (4 × 64)	0	2 (0.78 %)	2 (0.78 %)

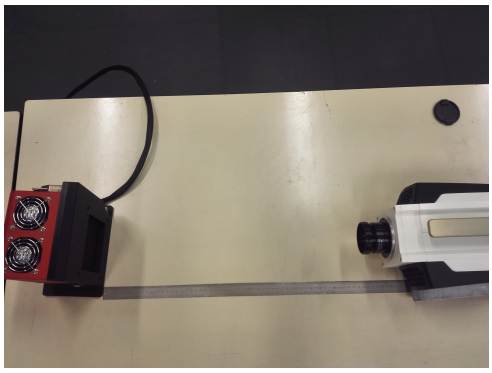

Figure 4.7: Experimental setup for the calibration of an IR camera.

rates. In each case, 500 frames were recorded to take into account the temporal noise. The camera was switched on at least one hour before the test's start to mitigate the camera's temperature drift due to its self-heating. Furthermore, a waiting time of 2 minutes for the blackbody's stabilization was set to ensure its spatial and temporal homogeneity. The experimental parameters are summarized in Table 4.2.

4.4 Calibration uncertainty

Naturally, a commercial software that allows the acquisition of directly calibrated temperatures is available. This is possible because an embedded calibration can be used during the recording. However, since the camera can be used for very different experimental conditions (in temperature and in IT), the embedded calibration is the more versatile possible [Tremblay *et al.*, 2010, Marcotte *et al.*, 2013]. As a result, it is very likely that better uncertainties can be reached when applying the presented methodology. In this section, the temperature measurement's uncertainties resulting from the IR camera embedded calibration will be compared to the ones resulting from the pixel wise calibration previously introduced.

Notice that interested readers can refer to [Tremblay *et al.*, 2010] in order to have

Table 4.2: IR camera calibration's parameters.

Test	FPS	IT	Frame size (pix)	Stabilization time	Camera launching time
1	3,000	22.31 µs	256 × 320	2 min	2 h
2	25,000	20 µs	32 × 64	2 min	2 h
3[1]	50,000	9.45 µs	16 × 64	2 min	[1]
4	95,000	5.02 µs	4 × 64	2 min	1 h
Set of temperatures					
From 25 to 40 °C with a 1 °C step From 40 to 80 °C with a 5 °C step From 80 to 130 °C with a 10 °C step					

[1] The test was done in two days: from 25 to 65 °C the first day, and 65 to 130 °C the last one. The camera launching time was 2 hours the first day, and 1 hour the second one.

further details about the IR camera's "built-in" calibration.

4.4.1 IR camera software settings

To apply the embedded calibration to the raw data, a set of parameters can be adjusted. The default parameters are summarized in Table 4.3.

Figure 4.8 depicts the influence on the temperature measurements of the two main user controlled parameters: the emissivity ϵ and the target distance. On the influence of the working distance, only the extrema are presented. In this figure the systematic error is considered, that is to say the spatio-temporal average of the error between the camera output and the blackbody's temperature. This figure shows that the real experimental conditions, an emissivity of 0.98 and a working distance of 50 cm, do not give a minimum error wise. The minimum is obtained when considering an emissivity of 1 and a working distance of 0 m, *i.e.* when the environment influence is neglected. We have no explanation regarding this point. Nevertheless, in order to have a fair comparison between the built-in calibration and the proposed methodology, the parameters used will be the one yielding in the minimal error: $\epsilon = 1$ and WD = 0 m.

4.4.2 Spatio-temporal uniformity

Figures 4.9 and 4.10 illustrate the comparison between the embedded calibration and the implemented one. The two figures are done for two different widows sizes (fullframe (256×320) for Fig. 4.9 and 32×64 pixels for Fig. 4.10), and for a blackbody at 50 °C. In these figures, the first row depicts the IR fields for a random frame (here the 342^{th} one), the second one shows the spatial standard deviation as a function of time. The last row of these figures shows the temporal standard deviation for each pixel.

The raw DL image shows a vignetting effect that is due to the lens. This vignetting disappears when a windowing is performed (see Fig. 4.10) as the windowing is done using the lens' center. It is interesting to note that this vignetting effect is not tackled by the "built-in" calibration. Indeed, an edge effect is still present with a gradient of 2 °C

Table 4.3: Default embedded calibration's parameters.

Air temperature	25 °C
Relative humidity	50 %
CO_2 concentration	100 ppm
Visibility	10 km
External optics temperature	25 °C
External optics transmittance	100 %
Environment temperature	25 °C
Target distance	0 m
Emissivity	1

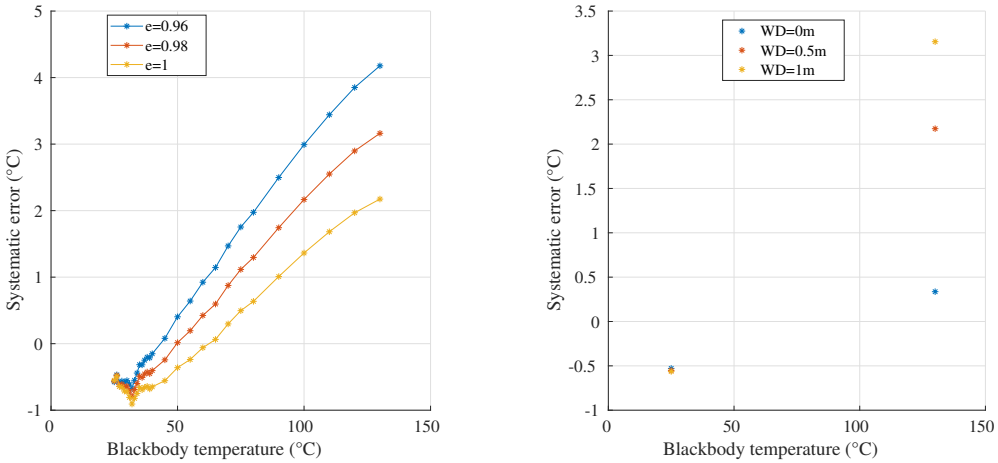

(a) Influence of ϵ, WD = 0.5 m, (b) Influence of the WD, $\epsilon = 1$,

Figure 4.8: Influence of the working distance and the emissivity on the systematic error.

(Fig. 4.9). Whereas the implemented methodology yields a homogeneous response of 50 ± 0.3 °C for a blackbody's temperature of 50 °C. It has been noticed that the vignetting progressively appears the higher the temperature gets (it is not presented here). This seems to demonstrate that the data base used for the embedded calibration is not rich enough to capture the sensor's behaviour in these conditions of very low IT (< 25 µs). Furthermore, it is worth noticing that for both the "built-in" and the implemented calibration, vertical bands appear in the temperature fields (see Fig. 4.9) with different frequencies. For the case of the "built-in" calibration, this may be linked to the pixel matrix and the read-out technology used. However, the origin is not clear for the implemented calibration and needs to be checked. At last, it can be noted that the spatial uniformity obtained with the "custom" calibration is in line with the thermal uniformity of the blackbody (0.3 °C at 50 °C).

By looking at the spatial standard deviation (Fig. 4.9), a 46 Hz (obtained by using an FFT) signal can be identified. This signal is present in all three plots: raw DL, "built-in" calibration and even in "custom" calibration despite its very low amplitude. Sub-windowing analysis have shown that this is not due to the edge effects. This may be due to either the camera's cooling system or the blackbody's temperature regulation. The blackbody's documentation [HGH-Infrared, nd] indicates a temperature stability of 0.5 mK, which is ten times lower than the variations observed for the embedded calibration. This is however in line with the variations observed for the implemented calibration, however this calibration considers the blackbody as perfect. This may hence confirm the first hypothesis. Nevertheless, there is a massive decrease of the spatial variation (from 250 mK to 78 mK) between the two calibrations. This is mainly due to the edge effect obtained in the temperature fields.

Additionally, no significant difference between the temporal standard deviations (which

can be interpreted as pixel noise) of the two calibrations can be seen. In both cases, a pixel noise of about 100 mK is obtained. This is explained by the fact that none of the calibration tries to correct the temporal noise.

Furthermore, when windowing in order to increase the frame rate, a particular artefact appears. Indeed, raw DL shows a systematic off-set of about 200 DL in the first line. This artefact is interestingly not corrected in the "built-in" calibration. This artefact leads to an overestimated temperature of 1 °C. This issue is likely to be a read-out issue and not a hardware one as it appears for every windowing size available despite the first line of pixels not being the same. One possible explanation for the non correction, is that the embedded calibration used is probably based on the fullframe one and then simply cropped whereas the implemented one was done specifically for the windowed data. If the first line is removed when computing the spatial uncertainty of the embedded calibration, it decreases to 100 mK which is close to the 80 mK obtained with the "custom" calibration.

Finally, it may be interesting to compare the uncertainty of measurement obtained here, with very low IT, to the one obtained in quasi-static condition that can be found in the literature. To do so, the temporal average of the error between the measured temperature and the one assigned to the blackbody is considered. Figure 4.11 compares the histogram of this error obtained at 28 °C for an IT of 22.31 µs in this study to the one obtained in [Bodelot, 2008] with an IT of 1.1 ms. This figure shows that the uncertainty obtained in this study is similar to the one found in literature, despite the significant decrease of the IT (from 1.1 ms to 22.31 µs), *i.e.* by increasing the frame rate from 140 to 95,000 fps.

4.4.3 Calibration uncertainties

After studying the spatial and temporal uniformity of the sensor for the built-in and the developed calibrations, the global systematic and random error will be studied. The global systematic, respectively random, error is the spatio-temporal average, respectively standard deviation, of the difference between the calibrated temperature and the blackbody's one. First, let us specify that the bad pixels identified previously are never taken into account in these quantities. These two given errors are indicators of the reliability of the temperature measured using the IR camera with either the embedded calibration or the presented one. Figure 4.12 summarizes these errors obtained using both calibrations for every tested IT. In the first row are plotted the errors obtained using the "built-in" calibration (in red) and the "custom" one (in blue) for the 4 IT considered. In the second row, using the same colours, are plotted the random bias.

The systematic errors obtained are about 10 times higher for the "built-in" calibration. Near room temperature, these errors can be up to 1 °C. The gap between the two calibrations increases as the IT decreases. It is to be noted that the "custom" calibra-

tion's errors oscillate around $0 \pm 50\,\text{mK}$, whereas the embedded calibration systematically underestimates the blackbody's temperature. Nevertheless, these biases decrease as the temperature increases (*i.e.* as the signal-to-noise ratio increases).

On the other hand, all random biases follow the same trends. The bias decreases when the temperature increases, but it increases when the IT decreases. The singular behaviour obtained with the embedded calibration using the fullframe (3,000 fps) can be explained with the edge effects. Indeed, the vignetting effect is stronger as the temperature increases.

To conclude, both methods yield temperature fields with random errors of the same order of magnitude. However, the implemented calibration is more accurate, while the "built-in" one systematically underestimates the temperature. The implemented calibration yields temperature fields with an accuracy of $100 \pm 300\,\text{mK}$ at worst over a temperature range of 25-65 °C, for IT over the range 22.31-5.02 µs. Hence, apart for thermoelastic phenomena, the IR camera with the proposed calibration can be used for high strain-rate tests. Obviously this precision is obtained at the cost of having to perform a calibration campaign for each integration time desired and over a specific range of temperature.

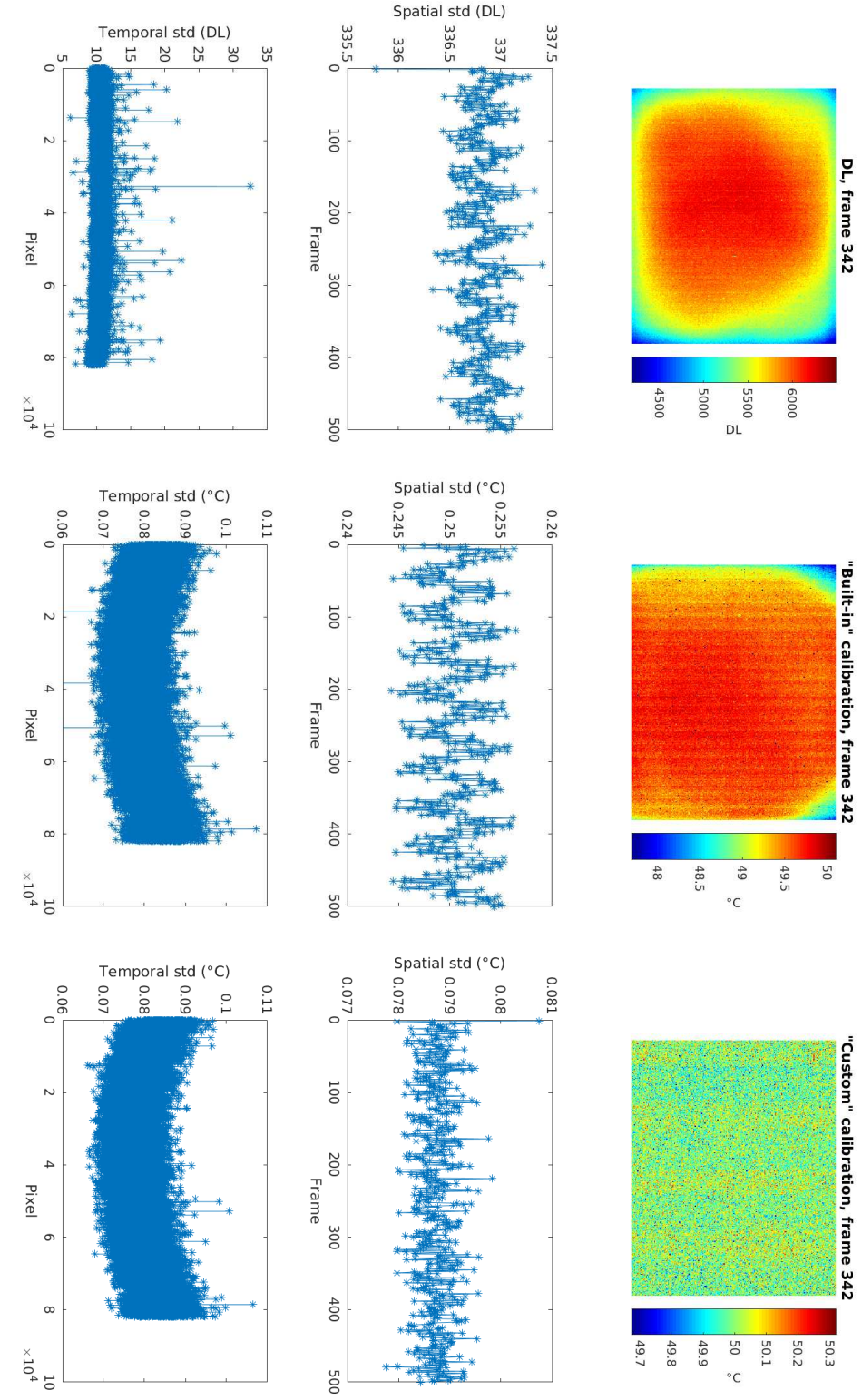

Figure 4.9: Comparison of the cartographies, spatial and temporal deviations obtained using the raw data, the "built-in" calibration or the one proposed when recording a blackbody at 50 °C with a fullframe image at 3k fps.

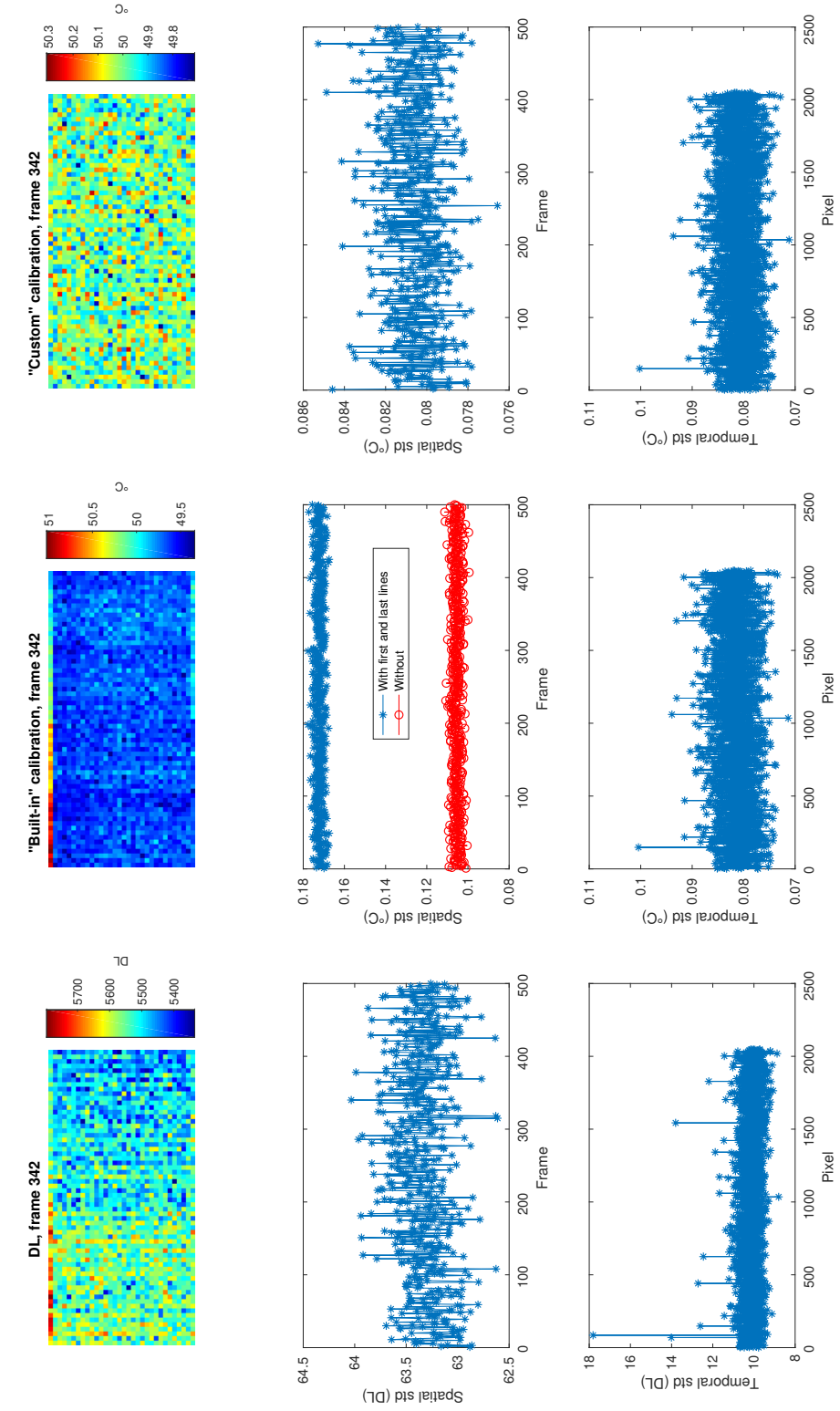

Figure 4.10: Comparison of the cartographies, spatial and temporal deviations obtained using the raw data, the "built-in" calibration or the one proposed when recording a blackbody at 50 °C with a windowed image at 25k fps.

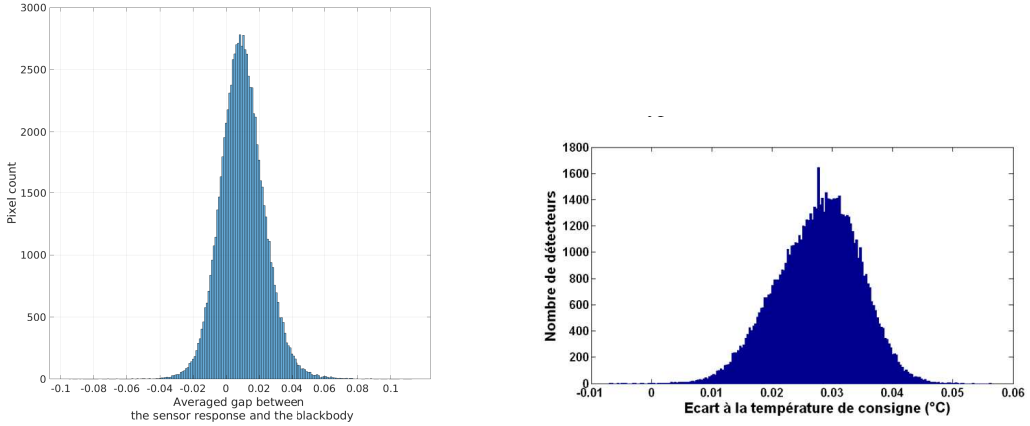

(a) IT = 22.31 µs, at 28 °C, (b) [Bodelot, 2008], IT = 1.100 µs, 28 °C,

Figure 4.11: Comparison of the systematic error's histogram obtained after the implemented calibration and the one found in [Bodelot, 2008].

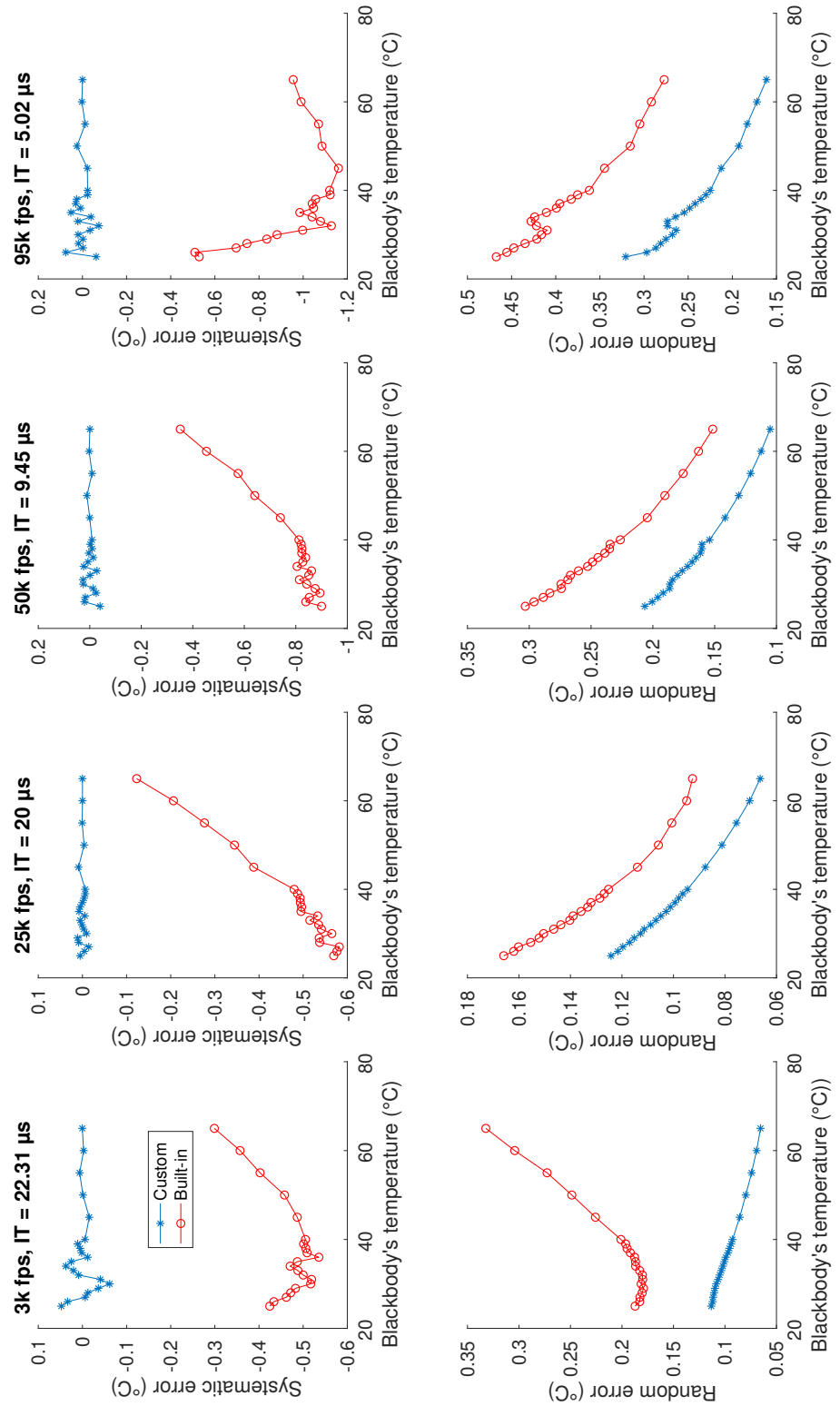

Figure 4.12: Systematic and random errors for different ITs and for the two calibrations used.

4.5 Lagrangian thermography

4.5.1 Methodology

Once extracted, the temperatures recorded by an infrared camera are available in the current deformed configuration (eulerian configuration). However, the kinematic data obtained through the help of DIC, are expressed in the initial configuration (lagrangian configuration). Hence, in order to be able to couple kinematic and thermal data, the temperature fields have to be expressed in the same configuration. The methodology proposed here is very similar to what is done in the literature [Bodelot, 2008, Toussaint *et al.*, 2012, Seghir *et al.*, 2013]. It is designed for experiments where each camera is recording one face of the specimen.

4.5.1.1 DIC measurements

The displacement fields are needed in order to map the temperature fields in the initial configuration. These kinematic fields are obtained using DIC and the methodology proposed in Chapter 3. In the end, the displacement fields are known at each node of the mesh used to describe the specimen.

4.5.1.2 Space and time synchronization

Since the spatial and temporal resolutions of both cameras differ, a space and time synchronization is required. Especially since the scenes captured by the two cameras may also differ slightly.

Since the acquisition rate of the IR camera is lower than the other camera, the temperature fields obtained are first interpolated linearly time-wise in order to have temperature fields in the same timeline as the kinematic fields.

Then, it is assumed in this methodology that the whole specimen is seen by both cameras when used in fullframe. The objective of the spacial synchronization is to place both visible and infrared images in the same POV. Since DIC has been performed, the pixel size and the initial position of the sample in the images recorded by the visible camera are both known. To obtain these informations for the IR images, the sample borders are selected manually using fullframe images. This step thus allows to transfer the resized DIC mesh into the IR images. The temperature fields from the IR images are then interpolated linearly onto this DIC mesh. Hence, at the end of this step, the temperature fields are available in the same deformed configuration as the kinematic data.

Finally, at the end of this space and time synchronization, the temperature fields are available in the same spatio-temporal coordinate system as the kinematic data. Let us note that the fields hence obtained are smoothed since two interpolations have been performed.

4.5.1.3 Lagragian thermography

Let us consider $\underline{X}_n$ a given point in the reference configuration. Since the kinematic data are available, the position $\underline{x}_n(t)$ of $\underline{X}_n$ at any given time t is known using the following relation:

$$\underline{x}_n(t) = \underline{X}_n + \underline{U}(\underline{X}_n, t). \tag{4.12}$$

As the temperature fields are available in the same spatio-temporal coordinate system as the kinematic data, $T(\underline{x}_n, t)$ can be retrieved as depicted in Fig. 4.13. Indeed, by attributing $T(\underline{x}_n, t)$ to $\underline{X}_n$, the temperature fields is then available in the lagrangian configuration *i.e.*: $T(\underline{X}_n, t)$ is known for any given point $\underline{X}_n$ in the reference configuration, at any given time t.

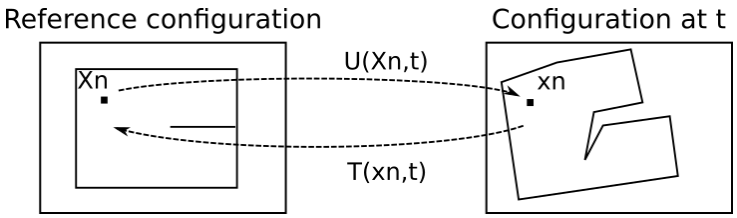

Figure 4.13: Schematic of the lagrangian thermography procedure.

In the presented methodology, it is supposed that the images from the two cameras can be synchronized spatially by performing only a rescaling and translations. This in particular, assumes for example that the cameras are perfectly aligned with the sample. Furthermore, the distortions induced by the objective lens used with the IR camera are not taken into account. However, methodologies have been developed to tackle more complex transformations between IR images and visible images if necessary [Toussaint *et al.*, 2012, Wang *et al.*, 2016b].

4.6 Outstanding issues

For a metrological analysis the setup is quite simple: it solely consists of a blackbody and the infrared camera. However, during an experiment all the machinery needed may be in the vicinity of the camera, potentially influencing the fluxes recorded. Hence, during an experiment a careful attention has to be given to the setup, in order to reduce the interferences of the environment on the thermal scene as much as possible. In particular in our case, the Cordin and its flashes will be used at the same time as the infrared camera. The flashes used are Xenon flashes (see Section 5.1.3), which emit 5 % of their output in the recording range of the IR camera (between 1500 nm and 5400 nm) (see Fig. 5.9b in Chapter 5 for a detailed graph). As a result, precautions have to be taken in order to

minimize the impact of the flashes and their eventual reflections on the fluxes recorded by the IR camera.

In order to isolate the IR camera from external interferences several techniques can be used. One can, for example, use a box that isolates the camera from the environment and focuses the camera on the sample only [Guzmán *et al.*, 2009, Wang *et al.*, 2016b]. This technique is used in Chapter 5 through the use of a tube, on which black paint is applied on its interior beforehand. Since in this work we focus only on experiments where each camera record its own face, another way to isolate the camera is to put a thermal barrier between the sample and the camera with an opening tailored to the sample's size. This is the approach used in Chapter 7 where an aluminium foil painted in black is put between the IR camera and the sample.

However, even though these techniques allow for a better control on the impact of the environment on the IR images, they do not tackle the influence of the flashes on the sample and thus the fluxes it emits. Indeed, since the flashes needed by the Cordin are very powerful, they may have an impact on the sample's temperature. In addition, one has to bear in mind that the sample's material may also be transparent for some wavelengths. Which, in turn may create an apparent raise of the sample's temperature. These points will be further discussed in Section 5.3.1 and 7.

4.7 Conclusion

In this chapter, a pixel-wise radiometric calibration for high-speed infrared camera is presented. The accuracy of the method has been assessed with the use of a blackbody and compared to the native calibration of the camera, for four different integration times over a medium temperature range. A strategy allowing the mapping of the temperature fields obtained from the deformed configuration into the reference configuration is then presented. The main conclusions are as follows:

- The proposed calibration procedure achieves an accuracy of 100 ± 300 mK over a temperature range of 25 – 65 °C, for IT over the range 5.02 – 22.31 µs. The accuracy obtained is in line with the ones found in the literature for significantly higher IT (*e.g.* 1.1 ms in [Bodelot, 2008]).
- The comparison with the embedded calibration highlights the relevance of performing a dedicated calibration. The random errors obtained with these calibrations are comparable. However, the native one yields systematic errors that are about 10 times higher, with errors near room temperature that reach 1 °C.
- A particular attention has to be given to the control of the thermal scene to minimize the interferences on the temperature measurement. Especially when performing experiments with coupled measurements where lights are used for the digital image correlation. Hence, in our case, since the flashes used are partly emitting in the wavelength range recorded by our IR camera, the isolation of the camera has to be ensured with great care.
- In order to be optimal, the present methodology requires, in practice, the realization of the calibration under experimental conditions (speed, IT, windowing, lens, temperature range).

Chapter 5

Coupled measurements: an experimental validation

Content

5.1 Experimental application

In Chapter 3, a methodology enabling the extraction of kinematic fields from images recorded using a multi-sensor, rotating mirror camera was presented. Furthermore, preliminary validation tests were performed. In Chapter 4, a calibration strategy is proposed in order to retrieve thermal fields from images recorded using an infrared camera. Furthermore, through the use of kinematic fields, a methodology to perform lagrangian thermography is also proposed. These methodologies will now be applied to an experimental validation test. This test is an impact test partly inspired on the one performed by Kalthoff [Kalthoff, 1988, Pierron *et al.*, 2014] (see Fig. 5.1). The experimental setup and the test results will be presented in this section.

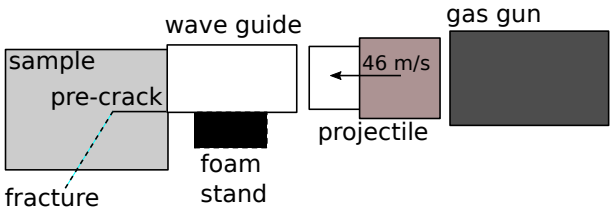

Figure 5.1: Principle of the experimental test.

5.1.1 Specimen material and geometry

For this experiment, a sample made of PMMA (Polymethylmethacrylate) of the brand Altuglas CN manufactured by Arkema is used. It is an amorphous thermoplastic polymer with a Vicat B 50 softening point at 115 °C. Its mechanical properties are known to be

dependent on the temperature and the strain rate. They have been extensively studied and constitutive models have been developed to describe its viscoelastic behaviour [Arruda *et al.*, 1995, Dar *et al.*, 2014].

The specimen used is a 100 mm × 75 mm × 5 mm PMMA sample, with a 37.5 mm long notch at half its height (see Fig. 5.2). The sample and the notch are obtained using a laser cutting machine. The size of its beam is approximately 200 µm. Hence, the width of the notch is estimated to be of the same size. Sample dimensions have been chosen to match the Cordin-580 images aspect ratio, with a slight margin to be able to keep the sample boundaries in the frame all along the recording. Finally, in order to apply the DIC procedure previously described, the tailored synthetic speckle pattern is carved into the sample using the laser cutting machine. The depth of the engraved speckle pattern is about 50 µm.

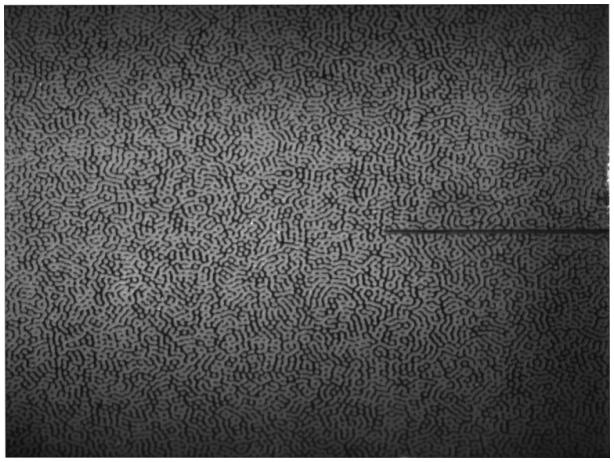

Figure 5.2: Specimen with an etched speckle pattern.

5.1.2 Loading and test configurations

As presented in Fig. 5.1, the test configuration can be described as a purely inertial impact loading. This configuration has been used in a series of recent papers [Pierron *et al.*, 2014, Fletcher and Pierron, 2018, Fletcher *et al.*, 2019]. It consists in impacting a self-supported flat sample glued on a wave-guide by means of a projectile. The wave-guide has two purposes: holding the sample in place and shaping the input wave, for instance, mitigating misalignment issues. The true interest of this configuration is the control of the boundary conditions. Indeed, all boundaries are free edges, except for the impact edge, where a smooth pulse is introduced. The sample is then simply loaded by its own acceleration. In the present case, by impacting the sample only along half of its height, a compression wave and a shear wave (at notch tip) are introduced. The applied compression stress in the wave-guide can be estimated using the following formula: $\sigma \sim \rho C V_p$, where ρ is the density of the material, C is its wave celerity, and V_p is the projectile speed. In

our case, using $\rho = 1190\,\mathrm{kg/m^3}$, $C = 2150\,\mathrm{m/s}$ and $V_p = 46\,\mathrm{m/s}$, it yields an estimated pulse stress of 118 MPa; *i.e.*, on the order of the expected intermediate strain-rate tensile strength ($\approx 100\,\mathrm{MPa}$ [Wu *et al.*, 2004]).

The impact is performed by propelling a cylinder projectile, made of POM (Polyoxymethylene), at high speed with a compressed air gun. The projectile has a diameter of 40 mm and is 80 mm long. The projectile's speed is controlled by the pressure imposed in the gas gun. In this test, a pressure of 0.20 MPa is used, which leads to an approximate speed of 46 m/s. The length of the wave-guide, which has the same dimension as the projectile, has been carefully chosen to ensure that no reflected wave enters the specimen before the crack starts.

Given that the alignment between the projectile and the specimen is critical in this kind of experiment, the specimen is placed as close as possible to the air gun exit. Moreover, the alignment is checked each time before the test by introducing a long dummy projectile at the gas gun end and verifying that the contact with the wave-guide is planar. Fig. 7.1a presents different views of the experimental setup and the specimen in place.

5.1.3 Experimental setup

The event is recorded using an ultra-high speed camera, the Cordin-580, equipped with a 90 mm Tamron objective, at 480k fps with a CCD gain [1] of 35 % and a CDS [2] gain of 0 dB. At such speed, the film duration is about 167 µs. In order to provide enough light, two Pro-10 Xenon flashes from Profoto are used. They are set in freeze mode, at 8.5 f-stops, thus delivering about 1600 J. In that configuration, the illumination typically lasts 1 ms. To trigger the flashes and the camera, an infrared light-gate system is used (SPX1189 series Honeywell). When obscured by the projectile, the optical system sends a 5 V TTL signal to the camera after a delay of 200 µs, which triggers the flashes immediately and itself after 170 µs. This light gate is thus placed as close as possible to the barrel's exit. The specimen is then placed in a manner that the wave-guide is 20 mm after the optical barrier, so that the Cordin starts recording when the waves enter the specimen. Let us note that the precision of the specimen's positioning is estimated to be about 2 mm. The 170 µs delay is set manually within the camera, estimating *a priori* the projectile flight time and the duration of the wave propagation within the wave-guide. This methodology is extremely dependent on the reliability of the gas gun to propel at a specific speed. Considering our equipment, the triggering reliability is about 40 to 50 µs, which is high compared to the recording length (167 µs).

1. Gain on a CCD camera represents the conversion factor from electrons (e^-) into digital counts, or Analog-Digital Units (ADUs). Gain is expressed as the number of electrons that get converted into a digital number, or electrons per ADU (e^-/ADU).

2. Correlated double sampling (CDS). In this method the output signal is sampled twice for each pixel - just after precharging capacitor and after the pixel charge packet is added. The difference between these two values does not include the noise component induced by the switch.

The inertial impact test is also recorded using an infrared camera, the Telops M3K, equipped with a Janos Technology (ASIOS SERIES 55 mm F/2.3 MWIR) objective. As depicted in Fig. 7.1a, the IR camera recorded the other face of the sample. In order to reduce the influence of the experimental setup (in particular the metallic parts which can reflect the flashes light), a tube with its interior painted in black is used. It is placed in such a manner that the camera is focused on the sample and the interferences caused by the setup is considered minimal. Furthermore, in order to ensure a high emissivity of the observed face, a small layer of black paint is deposited on it. The events are recorded at 40,000 fps with an integration time of 6 µs, and a windows size of 32×64 pixels^2 in order to keep a reasonable spatial resolution around the crack. This windows size allows for only a partial recording of the sample: approximately two third of its length and a little more than half of its height (see Fig. 5.10). Hence, it was chosen to record the upper left part of the sample, including the upper and left border of the sample as well as a part of the notch, in order to capture the events induced by the wave propagation near the notch's tip. The camera is triggered using the same light-gate system as for the Cordin. However, the camera starts recording as soon as it is obscured. *In fine*, 7 IR images are available during the recording time of the Cordin ($\approx$ 170 µs). Moreover, in order to apply the methodology previously described, full-frame images taken from the IR camera are needed. These images were taken prior to the experiment, in its exact configuration. Finally, the temperature fields were extracted, for a first approach, using the "built-in" calibration of the camera.

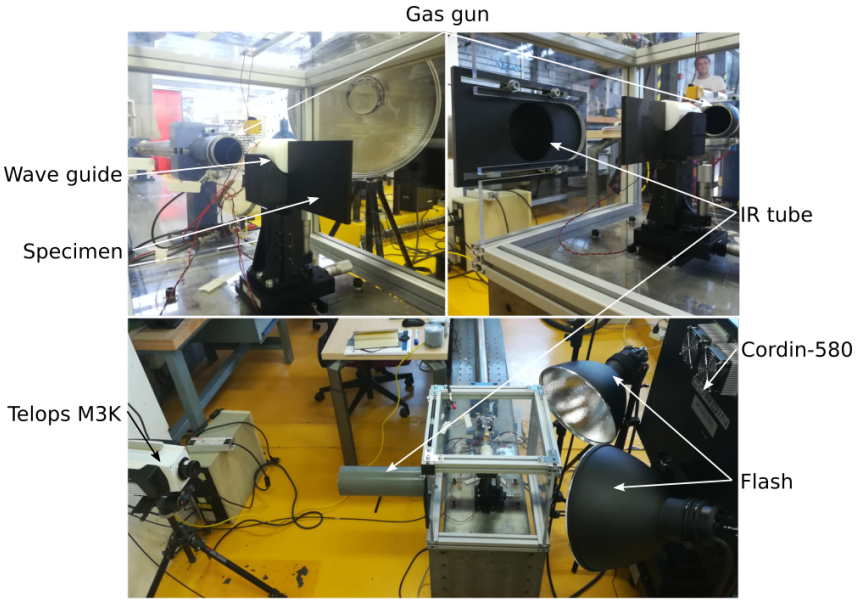

Figure 5.3: Experimental setup for an inertial impact test on a PMMA sample.

5.1.4 Mesh and DIC parameters

Since a crack is propagating in the sample during the test, a specific mesh is used. It is an unstructured mesh, with twin nodes along the crack path (see Fig. 5.4). The use of twin nodes allows the mesh to open in order to properly capture displacement jumps and strain localization at the crack location. The definition of such a mesh is done in two steps. First, DIC is performed on a continuous and structured mesh. This allows for transferring deformed images of the sample in the reference configuration. Then, the crack path can be defined in the undeformed configuration, a new unstructured mesh can be made, and the DIC run again. Fig. 5.4 presents the mesh, deformed and superimposed, in the last image of the test. The element size, defining the kinematic resolution, is 32 pixels on average, but less along the crack (about 20 pix). A Tikhonov regularization of 4 elements is used to filter-out spatial noise. This is achieved, within the DIC framework, by adding a penalty term in Equation 3.16. Finally, the pixel size, obtained by recording an image of a ruler prior to the test, is 33.7 µm. This leads to a field of view of 83.3 mm × 111.1 mm (see Tab. 5.1).

Prior to computing time derivatives, it is also usual to filter-out temporal noise at least when a simple finite difference scheme is used. In order to capture strain-rate fields, displacements are firstly pointwise convolved with a temporal Gaussian filtering kernel with a window size equal to 25 frames. The size of the Gaussian kernel is chosen manually, in order to obtain smooth first and second time derivatives of the displacement. Then strain-rates are obtained using a simple 1^{st} order finite difference scheme. Such data filtering marginally affects strain, but significantly decreases the amount of noise on strain-rates. An estimation of the strain-rate random error is given in Tab. 5.2. It is evaluated using the sequence of images, taken prior to the experiment, on a static sample.

5.2 Displacement and strain fields

To deconvolve the distortions and the real displacements, the global camera model built earlier for an acquisition rate of 480k fps is used. At this step, the pairing between the sensors and the mirror faces illuminating them is unknown. It requires the application of the 3 different parameter permutations to the experimental data. Using the same optical considerations previously mentioned, the optimal pairing is obtained by considering the displacement in the Y direction. Furthermore, using the reference shot performed before the test with the sample remaining static, changes in extrinsic parameters between the calibration procedure and the experiment (see Section 3.4.3), are evaluated. Once the correct pairing is identified and the model parameters are updated, displacement, strain and strain-rate fields can be extracted.

Let us first look at the temporal evolution of the axial displacement and speed of a

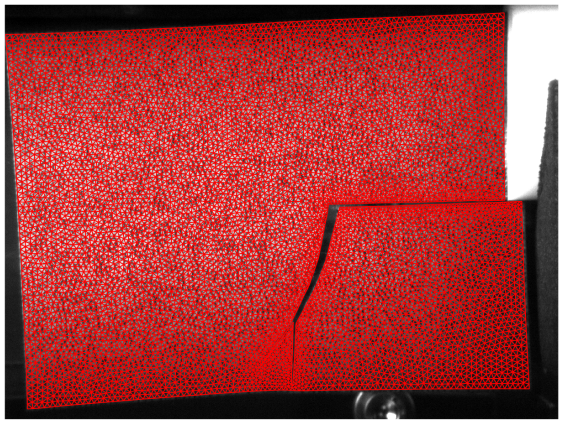

Figure 5.4: Unstructured mesh (in red) with twin nodes along the crack path, deformed and superimposed onto the final frame taken during an impact test.

Camera	Cordin-580
Image resolution	2472 pixels x 3296 pixels
Dynamic Range, Detector	12 bits
Dynamic Range, Image	16 bits
Acquisition Rate	480k fps
Lens	Tamron SP 90 mm Di Macro
Aperture	f/2.8
Field of view	83.3 mm × 111.1 mm
Image scale	1 pixel = 33.7 µm
Stand-off distance	50 cm
Patterning Technique	Laser etching of a synthetic speckle pattern
Pattern period size	32 pixels

Table 5.1: DIC hardware parameters.

DIC Software	Ufreckles [Réthoré, 2018]
Shape Function	linear FE triangle elements
Matching Criterion	element-wise ZNSSD
Image Filtering	sensor flattening (vignetting)
Data Processing	U : Tikhonov regularization over 4 elements
Experimental systematic and random error	U: 0.5 pix ± 0.2 pix ε: 100 µε ± 2.0 mε $\dot{\varepsilon}$: 0.5 s^{-1} ± 50 s^{-1}
Data Post-Processing	$\dot{\varepsilon}$: temporal Gaussian filter applied onto U (win = 25 fr)

Table 5.2: DIC analysis parameters.

node located at the middle of the impacted edge. Fig. 5.5 shows displacement in blue and speed in red. The four vertical dashed lines are the time steps for which associated fields will be discussed later-on. The two black circles depict, respectively, the crack initiation and crack branching time steps. The loading of the specimen induces, at the impact edge, a displacement ramp starting at 225 µs and reaching about 3 mm at the end of the record. Note that it corresponds to the range investigated above, in the method validation Section 3.4.5. The speed evidences three stages: between 170 µs and 210 µs the velocity increases in the positive direction, then there is a nearly linear increase in magnitude followed by a plateau at -40 m/s. The first stage can be explained by a clockwise rotation of the sample, this will be described later. The plateau is reached in approximately 60 µs, which corresponds to an acceleration on the order of $1 \times 10^6\,\mathrm{m\,s^{-2}}$. According to [Ravi-Chandar *et al.*, 1999], such loading leads to a brittle mode crack regime in PMMA. This is also confirmed by the data presented in Fig. 5.6.

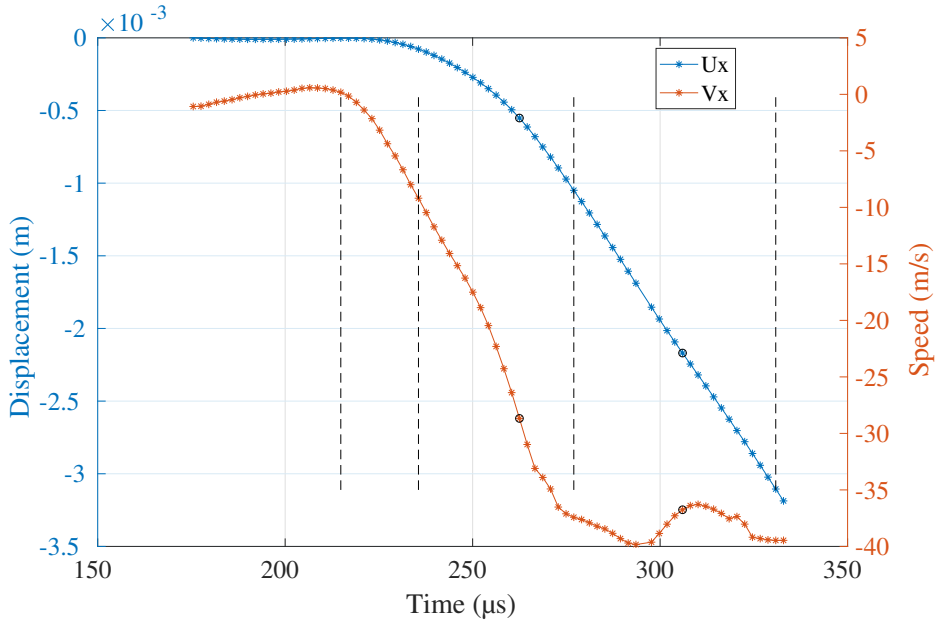

Figure 5.5: Temporal evolution of the displacement and speed in the X direction of a node located in the middle of the impacted edge.

Fig. 5.6, shows sample images and displacement fields in both directions for the four time steps introduced previously. In what follows, the time count starts when the optical barrier is cut; hence, the camera recording starts at 170 µs. During the first 55 µs, the displacement fields obtained are consistent with a clockwise rotation of the sample. This rotation can be explained by considering that, at the time of the impact, the sample and wave-guide were slightly misaligned with a small anti-clockwise angle. Thus, when the impact occurs the wave-guide will rotate. This initial inclination is thought to be induced by the air blast preceding the projectile, due to the lack of air exit in the barrel's nozzle. This is verified by comparing a frame of a calibration shot taken before the test to its

corresponding frame of the test; a rotation of 0.7° is found. The displacement field in the X direction at 235 µs further confirms this explanation, since the compression starts at the bottom corner of the impacted edge. Notice that it is not an issue, since the whole kinematic field history is captured. Then, as the wave enters the sample, the Poisson effect due to the compression is captured in the Y direction, as shown in Fig. 5.6 at t = 276.98 µs. Notice that, at that stage the crack has already initiated, which is highlighted by the opening of the mesh. This result shows that the crack initiates as the compression wave goes into the sample and not after any wave rebound. A proper capture of the displacement jump from crack initiation to branching is recovered. Branching of the crack is visible along both the X and Y directions at 330.84 µs. In line with [Ravi-Chandar *et al.*, 1999], the crack propagates globally with a 60° inclination.

Furthermore, strain fields can be obtained and Fig. 5.7 depicts some of them. The strain fields obtained at 214.84 µs confirm the fact that the displacement fields obtained in the early stages of the experiment are due to a rigid-body rotation of the sample. The compression wave in the X direction and the Poisson effect induced are captured by the strain fields (for example at 276.98 µs). The sample undergoes, on its top right part, a uni-axial compression of 30 mm/m. Under the assumption that only compression is taking place in this part of the sample, a Poisson ratio of $\nu = 0.38$ can be obtained. It is computed by averaging the ratios over a small vertical band, about 2 elements wide, located 18.5 mm away from the impacted edge. This spatially averaged ratio is then averaged in time between the 42^{nd} and the 65^{th} frames (*i.e.*, between 260 µs and 310 µs). This value is in line with the Poisson ratio obtained in the literature [Yee and Takemori, 1982], and the one given by the manufacturer (0.39). At the same time, ahead of the notch tip, the sample undergoes shear strain concentration but the crack does not propagate in this direction. It is interesting to note that at higher impact speeds (55 m/s), and in less fragile material such as polycarbonate, the crack would propagate horizontally [Ravi-Chandar *et al.*, 1999] within this shear region. Classically, this kind of propagation is associated with shear band formation. Performing such temporally and spatially resolved analysis for different impact speeds would certainly increase our understanding of the origin of such a Mode I / shear band fracture mechanism transition. Additionally, the axial strain-rate fields are depicted in Fig. 5.7. During the experiment, the axial strain-rate reaches $600\,\text{s}^{-1}$. Locally, at the crack tip, the axial strain-rate is even higher than $1.000\,\text{s}^{-1}$.

Finally, similarly to what has been done in Section 3.4.5, the effective displacement fields obtained when using a composition scheme can be compared to those that would have been obtained assuming an additive decomposition. The differences, which are the errors introduced when using a sensor-to-sensor approach, obtained in both directions for the last image taken during the test, and the errors induced on the strain field are depicted in Fig. 5.8. From Eq. 3.20, we know that these errors are, in a first order approximation,

linked to the effective displacement, the distortion's gradient and the difference between the distortions from the experiment and those from the calibration. The discrepancy has an amplitude of 6 pixels, which represents approximately 10% of the final displacements obtained during the experiment. Moreover, let us note that the differences obtained in the lower right part of the sample have an amplitude of 1 pixel. This can be explained by the fact that this part is subjected to nearly no deformation. Indeed, the differences are higher in the heavily translated and deformed parts of the sample. This is why the differences are highlighted in the regions where the effective displacement is important. Furthermore, the strain errors induced have an amplitude of about 15 mm/m, which is the same order of magnitude of the strains obtained during the experiment. This further demonstrates the necessity to correctly model the distortions. Furthermore, it justifies the need to compute the kinematic data in the undistorted reference configuration. Otherwise, strong errors and both strain levels and strain localization could be done.

Figure 5.6: Undistorted images and displacement fields obtained during an impact test for different time steps.

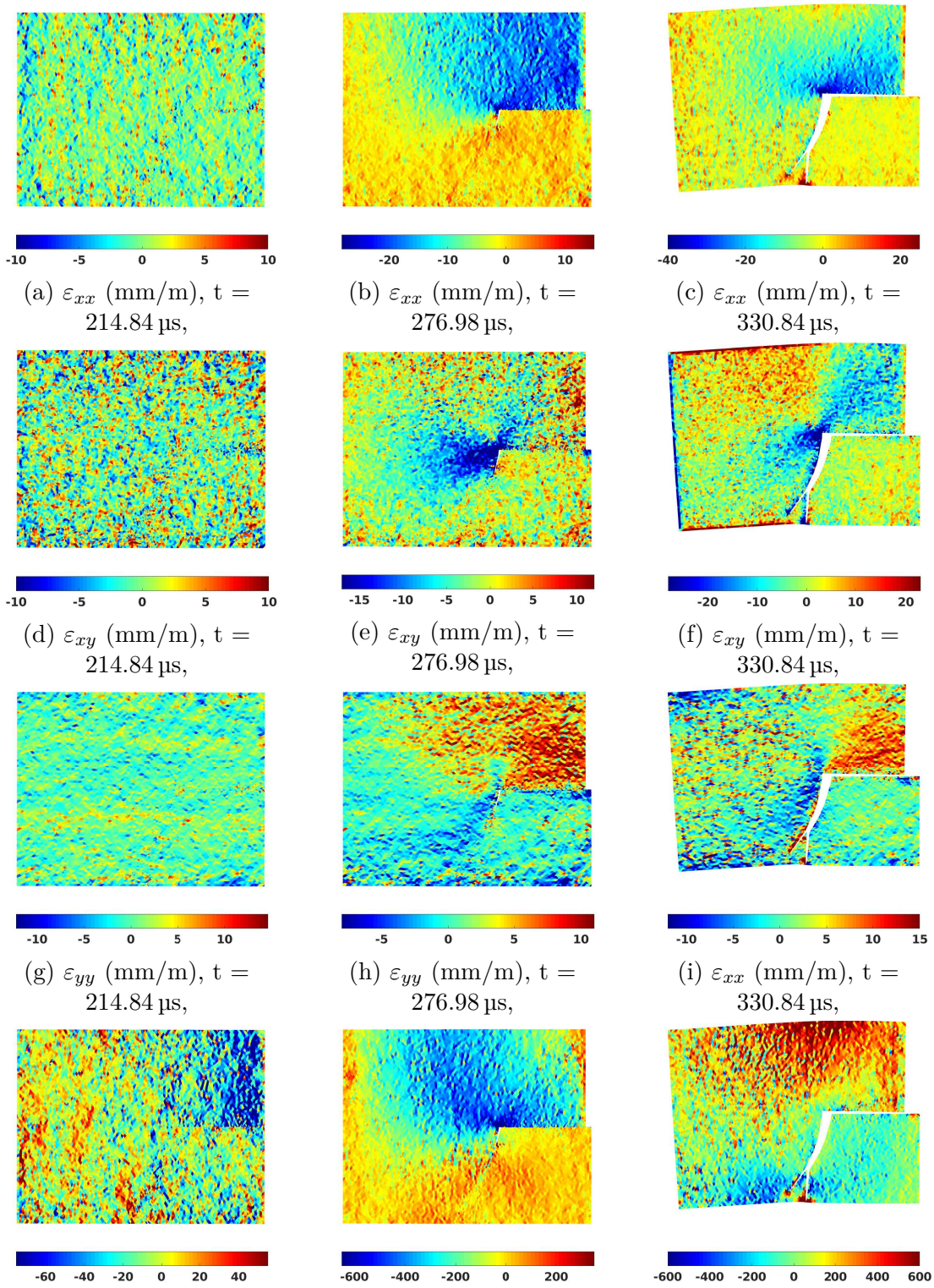

(a) ε_{xx} (mm/m), t = 214.84 µs, (b) ε_{xx} (mm/m), t = 276.98 µs, (c) ε_{xx} (mm/m), t = 330.84 µs,

(d) ε_{xy} (mm/m), t = 214.84 µs, (e) ε_{xy} (mm/m), t = 276.98 µs, (f) ε_{xy} (mm/m), t = 330.84 µs,

(g) ε_{yy} (mm/m), t = 214.84 µs, (h) ε_{yy} (mm/m), t = 276.98 µs, (i) ε_{xx} (mm/m), t = 330.84 µs,

(j) $\dot{\varepsilon}_{xx}$ (s^{-1}), t = 214.84 µs, (k) $\dot{\varepsilon}_{xx}$ (s^{-1}), t = 276.98 µs, (l) $\dot{\varepsilon}_{xx}$ (s^{-1}), t = 330.84 µs,

Figure 5.7: Strain and strain-rate fields obtained during an impact test for different time steps.

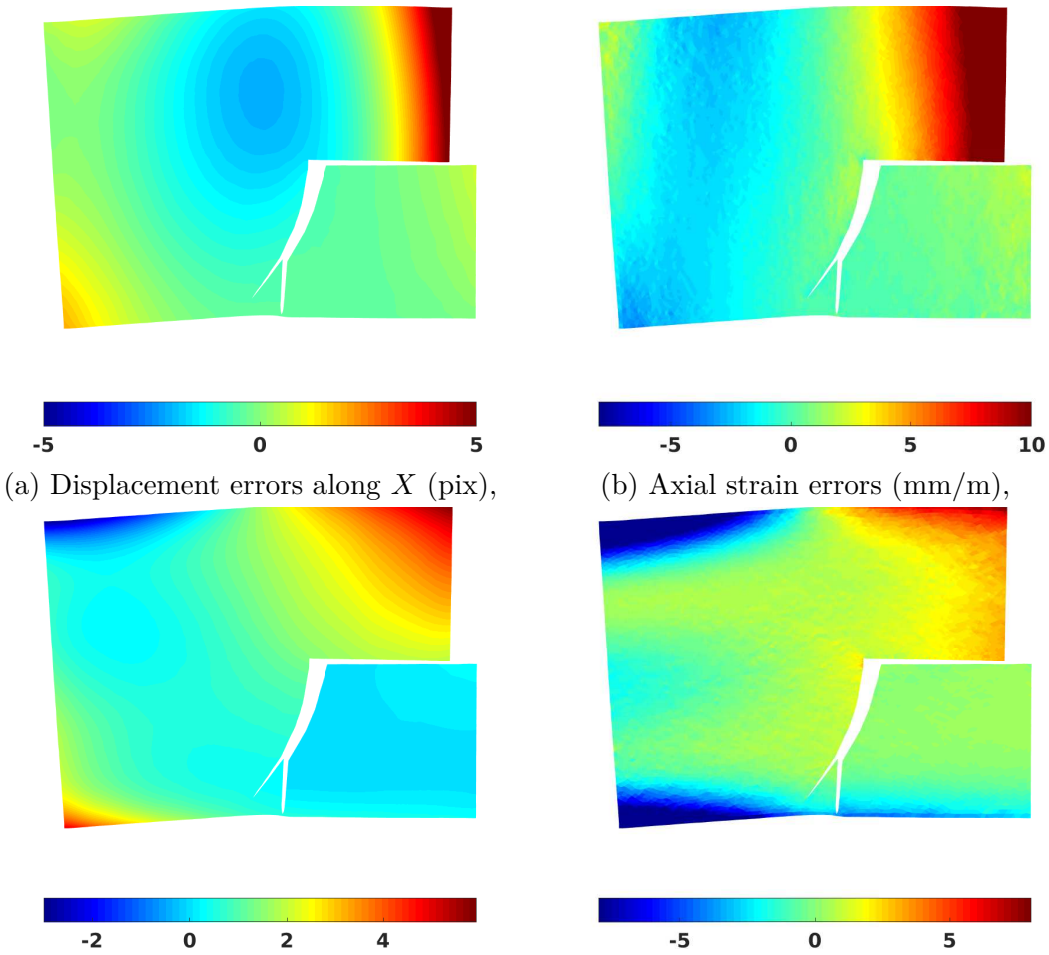

(a) Displacement errors along X (pix), (b) Axial strain errors (mm/m),

(c) Displacement errors along Y (pix), (d) Transverse strain errors (mm/m),

Figure 5.8: Estimation of the displacement errors committed when using a sensor-to-sensor (or additive) approach (ϵ in Eq. 3.20), and the associated strain errors.

5.3 Temperature fields

The main goal of the infrared measurement, on such an experiment, is methodological, *i.e.* trying to face and overcome all the practical constraints that coupled measurement induces as well as validate the practical achievement of quantitative thermography.

Indeed, PMMA, *i.e.* quasi-brittle material, subjected to a pure inertial impact test, *i.e.* subjected to a couple of percent of strain in compression and in tension, is not supposed to induce significant dissipation. This statement can be checked using Lord Kelvin equation. For a test on a homogeneous and isotropic material during linear elasticity and under adiabatic conditions:

$$\Delta T = -\frac{\alpha_T}{\rho C_\varepsilon} T_o \Delta\sigma, \tag{5.1}$$

where α_T is the thermal expansion coefficient, ρ its density, C_ε the specific heat, $\Delta\sigma$ the applied stress and T_o the room temperature. Using $\alpha_T = 70 \times 10^{-6}\,\mathrm{K}^{-1}$, $\rho = 1190\,\mathrm{kg/m^3}$, $C_\varepsilon = 1450\,\mathrm{J/(K\,kg)}$, $T_o = 298\,\mathrm{K}$ and the stress impulse estimated close to 120 MPa in Section 5.1.2, the formula yields $\Delta T = -1.45\,\mathrm{K}$, which in line with what is found in [Rodriguez and Filisko, 1986]. While such a variation is higher than the temperature measurement uncertainty, we will see that the main challenge of coupling IR and visible measurements at high speed consists, in this experiment, in getting rid of the bias induced by the flashes, the latter being significantly larger than the raw uncertainty of the camera itself.

5.3.1 Flash influence

In order to assess the influence of the flashes on the temperature measurements, 5 recordings were made before mechanical loading. During these recordings, the sample was in the same configuration as for the test and images were acquired before, during and after the flashes. Figure 5.9a depicts the raise of temperature, averaged over the sensor, caused by the flashes for the 5 recordings. In this figure, the time starts when the flash is triggered and ends after 525 µs. The dashed black lines represent the recording window of the Cordin-580 during the experiment.

The flashes induce an apparent raise of temperature of about 25 °C in 500 µs. Furthermore, the raise of temperature is highly reproducible. Indeed, the difference between the raises remains below 1 °C, except between 125 µs and 200 µs where the difference can reach 3 °C. Let us recall that the Telops M3k camera records wavelengths from 1500 nm to 5400 nm. Furthermore, the Xenon flashes used emit 5 % of their output in the same range wavelength. Hence, as PMMA transmits approximately 60 % of the infrared wavelengths between 1800 nm and 2100 nm, it has been concluded that the apparent raise of temperature is mainly induced by the transmission of these wavelengths and not by the heating of the sample. This is summarized in Figure 5.9b. This can be further validated using basic thermal conduction considerations. Let us suppose that one face of the sample is exposed

to a homogeneous source of temperature. The time needed for the opposite face to reach the same temperature can be roughly estimated using the following formula:

$$e^2 \approx \kappa\tau, \tag{5.2}$$

where e is the sample's thickness, τ an estimation of the time and κ the thermal diffusivity of the material. In this particular case $e = 5\,\text{mm}$, $\kappa = 9.85 \times 10^{-8}\,\text{m}^2\,\text{s}^{-1}$. Hence, a rough estimation of the time needed for the temperature to propagate through the thickness of a PMMA sample is $\tau \approx 250\,\text{s}$. As this estimation is several orders of magnitude higher than the raises of temperature obtained, this further validate the idea that these raises are not caused by a heating of the sample. So while this apparent raise in temperature can easily be understandable by the fact that the material is not opaque to flashes IR radiations, it remains unclear to us why the layer of black paint put on the sample for IR measurements did not significantly mitigate this effect. The raise in temperature may be the consequence of different phenomena, the transmission through PMMA thickness from the uncoated faced (observed by the Cordin) to the other face then conduction through the thin layer of paint could partly explain such a quick raise. Nevertheless, notice that a 10 µm thin layer of black paint will delay the signal by a little less than 1 ms, which remains long compared to the 500 µs observed.

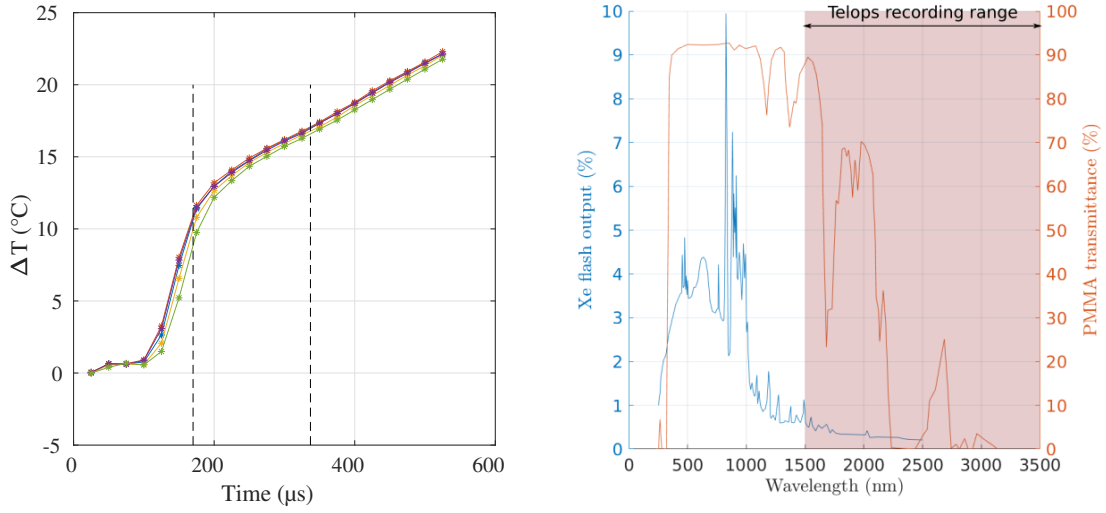

(a) Raise of temperature caused by the flashes for the 5 different recordings,

(b) Flash outputs and PMMA transmittance spectra,

Figure 5.9: Influence of the flashes on the temperature measurements and spectrum of the Xenon flash ouputs as well as the PMMA transmittance.

Finally, as the flashes induce an apparent raise of temperature with a high repeatability, their influence can be taken into consideration during real experiments. As a result, the raise of temperature will be averaged over the 5 acquisitions. The resulting apparent raise of temperature will then be subtracted to the temperature fields obtained during

the inertial impact test. Notice that the $\pm$ 1 °C variability remains.

5.3.2 Temperature fields from an inertial impact test

Once the apparent raise of temperature deducted from the experimental fields, the temperature room, 28 °C, is also subtracted. Then, using the methodology presented in Chapter 4, the resulting fields are transferred in the reference configuration. Figure 5.10 depicts the variation of temperature occurring during the experiment in the reference configuration for different time steps.

The methodology proposed in this work successfully replaced the temperature fields in the reference configuration. Due to the size of the infrared images, only half of the sample was observed and the crack did not propagate in it. The temperature variations captured during the experiment remain under 2 °C in all the sample except in the crack vicinity and no specific localization in line with strain maps are observed. The temperature evolution during the test consists in a homogeneous and slight increase of the sample temperature (see Figure E.7d). As previously said, it can be explained by the not so dissipative nature of the material. In addition, since the systematic error of the calibration used is about 1 °C, no relevant information is obtained using an infrared camera during this experiment. It is in line with the predictions made previously. Regarding the temperature raise at the crack lip, the uncertainty can not be guaranteed any longer due to the change in apparent emissivity, the light diffraction from behind...

(a) t = 171.34 µs, (b) t = 189.98 µs, (c) t = 214.84 µs, (d) t = 233.48 µs,

(e) t = 252.13 µs, (f) t = 270.77 µs, (g) t = 289.41 µs, (h) t = 308.06 µs,

Figure 5.10: Evolution of the temperature variation during an inertial impact test, displayed in the reference configuration.

5.4 Conclusion

In this chapter, an experimental validation test is performed. It consists in an inertial impact test performed on a pre-notched PMMA sample. The methodologies presented in Chapter 3 and 4 are used in order to retrieve both kinematic and thermal fields during the experiment. The main conclusions are as follows:

- Quantitative kinematic full-field data from an inertial impact test on a pre-notched PMMA sample have been acquired at a rate of 480,000 fps. These kinematic fields quantitatively captured the events occurring during the test, such as the compression wave and the Poisson effect induced, or the shear strain concentration at the notch tip.
- These kinematic fields have a better spatial sampling than what can traditionally be obtained with classically used high-speed cameras, at the price of higher strain random errors. In the present configuration we reach a spatial sampling of about 1 mm over a FOV of approximately 100 mm × 100 mm.
- The flashes used induce a highly reproducible apparent raise of the sample's temperature of about 25 °C in 500 µs. Hence, this apparent raise – induced by the transparency of PMMA to the IR wavelengths recorded by the camera – can be subtracted from the fields obtained during the experiment.
- The methodology presented to perform lagrangian thermography successfully replaced the temperature fields in the reference configuration. However, the temperature variations captured during the experiment remain under 2 °C in all the sample except near the crack. Hence, no relevant information is obtained using an infrared camera during this experiment.

Part II

Characterization of an XES steel, numerical and experimental investigation

Chapter 6

Numerical simulation and analysis of a dynamic tensile test

Content

6.1 Introduction

In the previous chapters, the visible light and infrared cameras that are used to record high strain-rate experiments are presented as well as their limitations (Chapter 3). First, these cameras, as all cameras, act as spatio-temporal low-pass filters, and limit the measurability of strong gradients (spatial or temporal). In addition, sensor noise and the intrinsic variability of the optical distortions involved in multi-sensors cameras also restrict the lowest strain that can be measured accurately, and for similar reasons the measurable temperatures are also affected. Since the non-parametric approach to estimate stress fields that will be used (presented in depth in Chapter 8) only relies on measurements, it is essential to design experiments with these restrictions in mind. To do so, numerical twins can be used to take into account the errors introduced at the different steps of the experimental procedure. The use of these twins hence allows to assess the ability to capture kinematic and temperature fields during the designed experiment and to have an estimation of the uncertainties achievable.

Historically, in dynamics, statically determined tests have been conducted using hydraulic machines or SHPB for instance. Characterizing the material response over a wide range of strain-rates used to require different setups. Indeed, hydraulic tensile machines are classically limited to a strain-rate range of $[1 \times 10^{-3}\,\mathrm{s}^{-1} - 1 \times 10^{2}\,\mathrm{s}^{-1}]$, while the SHPB covers the $[1 \times 10^{2}\,\mathrm{s}^{-1} - 1 \times 10^{3}\,\mathrm{s}^{-1}]$ range. This implies that the realization of tensile tests at $1 \times 10^{3}\,\mathrm{s}^{-1}$ or compressive tests at $1 \times 10^{1}\,\mathrm{s}^{-1}$, for instance, is not a given. However, the new opportunities opened with the inverse identification of either constitutive parameters

or of the stress distribution itself (see Chapter 8) allows to completely reconsider the experimental design. In particular, it allows to consider geometries and boundary conditions that would lead to heterogeneous fields, which in turn enable the analysis of couplings, localization phenomena as well as complex loadings history. One of the potential outcome would be, in one experiment, to characterize the material for wide spectra of strains, strain-rates and temperatures for loadings closer to real case. Such a route may be of great interest for industries.

As a side point, notice however that some limitations remain hard to overcome. In particular, the difficulty to accurately capture the external load during transient, highly dynamic loadings, even if an elegant solution has been proposed in [Pierron *et al.*, 2014] to get the load directly from images using particular loading configurations [Fletcher and Pierron, 2018, Seghir and Pierron, 2018, Fletcher and Pierron, 2020] and ultra-high speed imaging. Nevertheless, such methodologies do not provide, yet, a way to address significant strain levels (*e.g.* tens of percent).

In practice, for dynamic characterization two main routes are followed: the first one consists in devising complex experimental set-ups allowing to conduct statically determined tests. This was the strategy chosen by Haugou and his collaborators. In his work [Haugou *et al.*, 2006], a non direct tensile testing device using SHPB is proposed. Using this apparatus, the authors were able to model the constitutive behaviour of a XES steel and an aluminium alloy in tension for plastic strain-rates between $180\,\mathrm{s}^{-1}$ and $440\,\mathrm{s}^{-1}$. The results were consistent with previous studies performed with more traditional experimental set-ups. The other one is to go back to more traditional experiments, and perform statically undetermined tests using complex geometries, combined with inverse identification methods (see Section 6.3). Following this strategy, in 2019 Fourest and his collaborators [Fourest *et al.*, 2020] introduced strain concentrators in the sample geometry (see Section 6.3 for the geometry used). Then, using the Image-Based Inertial Impact test methodology and the Virtual Fields Method, the authors were able to identify one of the parameters (named C in our case, see Eq. 6.2.2.1) of the Johnson-Cook law used to model their titanium alloy (up to $500\,\mathrm{s}^{-1}$). Furthermore, they also demonstrated that the introduction of holes or notches induced non homogeneous fields and a significant gain in the strain and strain-rate spectra was observed.

In this PhD work, the latter strategy will be adopted. Hence, through the use of FE simulations, this Chapter aims to design a statically undetermined test which is compatible with our experimental restrictions. Furthermore, the accuracy of the measurements will be assessed. To this effect, the material that will be used in this work is first presented. Then the design of the geometry is discussed, based on FE simulations. Finally, using Virtual Image Deformation (VID), the measurability of the kinematic fields induced by the geometry is assessed. The chosen geometry will then be used to create a rich material

database in Chapter 7. The goal is then to use this rich database to characterize the material with a recently proposed and so called Data-Driven Identification method. This will be further discussed in Chapter 8.

6.2 Material and constitutive behaviour

The material chosen for this experimental campaign is the rate-dependent, low-carbon mild-steel XES (French standards). Its chemical composition is presented in Tab. 6.1. The quasi-static and dynamic behaviour of this material are relatively well-known. Indeed, for example in the mid 90s, methodologies were developed allowing to perform double-shear experiments on thin metal sheet in both quasi-static and high strain-rate conditions with highly homogeneous stress and strain states [Gary and Nowacki, 1994]. These methodologies were used to study the shear behaviour of the XES steel – in particular the evolution of the rate sensitivity, for strain-rates ranging from $1 \times 10^{-3}\,\mathrm{s}^{-1}$ to $1 \times 10^{3}\,\mathrm{s}^{-1}$ [Klepaczko *et al.*, 1999]. The tensile behaviour of this steel has also been investigated. For this purpose, Haugou and its collaborators [Haugou *et al.*, 2006] developed a tensile testing device for split Hopkinson bars. This device allows for non-direct tensile tests to be performed on metal sheets. The configuration was used to characterize the mild-steel for plastic strain-rates between $180\,\mathrm{s}^{-1}$ and $440\,\mathrm{s}^{-1}$. At last, more recently, some researchers focused on the modelling of spot weld for this material. For instance, using experiments based on Arcan principle, Langrand *et al.* [Langrand and Combescure, 2004, Langrand and Markiewicz, 2010] were able to model and characterize the joint when submitted to pure and mixed tensile/shear loads in both quasi-static and dynamic conditions. In 2016, Markiewicz *et al.* [Markiewicz *et al.*, 2016] went one step further and investigated the behaviour of the material when heat affected by spot welding. Furthermore, the authors studied the strain-rate dependency of the heat affected material and identified parameters for a visco-plastic model describing the material.

C	S	N	Mn	P	Si	Al	Ni	Cr
0.0268	0.0175	0.006	0.202	0.007	0.007	0.07	0.018	0.036
Cu	Mo	Sn	Nb	V	Ti	B	Ca	
0.014	0.002	0.004	0.001	0.002	0.002	≤ 0.0003	≤ 0.0003	

Table 6.1: XES chemical composition (in wt%), data from [Markiewicz *et al.*, 2016].

As a consequence, we use this material as model material to develop our heterogeneous high strain-rates tests as well as stress reconstruction approaches. In this Section, the material will be presented as well as the constitutive laws usually used at ONERA.

6.2.1 XES steel reference data

In the following, late results from an ONERA characterization campaign [Markiewicz *et al.*, 2016] will be used as a reference database. For this campaign, tensile tests were performed on samples respecting the standard ISO6892-1, using a hydraulic jack. Three different cross-head speeds were used for this experimental investigation: 5 mm/min, 0.01 m/s and 1 m/s, which lead to estimated average plastic strain-rates of respectively $0.006\,\mathrm{s}^{-1}$, $0.7\,\mathrm{s}^{-1}$ and $70\,\mathrm{s}^{-1}$. An optical extensometer and a piezoelectric load cell were used in order to retrieve the engineering strain ($\varepsilon_{\mathrm{eng}}$) and stress ($\sigma_{\mathrm{eng}}$) (see Section 2.2.3). The true stress-strain curves obtained are depicted in Figure 6.1a. As previously said, notice that dynamic measurements (see the curve for $1\,\mathrm{m\,s}^{-1}$) tends to be strongly affected by wave propagations [Markiewicz *et al.*, 2016]. This figure highlights the fact that the material considered in this work is heavily strain-rate dependent [Gary, 2000]. Indeed, both the elastic limit and the hardening modulus change with the strain-rate: while the elastic limit increases with the strain-rate, the hardening modulus decreases. Furthermore, it has been shown by other authors that this dependency fades away beyond $1 \times 10^2\,\mathrm{s}^{-1}$ [Haugou *et al.*, 2006], underlying a non-linear rate-dependency. This is illustrated in Fig. 6.1b, where the curves for strain-rates between $200\,\mathrm{s}^{-1}$ and $440\,\mathrm{s}^{-1}$ have the same behaviour and are nearly superimposed. As a side comment, notice how stress-strain relationships can be difficult to properly obtain beyond $1 \times 10^2\,\mathrm{s}^{-1}$(oscillations), even on such a basic uniaxial loading configuration.

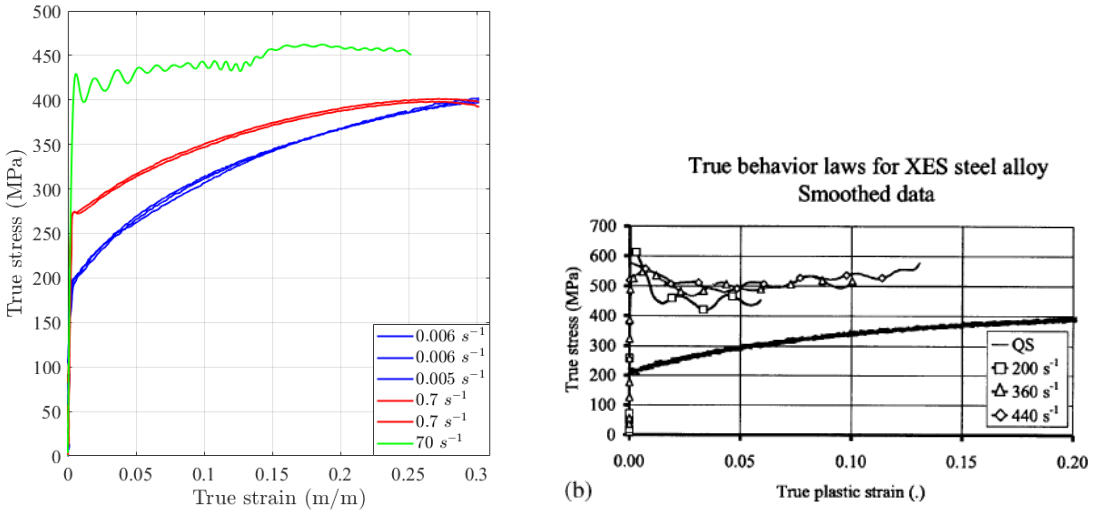

(a) True stress-strain curves for XES steel, reference data [Markiewicz *et al.*, 2016].

(b) True stress-strain curves for XES steel, figure from [Haugou *et al.*, 2006].

Figure 6.1: True stress-strain curves for XES steel obtained from reference data from ONERA, or found in the literature. The first is obtained using a dynamic hydraulic machine while the later is obtained from tensile Hopkinson Bar tests.

6.2.2 Constitutive model

From experimental data, one can extract constitutive parameters to model the behaviour of the material. In what follows, two phenomenological constitutive models are considered: the classical Johnson-Cook model and a dedicated one, named modified Krupkowsky model. The first one, even if not really predictive for the considered material (see the following section) is investigated since it is implemented by default in any commercial FE code and will be used later for simplicity's sake (see Section 6.3). The later, much more complex is analysed for its ability to accurately capture the complex material response of the XES.

6.2.2.1 Johnson-Cook model

The Johnson-Cook hardening model is one of the most well-known model for visco-plastic materials [Johnson and Cook, 1983]. This model is usually written as:

$$\sigma_{JC} = \left[A + B\varepsilon_p^n\right]\left[1 + C\ln\left(\frac{\dot{\varepsilon}_p}{\dot{\varepsilon}_0}\right)\right]\left[1 - \left(\frac{T - T_0}{T_m - T_0}\right)^m\right], \tag{6.1}$$

where σ_{JC} is the flow stress, ε_p is the equivalent plastic strain, T_m is the melting temperature of the material, T_0 and $\dot{\varepsilon}_0$ are respectively the reference temperature and equivalent plastic strain-rate. The material parameter A represents the initial yield stress at $0.2\,\%$, while B and n capture the isotropic strain hardening evolution. In addition, C captures the material's strain-rate dependency and m the temperature one. Let us note that the Johnson-Cook model is a multiplicative decoupled model [Hor *et al.*, 2013], indeed there is no coupling between the hardening, the strain-rate dependency and the temperature sensitivity. Such a model generally has a low number of parameters to identify (in this case 5). However, this comes at the price of a strong assumption: the initial yield stress and the hardening modulus have the same strain-rate and temperature dependency, which is not the case for the XES steel used in this work. To address this issue, several extensions of the model have been proposed introducing all sort of coupling [Khan and Liang, 1999, Kang and Huh, 2000, Bäker, 2006]. However, the models remain multiplicative.

For the present case, the thermal part of the expression is ignored since the temperature was not captured during these experiments. Nevertheless, A B and n can be identified on the quasi-static data using a curve fitting method. Then, using the whole data set from $\varepsilon_p = 0.01$ to 0.25, parameter C can be identified. The parameters are summarized in Tab. 6.2. In Figure 6.2 the reference data are compared to the model when using the parameters identified, for each average strain-rates. This figure clearly demonstrates that the Johnson-Cook model is unable to account for the whole material's strain-rate dependency.

A (MPa)	B (MPa)	n	C	$\dot{\varepsilon}_0$ (s^{-1})
186	511	0.626	0.0374	0.0056

Table 6.2: Johnson-Cook parameters identified using the reference data provided by ONERA.

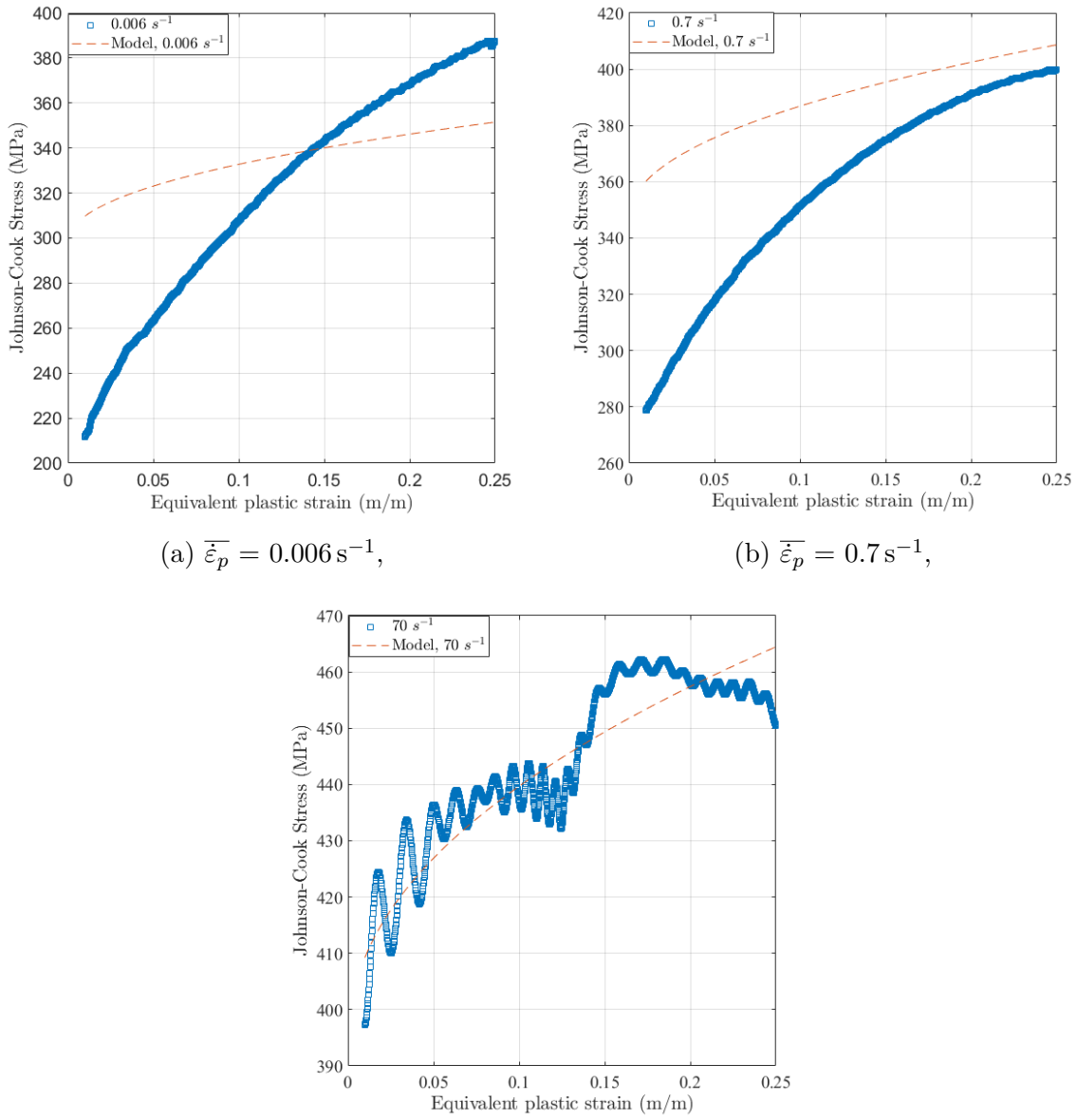

(a) $\overline{\dot{\varepsilon}_p} = 0.006\,\mathrm{s}^{-1}$, (b) $\overline{\dot{\varepsilon}_p} = 0.7\,\mathrm{s}^{-1}$,

(c) $\overline{\dot{\varepsilon}_p} = 70\,\mathrm{s}^{-1}$,

Figure 6.2: Comparison between the reference data, and the Johnson-Cook model previsions optimized for the data set.

6.2.2.2 Modified Krupkowsky model

The inability of the classically used Johnson-Cook constitutive equation to model accurately the mild-steel of this study has led researchers to use another model. It is a modified

Krupkowsky model [Priadi *et al.*, 1991]. This model is written as:

$$\begin{aligned} \sigma_{KR} &= KX^a \left(\varepsilon_0 X^b + \varepsilon_p\right)^{nX^c}, \\ X &= \frac{\dot{\varepsilon}_p}{\dot{\varepsilon}_0}, \end{aligned} \tag{6.2}$$

where K, a, b, c, n, ε_0 and $\dot{\varepsilon}_0$ are the model parameters to be identified. Let us remark that when $X = 1$, which is generally the case when performing tensile tests on homogeneous samples, the classical Krupkowsky model is retrieved. In addition, this model allows for a coupling between the hardening and the strain-rate dependency. However, this formulation does not allow the consideration of the temperature sensitivity.

The model parameters identified by the authors who performed the characterization campaign are summarized in Tab. 6.3. Using these parameters, the model can be confronted to the experimental data. To this effect, Fig. 6.3 depicts the comparison between the experimental data and the model, for each cross-head speed. This figure demonstrates the modified Krupkowsky model's ability to account for the strain-rate dependency. Indeed, the model curves match quite well the experimental ones. To assess the robustness of the inverse identification of the constitutive parameters, a series of slightly different experimental strain range has been used to perform identification using Matlab non-linear inverse identification functions. Table 6.3 shows for example the identification performed when data with strains below 1 % are discarded. Variations of up to 90 % are observed, in particular for exponents a and c. Nevertheless, the relative error between the stresses predicted using these parameters and the measured stresses from the reference data remains below 5 % as depicted by Fig. 6.4 where the relative error between model estimations and the reference database is calculated for the 3 strain-rates investigated. This observation further justifies the will to directly identify the material response rather than constitutive parameters. Indeed, due to the parameters interdependence, two different sets of parameters can be used to describe the same response. Furthermore, the parameters identification has been found to be very sensitive to the range of data considered, which can be partly explained by the influence of the oscillations captured for the data at $70\,\mathrm{s}^{-1}$.

Parameters	K (MPa)	ε_0	n	$\dot{\varepsilon}_0$ (s^{-1})	a	b	c
[Markiewicz *et al.*, 2016]	526.6	0.024	0.221	0.085	0.002	0.385	0.002
Identified	544.5	0.032	0.259	0.06	0.0002	0.328	0.0002
Relative variation (%)	−3.4 %	−33.3 %	−17.2 %	29.41 %	90 %	14.8 %	90 %

Table 6.3: Parameters for the modified Krupkowsky model from [Markiewicz *et al.*, 2016], and identified parameters.

As a summary, the mild-steel XES used in this study exhibits a complex strain-rate dependency that the classical multiplicative Johnson-Cook model [Johnson and Cook,

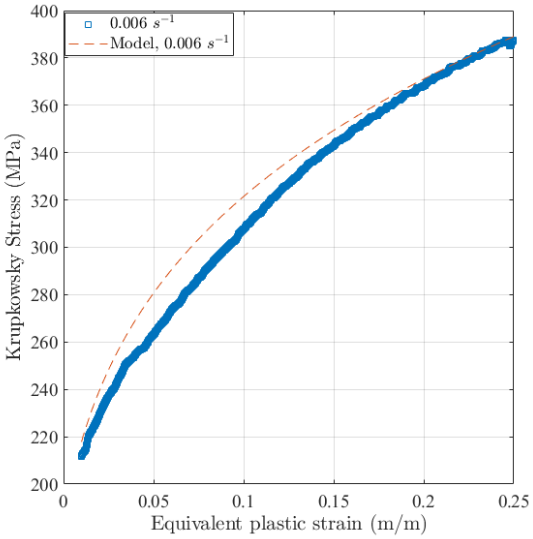

(a) $\overline{\dot{\varepsilon}_p} = 0.006\,\mathrm{s}^{-1}$,

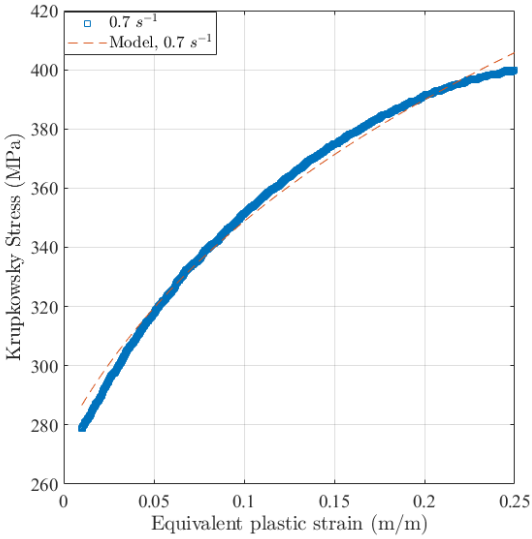

(b) $\overline{\dot{\varepsilon}_p} = 0.7\,\mathrm{s}^{-1}$,

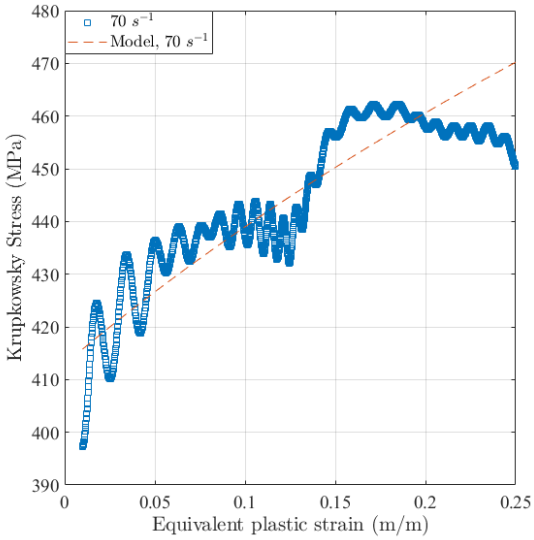

(c) $\overline{\dot{\varepsilon}_p} = 70\,\mathrm{s}^{-1}$,

Figure 6.3: Comparison between the reference data, and the modified Krupkowsky model previsions using the parameters from [Markiewicz *et al.*, 2016].

1983] is not able to describe. In particular, this model fails to describe the uncoupled dependencies of the initial yield stress and the hardening modulus. As a result, the use of a more complex model (the modified Krupkowsky model here) is needed. In the next chapter, both models will be confronted to experimental data obtained during heterogeneous 2D experiments. In addition, the stress flow estimation will be compared to the Data-Driven Identification results to investigate the ability of the modified Krupkoswky model to capture the material response when one deviates from homogeneous and uniaxial loading conditions in Chapter 8. Nevertheless, even if the modified Krupkowsky model clearly better captures the material response, we will use the Johnson-Cook model

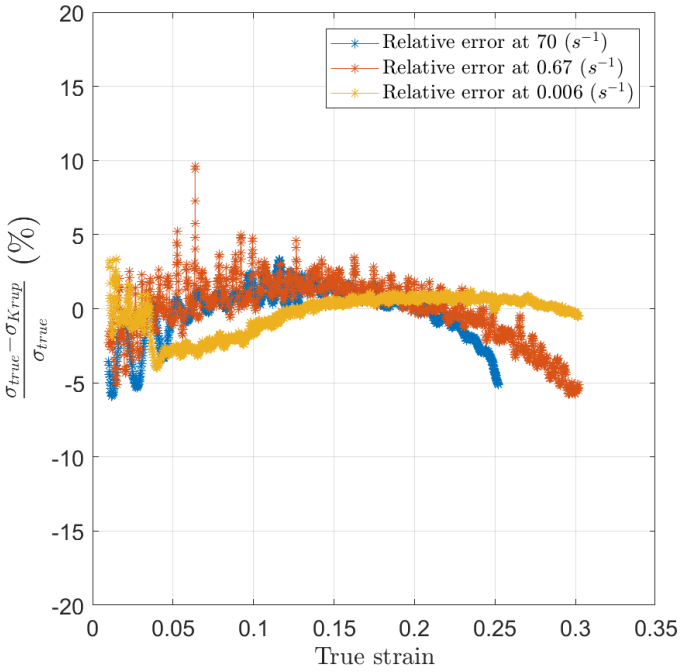

Figure 6.4: Relative errors between the reference data and the fit using the identified parameters.

for the sample geometry design and uncertainty quantification in this Chapter as it is implemented by default in FE solvers. It will not affect any of the conclusions.

6.3 Sample's geometry design

Thanks to the recent development in imaging technology, it is now possible to perform full-field measurements at high frame rates. Furthermore, recent identification techniques (FEMU, VFM or Data-Driven Identification for instance) now take advantage of the full-field measurements methods to identify the material behaviour using the external forces or the acceleration. These developments allow for the use of complex sample geometries which will no longer lead to homogeneous fields and will cover large spectra of strain and strain-rates. The question of their design is extremely vast. In the following, some potential design from recent studies will be presented briefly.

Bouda *et al.* [Bouda *et al.*, 2019] proposed a methodology to optimize sample geometries for visco-plasticity identification at high strain-rates. For a given test procedure (in this case the Image-Based Inertial Impact (IBII) tests), while assuming the material constitutive model, the authors investigated several geometries (based on heuristics) and the induced strain and strain-rate spectra through the use of Finite Element simulations. Moreover, by taking into account their camera's specifications (fps, number of pixel, noise...) they ensured the measurability of the kinematic fields and also investigated the

ability to correctly identify constitutive model parameters. Using the geometries presented in Fig. 6.5, the authors were able to design an experiment in which the sample undergoes strains in the range of $[0 - 1 \times 10^{-1}]$ and $[1\,\mathrm{s}^{-1} - 1 \times 10^{4}\,\mathrm{s}^{-1}]$ for strain-rates during an inertial impact test with a projectile velocity of 70 m/s. Similarly, Jones *et al.* [Jones *et al.*,

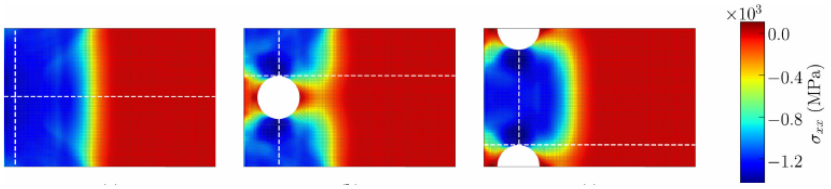

Figure 6.5: Reconstructed σ_{xx} cartographies obtained in [Bouda *et al.*, 2019] for different considered geometries.

2018] published a study in which they designed an original D-shaped specimen geometry (see Fig. 6.6). This geometry was optimized for tensile tests, in order to satisfy several criteria, among which the stress heterogeneity and the strain-rate spectra. By simulating a tensile test with a cross-head speed of $2.5\,\mathrm{mm\,s}^{-1}$ per grip, the specimen undergoes strains in the range of $[0 - 0.4]$ and $[1 \times 10^{-5}\,\mathrm{s}^{-1} - 1 \times 10^{-1}\,\mathrm{s}^{-1}]$ for strain-rates. Furthermore, while the stress states obtained are mainly tension along the tensile test direction, some amount of bi-axial and shear stress near the dominant tensile stress are observed. The main limitation of this D-shaped geometry is that since it is not symmetrical, bias in the load measurement may appear. It is important to note that in these studies, the specimen

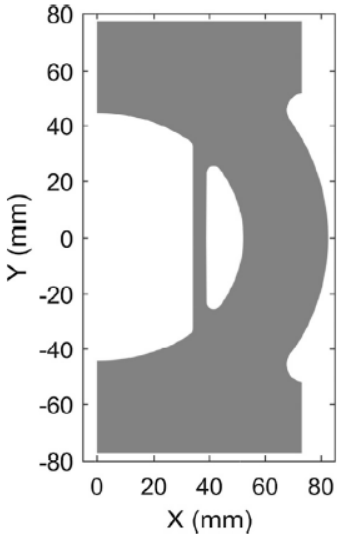

Figure 6.6: Sample geometry considered in [Jones *et al.*, 2018].

shape is constrained *a priori*, and thus only a few topological parameters are optimized. Another possibility is to rely on Topology Optimization and iterative procedure in order to optimize the specimen shape [Barroqueiro *et al.*, 2020, Chamoin *et al.*, 2020] with respect to chosen criteria (*e.g.* the covariance matrix of identified parameters with FEMU due to image noise [Roux and Hild, 2020]). Using this strategy, a specimen shape is obtained

without any *a priori* conditions on its shape. To this effect, in their work in 2020, Chamoin *et al.* [Chamoin *et al.*, 2020] designed a specimen in order to identify the shear modulus G_{12} for an orthotropic linear elastic material during a pure tensile test. The original shape designed (see Fig. 6.7) has then been used to identify the shear modulus of fir wood. Using a similar strategy, Barroqueiro and his collaborators [Barroqueiro *et al.*, 2020] obtained an optimized symmetrical shape and used it to characterize a Ti6Al4V titanium alloy with an elasto-plastic material model, during a tensile test at a strain-rate of $0.1\,\mathrm{mm\,s^{-1}}$. Using such a specimen geometry, the sample undergoes strains up to 0.165, and is submitted to heterogeneous stress states (tension, compression and shear, see Fig. 6.8). While the sample's geometry induces different stress states, it is important to note that since the test is a uniaxial tension one, the majority of the sample undergoes a tensile stress state. Nevertheless, the main disadvantages of such strategies are the computational costs of such algorithms, and above all the manufacturability of the obtained shapes.

Figure 6.7: Example of an optimized sample geometry manufactured in fir wood with a black and white paint speckle pattern, figure from [Chamoin *et al.*, 2020].

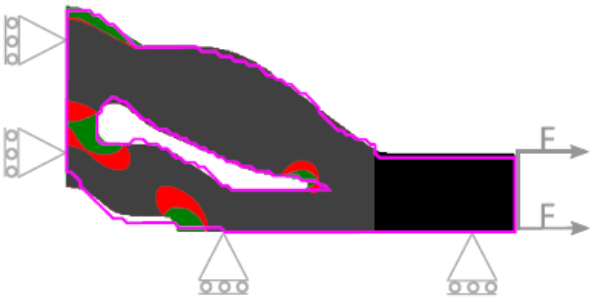

Figure 6.8: Example of an optimized sample geometry with the boundary conditions applied for a FE simulation, figure from [Barroqueiro *et al.*, 2020]. The colour map denotes the stress states: grey is for tension, red for shear and green for compression.

The use of Topological Optimization, though interesting, is beyond of the scope of the proposed work. As a result, in this work, similarly to what is done in [Jones *et al.*, 2018, Bouda *et al.*, 2019], several geometries (derived from an initial one) leading to heterogeneous fields are investigated. Hence, the limitations on the possible geometries and the criteria used to choose a relevant geometry will be presented. Then, the simulation results for some geometries will be presented and discussed.

6.3.1 Criteria and limitations

As explained previously, the goal is to choose a sample geometry that will lead to data as rich as possible. In this work, the richness of the data will be evaluated by looking at the stress heterogeneity: the stress states reached by the material during the experiment should span a large range of in-plane multi-axiality states. In addition, the spectra of the strain, strain-rate and temperature reached by the material will also be considered.

For practical reasons, some limitations are introduced on the geometries that can be considered in this work. Indeed, the XES steel investigated in this work is available in 0.8 mm-thick sheet. Hence, this will limit the geometry to a planar one. Furthermore, since the test will be conducted using a dynamic tensile test device (more information on the experimental setup are available in Section 7.1.2), the specimen length and width are also limited. As a result, the geometries that will be considered are based on the geometry classically used when using this device (see Appendix B). In addition, since the Data-Driven Identification method relies on the load recorded by the load cell (see Chapter 8), the sample needs to be symmetrical in the tensile test direction in order to avoid the introduction of any bias in the load measurement (*e.g.* transverse loading). At last, due to the limited frame rate of the infrared camera ($\leq$ 100k fps), the experiment has to be designed so that several thermal images can be acquired during the test. In addition, due to duration of the flashes used to provide the light necessary for the ultra high-speed camera, the experiment can not last too long either. Hence, the optimal duration of the experiment is estimated at around 1 ms.

With these limitations in mind, the geometries investigated are derived from the one depicted in Figure 6.9. Notches and a hole were introduced in the sample in order to create heterogeneous and multi-axial states (strain, strain-rates and stresses). The hole is in the centre of the sample. The radius of the notches and the hole as well as the vertical distance between the hole and the notches are geometrical parameters that will be investigated.

6.3.2 Simulation parameters

In order to study the impact of the geometrical parameters on the results, FE simulations were conducted. They were conducted using Abaqus, with the implicit solver (see Table 6.5 for the simulation parameters). The choice was made to perform the simulations using this solver since for the experiment considered (dynamic tensile test), inertia will have little to no effect. This assumption will be checked later in Appendix A.

The constitutive model used for these simulations is the Johnson-Cook model which is already implemented in the software. As previously mentioned this model fails to correctly capture the strain-rate dependency of the material, especially when calibrated with data covering strain-rates from quasi-statics to dynamics. Nevertheless, its strain-rate dependency saturates for values beyond $1 \times 10^2\,\mathrm{s}^{-1}$. Hence, as the sample's geometry is expected

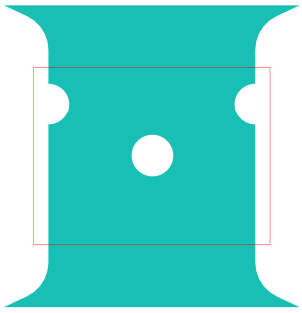

(a) Example of one of the geometries investigated, sample heads are not modelled,

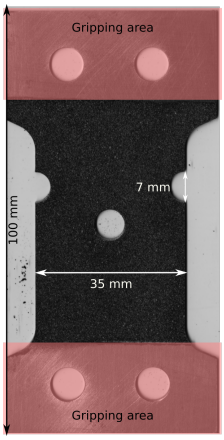

(b) Photography of an experimental sample,

Figure 6.9: Example of one of the geometries investigated, its principal features are two symmetrical notches and a central hole. The red square represent the region of interest (ROI) that will be used later. A photography of an experimental sample is also depicted, the simulations do not take into account sample heads and the gripping systems.

to lead to localization bands between the notches and the hole, it is expected that in these regions the strain-rate will reach values higher than $70\,\mathrm{s}^{-1}$ during the experiment. As a result, by using material parameters identified on high strain-rate reference data only, the simulations will still lead to representative strain and strain-rate spectra as well as stress heterogeneity in these regions, despite giving an overestimation of the stresses for low strain-rates. To this effect, the Johnson-Cook parameters are identified using the high strain-rate ($70\,\mathrm{s}^{-1}$) reference data only (see Section. 6.2.2.1). The Johnson-Cook parameters found are summarized in Table. 6.4.

A (MPa)	B (MPa)	n	C	$\dot{\varepsilon}_0$ (s^{-1})
394	146	0.471	0.0259	69.86

Table 6.4: Johnson-Cook parameters identified from the reference data provided by ONERA at $69.9\,\mathrm{s}^{-1}$.

For these simulations, the upper border of the sample is considered clamped, and an axial displacement is imposed on the lower border. The loading condition applied is thus a uniaxial tension at a loading rate of 1 m/s. This has been made considering the following points:

- The model has been calibrated from reference data obtained at this loading rate,
- The test duration, up to crack initiation ($\approx 30\,\%$), must be in the order of 1 ms, in order to have a decent number of IR images during the loading history as well as a decent spatial sampling.

- However, the test duration cannot exceed 1 ms since it is the optimal light duration that our flashes can provide.

The output data from the simulation are exported at a rate of 100 kfps for a total of 80 data snapshot, in order to replicate the data that a Cordin-580 would acquire for such an experiment. For the same reasons, a region of interest (ROI) centred on the central hole is chosen. Hence, in what follows all the data will represent what is observed in this ROI depicted by the red square in Figure 6.9.

Software	Abaqus
Solver	Implicit
Mesh size	between 0.25 mm and 1.5 mm
Constitutive model	Johnson-Cook
Export frame rate	100 kfps
Number of snapshots	80
Element type	CPS3T

Table 6.5: Finite Element simulation parameters used to investigate the different geometries.

6.3.3 Simulation results

In this section the results obtained when using different geometrical parameters will be presented. Two parameters were investigated: the radius of the notches and the hole and the vertical distance between their centres. The radius tested were 2 mm, 3.5 mm and 5 mm, while the vertical distances were 4 mm, 7 mm and 10 mm.

6.3.3.1 Influence of the geometrical parameters

In Figure 6.10, the equivalent plastic strain cartographies obtained for the different configurations are depicted for the 40^{th} snapshot (hence at mid-recording, t = 400 µs). Let us first remark that all the geometries lead to similar cartographies. Indeed, for each one of them, a strain concentration is evidenced between the notches and the central hole. As expected, the strain are higher near the hole and notches. In addition, secondary bands are evidenced. These bands go from the central hole to the edge of the sample with an angle of approximately 45°. For each geometry, the maximum plastic strain is reached in the central hole vicinity. As one can expect, the plastic strain decreases when the notches and hole radius increases. Furthermore, it can be observed that when the radius increases, the secondary bands tend to vanish. This is especially true for the biggest radius investigated. However, the vertical distance does not seem to have a significant impact on the plastic strain.

For this material, heuristically, the fracture strain is considered to be between 0.26 and 0.3 [Cherouat *et al.*, 2018]. As a result, for the geometries using a radius of 2 mm, fracture

has already happened or will very shortly happen at mid experiment. While obtaining data during fracture is valuable, this work is more focused on obtaining data prior to such an event. Hence, the geometries allowing to have about 60 snapshots before the fracture will be preferred, keeping the strain-rate as high as possible.

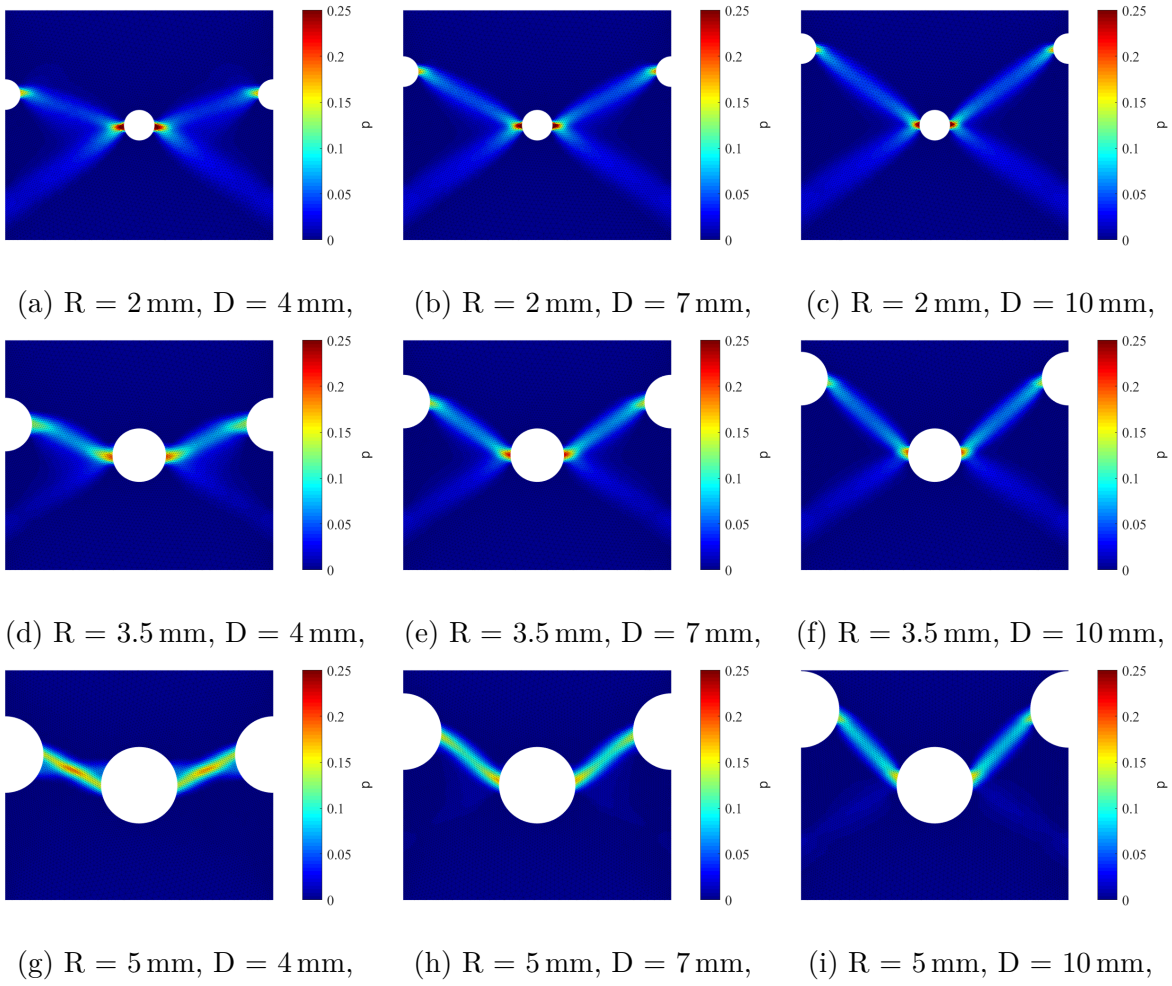

(a) R = 2 mm, D = 4 mm, (b) R = 2 mm, D = 7 mm, (c) R = 2 mm, D = 10 mm,

(d) R = 3.5 mm, D = 4 mm, (e) R = 3.5 mm, D = 7 mm, (f) R = 3.5 mm, D = 10 mm,

(g) R = 5 mm, D = 4 mm, (h) R = 5 mm, D = 7 mm, (i) R = 5 mm, D = 10 mm,

Figure 6.10: Plastic deformation cartographies obtained at the 40$^{\text{th}}$ snapshot for the different geometries considered.

In addition, plastic strain and plastic strain-rate ranges experienced by the sample during the test is investigated. To this effect, Figure 6.11 depicts the plastic strain *versus* plastic strain-rate occurrences that are observed through the chosen ROI during the whole test. White areas represent states that the sample never reached. Since the material considered has a plastic strain of fracture between 0.26 and 0.3 [Cherouat *et al.*, 2018], the x-axis is limited to a plastic strain of 0.35. This figure shows that most of the sample during the experiment undergoes small plastic strain as well as small plastic strain-rates. This is consistent with Fig 6.10. Furthermore, this figure shows that the plastic strain reaches 0.3 (so the material rupture) for all geometries, while the plastic strain-rate goes beyond 500 s^{-1}. Figure 6.11 shows that increasing the distance between the hole and the notches decreases the overall plastic strain-rate seen by the sample during the test, and also the

occurrences for high plastic strain at high plastic strain-rates. Furthermore, increasing the radius seems to have the same influence. These observations are consistent with the fact that small holes will create stronger localization phenomena, which in turn lead to greater plastic strain and strain-rates, that may additionally interact between themselves if they are sufficiently close.

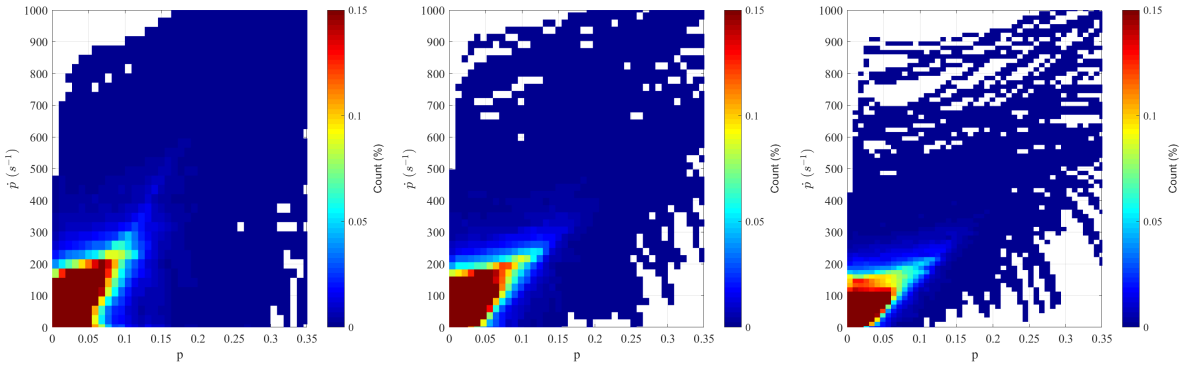

(a) R = 2 mm, D = 4 mm, (b) R = 2 mm, D = 7 mm, (c) R = 2 mm, D = 10 mm,

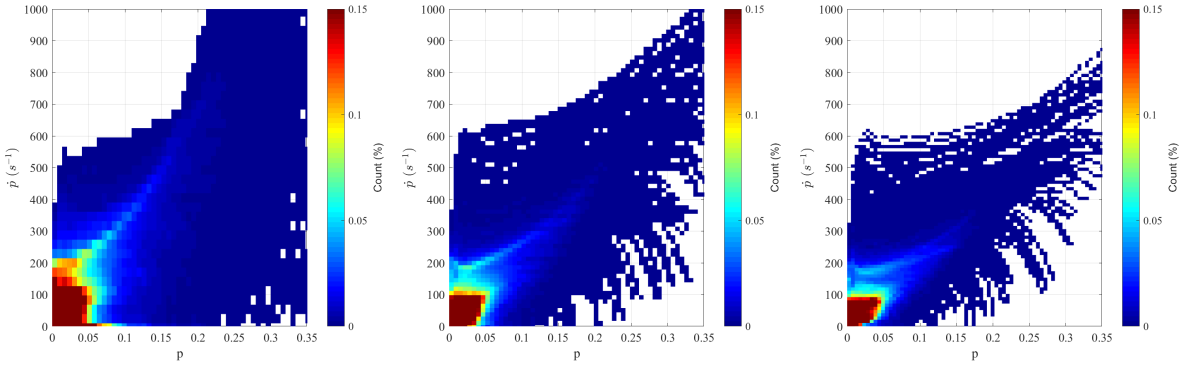

(d) R = 3.5 mm, D = 4 mm, (e) R = 3.5 mm, D = 7 mm, (f) R = 3.5 mm, D = 10 mm,

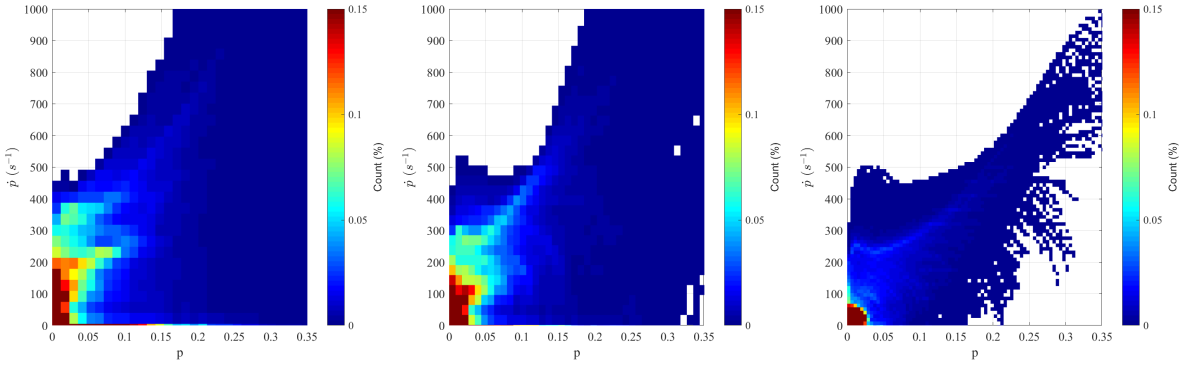

(g) R = 5 mm, D = 4 mm, (h) R = 5 mm, D = 7 mm, (i) R = 5 mm, D = 10 mm,

Figure 6.11: Plastic strain versus plastic strain-rate histograms. The colour corresponds to a 2D histogram plot. The count per bin is normalized by the number of element in the ROI multiplied by the number of time steps. The states that were never experienced by the sample remain white.

At last but not least, the heterogeneity of the stress obtained is investigated. To this

effect, Figure 6.12 depicts the stress states occurrences that is observed through the chosen ROI during the whole test, in the stress invariant space ($I_1(\sigma)$, $||\sigma||_{VM}$). White areas represent stress states that the sample never reached in the ROI and during the whole test. In addition, classical stress states such as uniaxial tension, pure shear or equibiaxial compression are represented in the figure by black dashed lines. This figure shows that the sample mostly undergoes uniaxial tension for all the considered geometries. Nevertheless, some shear states are reached as depicted by the red zones in the distributions. In addition, compression states are also reached, although very sporadically. Regarding the geometrical parameters the global trend is as follows:

- Increasing the distance between the hole and the notches restrains the stress states around the uniaxial tension state (*e.g.* the amount of shear states reduces). However, compression states are more frequents.

- Increasing the radius allows the sample to undergo more shear states and states between uniaxial and equibiaxial tension.

As a result, in order to have the best stress states distribution possible, a trade-off has to be made between the distance D and the radius R. Moreover, it is interesting to note that the limitation of the possible stress states induced by the increase of D seems to be compensated by a certain extent when the radius also increases. Hence, the geometries with $R \in [3.5\,\text{mm}\ 5\,\text{mm}]$ and D $\in [7\,\text{mm}\ 10\,\text{mm}]$ can be considered as good compromises.

Considering these figures, a compromise has to be made between the plastic strain and plastic strain-rate ranges (maximum for small R and D) and the stress states distribution (maximum for high values of R and D). In addition, in order to avoid "loss" of pixel of the camera, the hole and notches sizes have to be as small as possible. *In fine*, the radius chosen is 3.5 mm combined with a vertical distance of 8.75 mm. The blueprints for this sample geometry can be found in Appendix C.

6.3.3.2 Focus on the chosen geometry

This paragraph focuses on the chosen geometry. In Figure 6.13, the in-plane stress distribution in the space ($I_1(\sigma)$, $||\sigma||_{VM}$), the plastic strain vs the temperature increase distribution as well as the plastic strain vs plastic strain-rate distribution are depicted for the elements in the ROI and for the whole experiment. The stress distribution is, as expected, a compromise between Fig. 6.12e and 6.12f. Similarly, to plastic strain vs plastic strain-rate distribution shows that sample will undergo failure since the plastic strain reaches values higher than 0.3. In addition, the plastic strain-rates reach several hundreds of s^{-1} during the experiment. At last, the plastic strain versus the temperature increase distribution is plotted as well. The relevant information that can be extracted is that the sample in these test conditions will have an increase of temperature of 40 °C at

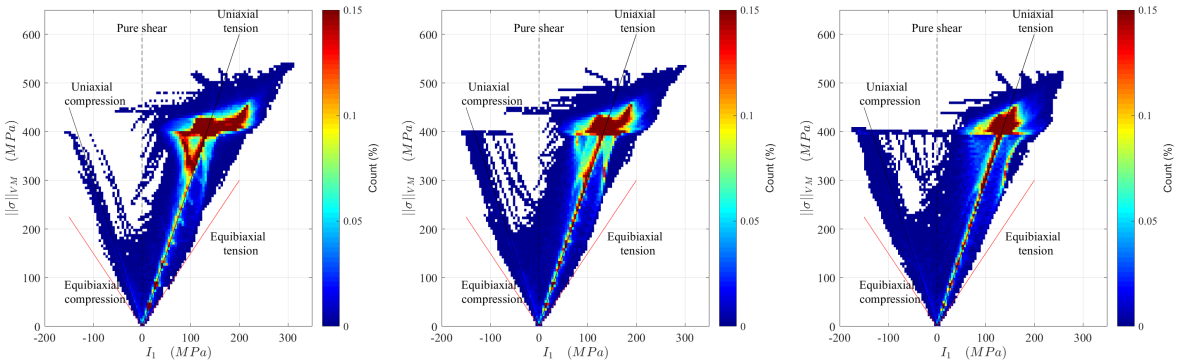

(a) R = 2 mm, D = 4 mm, (b) R = 2 mm, D = 7 mm, (c) R = 2 mm, D = 10 mm,

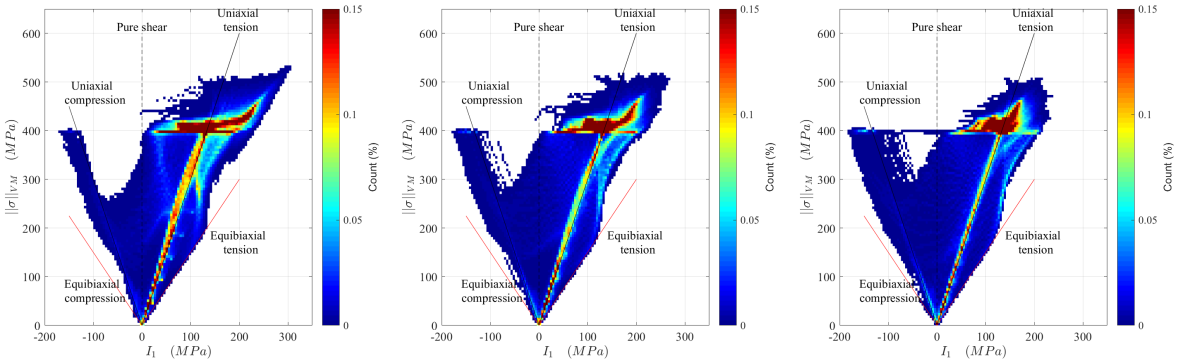

(d) R = 3.5 mm, D = 4 mm, (e) R = 3.5 mm, D = 7 mm, (f) R = 3.5 mm, D = 10 mm,

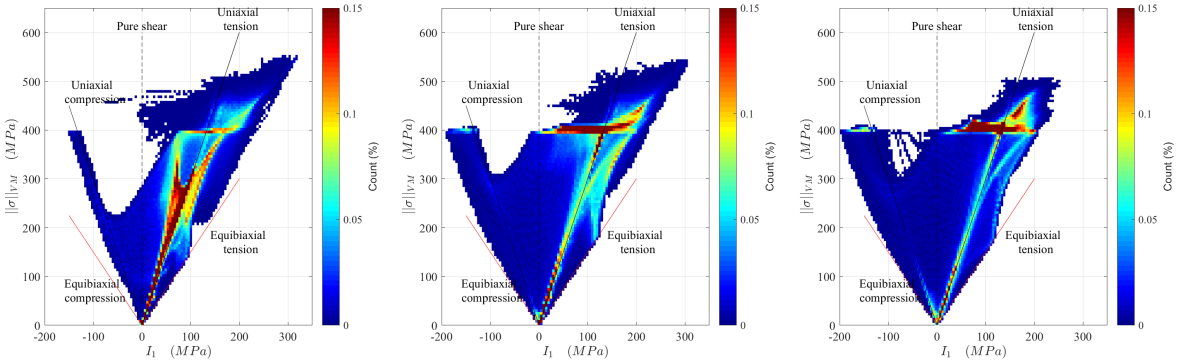

(g) R = 5 mm, D = 4 mm, (h) R = 5 mm, D = 7 mm, (i) R = 5 mm, D = 10 mm,

Figure 6.12: In-plane stress distributions obtained for the different geometries considered. The colour corresponds to a 2D histogram plot. The count per bin is normalized by the number of element in the ROI multiplied by the number of time steps. The stress states that were never experienced by the sample remain white.

most. The collinearity between the plastic strain and the temperature indicates that, in this experiment, the temperature increase is only induced by plastic dissipation and that the experiment is adiabatic. This will be further discussed in Chapter 8 and in particular the issues raised by this collinearity. Moreover, this moderate increase of temperature —that could only be increased by a massive increase in global strain-rate or by using an external heat source —will have an impact on the flow stress. This impact is expected

to remain very low, about 3 % according to Johnson-Cook parameters, which, as we will see in Chapter 8, is below the stress estimation uncertainty. However, these variations potentially allow to characterize the dissipative behaviour of the material, this will be discussed later on.

To go one step further, 5 different areas of the sample are studied (see Fig. 6.13f). Each region corresponds to a marker and a colour which are superimposed to the distribution figures. The stress distribution figure shows that, while the elements in the bands are under nearly uniaxial stress states with some shear, the elements located in the upper and lower part of the central hole are under compression. In addition, the plastic strain vs plastic strain-rate distribution highlights that the elements undergoing plasticity are mainly in the bands and their plastic strain-rate depends on their closeness to the notches or hole.

One notable shortcoming of this kind of experiment can already be pointed out. Fig. 6.13b clearly shows that part of the strain, strain-rate space will not be mapped. Indeed, with the designed experiment, a high plastic strain is never reached at a small plastic strain rate. Nevertheless, the chosen geometry creates important spectra of strain and strain-rates. Moreover, despite the stresses within the sample mainly being uniaxial tension, some shear and compression states are reached.

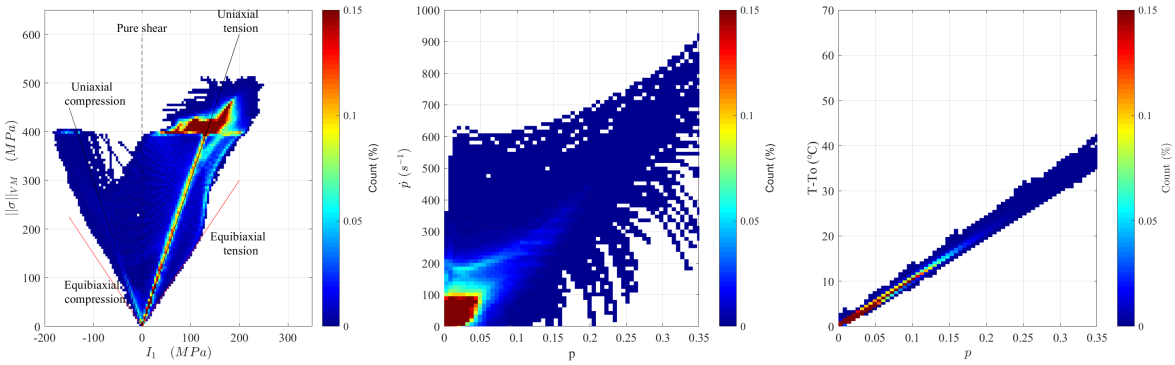

(a) In-plane stress distribution in $(I_1(\sigma), ||\sigma||_{VM})$,

(b) Plastic strain vs plastic strain-rate distribution,

(c) Plastic strain vs temperature distribution,

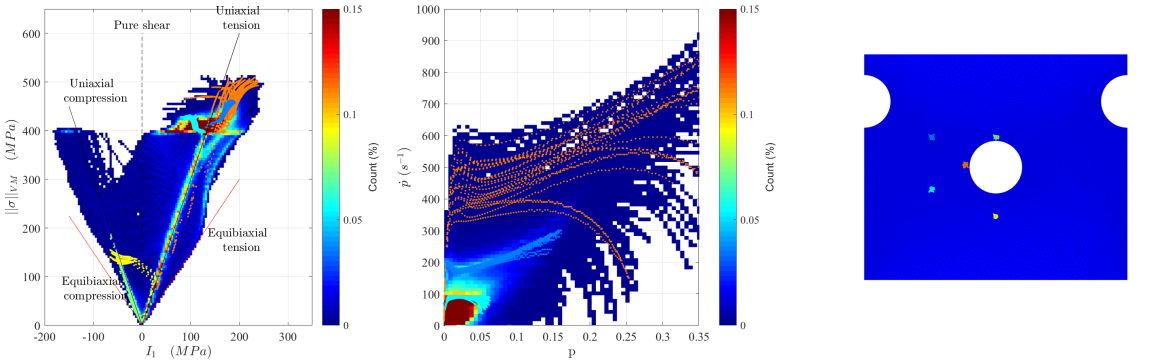

(d) In-plane stress distribution in $(I_1(\sigma), ||\sigma||_{VM})$ with different loading paths superimposed,

(e) Plastic strain vs plastic strain-rate distribution with different loading paths superimposed,

(f) Sample geometry zoomed on the ROI, the markers represent different elements observed,

Figure 6.13: In-plane stress distribution, plastic strain vs plastic strain-rate distribution and plastic strain vs temperature increase distribution. The different markers represent the loading path of different elements considered which are represented on the FE simulation mesh.

6.4 Virtual image deformation

The Virtual Image Deformation (VID) process consists in making a numerical twin of an experiment. The use of such a numerical twin allows to have access to a realistic estimation of the data that will be measured during the real experiment. Furthermore, it allows to qualify an experiment in terms of measurability of the fields of interest, and their uncertainties. It can also validate an identification procedure and its robustness with respect to realistic experimental conditions. In order for this procedure to be relevant, VID must take into account, as much as possible and as accurately as possible, experimental errors and uncertainties such as:

- The spatial resolution of the imaging system and the DIC sampling, which affects the ability to capture strain gradients,

- The temporal resolution of the imaging system, which affects the temporal derivatives (speed, acceleration),
- In our particular case, when using the Cordin, the bias induced by the camera's distortions which lead to low but still non-negligible displacement uncertainties (see Chapter 3)
- Sensor noise, which affects the optical flow conservation in DIC and thus displacement uncertainties as well as time derivatives.

Obviously such procedure is never perfect, for instance, it is difficult to take into account strong speckle transformation or even degradation in highly deformed regions during large strains [Witz *et al.*, 2017a], light variation, out-of-plane motions... For these reasons, the use of VID is becoming more and more systematic in the validation of an experimental procedure and of inverse identification procedure [Rossi *et al.*, 2015, Badaloni *et al.*, 2015, Rossi *et al.*, 2016, Jones *et al.*, 2018, Bouda *et al.*, 2019, Seghir and Pierron, 2018, Fletcher and Pierron, 2018, Pierron and Fletcher, 2019].

In particular, in their work, both Bouda [Bouda *et al.*, 2019] and Jones [Jones *et al.*, 2018] used the results from their FE simulation to virtually create and deform synthetic images. Then, using these images and the VFM, they identified model parameters and compared them to the reference parameters. Bouda also introduced experimental-like bias (*e.g.* camera noise, fill factor) and investigated the impact of the camera's spatio-temporal resolution on the parameters identified.

In this section a similar work is proposed. Using the chosen sample geometry from the previous section, the FE simulation results are used to deform virtual images. These images are then used to extract kinematic fields using the methodology presented in Chapter 3, which are then compared to the FE simulations. Hence, the methodology developed to create virtual deformed images is first presented. Then the kinematic fields extracted from these images are presented and compared to the reference ones.

6.4.1 Methodology

In order to be able to perform DIC on the synthetic images, a texture needs to be applied. However, the synthetic pattern used in Chapters 3 and 5 cannot be used for this experiment. Indeed, in the considered experiment the sample is approximately three time smaller than the PMMA sample considered in Chapter 5. Since the beam size of the laser-engraving machine is 200 µm, the speckle pattern cannot be scaled down. Hence, for this study a classical black and white paints speckle pattern is considered. The undistorted reference image is thus created using a high resolution camera to record a speckle pattern made with black and white paints. This reference image is then binned down to the

Cordin image size. Then, using the mesh from the FE simulations, this image is cropped resulting in the image in Figure 6.14a. Note that not the entire mesh was considered, but only the camera FOV during real experiment (depicted by the red square in 6.9a). The field of view (3 cm x 4 cm, see Table 6.6) matches the aspect ratio of the camera for a pixel size of 12 µm (*i.e.* a magnification of 0.45).

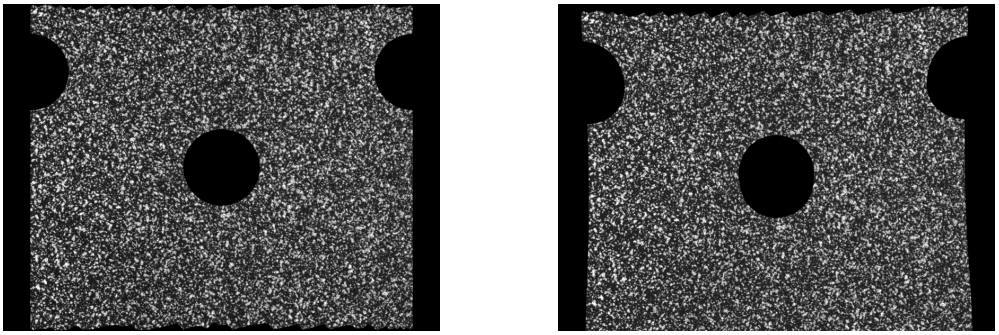

(a) Reference image created synthetically, (b) Deformed and distorted image,

Figure 6.14: Example of the reference image and a deformed and distorted image created synthetically.

Once, the reference image created, using the cropped mesh and the displacement fields from the simulations, the image is deformed (see Fig. 6.14b for an example). This is done by performing a loop on the elements of the deformed mesh. For each element, the pixels contained in it are known. Using shape functions and inverse mapping, their position in the undeformed picture is obtained. Their associated grey values can then be retrieved by performing a spatial bi-cubic spline interpolation of the grey value of the reference image. This process is summarized in Figure 6.15.

Figure 6.15: Schematic of the deformation procedure of a synthetic image for one triangular element. The black squares depict the pixels positions in the deformed configuration, while the grey squares depict the pixels positions in the reference one. The red crosses denote the pixels from the deformed configuration projected by an inverse mapping in the reference one. The deformed image for the element is obtained by interpolating the grey levels from the grey squares onto the crosses.

Furthermore, in order to be as representative of a real experiment as possible, measurement bias introduced by the distortion variability from one shot to another has to be taken into account. For simplicity purpose, two sets of distortion parameters obtained

experimentally are used. The first one (obtained for a specific calibration shot) is used to deform the images and the second one (which is from the statistical distortion model associated to the first set of parameters) is used to perform DIC. As a result, this allows to introduce the right order of magnitude of uncertainty in displacement measurement inherent to the method presented in Chapter 3. Using the composition relationship between the effective displacement u_{simu} and the first distortion field u_d, the imposed displacement u_{virtual} used to deform the images is computed as follows:

$$u_{\text{virtual}}(\underline{X}) = u_{\text{simu}}(\underline{X}) + u_d(\underline{X} + u_{\text{simu}}(\underline{X})). \tag{6.3}$$

Finally, the DIC procedure proposed in this thesis is then applied to the virtual deformed images created. To enable an easy comparison, the same mesh as from the FE simulation is used. With a pixel size of 12 µm resulting from the FOV choice, the mesh size is approximately 21 pixels in the most refined zones.

DIC Software	Ufreckles [Réthoré, 2018]
Image size	2472 x 3296 pixels
Field of view	3 cm x 4 cm
Cordin pixel size	5.5 µm
Image scale	1 pixel = 12 µm (Magnification of 0.45)
Mesh size	$\approx$ 21 pixels
Data Processing	U: Tikhonov regularization over 4 elements

Table 6.6: Virtual DIC parameters.

Finally, a realistic noise is added to the deformed and distorted synthetic images. The estimation of grey level noise, meaning apparent grey level variation of one material points from one image to another over time, has been estimated as follows:

- Images of a static reference shot of the sample (see Chapter 3) are deformed back to the undistorted configuration using identified distortion parameters. At that stage, each pixel sees the same material point over time.

- The grey level standard deviation over time of every pixel is computed and its normalized value (by the pixel's grey level) plotted as a function of the mean grey level value of the considered pixel. The plot is presented in Figure 6.16. This database can be fit with a polynomial P to get the trend of the apparent noise of the camera over its dynamic. The polynomial used is depicted in the figure by the black line.

- This result is used to add random noise to images proportional to pixel grey levels following this equation:

$$\text{noise}(F, p) = F(p) \cdot P(F(p)) \cdot \text{randn}(p), \tag{6.4}$$

where noise(F, p) is the noise that will be added to the pixel p of image F, $P(F(p))$ is the noise value fit by the polynomial for the grey value $F(p)$ and randn is a normally distributed random numbers matrix of the size of F.

At the first order, the polynomial fit shows that the apparent noise converges toward 5 % in the whites, reaches 10 % at about 12 bits (4000) then ramps up to 30 % in the blacks. Notice that, in practice, data presented in Figure 6.16 is not strictly speaking a noise. Indeed, pixel time variations are in our case not only due to CCD dark noise but to the offset and gain mismatch from one sensor to another, the focus mismatch, as well as the uncertainty on distortion estimation which does not allow for perfectly stabilizing images (± 0.1 pixel see Chapter 3). This is why we name it apparent noise. In addition, it explains why values are very high compared to mono-sensor ultra-high speed camera (*e.g.* in the order of 1 % of 16 bits for the Shimadzu HPV-X). Nevertheless, apparent noise will affects the optical flow conservation in a similar way to real noise and will have a strong impact on time derivatives.

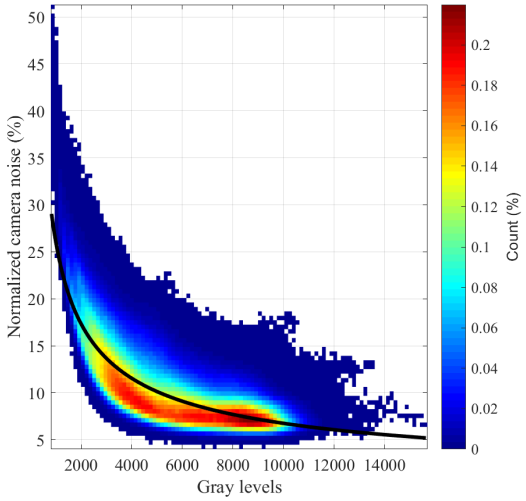

Figure 6.16: Normalized apparent camera noise (in %) versus the mean grey level. The colour denotes the counts (in %), while the black line denotes the polynomials used to model the camera noise.

As a summary, at this stage we are able to produce, from FE simulation, images that mimic the response of our imaging system. Applying the DIC procedure presented in Chapter 3 allows for capturing realistic displacement fields.

6.4.2 Analysis of the influence of the filtering of the displacement fields

In practice, these fields are pointwise convolved with a temporal Savitzky-Golay filtering kernel of order 2 to obtain smooth temporal derivatives. The influence of the windows size

is investigated in this section. To this effect, the smoothed axial and transverse velocities are averaged over a horizontal band of 4 elements near the bottom boundary. Theses averaged values are then compared to their simulation counterparts for each time step in a least-square sense. Hence, two indicators (one in the axial direction and the other one in the transverse direction) are obtained for each window size investigated. Figure 6.17 shows the evolution of both indicators with the Savitzky-Golay windows size. The indicator in the axial direction highlights the existence of a minimum for a windows size of 23. The one for the transverse direction shows no such behaviour, this is to be expected since the transverse fields hold less information than the axial one in the virtual test performed. As a result, the windows size of the filter is set to 23 in what follows.

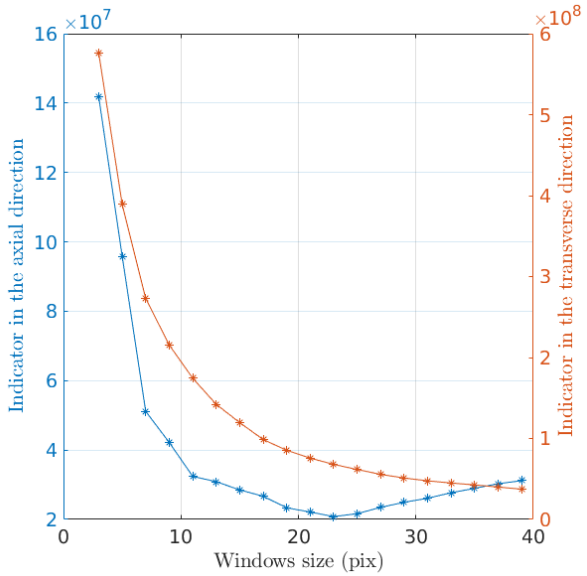

Figure 6.17: Influence of the windows size of a Savitzky-Golay filter.

6.4.3 Results and comparison to the simulation results

Once the DIC performed on the deformed images, the kinematic fields (displacement, strain and strain-rates) are available. Since the mesh used for DIC is the same as the one from the simulation, these fields can be directly compared without any interpolations. In Figure 6.18, the displacement field in the axial direction (Fig. 6.18a) and the error committed (Fig. 6.18b) are depicted at the 80^{th} time step. In addition, this figure depicts the random error (*i.e.* its standard deviation) on the axial displacement field versus the maximum displacement obtained at each time steps (Fig. 6.18c). While the random error increases with the imposed displacement, it remains below 0.26 pixels, which is in good accordance with the values found in the metrological analysis (see Chapter 3). Furthermore, Figure 6.18b shows that the displacement fields can be retrieved with a systematic error of about 1 pixel, even when the displacement reaches about 60 pixels (that is to say

2 % of displacement error locally). It also highlights the fact that the error is heterogeneous, especially in localization bands. These heterogeneous errors on the displacement fields lead to errors in the strain fields. The axial strain field obtained at the last time step is depicted in Fig 6.18d, and the strain errors induced by the displacement errors are depicted in Fig 6.18f. These errors are simply computed from analytical derivation of FE DIC shape functions applied to the displacement errors. As expected, the errors in strain fields are mainly localized in the bands appearing between the notches and the central hole: *i.e.* where there are significant gradients in displacement fields. These strain errors can reach up to 3 % near the notches and the hole, where the strain fields can reach 50 % in the simulations (so 6 % of strain error locally). Nevertheless, aside these regions, the errors remain in line with the values obtained in the metrological analysis of this work (see Chapter 3). Similarly to what is done for the displacements, Fig. 6.18f depicts the random error of the axial strain versus the maximal value of the axial strain. This figure shows that the uncertainty, despite being higher than the one obtained in the metrological analysis of the Cordin, remains below 6 mm/m. In addition, let us note that values this high will never be reached experimentally since fracture will occur before (around 30 %). Hence, the values given in this paragraph are upper bounds of the errors that will actually be reached during the real experiment. As a result, it can be concluded that in a real experiment, the uncertainties will globally be in line with those found in Chapter 3, but reasonably higher in localization bands. This emphasis the fact that, rigid body motion tests are not enough to get a real insight of uncertainties during complex experiments.

Similarly to what is done in Section 6.3, the Von-Mises norm of the total strain vs the Von-Mises norm of the total strain-rate distribution can be investigated for both the simulation and the DIC. To this effect, Figure 6.19 depicts these distributions obtained respectively for the FE simulations or with DIC. This figure highlights the fact that the DIC will not be able to capture both high strain and high strain-rates states. However, it is able to accurately capture the strain and strain-rates in the range of respectively [0 – 0.3] (until rupture) and [0 s^{-1} – 500 s^{-1}], which is the range of strain and strain-rates that most of the sample is submitted to.

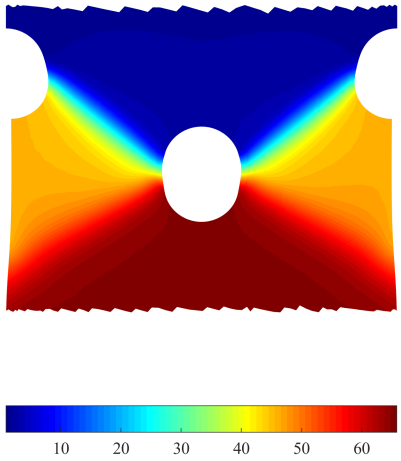

(a) U_y (pix) from DIC at the last time step,

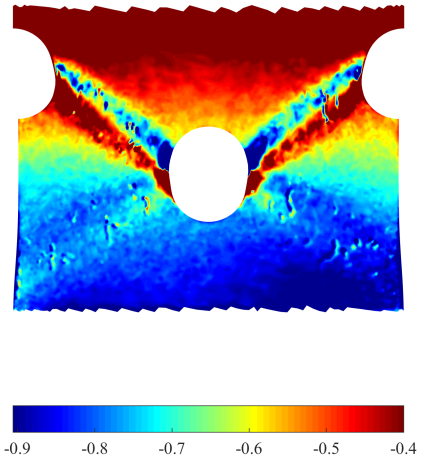

(b) U_y error (pix) at the last time step,

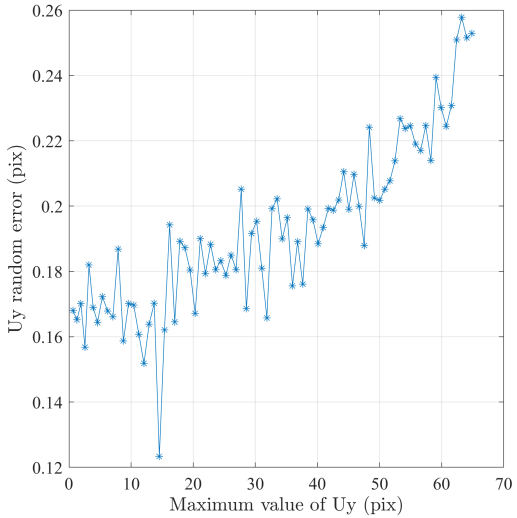

(c) U_y uncertainty (pix) in function its maximum value,

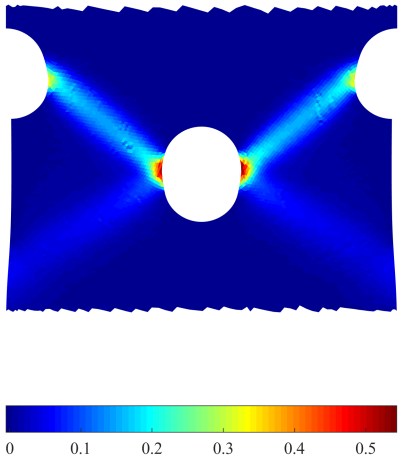

(d) Axial strain (m/m) from DIC at the last time step,

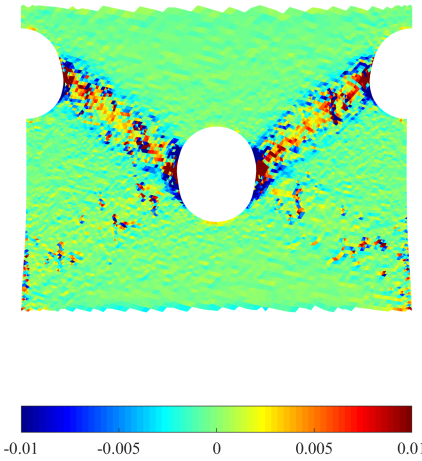

(e) Axial strain errors (m/m) at the last time step,

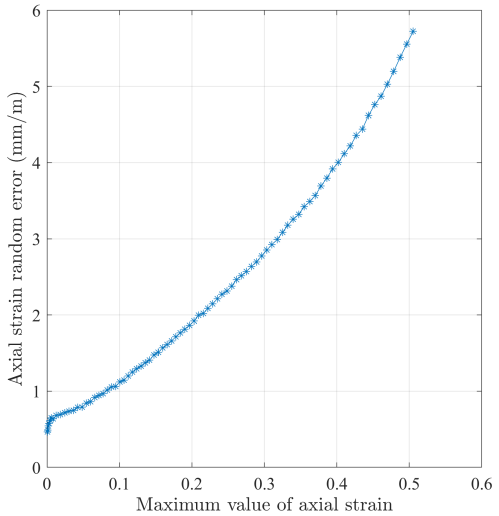

(f) Axial strain uncertainty (m/m) in function of its maximum value,

Figure 6.18: Comparison between the DIC results and the FE simulation results. The displacement and strain errors in the axial direction are plotted as well as their measurement uncertainties.

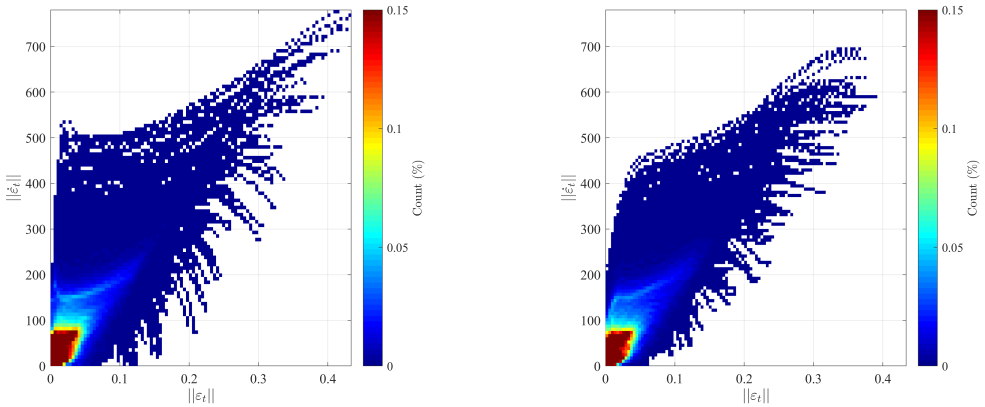

(a) Plastic strain vs plastic strain-rates distribution using FE simulations,

(b) Plastic strain vs plastic strain-rates distribution using DIC,

Figure 6.19: Comparison of the plastic strain vs plastic strain-rates distribution obtained through the FE simulations or DIC. The colour corresponds to a 2D histogram plot. The count per bin is normalized by the number of element in the ROI multiplied by the number of time steps. The strain and strain-rates states that were never experienced by the sample remain white.

6.5 Conclusion

In this chapter, the material that will be characterized was presented as well as the classical constitutive equations used to model this material. Finite Element simulations were then performed in order to investigate different specimen geometries. Once a geometry leading to wide spectra of strain and strain-rates as well as heterogeneous stress states in the sample chosen, synthetic images were virtually deformed. Using DIC, the kinematic fields retrieved from these images are then compared to the simulation ones. The main conclusions are as follows:

- Contrary to the modified Krupkowsky model, the Johnson-Cook model is not able to account for the whole material's strain-rate dependency.
- The introduction of notches and a central hole in the sample geometry induces heterogeneous stress states within it. Furthermore, in one experiment, large spectra of strain and strain-rates can be obtained using this geometry.
- Nevertheless, the use of a single actuator, even with a complex geometry, does not allow to characterize a wide spectrum of stress triaxiality. Indeed, the material will remain mainly under uniaxial tension and the density of points that will be submitted to different stress states is relatively low.
- Using virtual image deformation, the ability to retrieve these rich and complex kinematic fields is proven. Indeed, with the use of DIC, the displacement uncertainties remains below 0.3 pixels. Moreover, the maximal error on the strain fields is about 3 % in the hole and notches vicinity when the strain reaches 50 %.

Chapter 7

Dynamic tensile test for the characterization of an XES steel

Content

7.1 Experimental application

In Part I the methodologies enabling the extraction of kinematic fields from images recorded using both a multi-sensor rotating mirror camera and an infrared camera were presented. Furthermore, in the previous Chapter, simulations were performed in order to choose a sample geometry respecting given criteria. It was also ensured that the fields could be retrieved using our cameras through the use of virtually deformed synthetic images. These methodologies will now be applied to an experimental test. It consists in a dynamic tensile test performed on a metal sheet using the geometry defined in Chapter 6. The experimental setup and the test results will be presented in this Chapter.

7.1.1 Specimen material and geometry

For this experiment, the material used is an XES steel presented in Chapter 6, known to be strain-rate dependent up to $1 \times 10^2\,\mathrm{s}^{-1}$. The geometry used was also presented in the previous Chapter. Its main features are two notches and a central hole which will act as strain concentrators and thus induce heterogeneous and multi-axial fields. The samples for the experiment were cut from a 0.8 mm-thick metal sheet. The samples were cut in the rolling direction.

In order to be able to perform DIC a speckle pattern needs to be applied on the sample. For these experiments a speckle pattern is spray painted on one face using black and white paints. Furthermore, for the infrared camera, black paint is also applied on the other side of the sample to ensure its high emissivity.

7.1.2 Experimental and imaging setup

The tests conducted in this work are dynamic tensile tests. They are conducted using a hydraulic tensile test machine (MTS-819, 20 kN). On this machine, the upper grip is mounted on a modified Hopkinson bar, similarly to the device from [LeBlanc and Lassila, 1996]. This bar is made in steel (42CD4 rectified) and is instrumented with strain gauges in order to act like a load cell (see Figure 7.1b). In addition, the lower grip is mounted on a sliding bar. The sliding bar is in an enclosing case linked to the actuator. The sliding bar, through the control of the "free fall" length, allows the actuator to reach the imposed displacement speed before loading the sample. The maximum actuator velocity allowing an accurate load measurement, *i.e.* $5\,\mathrm{m\,s^{-1}}$, is used for this experiment.

For this work, the actuators only allowed for an imposed displacement speed of about $4\,\mathrm{m\,s^{-1}}$ to $5\,\mathrm{m\,s^{-1}}$. The "free fall" distance was accordingly set to 25 mm.

The experiment is recorded using the Cordin-580 equipped with a 90 mm Tamron objective, at 68k fps with a CCD gain of 15 % and a CDS gain of -3 dB. This low frame rate has been chosen in accordance with the limited frame rate of the IR camera: it is a compromise that allows for recording both IR and visible images with a decent temporal sampling. At such speed, the film duration is about 1.18 ms. In order to provide enough light, two Pro-10 (2400 J each at 10-stops) Xenon flashes from Profoto are used. They are set in normal mode, at 10 f-stops. In that configuration, the illumination typically lasts 2.4 ms with a stable and optimal plateau of 1.1 ms. The flashes and the camera are triggered separately in this experiment. The flashes are triggered using an infrared light-gate system (SPX1189 series Honeywell). It is placed in such manner that it is obscured by the enclosing case. The optical gate will then send a 5 V TTL signal when the enclosing case is at a given distance to the contact with the sliding bar. This distance has to take into account the speed of the actuator as well as the raising time of the flashes (150 µs). It has been heuristically determined and set at 3.7 mm from the contact point. The Cordin-580 is triggered using the load cell. When the load reaches a chosen threshold (in this study 6231.5 N, $\approx$ half of the plastic yield), a trigger is sent to the camera. Upon receiving the trigger, the camera will record the following images, as well as the ones taken up to 100 µs before (this is named post-triggering). These parameters were determined heuristically through preliminary tests. The working distance between this camera and the sample is about 31 cm.

This dynamic tensile test is also recorded using the Telops M3K, equipped with a Janos Technology (ASIOS SERIES 50 mm F/2.3 MWIR) objective. Similarly to the previous experiment conducted, the IR camera recorded the other face of the sample. In order to reduce the influence of the experimental setup, a black aluminium foil is placed between the camera and the sample, with a small opening allowing the sample to be observed (Fig. 7.1a). The influence of the experimental setup, in particular the one of the flashes,

will be further discussed in Section 7.2.2. The experiment is recorded at 35k fps, with an integration time of 6.24 µs and a windows size of 44 × 64 pixels^2. This acquisition speed is chosen in order to have approximately 1 infrared image every 2 visible-light images. In order to optimize the spatial sampling of the IR camera, the symmetry of the sample will be taken into account and only one half of the sample will be observed (see Fig. 7.1c to have an example of the different POV during an experiment). During the preliminary tests, it was observed that the crack always initiated in the same side of the sample, hence the IR camera observed this side. Some explanations of this phenomenon are proposed in Section 7.4. In addition, the Telops started to record the events before the experiment as the quantity of data recorded is not an issue. To enable the synchronization with the kinematic data, a trigger is sent to this camera at the same time as for the Cordin-580, creating a time stamp in the data recorded by the IR camera.

Additionally, in order to guarantee that the sample is in the focal plane of the Cordin-580, the same optical device that is described in Chapter 5 was used. This setup using a laser was used prior to each test in order to verify the sample's alignment after it was fixed.

7.1.3 Experimental reproducibility

In Figure 7.2 the loads recorded during the three dynamic tensile tests are plotted. These three curves match quite well, demonstrating the high reproducibility of the experiments. During the experiment the load ramps up until about 8000 N, where it remains constant for the rest of the experiment. The load spike observed around t = 980 µs is explained by the fact that the load cell is a 2.5 m long instrumented bar inspired from Hopkinson bar strategy to delay wave reflections. Indeed, by considering a wave speed of about 5 km s^{-1} in the bar, the initial wave — induced by the shock between the enclosing case and the sliding bar — will have bounced back and reached the sample in about 1 ms. This is therefore an artefact and the analysis of the experiment must be stopped before.

Due to the high reproducibility of the experiment, in what follows only one of the test will be investigated further. However, more elements of comparison can be found in Appendixes D and E.

7.1.4 Calibration of the different cameras

In order to be able to use the DIC methodology proposed in this work, a reference image is needed. Since for this application a speckle pattern is painted on each sample, a reference image is needed for each sample. To this effect, samples images were recorded using a high definition camera (50M pix, Prosilica GT from Stemmer) combined with the same objective lens as the one used with the Cordin-580, prior to the test. Furthermore, 12 calibration shots were taken with the Cordin camera when the first sample was mounted,

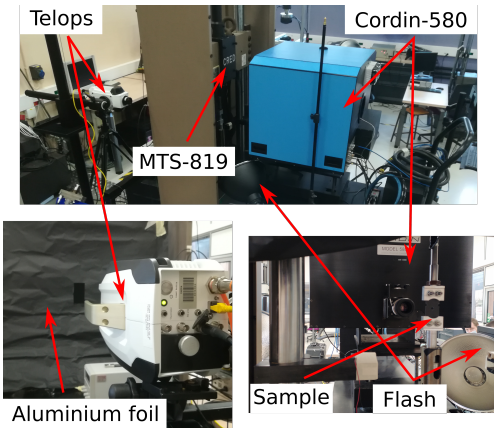

(a) Experimental setup for a dynamic tensile test,

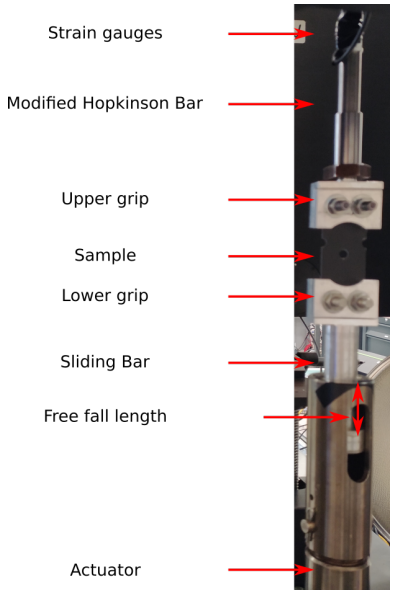

(b) Photo of the dynamic tensile machine setup,

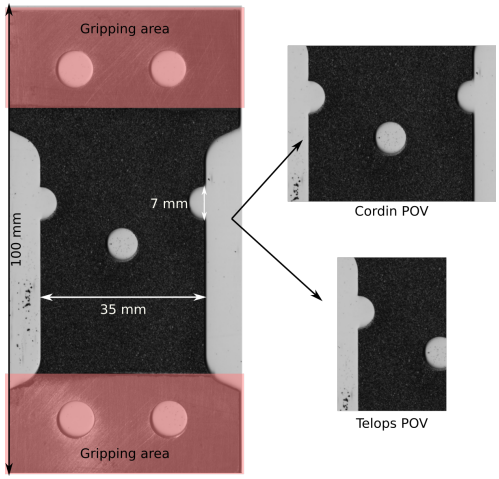

(c) Sample geometry and the associated POV for the two cameras,

Figure 7.1: Experimental setup for a dynamic tensile test, recorded using a visible-light camera and an infrared one.

prior to the test. These calibration shots are used in order to create a representative model of the distortions induced by the camera in experimental conditions (lens, working distance, magnification, frame rate). Then, in order to correct the eventual rigid body motion between one experiment and the other, a single calibration shot is performed before each of the other experiment.

In addition, a calibration campaign was also performed for the Telops using a blackbody. The blackbody was placed at the sample's place (see Fig. 7.4a). The calibration was conducted using the same IT, fps and windows size than for the experiment and for temperatures from 20 °C to 150 °C. Besides, before each experiment a fullframe image was taken with the infrared camera. This fullframe image is used in order to perform lagrangian thermography, especially to find the rigid body transformation that allows to

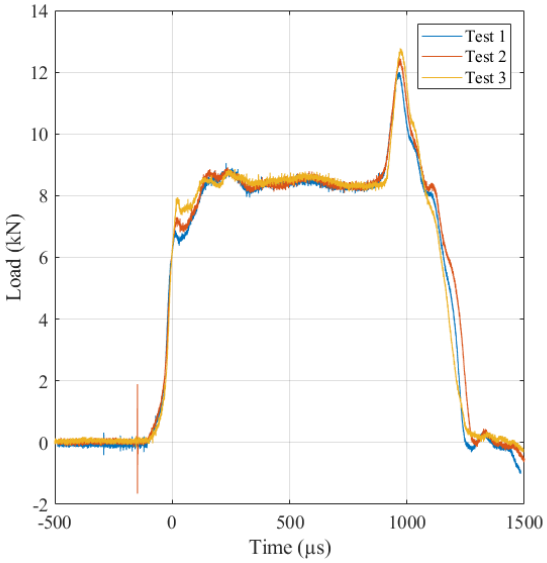

Figure 7.2: Loads evolution obtained for three different tests.

pass from the Cordin-580 reference configuration to the Telops one.

7.1.5 Mesh and DIC parameters

Contrary to the preliminary test presented in Chapter 5, we use here a continuous mesh, that is to say without twin nodes along the crack paths. This choice will be motivated later when the stress identification approach (DDI) will be presented. However, since it is known that strain localization appears in 2 principal bands, the mesh is refined along these bands and in the vicinity of the notches and the hole as well. The element size, is 32 pixels on average, but finer along the crack (about 26 pix). A Tikhonov regularization of the DIC problem of 4 elements is used to filter-out spatial noise. Finally, the pixel size, obtained by recording an image of a ruler prior to the test, is 14.5 µm. This leads to a field of view of 35.8 mm x 47.8 mm (see Tab. 7.1).

The same procedure as in Chapter 5 is used to compute time derivatives, it is recalled quickly here. The displacements are firstly pointwise convolved with a rolling temporal Savitzky-Golay filtering window of second order with a window size equal to 23 frames. The size of the kernel is chosen based on the analysis conducted in Section 6.4. Then strain-rates are obtained from strains using a simple 1^{st} order finite difference scheme. Such data filtering marginally affects strain, but significantly decreases the amount of noise on strain-rates.

Camera	Cordin-580
Image resolution	2472 pixels × 3296 pixels
Dynamic Range, Detector	12 bits
Dynamic Range, Image	16 bits
Acquisition Rate	68k fps
Lens	Tamron SP 90 mm Di Macro
Aperture	f/2.8
Field of view	35.8 mm × 47.8 mm
Image scale	1 pixel = 14.49 µm
Stand-off distance	31 cm
Patterning Technique	Black and White paint

Table 7.1: DIC hardware parameters.

DIC Software	Ufreckles [Réthoré, 2018]
Shape Function	linear FE triangle elements
Matching Criterion	element-wise ZNSSD
Image Filtering	sensor flattening (vignetting)
Data Processing	U : Tikhonov regularization over 4 elements
Data Post-Processing	$\dot{\varepsilon}$: temporal Savitzky–Golay filter of order 2 applied onto U (win = 23 fr)
Experimental systematic and random error 3	U: 0.5 pix ± 0.2 pix ε: 100 µε ± 2.0 mε $\dot{\varepsilon}$: 0.5 s^{-1} ± 50 s^{-1}

Table 7.2: DIC analysis parameters.

Camera	Telops M3K
Image resolution	44 pixels × 64 pixels
Acquisition Rate	35k fps
Lens	ASIOS SERIES 50 mm
Aperture	f/2.3
Field of view	20.8 mm × 30.3 mm
Image scale	1 pixel = 472.97 µm
Stand-off distance	≈ 1 m

Table 7.3: IR hardware parameters.

7.2 Technical issues and solutions

Due to the complexity of the experiments conducted, some technical issues have to be tackled. This is the aim of this section.

7.2.1 Load measurement

The load is captured by the load cell during the experiment. However, it has to be adjusted time-wise: indeed, the load is measured by strain gauges while the information is needed on the mesh boundary, in particular for the DDI (see Chap. 8). Hence, due to the distance between the mesh boundary and the strain gauges, a delay has to be taken into account. Figure 7.3 reminds the experimental apparatus, with in particular the distances of interest: the distance between the strain gage and the grip (120 mm using the constructor's data) as well as the distance between the grip and the ROI (≈35 mm measured manually). Then, using the modified bar's properties ($E = 205\,\text{GPa}$ and $\rho = 7850\,\text{kg/m}^3$), the delay is computed as follows: $\tau = \frac{\sqrt{\rho}}{\sqrt{E}}$, which yields a delay of 30 µs. This is in the order of magnitude of two Cordin interframes for this experiment. Furthermore, note that even an error of 1 cm in the distance between the grip and the ROI leads to an error of 2 µs for τ, which is negligible regarding our time resolutions.

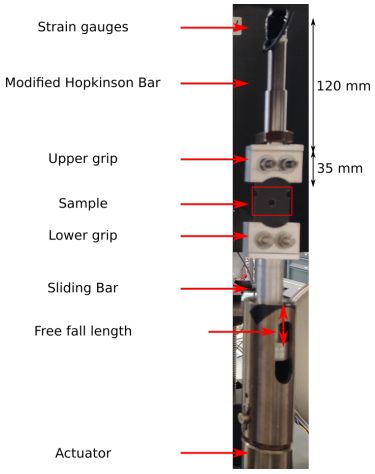

Figure 7.3: Photo of the dynamic tensile machine setup, with a focus on the distances between the strain gage, the grip and the ROI.

7.2.2 Influence of the flashes

The requirements for ultra-high speed DIC imaging and infrared measurements around room temperature are antagonists. Indeed, a large amount of light is required for the UHS imaging, which usually cover a large spectrum of wavelength, while the IR measurements require no disturbances within its wavelength bandwidth of recording.

First, tests were conducted in order to investigate the flashes influence on the temperature measurement. To this effect, a blackbody was placed at the sample's location and was set at 25 °C (see Figure 7.4a) while the other experimental conditions remained the same (IT, fps, windows size and the aluminium foil was also used) in order to be as representative as possible. Then, the flashes were activated manually and the thermal scene was recorded. This procedure has been performed twice, the results are represented in Fig. 7.4b. The temperatures are obtained using the embedded calibration from the camera. This figure highlights the reproducibility of the phenomenon. The shape of the temperature raise can be explained by the light intensity delivered by the flashes. Indeed, in Fig. 7.4c the normalized light intensity delivered by the flashes in the experimental conditions is captured through the use of a high speed luxmeter (Sekonic L-858). We can retrieve the fact that there is a spike of the light intensity after approximately 1.1 ms and that the flashes duration is about 2.4 ms. Furthermore, since the IR camera is recording the centre of a blackbody at room temperature, the increase of temperature is non-physical. Hence, it leads to the conclusion that the flashes, due to their light being emitted partially in the infrared range recorded by the IR camera (see Fig. 7.4d), induce an apparent raise of temperature captured by the camera. During the recording of the experiment, denoted by the black dashed lines, this apparent raise of temperature reaches about 1 °C ± 0.25 °C. Additionally, this apparent raise of temperature is spatially homogeneous as it is showed in Fig 7.4e. Since this phenomenon is very reproducible, a correction can be applied to the experimental temperatures in order to retrieve the effective sample's temperature. The systematic and random errors obtained after the correction are 0 °C ± 0.230 °C. These values are obtained when applying the correction to the data from Fig. 7.4b. This remains in the order of magnitude of the uncertainties evaluated in "perfect" conditions without any flash (see Chapter 4).

7.2.3 Pre-stressed sample

The experimental setup is hyper-static, and as a result, the sample when fixed is already pre-constrained. Indeed, the griping device relies on two metallic rods on each side of the sample to maintain it. However, due to its use, the rods are deformed. As a result the sample may be already slightly deformed when placed, before the experiment. This can be evidenced by looking at the displacement fields obtained for the shot taken when the sample is in place and static. A rigid-body motion identified on the first image is subtracted to these fields in order to account for a possible small rotation between the reference image (taken with another camera in a different set-up) and the Cordin images. Figure 7.5 depicts the averaged over time of the axial and transverse displacement fields with the rigid-body motion subtracted as well as the averaged over time Von-Mises norm of the total strain. This figure shows that the sample is under vertical tension on the

(a) Blackbody placed at the sample's location to investigate the flashes influence,

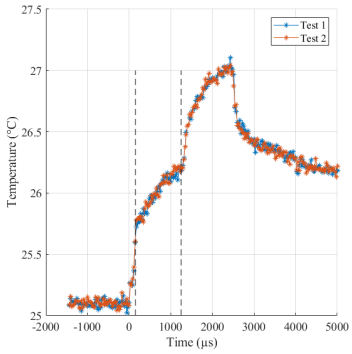

(b) Temperature raise induced by the flashes,

(c) Light intensity delivered by the flashes in experimental conditions,

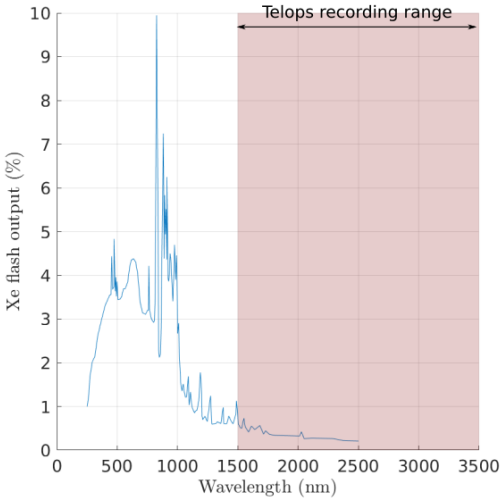

(d) Emission spectrum of Xenon flashes [Products, nd],

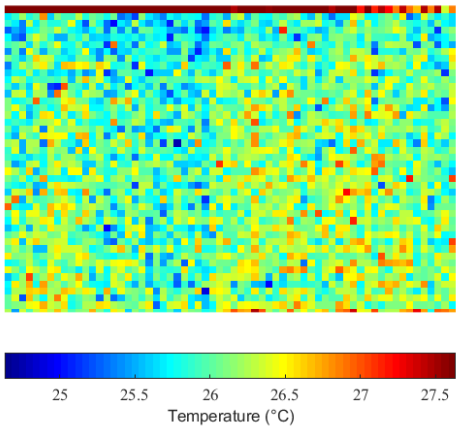

(e) Example of the temperature fields obtained at the end of experiment recording (°C),

Figure 7.4: Experimental setup for the investigation of the flashes influence on the thermal scene.

right-hand side, as well as horizontal tension on the bottom. Nevertheless, the amplitude of these tensions are about $\pm$ 1 pixels. Furthermore, the averaged over time Von-Mises norm of the total strain clearly shows that the sample is slightly deformed (less than $3\,\mathrm{mm\,m^{-1}}$), which is in the same order of magnitude as the strain measurement uncertainty. Hence, the sample may be pre-constrained by the experimental setup, nevertheless this phenomenon is not significant.

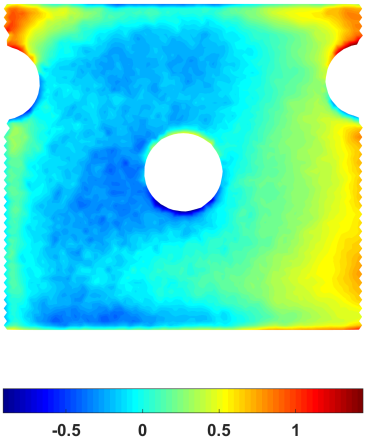

(a) U_y averaged over time (pix) (1 pixel = 14.5 µm),

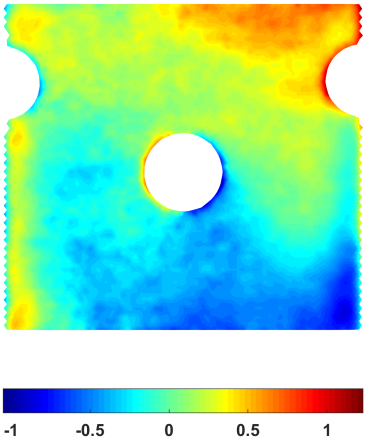

(b) U_y averaged over time(pix) (1 pixel = 14.5 µm),

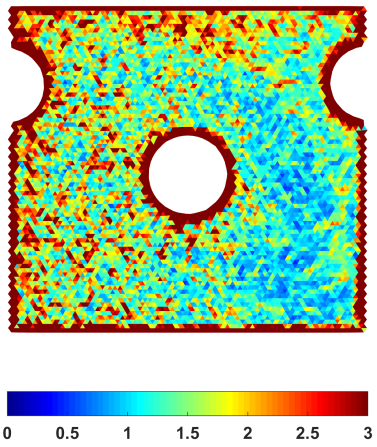

(c) $||\varepsilon_t||_{VM}$ averaged over time ($\mathrm{mm\,m^{-1}}$),

Figure 7.5: Averaged over time displacement fields and Von-Mises norm of the total strain when the sample is placed in the gripping device and static.

7.3 Evolution of macroscopic quantities during the test

The deconvolution between the distortions and the effective displacements is made using the camera model built using the 12 calibration shots. In addition, using the reference shot taken prior to the test, the changes of the extrinsic parameters can be taken into account. Finally, the correct pairing between the sensors and the mirror faces is identified using optical considerations (Chapter 3). This allows the displacement, strain and strain-rate fields to be extracted. In a similar manner, using the calibration campaign of the IR camera performed in the same experimental conditions as the experiments, the temperatures can be extracted from the raw data capture by the Telops. Furthermore, using the displacement fields obtained with the Cordin-580 and following the Lagrangian Thermography procedure (see Chapter 4), the temperatures are obtained in the reference configuration. In addition, the apparent raise of temperature induced by the flashes is deducted in order to retrieve the sample's temperature. Finally, similarly to what is done to the kinematic fields, the lagrangian temperatures are pointwise convolved with a temporal Savitzky-Golay filtering kernel of order 2 with a window size equal to 23 frames (after interpolation on the Cordin timeline).

Figure 7.6 depicts the evolution of different quantities of interest during the experiment.

First, let us look at the temporal evolution of the averaged axial displacement and velocity obtained in the whole sample (depicted by the simple lines) and of the nodes located at the bottom of the mesh (depicted by the lines with markers), *i.e.* close to the sample head where the loading is applied. Figure 7.6a shows displacement in blue and velocity in red. The three vertical dashed lines are the time steps for which associated fields will be discussed later-on. Note that the zero in the timeline correspond to the time when the Cordin-580 is triggered by the load cell, hence the negative times for the first images. The loading of the specimen induces immediately on the loaded edge a displacement ramp, reaching about 2.8 mm before the initiation of the crack. The averaged axial displacement in the whole sample has a similar behaviour, with a lower slope, and reaches about 2 mm. The velocities in the whole sample or for the nodes at the bottom of the mesh have the same trend. The velocities evidence two stages: from the beginning to approximately t = 370 µs the velocities increase in the tension direction, then from t = 370 µs to t = 620 µs they decrease. The second stage can be explained by considering the possibility that the contact between the sliding bar and its enclosing case is not permanent. Indeed, if the sample goes faster than the actuator, then when there is no more contact its speed will naturally decrease until there is contact again. One way to verify this hypothesis would have been to record accurately the speed of the actuator (using DIC with a high speed camera for instance). However, this was not done for these experiments. During the

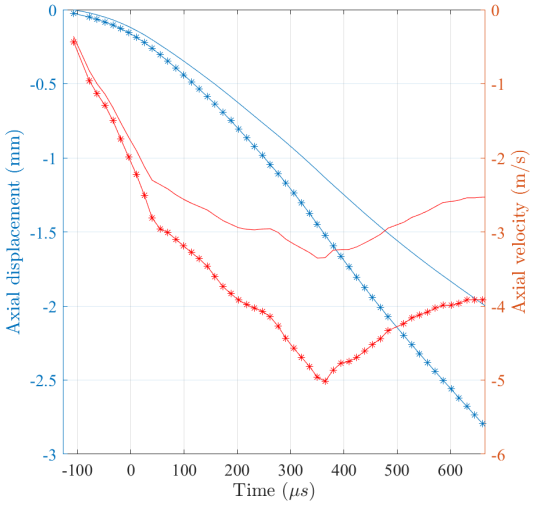

(a) Average U_y and V_y,

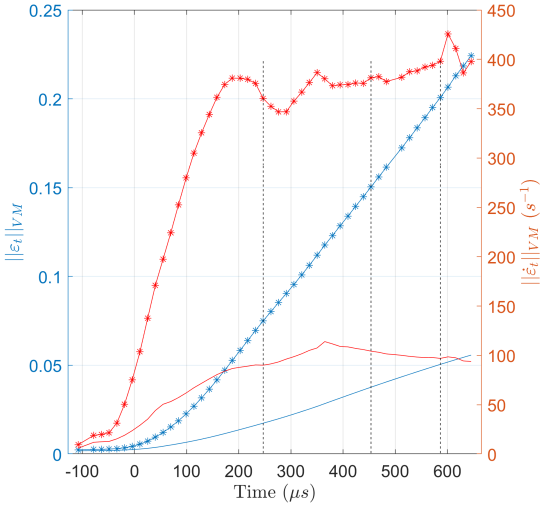

(b) Average total strain and strain-rates,

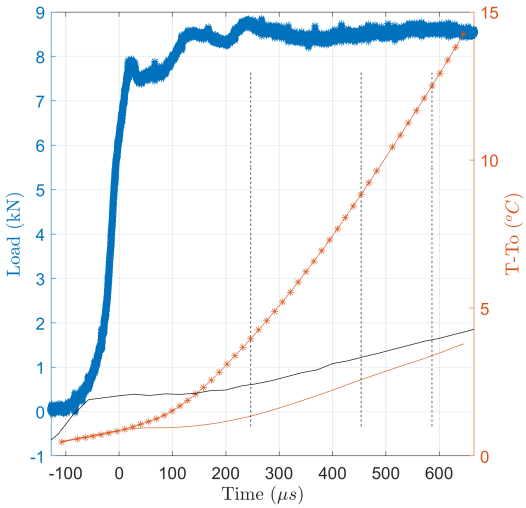

(c) Average temperature raise as well as the load, the black line shows the average temperature increase over the sample before correction,

Figure 7.6: Evolution of different quantities of interest during an heterogeneous test. A simple line denotes the evolution of the considered quantity averaged in the whole sample, while a line with marker denotes its evolution in a particular zone (either the bottom of the mesh or the localization band).

experiment, the maximum speed reached on the loaded edge is about $4.8\,\mathrm{m\,s^{-1}}$ in about 476 µs which represent an acceleration on the order of $1 \times 10^4\,\mathrm{m\,s^{-2}}$; while the maximum speed experienced by the whole sample is about $3.5\,\mathrm{m\,s^{-1}}$.

Figure 7.6b plots the evolution of the Von-Mises norm of both the total strain (in blue) and total strain-rates (in red) either in the whole sample (depicted by the simple lines) or in a localization band during the experiment (depicted by the lines with markers). This figure shows that during the first 100 µs of the experiment, the sample is mainly

in an elastic regime ($||\varepsilon_t||_{VM} \leq 0.005$). Furthermore, the total strain in the localization band goes past 0.01 after about 150 µs, after which it increases following a ramp until about 0.22 before the crack initiation. On the other hand, the global total strain reaches only 0.05 before the crack initiation, which shows that deformation mainly occurs in the localization bands. In the considered band, two stages of the normalized total strain-rate can be observed. First, it ramps up to $375\,\mathrm{s}^{-1}$ in about 300 µs. Then, the normalized total strain-rate reaches a plateau and oscillates between $350\,\mathrm{s}^{-1}$ and $400\,\mathrm{s}^{-1}$. Similarly to the total strain, the total strain-rate in the whole sample is lower than the one observed in the bands as it reaches only $100\,\mathrm{s}^{-1}$.

At last, Figure 7.6c shows the evolution of the load during the experiment (in blue). It also depicts the average temperature increase (in red) either in the whole sample (depicted by the simple line) or in the considered band (depicted by the line with markers). In addition, the black line depicts the average temperature raise in the whole sample prior to the flashes correction. Two stages can be evidenced for the load. During the first 150 µs the load ramps up until 8 kN. Then it reaches a plateau and oscillates around 8.5 kN. Considering an initial surface S_0 equal to $1.68 \times 10^{-5}\,\mathrm{m}^2$ (subtracting the holes), the engineering stress can be estimated at 500 MPa. This value is in line with the ones obtained in [Haugou *et al.*, 2006]. The comparison between the uncorrected temperature (black line) and the corrected temperature (red line) shows that most of the apparent temperature increase induced by the flashed is removed. Nevertheless, a slight increase of about 0.3 °C remains while the sample should slightly cool down by the same amount due to thermoelasticity. This reveals that the calibration procedure, while allowing to remove most of the bias, is not reproducible enough to entirely get ride of small variations, and thus does not allow to capture thermoelasticity. However, note that thermoelasticity would have been almost impossible to capture anyway when considering the measurement uncertainty obtained in Chapter 4 (as a reminder: 300 mK), which is already in the same order of magnitude than thermoelastic effects. Nevertheless, after 100 µs, the temperature increases follow the same trend as the normalized total strains, as expected. The sample temperature increase reaches 15 °C on average in the localization band before crack initiation with a rate in the order of 25 K/ms, which is in line with the values obtained with FE simulations. On the other hand, the temperature increase in the whole sample reaches about 4 °C before crack initiation.

7.4 Displacement and temperature fields

Figure 7.7 shows sample images, displacement fields in both directions, the axial strain fields as well as the temperatures for the three time steps introduced previously. The displacement fields obtained are consistent with a tensile test. The first two images underline the fact that the tensile test is not perfectly vertical. Indeed, the axial displacements are

higher in the left-hand side of the sample. This phenomenon was observed for all the experiment performed as well as on the preliminary tests. In turn, crack initiation systematically begins on the left-hand side of the sample before the right-hand side. No clear explanations have been found for this observation. It may partly due to the fact that the sample is already pre-constrained, and a non-planar contact between the sliding bar and its enclosing case may also come into play. However, no clear evidences have been found to confirm these hypotheses. The strain fields at 246.79 µs further confirm the fact that the load imposed on the sample is not symmetrical since strains are higher in the left band. The sample geometry induces localization bands as predicted by the FE simulations with little strain everywhere else. Regarding the temperatures, Figures 7.7m, 7.7n and 7.7o show that the sample's temperature raises mainly in the strain localization bands. During the first 782 µs (*i.e.* before the crack initiation), the temperature increase reaches up to 35 °C near the hole and the notches, with an average of about 15 °C in the bands. These values are in line with the temperature elevation obtained for the simulation predictions (see Fig 6.13c).

In the same spirit as in the previous Chapter, the normalized total strain vs total strain-rate distribution is presented in Figure 7.8. Let us first note that before cracking, only a few points reach a total strain higher than 0.25. Nevertheless, the results are quite in agreement with the prediction made in Section 6.4. The strain and strain-rates in the range of respectively [0 – 0.25] and [0 s^{-1} – 500 s^{-1}] predicted by the numerical twin are recovered quite nicely. In addition, Figure 7.9 depicts the temperature vs Von-Mises norm of the total strain distribution for elements in the bands up to crack initiation. This figure highlights the fact that the temperature is mainly proportional to the Von-Mises norm of the total strain as predicted by simulations.

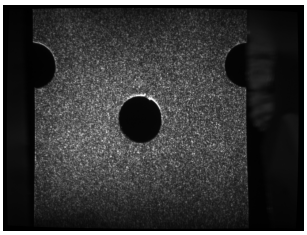

(a) Undistorted image,

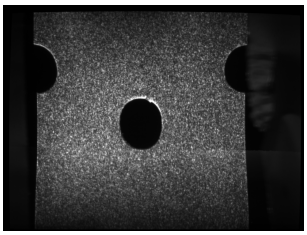

(b) Undistorted image,

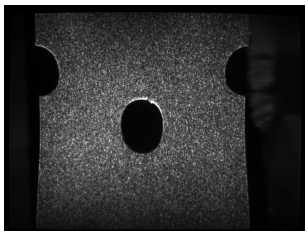

(c) Undistorted image,

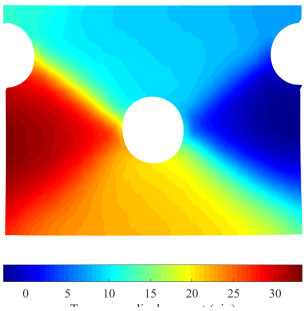

(d) U_x (pix), t = 246.79 µs,

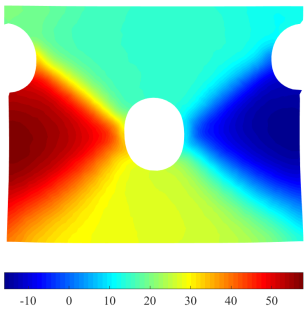

(e) U_x (pix), t = 468.22 µs,

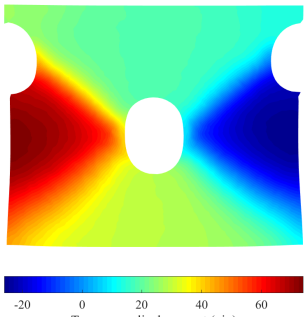

(f) U_x (pix), t = 615.83 µs,

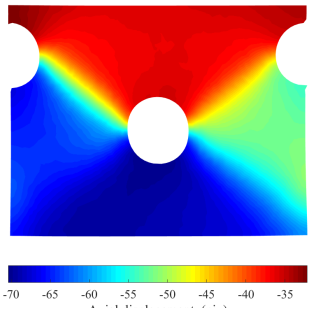

(g) U_y (pix), t = 246.79 µs,

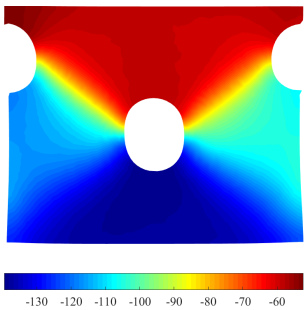

(h) U_y (pix), t = 468.22 µs,

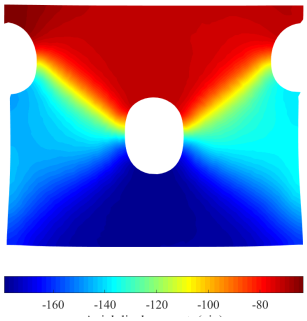

(i) U_y (pix), t = 615.83 µs,

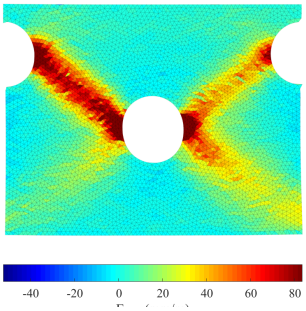

(j) Axial strain (m/m), t = 246.79 µs,

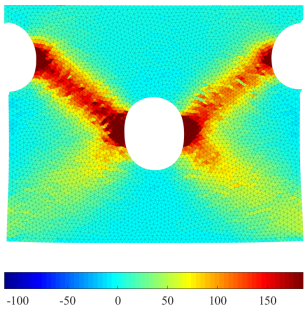

(k) Axial strain (m/m), t = 468.22 µs,

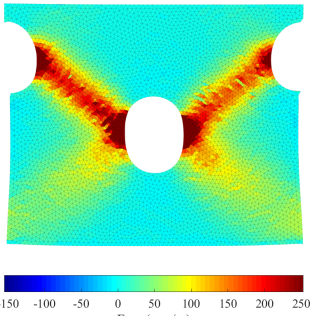

(l) Axial strain (m/m), t = 615.83 µs,

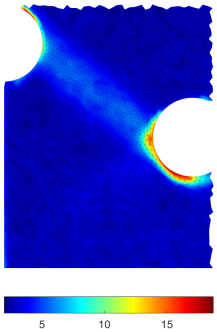

(m) T-To (°C) at t =246.79 µs,

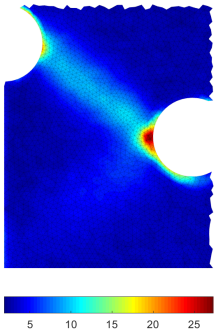

(n) T-To (°C) at t =468.22 µs,

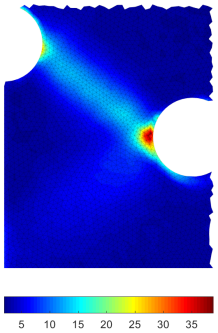

(o) T-To (°C) at t =615.83 µs,

Figure 7.7: Undistorted images, displacement fields, strain fields as well as temperature fieldsobtained during a dynamic tensile test, for different time steps.

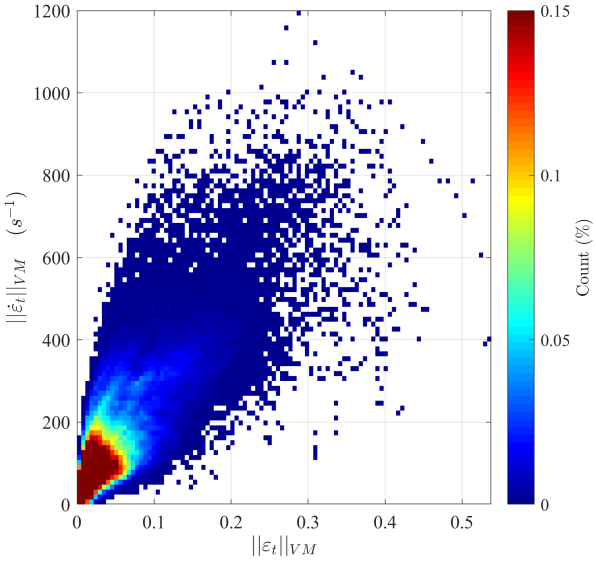

Figure 7.8: Von-Mises norm of the strain vs Von-Mises norm of the strain-rates distribution obtained during the experiment, prior to crack initiation. The colour corresponds to a 2D histogram plot. The count per bin is normalized by the number of element in the ROI multiplied by the number of time steps. The stress states that were never experienced by the sample remain white.

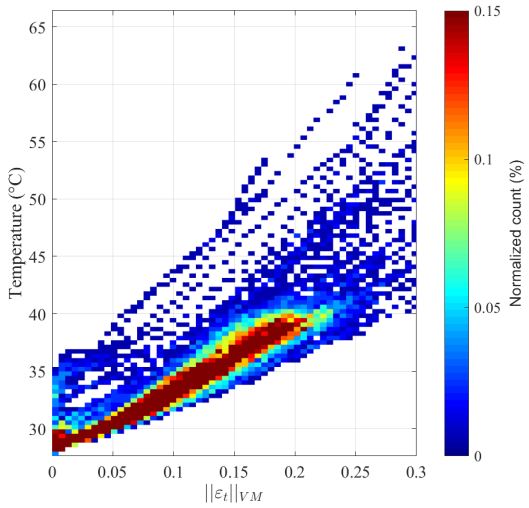

Figure 7.9: Temperature vs Von-Mises norm of the total strain distribution for elements in the main localization band before crack initiation.

7.5 Conclusion

In this chapter, a dynamic tensile test on an XES steel using a sample geometry defined in the previous chapter is presented. This experiment was instrumented with an ultra-high speed rotating mirror camera: a Cordin-580, as well as with a high speed infrared camera: a Telops M3k. The main conclusions are as follows:

- Quantitative kinematic and thermal full-field data from a dynamic tensile test performed on an XES steel have been acquired at a rate of 68,000 fps and 35,000 fps respectively.
- The apparent raise of temperature induced by the flashes is reproducible within less than 1 °C variation. Thus, a correction is applied to the thermal data obtained experimentally. The temperature measurement is found to be relevant once strains are beyond the elastic limit.
- During the experiment, the loading velocity reaches up to $4.8\,\mathrm{m\,s^{-1}}$, but is not constant. In addition, in the strain localization bands, the total strain reaches 0.22 and the strain-rates $500\,\mathrm{s^{-1}}$. Moreover, despite being unable to capture the material's thermoelastic response, the raise of temperature induced by plastic work is captured. In the band, the temperature increases up to 35 °C close to the concentrators, but only 15 °C on average in the bands.

Part III

Stress fields estimation using a non-parametric method

Chapter 8

Data-Driven Identification strategy and numerical validation

Content

8.1 Introduction

Recently, several strategies have been adopted to estimate stress fields in non-standard experiments without using a constitutive law. These strategies all rely on full-field measurements and a regularization of the ill-posed mechanical problem, but differ on the chosen regularization.

In 2014, Pierron and his co-authors [Pierron *et al.*, 2014] devised a strategy to estimate stress fields in dynamics without using a constitutive law. To this effect, the strategy relies on the use of a statically determined configuration (an inertial impact test for instance). Under the assumptions of plane stress, and a homogeneous and constant density of the material, the authors are able to estimate the mean stress field profile in the specimen. For this strategy, the acceleration acquired experimentally acts as a load cell, which requires recording kinematic fields at ultra-high speed ($\geq$ 1M fps). This work opened the way to the so called Image-Based Inertial Impact Tests (IBII). Among other, it allowed the authors to identify the elastic modulus and tensile strength of tungsten carbide cermets [Fletcher and Pierron, 2018] and a composite [Fletcher *et al.*, 2019] at high strain-rate. More recently, the strategy was also applied in a new experimental configuration: the Image-Based Inertial Release (IBIR) test [Fletcher and Pierron, 2020]. This new configuration allowed the identification of both quasi-static and high strain-rate elastic modulus and Poisson's ratio for PMMA. In these examples, the boundary conditions (purely inertial test and uniaxial) regularize the problem. If the test is not uniaxial any more, the authors proposed an elegant solution in the case of elastic orthotropic material [Pierron and Fletcher, 2019].

Even more recently, in 2021, Liu *et al.* [Liu, 2021] and Cameron and his co-author [Cameron and Tasan, 2021] devised another strategy to estimate stress fields without postulating a constitutive equation. Assuming that the material is isotropic, the methods developed by these authors rely on the alignment of the principal directions of stress with strain or strain-rate. This assumption then allows obtaining a mathematically closed problem, and thus the analytical estimation of stresses. These methods have been tested on numerical example and experimentally in [Liu, 2021]. In [Cameron and Tasan, 2021], the authors discuss the range of validity of such an assumption: mainly in isotropic elasticity, plasticity with associative flow rules and for associative flow rules with an isotropic yield function. Furthermore, this method cannot address the problem of elasto-plastic transition where stresses are not aligned with strains anymore and not aligned with plastic strain-rates yet.

The recent developments in computer science and in particular in the data science field, has lead to the emergence of a third kind of strategy relying on data in the past 4 years: the so called Data-Driven approaches. These methods can be used to either solve the direct problem [Kirchdoerfer and Ortiz, 2016] or the inverse mechanical problem [Leygue *et al.*, 2018]. The so called Data-Driven methods were first introduced in the context of computational mechanics by Kirchdoerfer and Ortiz [Kirchdoerfer and Ortiz, 2016, Kirchdoerfer and Ortiz, 2017]. In their work, the authors replaced the constitutive equation by a minimization process and a material database. A solution is found by minimizing a distance (which they defined) between computed mechanical states (strains and stresses) and a set of admissible material states. The authors then extended their methods to dynamics [Kirchdoerfer and Ortiz, 2018]. These methods called Data-Driven Computational Mechanics are used to solve the direct problem: find the response of structure (strains and stresses) using a set of admissible material states, which have to be found experimentally. These works were then derived in order to formulate inverse Data-Driven approaches. Hence, in their work Leygue and his co-authors [Leygue *et al.*, 2018, Leygue *et al.*, 2019] formulated the inverse problem associated to the Data-Driven Computational Mechanics. This new problem aims to estimate stress fields from heterogeneous experiments without having to explicit any constitutive equation. Using synthetic data, the authors demonstrated the ability of their algorithm to estimate admissible stresses in a structure for various loading cases (quasi-static and dynamic problems) as well as different material behaviours (hyperelasticity, elasto-plastiticy). This Data-Driven method was then applied to experimental data by Dalémat *et al.* in [Dalémat *et al.*, 2019]. In this study, perforated hyperelastic membranes are submitted to uniaxial tensile tests. In addition, in a recent paper [Dalémat *et al.*, 2021] extensively discuss the proper way to handle imperfect experimental data. The authors especially discuss the boundary conditions for imperfectly defined edges and the way to tackle the issue of missing data. More recently, the Data-Driven strategy was applied by Langlois and his co-authors to experiments on history dependent materials [Langlois *et al.*, 2022]. The use of this method enabled them

to estimate stress fields for an elasto-platic material that is subjected to the formation of Piobert-Lüders bands. In these strategies, the regularization comes from the assumption that the material response lies on a manifold in a constitutive space which remains to be determined. The underlying hypothesis of this method will be presented later-on in this Chapter. Furthermore, one could imagine combining this method with the IBII method in order to estimate heterogeneous 2D stress fields in dynamics without needing load measurements.

These emergent strategies can potentially help to assess, without making any assumptions, the validity of material constitutive equations outside their validity domain (*e.g.* heterogeneous tests, with multi-axiality, couplings...). In that context, the Data-Driven Identification formulation and resolution strategy for visco-elasto-plastic materials will first be recalled. Then, a numerical test case is built to investigate the ability of such a method to estimate stress fields, and especially its accuracy.

8.2 Data-Driven Identification

8.2.1 Problem formulation and resolution

Data-Driven Identification relies on rich databases of displacement fields (obtained for example with DIC) combined with the imposed forces (usually obtained with a load cell) in order to reconstruct the stress states without using an explicit parametric constitutive relation. In the following, the mechanical problem introduced in [Leygue *et al.*, 2018, Leygue *et al.*, 2019] extended by Eggersmann and his co-authors [Eggersmann *et al.*, 2019] for history dependent materials is used. Furthermore, the modified strategy proposed in [Leygue *et al.*, 2019] is adopted. The formulations and notations that will be recalled and used in this work are the one introduced by Langlois and his co-authors in [Langlois *et al.*, 2022]. The problem is formulated here in small strain, however it has been implemented and used in finite strain in [Dalémat *et al.*, 2019, Platzer *et al.*, 2021].

In the Data-Driven Identification (DDI) strategy used in this work, a 2D structure made of deformable material is considered. This structure is discretized using a Finite Element mesh with N_e elements and N_n nodes. Furthermore, the data obtained experimentally, available at each time step $j \in [1,\, N_t]$ are the following:

- $\mathbf{u}_k^j$: the displacement measured at every node k of the mesh
- $\mathbf{B}_{ek}$: the classical FEM divergence operator, calculated from the geometry and mesh connectivity allowing to compute the strain tensor at every integration point e:

$$\boldsymbol{\varepsilon}_e^j = \sum_{k=1}^{N_n} \mathbf{B}_{ek} \cdot \mathbf{u}_k^j, \tag{8.1}$$

- F^j: the net force of the nodal forces on a boundary ∂F

$$F^j = h \sum_k \mathbf{f}_k^j \quad \forall k \in \partial F, \tag{8.2}$$

with h the thickness of the structure, supposed to be constant and $\mathbf{f}_k^j$ the nodal forces at each node along the boundary ∂F.

The definition of a scalar distance between strain and stress tensors in a constitutive space requires to introduce a norm, built from a symmetric positive definite fourth-order tensor $\mathbb{C}_o$. Following [Kirchdoerfer and Ortiz, 2016, Leygue *et al.*, 2019], the $\|\|\|_{\mathbb{C}_o}$ norm is introduced as follows:

$$\|(A, B)\|_{\mathbb{C}_o}^2 = (A : \mathbb{C}_o : A + B : \mathbb{C}_o^{-1} : B), \tag{8.3}$$

with A and B two second-order tensors.

In addition, following Eggersman *et al.* recommendations [Eggersmann *et al.*, 2019], the history and time-dependent behaviour of the material will be described using strain, stress and their first order time derivatives. To this effect, similarly to what is done in [Langlois *et al.*, 2022], an incremental approach will be used, which means that the stress reconstructed at time step j will depend on the strain at j as well as the strain and stress at $j-1$. As a result, the constitutive space that will be considered in this work is $(\boldsymbol{\varepsilon}^j, \boldsymbol{\varepsilon}^{j-1}, \boldsymbol{\sigma}^j, \boldsymbol{\sigma}^{j-1})$. The reconstruction of stress field is an ill posed problem. Traditionally, the use of constitutive equations allows to bypass this difficulty. In the Data-Driven Identification method, this issue is tackled by introducing a set of N^* unknown states $(\boldsymbol{\varepsilon}^*, \boldsymbol{\varepsilon}^{**}, \boldsymbol{\sigma}^*, \boldsymbol{\sigma}^{**})$, where $\bullet^*$ are related to the current state and $\bullet^{**}$ to the former state. These N^* states are, in practice, centroid or barycentre of mechanical states clusters. These clusters regroup the set of strains and searched stresses $(\boldsymbol{\varepsilon}_e^j, \boldsymbol{\varepsilon}_e^{j-1}, \boldsymbol{\sigma}_e^j, \boldsymbol{\sigma}_e^{j-1})_{e,j\in[2,N_t]}$ that are close in the $\|\|\|_{\mathbb{C}_o}$ norm sense. The set $(\boldsymbol{\varepsilon}^*, \boldsymbol{\varepsilon}^{**}, \boldsymbol{\sigma}^*, \boldsymbol{\sigma}^{**})$ is called material states, it can be interpreted as a sampling of the strain-stress manifold.

Leygue *et al.* [Leygue *et al.*, 2019] proposed to initialize the method with $\bar{\boldsymbol{\sigma}}_e$, obtained from a FE simulation under prescribed loads. Hence, the DDI method consists eventually in finding a self-balanced correction $\mathbf{d}\boldsymbol{\sigma}_e$, *i.e.* whose net force over the boundary is null:

$$\begin{aligned} &\sum_{e=1}^{N_e} w_e \mathbf{B}_{ek}{}^T \cdot \mathbf{d}\boldsymbol{\sigma}_e^j = \mathbf{f}_k^j \quad \forall j, k, \\ &\text{with} \quad \mathbf{f}_k^j = \mathbf{0} \quad \text{in the volume,} \quad \text{and} \quad \sum_{k\in\partial F} \mathbf{f}_k^j = \mathbf{0}, \end{aligned} \tag{8.4}$$

where w_e is the integration weight for element e. This can be rewritten as:

$$\begin{aligned}
&\sum_{e=1}^{N_e} w_e {\mathbf{B}_{ek}}^T \cdot \mathbf{d}\boldsymbol{\sigma}_e^j = \mathbf{0} \quad \forall j, \quad \forall k \quad \text{in the volume,} \\
&\sum_{e=1}^{N_e} w_e \left(\sum_{k \in \partial F} {\mathbf{B}_{ek}}^T \right) \cdot \mathbf{d}\boldsymbol{\sigma}_e^j = \mathbf{0} \quad \forall j.
\end{aligned} \tag{8.5}$$

This set of $\hat{N} = N_n - \text{card}(\partial F) + 1$ equations naturally leads to the definition of the operator ${\hat{\mathbf{B}}_{el}}^T$ that simplifies the previous equilibrium equations into a single one:

$$\sum_{e=1}^{N_e} w_e {\hat{\mathbf{B}}_{ek}}^T \cdot \mathbf{d}\boldsymbol{\sigma}_e^j = \mathbf{0} \quad \forall j, \quad \forall k \in [1, \hat{N}]. \tag{8.6}$$

In practice, this operator is obtained from $({\mathbf{B}_{ek}}^T)$ by performing the linear combination that appears in Eq. 8.5. As a result, the problem is written as a global minimization problem:

$$\begin{aligned}
&\min_{\substack{\mathbf{d}\boldsymbol{\sigma}, \boldsymbol{\varepsilon}^*, \boldsymbol{\varepsilon}^{**}, \\ \boldsymbol{\sigma}^*, \boldsymbol{\sigma}^{**}, \mathcal{S}}} \Psi(\mathbf{d}\boldsymbol{\sigma}, \boldsymbol{\varepsilon}, \boldsymbol{\varepsilon}^*, \boldsymbol{\varepsilon}^{**}, \boldsymbol{\sigma}^*, \boldsymbol{\sigma}^{**}, \mathcal{S}), \\
\text{with} \quad \Psi = &\sum_{j=2}^{N_t} \sum_{e=1}^{N_e} p_e \| \boldsymbol{\varepsilon}_e^j - \mathcal{S}_e^j \boldsymbol{\varepsilon}^*, \bar{\boldsymbol{\sigma}}_e^j + \mathbf{d}\boldsymbol{\sigma}_e^j - \mathcal{S}_e^j \boldsymbol{\sigma}^* \|_{\mathbb{C}_o}^2 \\
&+ p_e \| \boldsymbol{\varepsilon}_e^{j-1} - \mathcal{S}_e^j \boldsymbol{\varepsilon}^{**}, \bar{\boldsymbol{\sigma}}_e^{j-1} + \mathbf{d}\boldsymbol{\sigma}_e^{j-1} - \mathcal{S}_e^j \boldsymbol{\sigma}^{**} \|_{\mathbb{C}_o}^2,
\end{aligned} \tag{8.7}$$

under the constraint that the equilibrium (Eq. 8.6) is respected. This equilibrium is enforced during the resolution using Lagrange multipliers $(\boldsymbol{\lambda}_k^j)_{j,k}$. p_e is the weight of the integration point e for the considered cost function Ψ, $\mathcal{S}^j$ is a selection matrix that maps the material states to the mechanical states at time j, $\mathcal{S}_e^j$ is its line e.

The choice of p_e has been investigated in the work of Langlois [Langlois *et al.*, 2022]. The authors showed that the choice of this parameter does not change significantly the convergence and the solution with respect to a given norm. Furthermore, choosing p_e equal to 1 led to a better temporal stability of the stress correction element wise (*i.e.* a smaller standard deviation in time of the stress correction for each element). This choice implies that each element will have the same weight in the functional to minimize, regardless of its localization and its size. This leads to the following problem:

$$\begin{aligned}
\delta \Bigg(&\sum_{j=2}^{N_t} \sum_{e=1}^{N_e} \| \boldsymbol{\varepsilon}_e^j - \mathcal{S}_e^j \boldsymbol{\varepsilon}^*, \bar{\boldsymbol{\sigma}}_e^j + \mathbf{d}\boldsymbol{\sigma}_e^j - \mathcal{S}_e^j \boldsymbol{\sigma}^* \|_{\mathbb{C}_o}^2 \\
&+ \sum_{j=2}^{N_t} \sum_{e=1}^{N_e} \| \boldsymbol{\varepsilon}_e^{j-1} - \mathcal{S}_e^j \boldsymbol{\varepsilon}^{**}, \bar{\boldsymbol{\sigma}}_e^{j-1} + \mathbf{d}\boldsymbol{\sigma}_e^{j-1} - \mathcal{S}_e^j \boldsymbol{\sigma}^{**} \|_{\mathbb{C}_o}^2 \\
&+ \sum_{j=1}^{N_t} \sum_{e=1}^{N_e} \sum_{k=1}^{\hat{N}} (w_e {\hat{\mathbf{B}}_{ek}}^T \cdot \mathbf{d}\boldsymbol{\sigma}_e^j) \cdot \boldsymbol{\lambda}_k^j \Bigg) = 0.
\end{aligned} \tag{8.8}$$

Taking all possible variations yields the following set of equations:

$$\delta\boldsymbol{\varepsilon}_i^* \Rightarrow \quad \sum_{j=2}^{N_t} \sum_{e/\mathcal{S}_e^j\boldsymbol{\varepsilon}^*=\boldsymbol{\varepsilon}_i^*} \mathbb{C}_o : (\boldsymbol{\varepsilon}_e^j - S_e^j\boldsymbol{\varepsilon}^*) = \mathbf{0} \quad \forall i, \tag{8.9}$$

$$\delta\boldsymbol{\varepsilon}_i^{**} \Rightarrow \quad \sum_{j=2}^{N_t} \sum_{e/\mathcal{S}_e^j\boldsymbol{\varepsilon}^{**}=\boldsymbol{\varepsilon}_i^{**}} \mathbb{C}_o : (\boldsymbol{\varepsilon}_e^{j-1} - S_e^j\boldsymbol{\varepsilon}^{**}) = \mathbf{0} \quad \forall i, \tag{8.10}$$

$$\delta\boldsymbol{\sigma}_i^* \Rightarrow \quad \sum_{j=2}^{N_t} \sum_{e/\mathcal{S}_e^j\boldsymbol{\sigma}^*=\boldsymbol{\sigma}_i^*} \mathbb{C}_o^{-1} : (\bar{\boldsymbol{\sigma}}_e^j + \mathbf{d}\boldsymbol{\sigma}_e^j - S_e^j\boldsymbol{\sigma}^*) = \mathbf{0} \quad \forall i, \tag{8.11}$$

$$\delta\boldsymbol{\sigma}_i^{**} \Rightarrow \quad \sum_{j=2}^{N_t} \sum_{e/\mathcal{S}_e^j\boldsymbol{\sigma}^{**}=\boldsymbol{\sigma}_i^{**}} \mathbb{C}_o^{-1} : (\bar{\boldsymbol{\sigma}}_e^{j-1} + \mathbf{d}\boldsymbol{\sigma}_e^{j-1} - \mathcal{S}_e^j\boldsymbol{\sigma}^{**}) = \mathbf{0} \quad \forall i, \tag{8.12}$$

$$\delta\boldsymbol{\lambda}_k^j \Rightarrow \quad \sum_{e=1}^{Ne} w_e \hat{\mathbf{B}}_{ek}{}^T \cdot \mathbf{d}\boldsymbol{\sigma}_e^j = \mathbf{0} \quad \forall j, \quad \forall k, \tag{8.13}$$

$$\text{and} \quad \delta\mathbf{d}\boldsymbol{\sigma}_e^j \Rightarrow \begin{cases} 2\left(\mathbb{C}_o^{-1} : (\bar{\boldsymbol{\sigma}}_e^j + \mathbf{d}\boldsymbol{\sigma}_e^j - S_e^{j+1}\boldsymbol{\sigma}^{**})\right) + \sum_k w_e \hat{\mathbf{B}}_{ek} \cdot \boldsymbol{\lambda}_k^j = \mathbf{0}, & \text{if } j = 1 \\ \Big[2\left(\mathbb{C}_o^{-1} : \left((\bar{\boldsymbol{\sigma}}_e^j + \mathbf{d}\boldsymbol{\sigma}_e^j - \mathcal{S}_e^j\boldsymbol{\sigma}^*) + (\bar{\boldsymbol{\sigma}}_e^j + \mathbf{d}\boldsymbol{\sigma}_e^j - \mathcal{S}_e^{j+1}\boldsymbol{\sigma}^{**})\right)\right) \\ \quad + \sum_k w_e \hat{\mathbf{B}}_{ek} \cdot \boldsymbol{\lambda}_k^j\Big] = \mathbf{0}, \quad \forall j \in [2, N_t - 1], \\ 2\left(\mathbb{C}_o^{-1} : (\bar{\boldsymbol{\sigma}}_e^j + \mathbf{d}\boldsymbol{\sigma}_e^j - S_e^j\boldsymbol{\sigma}^*)\right) + \sum_k w_e \hat{\mathbf{B}}_{ek} \cdot \boldsymbol{\lambda}_k^j = \mathbf{0}, & \text{if } j = N_t. \end{cases} \tag{8.14}$$

Let us note, for clarification purposes, that the summation $\sum_{j=2}^{N_t} \sum_{e/\mathcal{S}_e^j\boldsymbol{\varepsilon}^*=\boldsymbol{\varepsilon}_i^*}$ simply denotes the summation over the spatio-temporal elements that are regrouped in the i$^{\text{th}}$ material cluster. The resolution of such a problem is extensively discussed in [Leygue *et al.*, 2019, Stainier *et al.*, 2019]. It relies on a staggered algorithm that computes alternatively the correction of the stress field and the lagrangian multipliers for a given material state set and selection matrices (this will be called the mechanical problem), and then the update of the material states set and selection matrices for given stresses and lagrangian multipliers (this will be called the material problem). These two steps will be further discussed later on.

8.2.1.1 Data normalization

The computation of the selection matrices for given stresses and lagrangian multipliers relies on clustering algorithm such as k-means – this procedure will be discussed later on. However, since the material and constitutive space considered combine strains and stresses, which differ from several orders of magnitude, a normalization of the data is introduced in this paragraph. The changes induced by this normalization on the equations will be also presented.

To normalize the data we introduce the following quantities:

$$\begin{aligned} \underline{\boldsymbol{\varepsilon}} &= \sqrt{\mathbb{C}_o} : \boldsymbol{\varepsilon}, \\ \underline{\boldsymbol{\sigma}} &= \sqrt{{\mathbb{C}_o}^{-1}} : \boldsymbol{\sigma}, \end{aligned} \tag{8.15}$$

where $\mathbb{C}_o$ is the fourth-order tensor introduced earlier. Using these new quantities, the norm $\|(\underline{A}, \underline{B})\|_r^2$ can be defined as:

$$\|(\underline{A}, \underline{B})\|_r^2 = (\underline{A} : \underline{A} + \underline{B} : \underline{B}), \tag{8.16}$$

with $\underline{A}$ and $\underline{B}$ two normalized second-order tensors. It follows that the new constitutive space considered is $(\underline{\boldsymbol{\varepsilon}}_e^j, \underline{\boldsymbol{\varepsilon}}_e^{j-1}, \underline{\boldsymbol{\sigma}}_e^j, \underline{\boldsymbol{\sigma}}_e^{j-1})_{e,j\in[2,N_t]}$, and the set of material states becomes $(\underline{\boldsymbol{\varepsilon}}^*, \underline{\boldsymbol{\varepsilon}}^{**}, \underline{\boldsymbol{\sigma}}^*, \underline{\boldsymbol{\sigma}}^{**})$. Hence the minimization problem from Eq. 8.7 is rewritten:

$$\begin{aligned} &\min_{\substack{\underline{\mathbf{d}\boldsymbol{\sigma}}, \underline{\boldsymbol{\varepsilon}}^*, \underline{\boldsymbol{\varepsilon}}^{**}, \\ \underline{\boldsymbol{\sigma}}^*, \underline{\boldsymbol{\sigma}}^{**}, \mathcal{S}}} \underline{\Psi}(\underline{\mathbf{d}\boldsymbol{\sigma}}, \underline{\boldsymbol{\varepsilon}}, \underline{\boldsymbol{\varepsilon}}^*, \underline{\boldsymbol{\varepsilon}}^{**}, \underline{\boldsymbol{\sigma}}^*, \underline{\boldsymbol{\sigma}}^{**}, \mathcal{S}), \\ \text{with} \quad \underline{\Psi} = &\sum_{j=2}^{N_t} \sum_{e=1}^{N_e} \|\underline{\boldsymbol{\varepsilon}}_e^j - \mathcal{S}_e^j \underline{\boldsymbol{\varepsilon}}^*, \bar{\boldsymbol{\sigma}}_e^j + \underline{\mathbf{d}\boldsymbol{\sigma}}_e^j - \mathcal{S}_e^j \underline{\boldsymbol{\sigma}}^*\|_r^2 \\ &+ \|\underline{\boldsymbol{\varepsilon}}_e^{j-1} - \mathcal{S}_e^j \underline{\boldsymbol{\varepsilon}}^{**}, \bar{\boldsymbol{\sigma}}_e^{j-1} + \underline{\mathbf{d}\boldsymbol{\sigma}}_e^{j-1} - \mathcal{S}_e^j \underline{\boldsymbol{\sigma}}^{**}\|_r^2, \end{aligned} \tag{8.17}$$

under the constraint that

$$\begin{aligned} &\sum_{e=1}^{N_e} w_e {\underline{\hat{\mathbf{B}}}_{ek}}^T \cdot \underline{\mathbf{d}\boldsymbol{\sigma}}_e^j = \mathbf{0} \quad \forall j, k, \\ &\text{with} \quad {\underline{\hat{\mathbf{B}}}_{ek}}^T = {\hat{\mathbf{B}}_{ek}}^T : \sqrt{\mathbb{C}_o}. \end{aligned} \tag{8.18}$$

Since the new norm verifies $\|(\underline{A}, \underline{B})\|_r^2 = \|(A, B)\|_{\mathbb{C}_o}^2$, the following relation is also verified: $\underline{\Psi}(\underline{\mathbf{d}\boldsymbol{\sigma}}, \underline{\boldsymbol{\varepsilon}}, \underline{\boldsymbol{\varepsilon}}^*, \underline{\boldsymbol{\varepsilon}}^{**}, \underline{\boldsymbol{\sigma}}^*, \underline{\boldsymbol{\sigma}}^{**}, \mathcal{S}) = \Psi(\mathbf{d}\boldsymbol{\sigma}, \boldsymbol{\varepsilon}, \boldsymbol{\varepsilon}^*, \boldsymbol{\varepsilon}^{**}, \boldsymbol{\sigma}^*, \boldsymbol{\sigma}^{**}, \mathcal{S})$. Hence, the solutions of the reformulated minimization problem remain solutions of the previous one, once the strains and stresses are renormalized correctly. Furthermore, the stationarity of this global minimization problem leads to the following new set of equations:

$$\delta \underline{\boldsymbol{\varepsilon}}_i^* \Rightarrow \qquad \sum_{j=2}^{N_t} \sum_{e/\mathcal{S}_e^j \underline{\boldsymbol{\varepsilon}}^* = \underline{\boldsymbol{\varepsilon}}_i^*} \underline{\boldsymbol{\varepsilon}}_e^j - S_e^j \underline{\boldsymbol{\varepsilon}}^* = \mathbf{0} \quad \forall i, \tag{8.19}$$

$$\delta \underline{\boldsymbol{\varepsilon}}_i^{**} \Rightarrow \qquad \sum_{j=2}^{N_t} \sum_{e/\mathcal{S}_e^j \underline{\boldsymbol{\varepsilon}}^{**} = \underline{\boldsymbol{\varepsilon}}_i^{**}} \underline{\boldsymbol{\varepsilon}}_e^{j-1} - S_e^j \underline{\boldsymbol{\varepsilon}}^{**} = \mathbf{0} \quad \forall i, \tag{8.20}$$

$$\delta \underline{\boldsymbol{\sigma}}_i^* \Rightarrow \qquad \sum_{j=2}^{N_t} \sum_{e/\mathcal{S}_e^j \underline{\boldsymbol{\sigma}}^* = \underline{\boldsymbol{\sigma}}_i^*} \bar{\boldsymbol{\sigma}}_e^j + \underline{\mathbf{d}\boldsymbol{\sigma}}_e^j - S_e^j \underline{\boldsymbol{\sigma}}^* = \mathbf{0} \quad \forall i, \tag{8.21}$$

$$\delta \underline{\boldsymbol{\sigma}}_i^{**} \Rightarrow \qquad \sum_{j=2}^{N_t} \sum_{e/\mathcal{S}_e^j \underline{\boldsymbol{\sigma}}^{**} = \underline{\boldsymbol{\sigma}}_i^{**}} \bar{\boldsymbol{\sigma}}_e^{j-1} + \underline{\mathbf{d}\boldsymbol{\sigma}}_e^{j-1} - \mathcal{S}_e^j \underline{\boldsymbol{\sigma}}^{**} = \mathbf{0} \quad \forall i, \tag{8.22}$$

$$\delta\boldsymbol{\lambda}_k^j \Rightarrow \qquad \sum_{e=1}^{Ne} w_e \underline{\hat{\mathbf{B}}}_{ek}{}^T \cdot \underline{\mathbf{d}\boldsymbol{\sigma}}_e^j = \mathbf{0} \quad \forall j, \quad \forall k, \tag{8.23}$$

$$\text{and} \quad \delta\underline{\mathbf{d}\boldsymbol{\sigma}}_e^j \Rightarrow \begin{cases} 2\left(\bar{\underline{\boldsymbol{\sigma}}}_e^j + \underline{\mathbf{d}\boldsymbol{\sigma}}_e^j - S_e^{j+1}\underline{\boldsymbol{\sigma}}^{**}\right) + \sum_k w_e \underline{\hat{\mathbf{B}}}_{ek} \cdot \boldsymbol{\lambda}_k^j = \mathbf{0}, & \text{if } j = 1 \\ \Big[2\left(\bar{\underline{\boldsymbol{\sigma}}}_e^j + \underline{\mathbf{d}\boldsymbol{\sigma}}_e^j - \mathcal{S}_e^j\underline{\boldsymbol{\sigma}}^* + \bar{\underline{\boldsymbol{\sigma}}}_e^j + \underline{\mathbf{d}\boldsymbol{\sigma}}_e^j - \mathcal{S}_e^{j+1}\underline{\boldsymbol{\sigma}}^{**}\right) \\ + \sum_k w_e \underline{\hat{\mathbf{B}}}_{ek} \cdot \boldsymbol{\lambda}_k^j\Big] = \mathbf{0}, \quad \forall j \in [2, N_t - 1], \\ 2\left(\bar{\underline{\boldsymbol{\sigma}}}_e^j + \underline{\mathbf{d}\boldsymbol{\sigma}}_e^j - S_e^j\underline{\boldsymbol{\sigma}}^*\right) + \sum_k w_e \underline{\hat{\mathbf{B}}}_{ek} \cdot \boldsymbol{\lambda}_k^j = \mathbf{0}, & \text{if } j = N_t. \end{cases} \tag{8.24}$$

In the rest of this Chapter, the data is considered normalized and thus the reformulated global minimization problem will be tackled.

8.2.1.2 Resolution of the mechanical problem

As mentioned previously, the resolution of the global minimization problem relies on the use of staggered algorithm. In this paragraph, the computation of $(\underline{\mathbf{d}\boldsymbol{\sigma}}_e^j)_{e,j}$ and $(\boldsymbol{\lambda}_k^j)_{k,j}$ will be presented. Let us consider a given set $(\underline{\boldsymbol{\varepsilon}}^*, \underline{\boldsymbol{\varepsilon}}^{**}, \underline{\boldsymbol{\sigma}}^*, \underline{\boldsymbol{\sigma}}^{**})$ and given selection matrices $(\mathcal{S}^j)_j$. The computation of desired quantities relies on Eq. 8.23-8.24. First, the lagrangian multipliers are computed by multiplying Eq. 8.24 by $w_e \underline{\hat{\mathbf{B}}}_{el}{}^T$ and then by performing a sum over all the elements. Using, Eq. 8.23, this leads to the following set of linear equations in the lagrangian multipliers:

$$\forall l, j \Rightarrow \begin{cases} \sum_e 2w_e \underline{\hat{\mathbf{B}}}_{el}{}^T \cdot (\bar{\underline{\boldsymbol{\sigma}}}_e^j - S_e^{j+1}\underline{\boldsymbol{\sigma}}^{**}) + \sum_e \sum_k {w_e}^2 \underline{\hat{\mathbf{B}}}_{el}{}^T : \underline{\hat{\mathbf{B}}}_{ek} \cdot \boldsymbol{\lambda}_k^j = \mathbf{0}, & \text{if } j = 1 \\ \sum_e 2w_e \underline{\hat{\mathbf{B}}}_{el}{}^T \cdot \left(\bar{\underline{\boldsymbol{\sigma}}}_e^j - \mathcal{S}_e^j\underline{\boldsymbol{\sigma}}^* + \bar{\underline{\boldsymbol{\sigma}}}_e^j - \mathcal{S}_e^{j+1}\underline{\boldsymbol{\sigma}}^{**}\right) \\ + \sum_e \sum_k {w_e}^2 \underline{\hat{\mathbf{B}}}_{el}{}^T : \underline{\hat{\mathbf{B}}}_{ek} \cdot \boldsymbol{\lambda}_k^j = \mathbf{0}, \quad \forall j \in [2, N_t - 1], \\ \sum_e 2w_e \underline{\hat{\mathbf{B}}}_{el}{}^T \cdot (\bar{\underline{\boldsymbol{\sigma}}}_e^j - S_e^j\underline{\boldsymbol{\sigma}}^*) + \sum_e \sum_k {w_e}^2 \underline{\hat{\mathbf{B}}}_{el}{}^T : \underline{\hat{\mathbf{B}}}_{ek} \cdot \boldsymbol{\lambda}_k^j = \mathbf{0}, & \text{if } j = N_t. \end{cases} \tag{8.25}$$

This set of equation describes N_t linear systems of equations that can be written in the form $([M][\boldsymbol{\lambda}]^j = [\mathbf{F}]^j)_j$, where $[M]$ is a square matrix of $\hat{N}$ by $\hat{N}$, $[\boldsymbol{\lambda}]^j$ is the vector containing the lagrangian multipliers at j and $[\mathbf{F}]^j$ is a vector containing internal force mismatch between the mechanical states and their material states at j. $[M]$ and $[\mathbf{F}]$ follow the relations:

$$\forall k, l, \ [M]_{k,l} = \sum_e {w_e}^2 \underline{\hat{\mathbf{B}}}_{el}{}^T : \underline{\hat{\mathbf{B}}}_{ek}, \tag{8.26}$$

$$\forall l\ [\mathbf{F}]_l^j = \begin{cases} -\sum_e 2w_e \hat{\underline{\mathbf{B}}}_{el}^{\ T} \cdot (\bar{\boldsymbol{\sigma}}_e^j - S_e^{j+1}\underline{\boldsymbol{\sigma}}^{**}), & \text{if } j=1, \\ -\sum_e 2w_e \hat{\underline{\mathbf{B}}}_{el}^{\ T} \cdot \left(\bar{\boldsymbol{\sigma}}_e^j - \mathcal{S}_e^j\underline{\boldsymbol{\sigma}}^* + \bar{\boldsymbol{\sigma}}_e^j - \mathcal{S}_e^{j+1}\underline{\boldsymbol{\sigma}}^{**}\right), & \forall j \in [2, N_t-1], \\ -\sum_e 2w_e \hat{\underline{\mathbf{B}}}_{el}^{\ T} \cdot (\bar{\boldsymbol{\sigma}}_e^j - S_e^j\underline{\boldsymbol{\sigma}}^*), & \text{if } j=N_t. \end{cases} \tag{8.27}$$

These N_t linear systems are solved using a Cholesky decomposition of $[M]$ computed once. Once the lagrangian multipliers obtained, the stresses can be updated using directly Eq. 8.24.

8.2.1.3 Resolution of the material problem

In this paragraph, the update of the material states set and selection matrices for given stresses will be presented. First, the selection matrices $(\mathcal{S}^j)_j$ are obtained by solving the minimization problem from Eq. 8.17, for given stress fields and the actual set of material states. Once these matrices obtained, the set of material states $(\underline{\boldsymbol{\varepsilon}}^*, \underline{\boldsymbol{\varepsilon}}^{**}, \underline{\boldsymbol{\sigma}}^*, \underline{\boldsymbol{\sigma}}^{**})$ is actualized using Eq. 8.19-8.22. These equations simply state that the material states are the barycentres of the mechanical states associated, *i.e.*:

$$\forall i, \underline{\boldsymbol{\varepsilon}}_i^* = \frac{1}{n_i}\sum_{j=2}^{N_t} \sum_{e/\mathcal{S}_e^j\underline{\boldsymbol{\varepsilon}}^* = \underline{\boldsymbol{\varepsilon}}_i^*} \underline{\boldsymbol{\varepsilon}}_e^j \tag{8.28}$$

$$\forall i,\ \underline{\boldsymbol{\varepsilon}}_i^{**} = \frac{1}{n_i}\sum_{j=2}^{N_t} \sum_{e/\mathcal{S}_e^j\underline{\boldsymbol{\varepsilon}}^{**} = \underline{\boldsymbol{\varepsilon}}_i^{**}} \underline{\boldsymbol{\varepsilon}}_e^{j-1}, \tag{8.29}$$

$$\forall i,\ \underline{\boldsymbol{\sigma}}_i^* = \frac{1}{n_i}\sum_{j=2}^{N_t} \sum_{e/\mathcal{S}_e^j\underline{\boldsymbol{\sigma}}^* = \underline{\boldsymbol{\sigma}}_i^*} \bar{\boldsymbol{\sigma}}_e^j + \underline{\mathbf{d}\boldsymbol{\sigma}}_e^j, \tag{8.30}$$

$$\forall i,\ \underline{\boldsymbol{\sigma}}_i^{**} = \frac{1}{n_i}\sum_{j=2}^{N_t} \sum_{e/\mathcal{S}_e^j\underline{\boldsymbol{\sigma}}^{**} = \underline{\boldsymbol{\sigma}}_i^{**}} \bar{\boldsymbol{\sigma}}_e^{j-1} + \underline{\mathbf{d}\boldsymbol{\sigma}}_e^{j-1}, \tag{8.31}$$

$$\tag{8.32}$$

where n_i denotes the size of the i^{th} material state.

8.2.1.4 Resolution of the global minimization problem

To solve the global minimization problem considered, *i.e.* to compute $(\underline{\boldsymbol{\varepsilon}}_i^*, \underline{\boldsymbol{\varepsilon}}_i^{**}, \underline{\boldsymbol{\sigma}}_i^*, \underline{\boldsymbol{\sigma}}_i^{**})_i$, $(\underline{\mathbf{d}\boldsymbol{\sigma}}_e^j)_{j,e}$ and $(\mathcal{S}^j)_j$, the following algorithm is followed [Langlois *et al.*, 2022]:

1. initialize $(\underline{\boldsymbol{\sigma}}_e^j)_{j,e}$ using a FE simulation,
2. initialize $(\underline{\boldsymbol{\varepsilon}}_i^*, \underline{\boldsymbol{\varepsilon}}_i^{**}, \underline{\boldsymbol{\sigma}}_i^*, \underline{\boldsymbol{\sigma}}_i^{**})_i$ and $(\mathcal{S}^j)_j$ by a k-means algorithm [MacQueen *et al.*, 1967] on $(\underline{\boldsymbol{\varepsilon}}_e^j, \underline{\boldsymbol{\varepsilon}}_e^{j-1}, \bar{\boldsymbol{\sigma}}_e^j, \bar{\boldsymbol{\sigma}}_e^{j-1})_{e,j}$,

3. solve the mechanical problem as explained in Paragraph. 8.2.1.2,

4. solve the material problem as explained in Paragraph. 8.2.1.3,

5. iterate step 4 until convergence of $(\mathcal{S}^j)_j$. It usually takes less than 3 iterations to converge,

6. iterate steps 3 through 5 until convergence of $(\mathcal{S}^j)_j$ and $(\underline{\mathbf{d}\boldsymbol{\sigma}}_e^j)_{j,e}$. One iteration from step 3 to 5 will be called a cycle.

8.2.2 Parameters of the method

In the proposed methodology, two parameters can be adjusted by the user. The first one is the number of material states N^*, *i.e.* the cardinal of the set $(\underline{\boldsymbol{\varepsilon}}^*, \underline{\boldsymbol{\varepsilon}}^{**}, \underline{\boldsymbol{\sigma}}^*, \underline{\boldsymbol{\sigma}}^{**})$. The second one lies in the choice of the fourth-order tensor $\mathbb{C}_o$. In their work, Dalémat and her co-authors [Dalémat *et al.*, 2021] investigated the impact of these parameters on the result of the Data-Driven Identification. They compared the stresses of FE simulations, considered as the reference, to the one obtained using the DDI with different parameter values. They concluded that a small number of material states leads to an insufficient sampling of the strain-stress manifolds, and thus, to significant error. A high number of material states also leads to significant error, since it will give more weight to outliers and increase the sensitivity to noise (similarly to the overfitting phenomenon for regressions). In their work, the authors recommend a number of material states so that $20 \leq \frac{(N_t-1)\cdot N_e}{N^*} \leq 100$. In addition, the influence of the choice of the magnitude of $\mathbb{C}_o$ is straightforward. Indeed, Eq. 8.15 shows that by choosing a tensor with high values, the mapping between mechanical states and material states will emphasizes the strain values rather than the stresses values. This is relevant since the strains are obtained experimentally, while the stresses are unknowns and change during the method. In the present work, the fourth-order tensor that will be used is a Hooke tensor for an isotropic material, hence its definition will only be dependent of the choice of a pseudo-Young modulus E_o and a pseudo-Poisson ratio ν_o. Let us note that, while the influence of the magnitude of $\mathbb{C}_o$ is straightforward, the influence of the symmetry class of the tensor remains unknown. Intuitively, one would assume that the use of a pseudo isotropic elastic tensor would not lead to a satisfying clustering of anisotropic plastic mechanical states. However, this question of the influence of the symmetry class of $\mathbb{C}_o$ has yet to be investigated. In the following section, the influence of the parameters will be further discussed using numerical applications.

Moreover, two convergence criteria are needed for the proposed resolution algorithm: one for the convergence of $(\mathcal{S}^j)_j$ and one for the convergence of $(\underline{\mathbf{d}\boldsymbol{\sigma}}_e^j)_{j,e}$. In this work, they are defined as follows:

- For the selection matrices criterion, we consider for each iteration i the convergence

rate of the data-driven distance $\underline{\Psi}$. That is to say: $\frac{|\underline{\Psi}_i - \underline{\Psi}_{i-1}|}{\underline{\Psi}_0}$, where $\underline{\Psi}_0$ is its initial value.

- For the stress corrections criterion, we consider for each iteration i its convergence rate. That is to say: $\frac{\sqrt{\sum_e \sum_j |\underline{\mathbf{d}\boldsymbol{\sigma}}^j_{ei} - \underline{\mathbf{d}\boldsymbol{\sigma}}^j_{ei-1}|^2}}{\sqrt{\sum_e \sum_j |\underline{\bar{\sigma}}^j_e|^2}}$.

8.2.3 Outputs of the method

The proposed Data-Driven algorithm yields four major outputs.

- A set of mechanical states $(\boldsymbol{\varepsilon}^j_e, \boldsymbol{\varepsilon}^{j-1}_e, \boldsymbol{\sigma}^j_e, \boldsymbol{\sigma}^{j-1}_e)_{e,j\in[2,N_t]}$. This data set corresponds to spatio-temporal strain and equilibrated stress fields during the experiment.

- A set of material states $(\boldsymbol{\varepsilon}^*, \boldsymbol{\varepsilon}^{**}, \boldsymbol{\sigma}^*, \boldsymbol{\sigma}^{**})$. These points can be interpreted as a sampling of the material's response in the constitutive space considered – here: ($\boldsymbol{\varepsilon}^j$, $\boldsymbol{\varepsilon}^{j-1}$, $\boldsymbol{\sigma}^j$, $\boldsymbol{\sigma}^{j-1}$). They do not verify the mechanical equilibrium. In practice, these material states are barycentres of clusters that regroup mechanical states that are close in the $\|\|\|_{\mathbb{C}_o}$ norm sense.

- Selection matrices that map each mechanical state to a material state.

- The norm $\|\|\|_{\mathbb{C}_o}$. This norm can be used to retrieve the distance of each mechanical state to its corresponding material state.

The set of mechanical states, the set of material states as well as the norm $\|\|\|_{\mathbb{C}_o}$ will be used to analyse and discuss the results from the numerical test case presented in Section 8.3 and then the experimental results (Section 9).

Table 8.1 summarizes the inputs, outputs, parameters and assumptions needed for the proposed Data-Driven Identification method.

Inputs	Outputs	Parameters	Formulation assumptions
$(\boldsymbol{\varepsilon}^j_e)_{j,e}$ from DIC	$(\mathcal{S}^j)_j$	$\mathbb{C}_o$	Plane stress
$(\bar{\boldsymbol{\sigma}}^j_e)_{j,e}$ from FE	$(\mathbf{d}\boldsymbol{\sigma}^j_e)_{j,e}$	N^*	Small strain
Mesh and connectivity	Material states	Convergence criteria	Constitutive space
	Ψ		Boundary conditions
			$\mathbb{C}$ already identified

Table 8.1: Summary of the inputs, outputs, parameters and the assumptions needed for the Data-Driven Identification method proposed in this work. In this table, $\mathbb{C}$ is the material's elasticity tensor, supposed already identified.

8.3 Numerical test case

In order to investigate the Data-Driven Identification method presented earlier, a numerical test case is conducted and is presented in this Section.

Note that, contrary to classical 1D tests cases, the presented work relies on data existing in a 13 dimension space (3 for $\boldsymbol{\varepsilon}$, 3 for $\dot{\boldsymbol{\varepsilon}}$, 3 for $\boldsymbol{\sigma}$, 3 for $\dot{\boldsymbol{\sigma}}$), or 14 if we consider the temperature T. Such high dimensionality requires developing new ways to display results. Nevertheless, such developments go beyond the scope of this work. Hence, for the sake of simplicity the majority of the results will be presented in reduced spaces using invariant based norms (*e.g.* I1, Von-Mises). Note that this is not a requirement but just a graphic choice. Any other mechanical norms could have been chosen.

In addition, in all the sections that follow, the DDI will be applied using coarse meshes (about 3000 to 4000 elements) in order to limit the computing time.

8.3.1 Methodology

To investigate the sensitivity to the method parameters, several FE simulations will be performed using the experimental sample's geometry. To this effect, these simulations are conducted using Abaqus with the implicit solver using CPS3T elements. Furthermore, in all the FE simulations the Johnson-Cook model will be used.

Creation of a reference solution (U^{ref}, $\boldsymbol{\sigma}^{\text{ref}}$) In order to create a reference solution that will be used to investigate the DDI algorithm, a first FE simulation is conducted using the model parameters identified in Part II, they are recalled in Tab. 8.2 (Model A). The simulation is performed under imposed displacements on the upper and lower boundaries. The displacements prescribed for this simulation are obtained by linearly interpolating the experimental displacement fields (see Chapter 7) onto the coarser mesh used here. The outputs of this simulation – namely the displacement fields U^{ref}, the stress fields $\boldsymbol{\sigma}^{\text{ref}}$ and the vertical net force on the upper boundary F_y^{ref} – will be used as references for what follows. In this numerical test case, these outputs (except the stress fields) represent the experimental data that will be used when applying the DDI strategy for the real experiment.

Creation of a statically admissible initial solution using a "wrong" model The creation of an initial guess for the stress field that will be used as an input for the DDI algorithm requires two consecutive Finite-Element simulations. To validate the DDI procedure, an initialization reasonably far from the solution is chosen. To this effect, the same model as the reference one is chosen but the constitutive parameters are significantly modified. Hence, the initial yield is decreased, whereas the hardening modulus is increased. In addition, to investigate the ability of the DDI to accurately retrieve the strain-rate

dependency, the strain-rate dependency is set close to zero. The exact parameters are given in Tab. 8.2 (Model B).

- The first simulation is conducted under imposed displacements, using U^{ref}. The load profile on the upper boundary is extracted from this simulation. This profile is then rescaled in such a manner that, in the end, the net force on the upper boundary is equal to the reference net force F_y^{ref}. The role of this first simulation is to get a nice estimation of the load distribution at the upper bound of the sample.

- The second simulation is then performed under mixed boundary conditions: imposed displacements on the lower boundary, imposed displacements in the X direction and imposed rescaled vertical distribution of forces on the upper bound. This simulation allows to obtain statically admissible stresses $\boldsymbol{\sigma}^{\text{false}}$.

The whole procedure is summarized in Figure 8.1. In the end, the DDI will be given the total strains $\boldsymbol{\varepsilon}_t^{\text{ref}}$ (computed from U^{ref}) and $\boldsymbol{\sigma}^{\text{false}}$ as inputs. In addition, for comparison purposes, the plastic strains $\boldsymbol{\varepsilon}_p^{DDI}$ associated to the stresses $\boldsymbol{\sigma}^{DDI}$ are computed from the total strains $\boldsymbol{\varepsilon}_t^{DDI}$ using Hooke law, the plastic incompressibility and the small strain assumption: $\boldsymbol{\varepsilon}_p^{DDI} = \boldsymbol{\varepsilon}_t^{DDI} - \mathbb{C}^{-1} : \boldsymbol{\sigma}^{DDI}$. This section will investigate the ability of the proposed identification method to retrieve the stress fields sought $\boldsymbol{\sigma}^{\text{ref}}$.

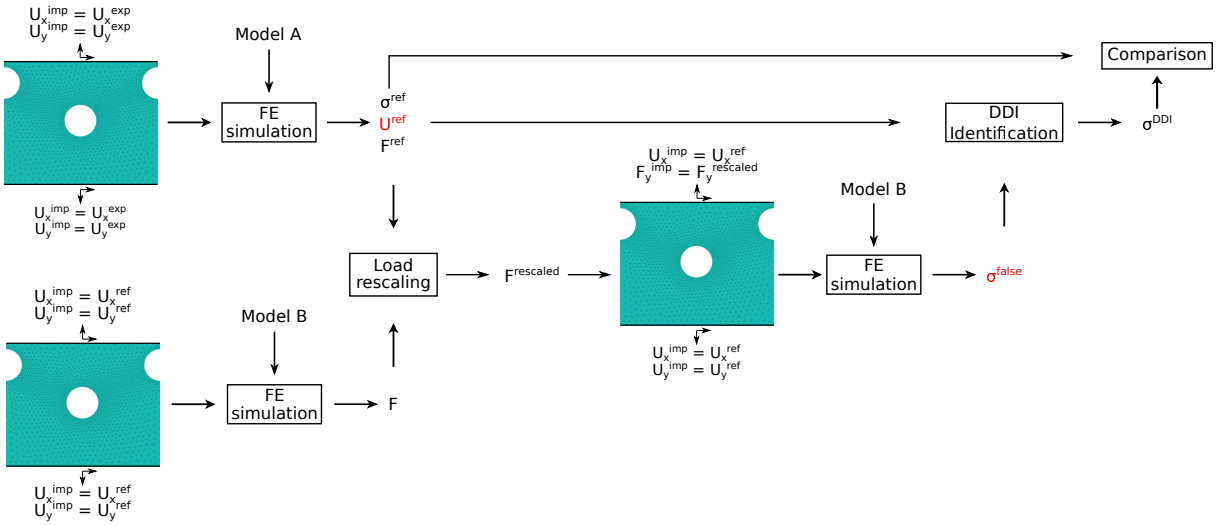

Figure 8.1: Schematic of the numerical test case procedure. In red are the inputs of the DDI algorithm.

	A (MPa)	B (MPa)	n	C	$\dot{\varepsilon}_0$ (s^{-1})	m	T_o (K)	T_{melt} (K)
Model A	394 MPa	136 MPa	0.471	0.0259	$69.86\,\text{s}^{-1}$	1.11	300	1350
Model B	315 MPa	272 MPa	0.6123	2.56×10^{-4}	$69.86\,\text{s}^{-1}$	1.11	300	1350

Table 8.2: Parameters of the two Johnson-Cook model used for the FE simulations to investigate the DDI algorithm.

8.3.2 Parameters Influence

In what follows the influence of the two parameters of the DDI method is investigated. To this effect, two indicators will be used: the average and the standard deviation of the Von-Mises norm of the error between the DDI solution and the reference one: $(\|\bar{\boldsymbol{\sigma}}_e^j + \mathbf{d}\boldsymbol{\sigma}_e^j - \boldsymbol{\sigma}_e^{j,\text{ref}}\|_{VM})_{j,e}$.

8.3.2.1 Influence of the pseudo-elastic fourth-order tensor $\mathbb{C}_o$

First, the influence of the choice of $\mathbb{C}_o$ will be investigated, the other parameters being fixed. The ratio between the number of mechanical states and material states is fixed to 80 and both convergence criteria set to 5×10^{-3}. The pseudo-Young modulus E_o tested ranges from 1 to 1000 GPa, while ν_o is fixed at 0.29. Figure 8.2a depicts the evolution of the systematic error (or bias) as a function of the evolution of E_o, while Fig. 8.2b depicts the evolution of the random error (or uncertainty). This figure shows that increasing the value of E_o will decrease both systematic and random errors, until the Young modulus of the considered steel is reached. In addition, it shows that both errors reach a plateau at 34 MPa $\pm$ 25 MPa, and increasing the pseudo-modulus beyond the material Young modulus does not lead to a significant decrease of the errors. This is consistent with what was explained in Section 8.2.2 and with what was found by Dalémat and her co-authors. Hence, in the rest of this work, E_o is fixed to 210 GPa.

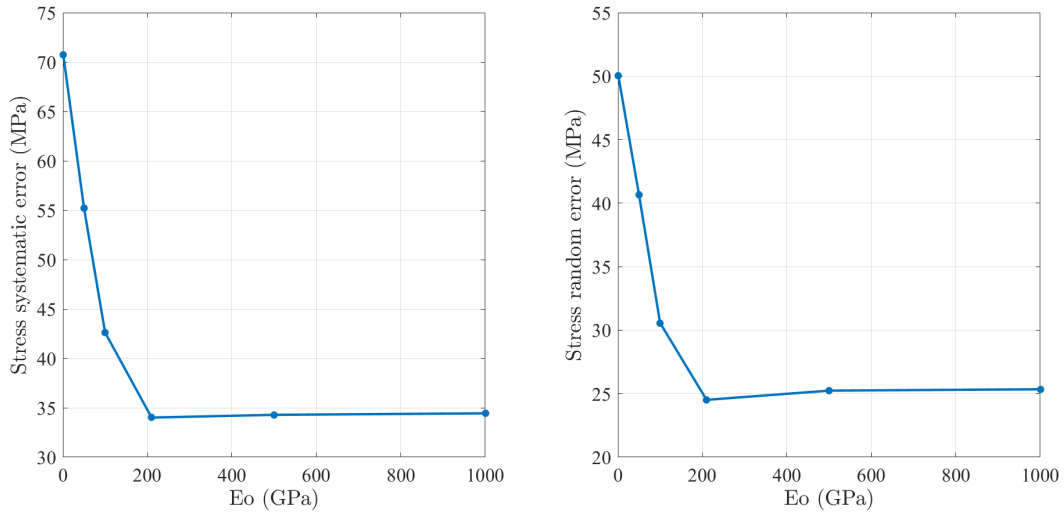

(a) Stress systematic error versus E_o, (b) Stress random error versus E_o,

Figure 8.2: Stress errors evolution according to the value of E_o.

8.3.2.2 Influence of the ratio of the number of mechanical states and material states

Now, E_o is fixed to 210 GPa. The influence of the ratio r^* between the number of mechanical states ($N_e \cdot (N_t - 1)$) and the number of material states (N^*) is investigated. To this effect, the ratio tested ranges from 30 to 500, which leads to N^* between 205 and 3416. Figure 8.3a depicts the evolution of the systematic error with the evolution of N^*, while Fig. 8.3b depicts the evolution of the random error. This figure shows that increasing the value of N^* will decrease both systematic and random errors. This is consistent with what was explained in Section 8.2.2 and with what was found by Dalémat *et al.* [Dalémat *et al.*, 2021]. Another consideration to take into account to select the value of r^* is the computation time. Indeed, increasing the number of material states severely increases the computation time, in particular for the K-means algorithm used for the initialization. This is highlighted by Fig. 8.3c where a nearly linear relationship between N^* and the computation time is evidenced. As a result, a ratio of 50 (*i.e.* 2050 material states for this case) is considered as a good trade-off. Indeed, it allows to have stress errors of 31 MPa $\pm$ 23 MPa for a computation time of about one hour. Moreover, further increasing the number of material states does not lead to a significant reduction of these errors, while the computation time increases at the same rate. Hence, in the rest of this work, r^* is fixed to 50. Notice that 2050 material states means, in practice, that out of 105,490 data points (number of elements $\times$ time steps) 2050 barycentres will be used to sample the material manifold in the 13 dimensions of the considered constitutive space.

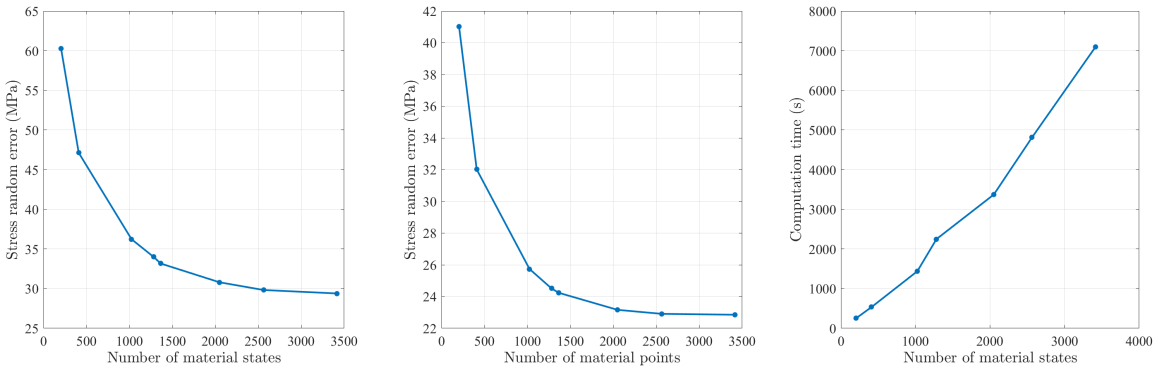

(a) Stress systematic error versus N^*, (b) Stress random error versus N^*, (c) Computation time of the algorithm versus N^*,

Figure 8.3: Stress errors and computation time evolution according to the number of material states N^*.

8.3.2.3 Influence of the convergence criteria

Once the ratio r^* fixed to 50 and the pseudo-Young modulus E_o fixed to 210 GPa, the influence of the two convergence criteria are investigated. In the implementation of the

proposed DDI algorithm, both criteria have to be met. Furthermore, they both evaluate a convergence speed. As a result, the values of both criterion can be set at the same value, which will range from 1×10^{-3} to 1×10^{-1}. Figure 8.4a depicts the evolution of the systematic error with the evolution of the criterion value, while Fig. 8.4b depicts the evolution of the random error. Additionally, Fig. 8.4c depicts the computation time evolution. These figures highlight the need to choose a criterion below 5×10^{-2}. Indeed, for higher values, the systematic and random errors are higher than 50 MPa and 40 MPa. This is explained by the fact that for these values, the criterion is reached after a very small number of cycle (less than 10). Furthermore, the errors seem to stabilize for values below 5×10^{-3} (this value included). However, the computation time significantly increases for criterion values below 5×10^{-3}. Thus, in the rest of this work, the criterion is fixed to 5×10^{-3} which is considered as a good trade-off between computation time and accuracy.

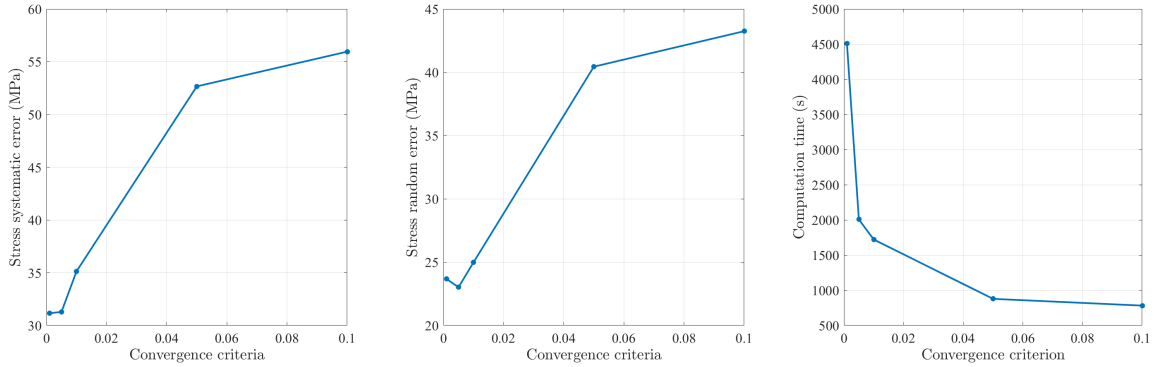

(a) Stress systematic error versus the criterion, (b) Stress random error versus the criterion, (c) Computation time of the algorithm versus the criterion,

Figure 8.4: Stress errors and computation time evolution according to the criterion.

8.3.3 Analysis of the DDI results using the identified method's parameters

Once the parameters for the DDI algorithm fixed, its outputs can be further analysed and compared to the inputs. Hence, the DDI was applied to the simulations for 50 time steps. Its results will be presented and discussed.

8.3.3.1 Outliers selection

As previously said two main outputs of the DDI can be analysed: the mechanical states which are in equilibrium and distributed (as close as possible in the least square sense) around a manifold in the constitutive space, and the material states which are not equilibrated, but they sample this manifold. Two pathological behaviours can be observed from both quantities:

- A material state clustering very few mechanical states. In that case, the material state has converged toward an epiphenomenon (spatially and/or temporarily) and its associated stress state may be unrealistic. This state can be seen as an outlier.

- Some mechanical states remain very far (with respect to $\|\|\|_{\mathbb{C}_o}$) from their material states. In that case, it has been impossible, within the convergence criteria, to converge toward an equilibrated solution packed around the manifold. Such states can also be considered as outliers.

The following part proposes a methodology to discard such mechanical and material outliers. The following must be seen as a first attempt to clean up the results from this complex inverse problem. A more elegant and less user dependent solution is still to be found (see Outstandings 9.4).

Let us first consider the stresses obtained with the DDI and compare them to the reference ones. For this purpose, Figure 8.5 depicts these stresses in a sub space of the constitutive space built using the Von-Mises norm: ($\|\boldsymbol{\varepsilon}_p\|_{VM}$, $\|\dot{\boldsymbol{\varepsilon}}_p\|_{VM}$, $\|\boldsymbol{\sigma}\|_{VM}$) as well as one projection in the space ($\|\boldsymbol{\varepsilon}_p\|_{VM}$, $\|\boldsymbol{\sigma}\|_{VM}$). The reference solution is depicted by the red crosses, while the solution from the DDI is represented by the coloured dots. The colour and the size of the dots are related to the size of the associated material state cluster. First, one can observe that the biggest clusters (depicted by the big yellow dots) are associated to mechanical states under elasticity. This is expected considering the fact that plasticity mainly occurs in the bands presented in Chapter 7, and after a certain loading step. Hence, most of the sample is under elasticity or very small plastic strains during most of the experiment time. Furthermore, the fit between the DDI solution and the reference seems to be acceptable for strains up to 0.3. Beyond, the error reaches up to 80 MPa. This can be explained by the fact that higher values of strain are reached by only a few elements toward the end of the experiment. As a result, these mechanical states are regrouped in material state clusters that have a relatively small size (less than 10 mechanical states while 50 time steps are considered). Due to their small size, these clusters are less constrained and thus their material states (*i.e.* their barycentres) may not capture the material behaviour as well as for bigger clusters. Furthermore, other small clusters can be observed for different strain and strain-rates values. These very small clusters can be considered as outliers, since it is very likely that they are not representative of the material behaviour but rather capture epiphenomena that may occur near the free edges or near the holes for example. In addition, it is important to note that these epiphenomena are independent of the Data-Driven Identification algorithm, but can be explained by the difficulty to have accurate measurements near the free edges and the holes, and also the mesh used for both DIC and the FE simulations for instance. As a result, since these epiphenomena will always be captured by the DDI algorithm and small clusters will always exist, it is of interest to define a criterion to discard these clusters.

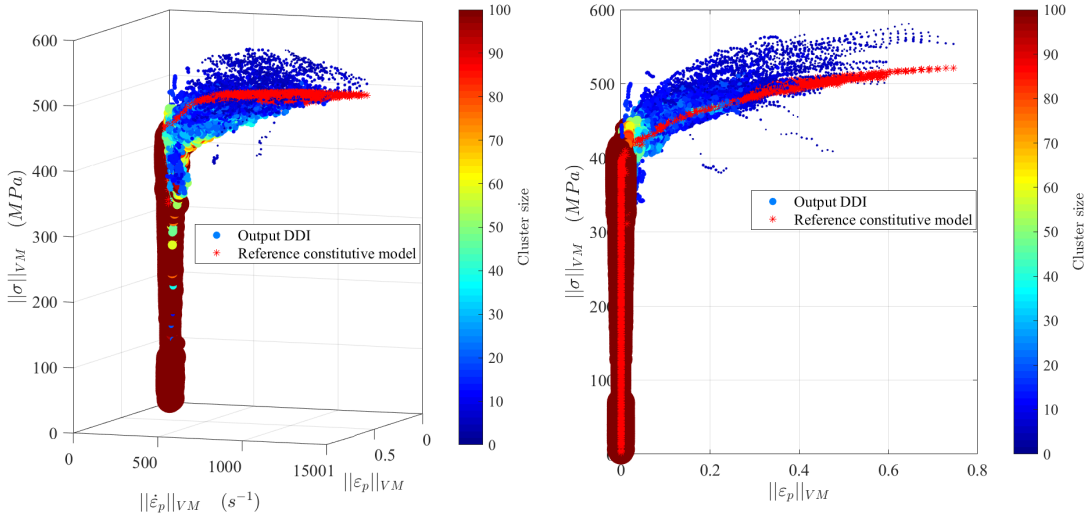

(a) $\|\boldsymbol{\sigma}\|_{VM}$ evolution versus ($\|\boldsymbol{\varepsilon}_p\|_{VM}$, $\|\dot{\boldsymbol{\varepsilon}}_p\|_{VM}$),

(b) $\|\boldsymbol{\sigma}\|_{VM}$ evolution versus $\|\boldsymbol{\varepsilon}_p\|_{VM}$,

Figure 8.5: Comparison of the DDI output versus the reference solution (in red) in the constitutive space ($\|\boldsymbol{\varepsilon}_p\|_{VM}$, $\|\dot{\boldsymbol{\varepsilon}}_p\|_{VM}$, $\|\boldsymbol{\sigma}\|_{VM}$), and in one projection. The marker size and colour for the DDI output are related to the size of the cluster containing the mechanical state.

Figure 8.6a depicts the evolution of the cumulative sum of the mechanical states versus the size of the clusters. This figure highlights the fact that all the clusters with a size smaller than 20 amounts for less than 10 % of the total mechanical states. Heuristically, the cluster size criterion is chosen as 20. This represents 40 % of the average cluster size r^*. Using this criterion, 42 % of the material states are disregarded which only represents 9 % of the mechanical states. Figure 8.6b shows the spatial cartography of the elements that will be kept and the colour denotes the ratios at which they are used (*e.g.* 50 % means that the element is selected for half of the time steps). This figure shows that the small clusters are mainly related to epiphenomena that are occurring near the notches and holes. In addition, it also shows that elements in the bands are sometime disregarded. As explained earlier this is due to the fact that near the end of the experiment, only a few elements reach their values of strain and strain-rates.

Aside from the clusters' size, another key information resides in the distance between the mechanical states and their corresponding material states, which is given by the DDI norm. Figure 8.7 depicts the spatial cartographies of the temporal average and standard deviation of the DDI norm $\|\|_r$. This shows that the distance is higher in the bands and especially near the hole and notches, which is consistent with the previous observations. In short, close to notches and the hole, and within the band (when approaching the end of the test) mechanical states tend to deviate from the manifold. As a result, since a mechanical state can be associated to a material state with a proper size, but still be distant of this material state, a selection criterion using the norm is searched. For this purpose, Figure 8.8

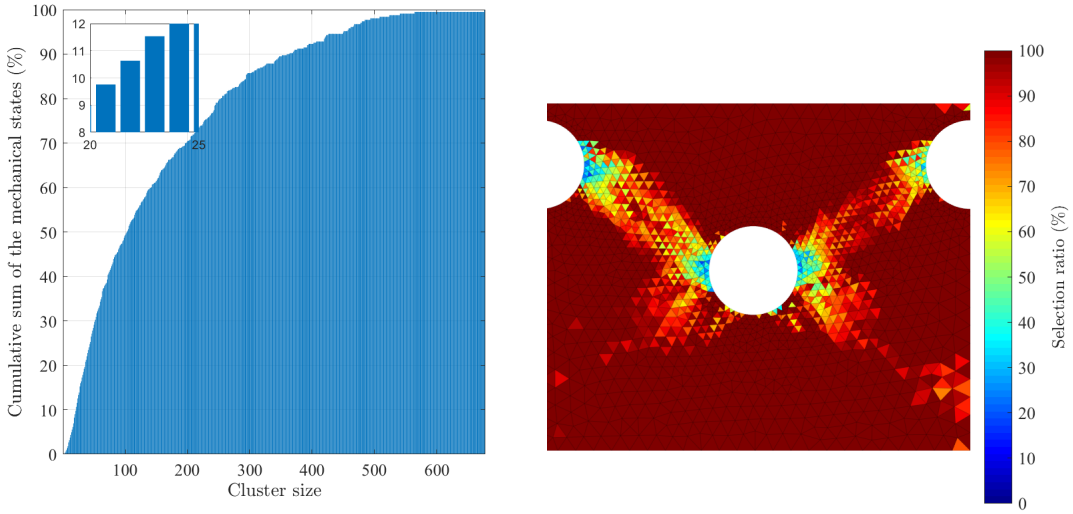

(a) Histogram of the cumulative sum of the mechanical states versus the cluster size,

(b) Cartography of the selected elements and their selection ratios,

Figure 8.6: Investigation of a selection criterion based on the cluster size.

displays the histogram of the DDI norm computed between the selected clusters and their associated mechanical states. It can be observed that 20 % of the mechanical states are at a distance of approximately 200 (in term of the DDI distance) from their material states. The black vertical dashed line is located at one standard deviation from the peak observed. This black line has been empirically chosen as the norm criterion to discard mechanical states outliers. Adding this criterion leads to disregarding 26 % of the total mechanical states. Similarly to the previous figure, Fig. 8.8b shows the cartography of the selected elements and their ratios. This figure shows that this criterion mainly discriminates the elements in the bands when approaching the end of the test, which again is to be expected since they reach strain and strain-rate values that are not often reached.

Finally, Figure 8.9 depicts the same data as the Fig. 8.5, but only for the selected mechanical states using both criteria. As expected, the spread between the DDI solution and the reference one is reduced. However, this is done at the cost of a reduction of the strain and strain-rate range spectra which went from respectively $[0 - 0.75]$, $[0\,\mathrm{s}^{-1} - 1350\,\mathrm{s}^{-1}]$, down to $[0 - 0.18]$, $[0\,\mathrm{s}^{-1} - 650\,\mathrm{s}^{-1}]$. In the rest of this work, the data will always only concern the selected clusters and the selected mechanical states.

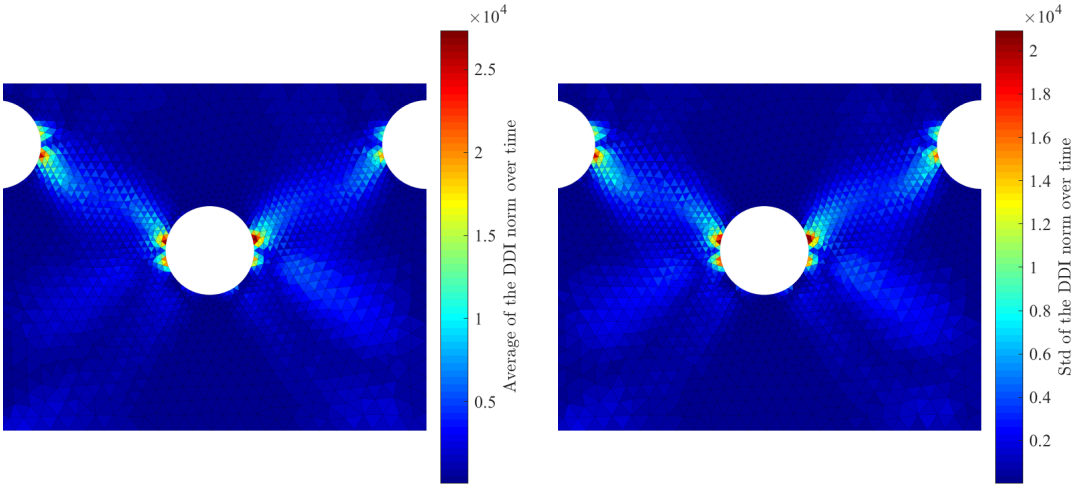

(a) Cartography of the DDI norm average, (b) Cartography of the standard deviation of the DDI norm,

Figure 8.7: Temporal average and standard deviation of each element of the mesh.

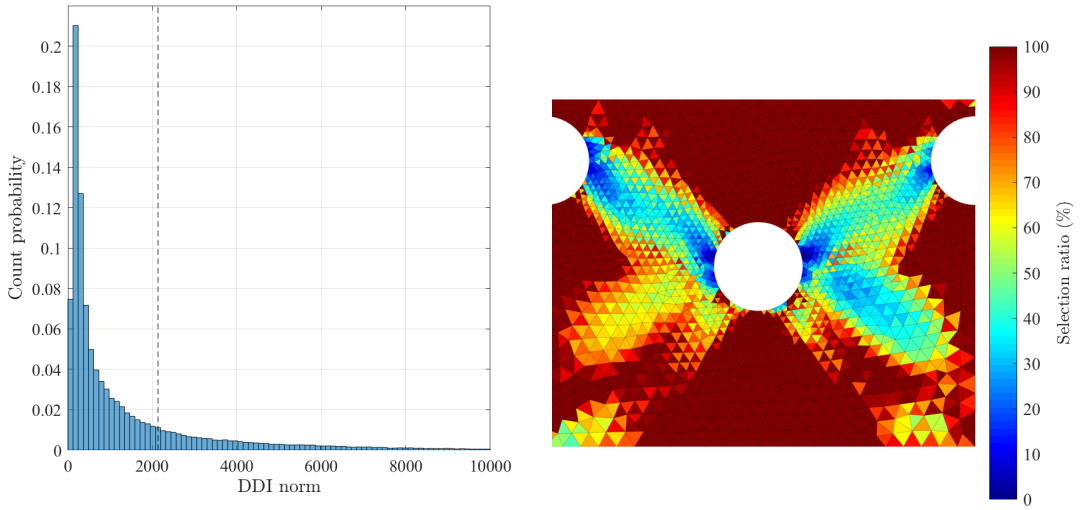

(a) Histogram of the DDI norm for the already selected elements, (b) Cartography of the selected elements and their selection ratios,

Figure 8.8: Investigation of a selection criterion based on the $\|\|\|_r$ norm for the already selected clusters and associated elements.

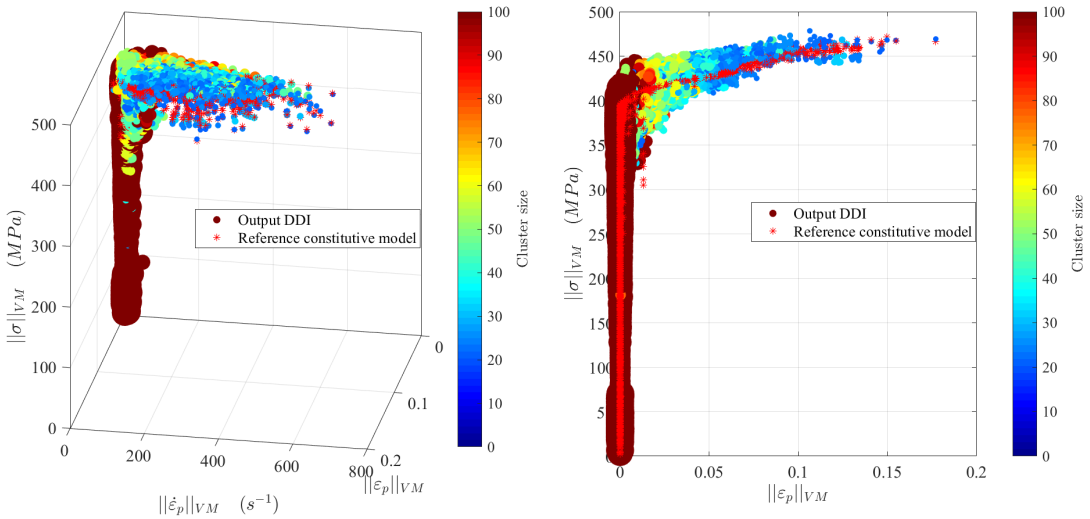

(a) $\|\boldsymbol{\sigma}\|_{VM}$ evolution versus ($\|\boldsymbol{\varepsilon}_p\|_{VM}$, $\|\dot{\boldsymbol{\varepsilon}}_p\|_{VM}$),

(b) $\|\boldsymbol{\sigma}\|_{VM}$ evolution versus $\|\boldsymbol{\varepsilon}_p\|_{VM}$,

Figure 8.9: Comparison of the DDI output versus the reference solution (in red) in the constitutive space ($\|\boldsymbol{\varepsilon}_p\|_{VM}$, $\|\dot{\boldsymbol{\varepsilon}}_p\|_{VM}$, $\|\boldsymbol{\sigma}\|_{VM}$), and in one projection. The marker size and colour for the DDI output are related to the size of the cluster containing the mechanical state. Only the mechanical states contained in the selected clusters are represented.

8.3.3.2 Analysis of the mechanical states

Now the results of the Data-Driven Identification algorithm will be presented and discussed. Figure 8.10 depicts both the temporal systematic and random errors for each element of the geometry, for the initial stress fields (obtained when using model B) as well as the ones obtained after the DDI. The first two cartographies show that the initial error is mainly located near the mesh boundaries, as well as where the sample is not submitted to high plastic strains. The initial error is also important near the central hole and notches, where the strain-rate reaches high values. On the other hand, the improvement of the solution by the DDI algorithm is clearly highlighted when one considers the error cartographies of the DDI solutions. Indeed, the errors are lower in most of the elements. The remaining errors are located on the edges of the sample: where the mesh is coarser. Hence, it is expected that the use of a finer mesh may help to improve the results. Furthermore, it is important to note that the error also remain important just below the central holes: where the plastic strain remain low. Incidentally it is also where the sample is in compression.

In addition, Fig. 8.11 depicts the stress relative error for the selected mechanical states in function of the Von-Mises norm of the plastic strain. The red points represent the mechanical states under a compressive state ($I_1 \leq 0$) while the blue ones are under a tensile state ($I_1 \geq 0$). This figure shows that the DDI yields relative errors in the order of 5 % when the material's elasto-plastic transition is passed. This is particularly highlighted by the quadratic fit for all the data with a plastic strain above 0.01 (the red line in the figure). The grey area represents one standard deviation of the error made by the fit. Hence, aside from the elastic behaviour of the material, the DDI has an accuracy of 5.4 % $\pm$ 3.7 %. In addition, let us note that most of the mechanical states under compression remain below a plastic strain of 0.005, *i.e.* in elasticity which explains why they are badly estimated by the DDI. It is important to remind that these errors are obtained using noisefree data. The impact of the camera noise on the accuracy will be discussed in Section 8.4.

To further discuss the impact of the proposed algorithm, one can also consider the relative error distribution in the ($\|\boldsymbol{\varepsilon}\|_{VM}$, $\|\dot{\boldsymbol{\varepsilon}}\|_{VM}$) space. Thus, Figure 8.12 presents the relative error cartographies of, respectively, the stresses obtained from FE simulations using model B and the ones corrected by the DDI in the ($\|\boldsymbol{\varepsilon}\|_{VM}$, $\|\dot{\boldsymbol{\varepsilon}}\|_{VM}$) space. The cartography of the initialization error (Fig. 8.12a) clearly highlights two main zones of errors. The first one, for values of strain below 0.1 and values of strain-rate below $100\,\mathrm{s}^{-1}$, is explained by the difference in both the initial yield stress and the hardening modulus between model A and model B (Tab. 8.2) used in the FE simulations. Furthermore, the second zone of errors where strain-rates are higher than $500\,\mathrm{s}^{-1}$ illustrates the fact that the Johnson-Cook model used to get the initial stress fields has very little strain-rate

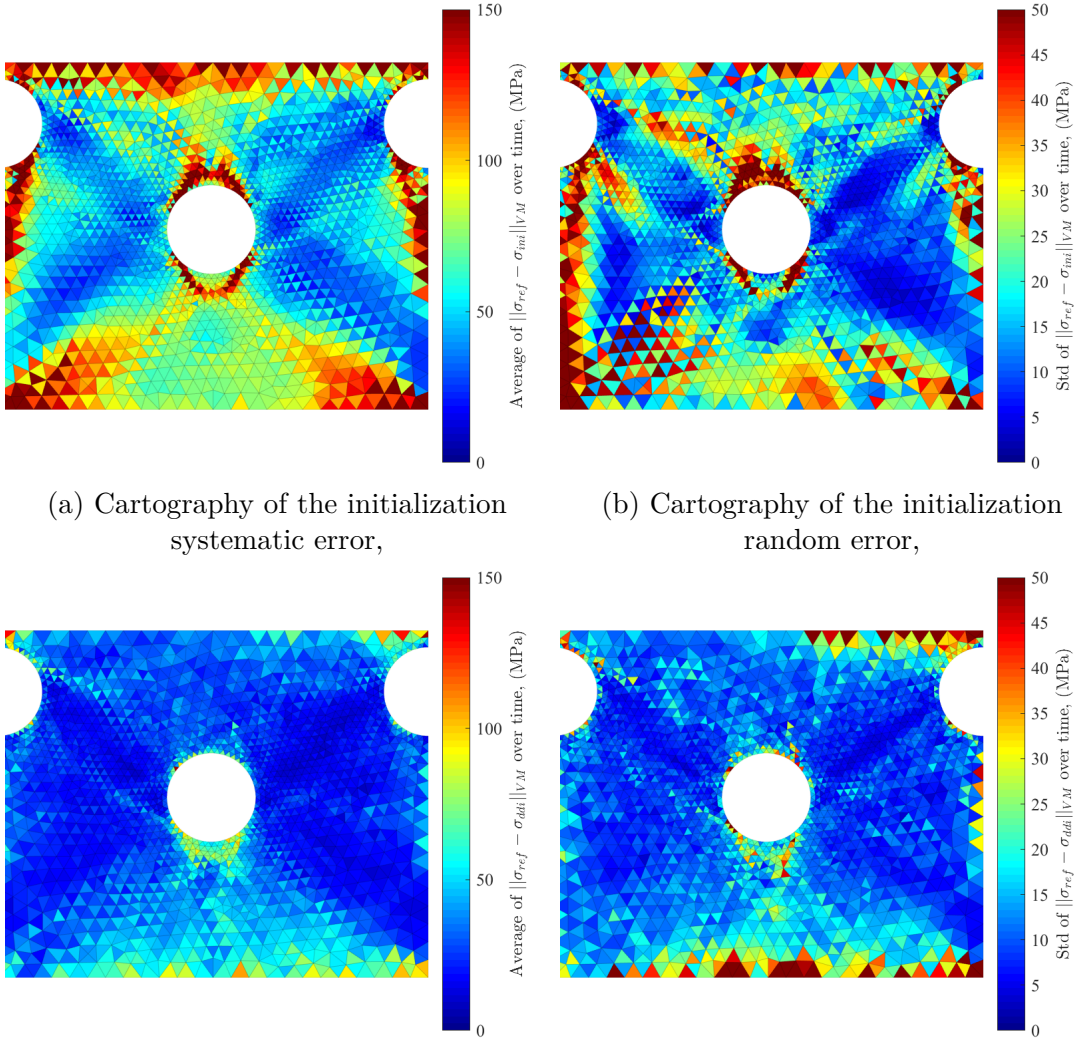

(a) Cartography of the initialization systematic error,

(b) Cartography of the initialization random error,

(c) Cartography of the DDI systematic error,

(d) Cartography of the DDI random error,

Figure 8.10: Temporal systematic and random errors of each element of the mesh. The errors are computed for both the initial stress fields and the ones obtained with the DDI.

dependency. Indeed, for a given value of strain, the error increases with the strain-rate which indicates that the two models have different strain-rate dependencies. Through Fig. 8.12b, the impact of the algorithm can be clearly seen. Indeed, the overall relative error decreased below 10 %. In addition, this figure shows that the proposed algorithm was able to accurately capture the strain-rate dependency: the error do not increase systematically with the strain-rate anymore. Moreover, the method also corrected the error induced by the difference of initial yield stress since the error for low values of strain and strain-rates decreased. However, it can be noted that errors are still important for very low values of strain (when the mechanical states are near an elastic state).

To further investigate the ability of the DDI method to capture the strain-rate dependency, stress-strain curves can be plotted for different average strain-rates (see Figure. 8.13a). To plot such a figure, the average strain-rate over time for each element is

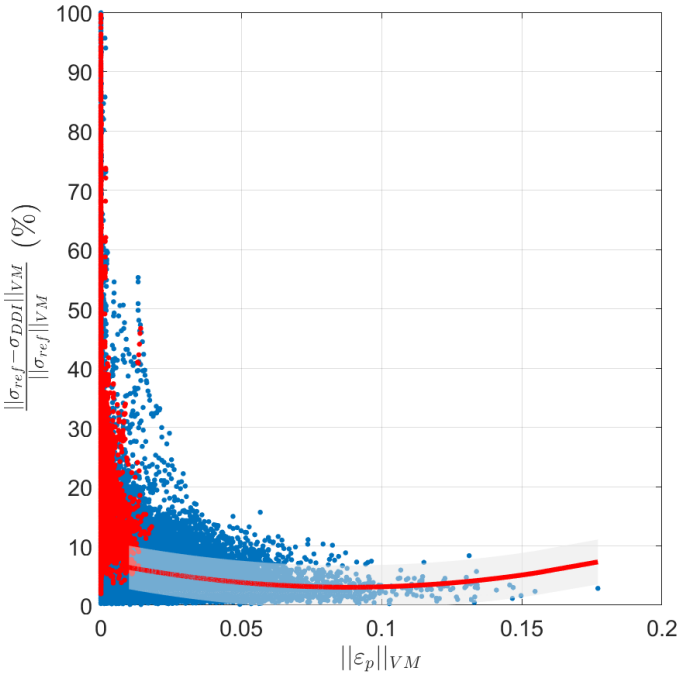

Figure 8.11: Relative error of the stress estimation for the selected mechanical states in function of the Von-Mises norm of the plastic strains. The red line is the quadratic fit of the data presented for $|||\varepsilon_p||_{VM} \geq 0.01$ and the grey area represents one standard deviation of the fit. The red points represent the mechanical states under compression ($I_1 \leq 0$) and the blue points represent the states under tension ($I_1 \geq 0$).

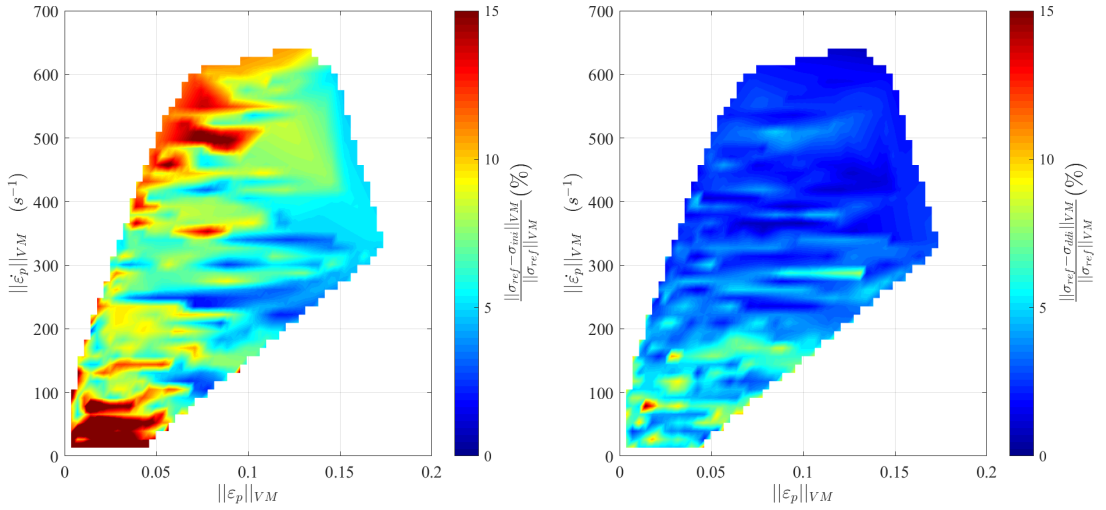

(a) Cartography of the relative initialization error,

(b) Cartography of the relative DDI error,

Figure 8.12: Comparison of the relative error cartographies between the reference solution and respectively, the initial solution or the DDI solution.

computed[1]. Then, using a clustering algorithm (here k-means), these average strain-rates

1. Note that this computation is performed only on the selected mechanical states, *i.e.* for a given element this average is computed only for the temporal time steps at which it is selected.

are regrouped in 10 clusters. The stress-strain curves are then obtained by averaging the stresses and strains for each cluster. Figure. 8.13b then shows the relative stress errors at $||\varepsilon_p||_{VM} = 0.002$ and 0.05 for the 10 average strain-rates. The circles depict the FE solution using model B, while the stars depict the DDI solution. First, Figure 8.13a evidences that a strain-rate sensitivity naturally emerges from the DDI solution. The material hardens more and more with the strain-rate. This is obtained when using the initial guess obtained with model B — which has, as already said, almost no rate sensitivity — as input to the DDI algorithm. This can be observed on Figure 8.13b. Indeed, in this figure we retrieve the fact that model A (the reference) and model B have different strain-rate dependencies. This is especially highlighted by the relative error at 5 % strain. Indeed, using model B, the error increases up to a relative error of -11 % with the strain-rate, while the DDI solution remains quasi-constant with an error around 1 %. In addition, the initial yield stress, represented by the curves for 0.2 % strain, is also better captured by the DDI. Indeed, the use of DDI allows to reduce the stress relative error lower than 5 %.

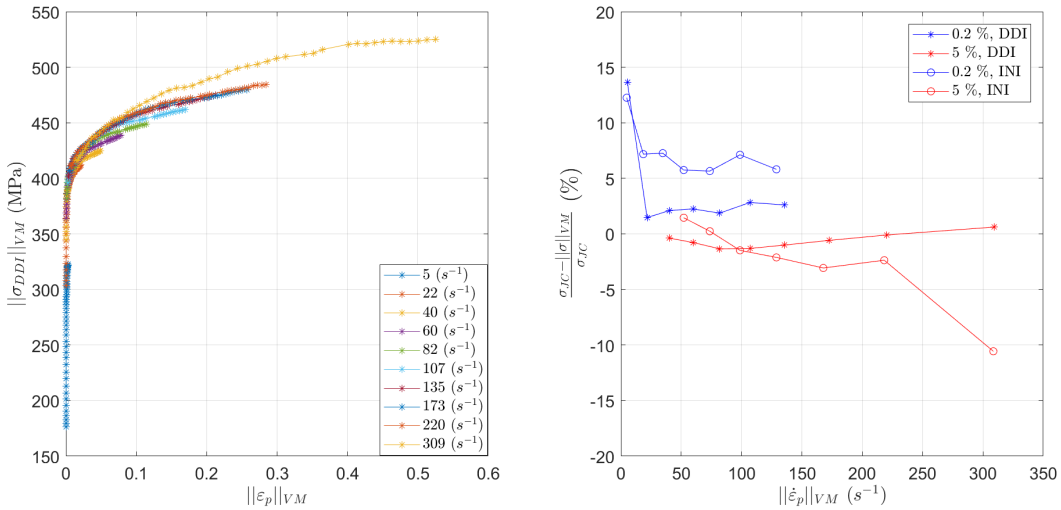

(a) Stress-strain curves for different averaged strain-rates obtained in one experiment,

(b) Relative stress error evolution with the strain-rate, computed at different strains, using the DDI solution or FE solution,

Figure 8.13: Assessment of the DDI impact on stress-strain curves for different averaged strain-rates, using a numerical test case.

At last but not least, it is also of interest to consider the DDI relative error distribution in the space of the stress tensor invariants. For this reason, Figure 8.14 depicts the DDI error in the space I_1 versus $\|\boldsymbol{\sigma}\|_{VM}$. In addition, a few classical stress states are represented by lines on the figure. This figure shows that the error committed by the method remains below 10 % for uniaxial tension states or in its vicinity as well as when the stress is higher than 200 MPa, *i.e.* when a reasonable amount of material states maps the space considered and when plasticity occurs. When the sample undergoes compression, the error reaches about 30 %. This can be explained by the sparsity of data for these states but also

the very small strain experienced by them, as illustrated by the figure with the material states superimposed.

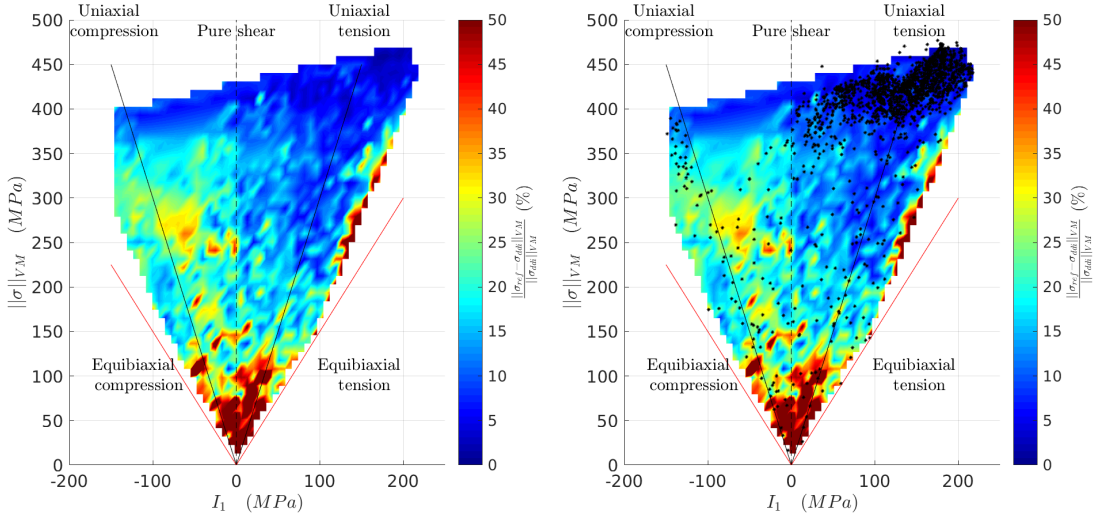

(a) Distribution of the DDI relative error in the space of the stress tensor invariants.

(b) With the selected material states in black,

Figure 8.14: Distribution of the DDI relative error (in %) in the space of the stress tensor invariants with the selected material states in black.

To summarize, the use of the proposed algorithm lead to a significant reduction of the systematic and random errors, both spatially and temporally compared to the FE initialization using model B. Furthermore, the algorithm is able to retrieve the sought material strain-rate dependency, despite the use of a very little rate-dependent material for the stress initialization. These observations underline the relevance of the use of such an algorithm for the behaviour characterization of a material. In addition, the importance of the heterogeneity of the test is highlighted: the material behaviour is properly characterized for stress states well mapped by the experiment. Finally, the DDI stress estimation accuracy is estimated to be about $5.4\,\% \pm 3.7\,\%$ (relative error). Moreover, when considering stress-strain curves for different averaged strain-rates, the DDI is able to retrieve the initial yield stress and the hardening modulus with a relative error below $5\,\%$.

8.3.3.3 Analysis of the material states

For the moment only the mechanical states have been presented and investigated. However, another output of the algorithm is also the set of material states. As explained in the Section 8.2, these material states can be interpreted as a sampling of the strain-stress and their first derivatives manifold. It results that the investigation of the manifold described by these points is of interest when modelling is the main target and a raw probing of the

local stress response is not desired.

Similarly to what is done previously, Figure 8.15 depicts the comparison of the reference solution and the material states in two projections of the constitutive space ($\|\boldsymbol{\varepsilon}_p\|_{VM}$, $\|\dot{\boldsymbol{\varepsilon}}_p\|_{VM}$, $\|\boldsymbol{\sigma}\|_{VM}$). The figure clearly shows that the set of material states samples the reference solution with a spread of about 25 MPa. In addition, Figure 8.16 depicts the relative error cartography between the reference solution and the manifold described by the set of material states obtained with the DDI. Indeed, using the selection matrices $(\mathcal{S}^j)_j$, the reference solution and the material states can be compared directly for each element and time step. Then, these sparse data are projected on a regular grid for visualization purposes. This cartography also highlights the ability of the material states to accurately represent the material behaviour (here given by the reference solution). Indeed, the average relative error is below 5 %. The error remains important ($\geq$ 10 %) for low values of strain and strain-rate as expected.

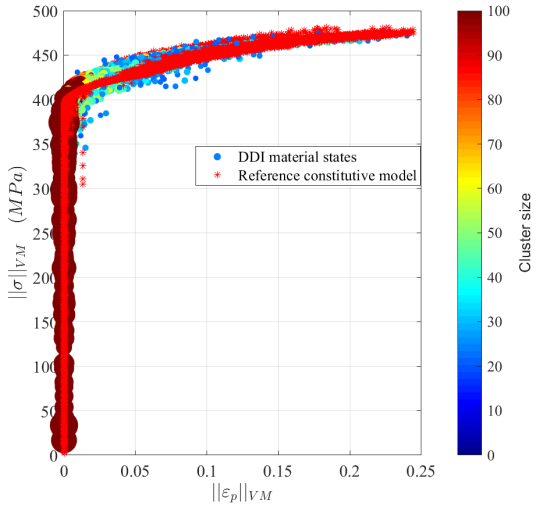

Figure 8.15: Comparison of the DDI material states versus the reference solution (in red) in one projection of the constitutive space ($\|\boldsymbol{\varepsilon}_p\|_{VM}$, $\|\boldsymbol{\sigma}\|_{VM}$). The marker size and colour for the DDI output are related to the size of the cluster. Only the selected clusters are represented.

As a conclusion, the Data-Driven Identification method that is proposed yields two main outputs which usages are different. The first output presented in this work is the corrected stress fields. These fields are of interest to probe without any *a priori* the local stress response of the material. These values are obviously more noisy but can deviate locally from the global smooth manifold, potentially giving access to local material heterogeneities. On the other hand, the DDI method also gives material states that can be interpreted as a sampling of the manifold that is a discrete version of a potential constitutive equation. As a consequence these points best represent the global response of the material, however they do not comply to the equilibrium. As a summary, Figure 8.17 depicts several cartographies of the method's error. These cartographies show where the

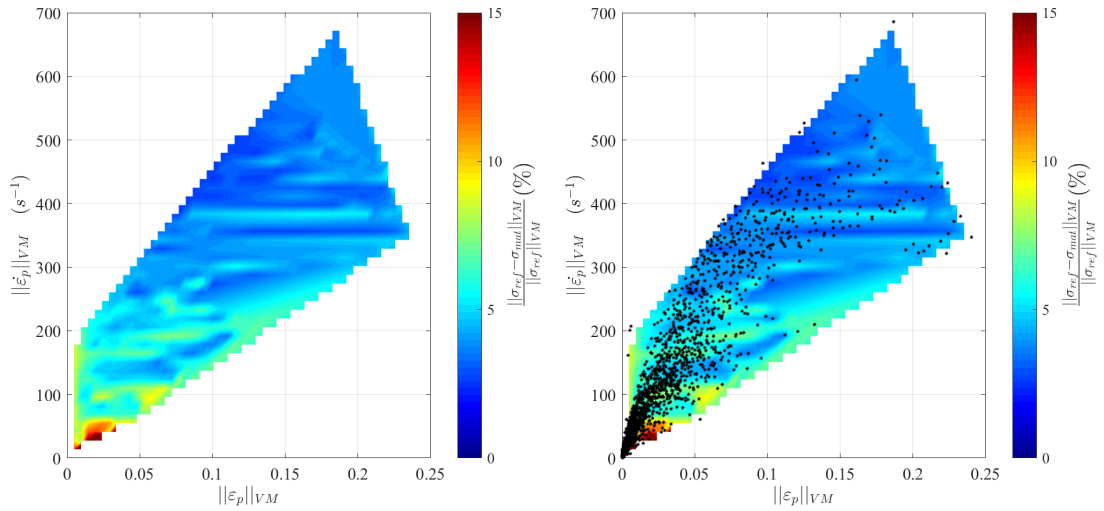

(a) Error cartography between the reference and the material states,

(b) The material states are superimposed with black markers,

Figure 8.16: Error cartographies between the reference solution and the DDI material states. The material states are superimposed with black markers on the second one. Only the selected clusters are represented.

data lead to confident stress estimation in respectively, the specimen's geometry, the strain versus strain-rate space for both the mechanical and material states as well as in the stress invariant space which denotes the stress state of the mechanical states.

Note that for the cartographies presented in this section, the data are sparse and then projected on a regular grid for visualization purposes. Hence, some points may be missing and some others are obtained after an interpolation. In addition, it is important to note that since the cartographies are projections in different spaces, some data represented in one figure may not appear clearly in the other one. For example, the stress errors higher than 80 MPa in compression that can be observed in Fig. 8.17d are hardly represented in Fig. 8.17b since they are related to points in the elastic domain, which is nearly not depicted in the later cartography. At last but not least, the cartographies presented here are not intrinsic to the method but are test case dependent. For instance, in the chosen test case configuration, the constitutive space is sparsely sampled with a database sampling more uniaxial tension, and some loadings closely related. In that context, the stress identification perform well only in these regions.

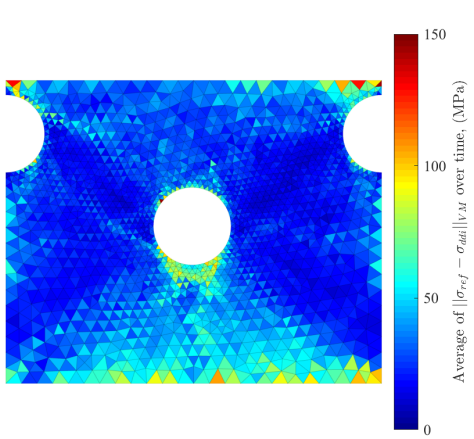

(a) Spatial cartography of the error,

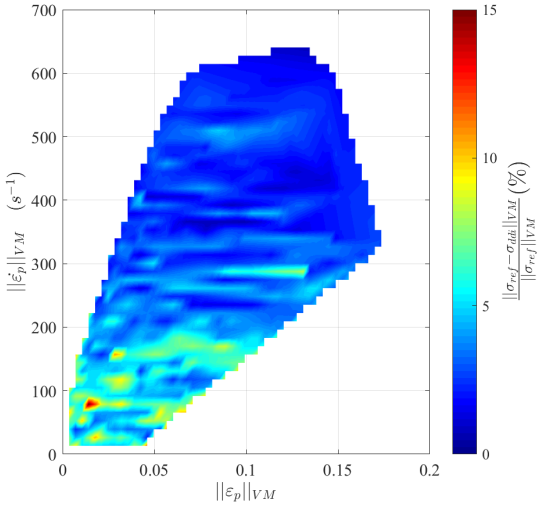

(b) Cartography of the relative error in $(\|\boldsymbol{\varepsilon}_p\|_{VM}, \|\dot{\boldsymbol{\varepsilon}}_p\|_{VM})$ for mechanical states,

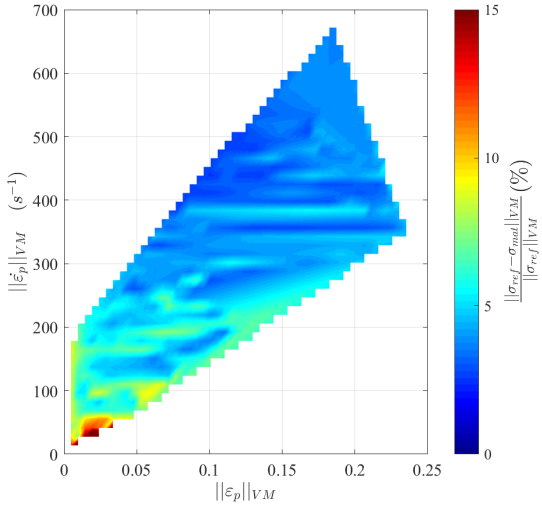

(c) Cartography of the relative error in $(\|\boldsymbol{\varepsilon}_p\|_{VM}, \|\dot{\boldsymbol{\varepsilon}}_p\|_{VM})$ for material states,

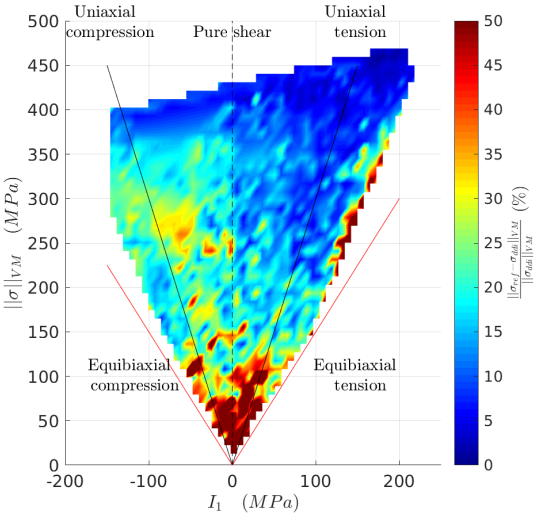

(d) Cartography of the relative error in $(I_1, \|\boldsymbol{\sigma}\|_{VM})$ for the mechanical states,

Figure 8.17: Cartographies of the stress estimation error in respectively, the geometrical space, the strain versus strain-rate space for mechanical and material states, and then in the stess invariant space.

8.4 Uncertainty estimation using data with noise

In the previous section, the accuracy of the Data-Driven Identification method has been assessed using a perfect numerical test case. In particular, the kinematic fields used are not affected by the systematic and random errors that exist experimentally. Thus, the accuracy previously obtained is a lower-bound of the experimental accuracy that can be achieved with DDI.

In order to better take into account such source of errors, the experimental displacement fields and the experimental mesh are used to virtually deform images. Through the

use of the VID procedure, kinematic fields are obtained on a coarser mesh. The same procedure as for the numerical test case is then followed, where U^{imp} becomes the VID kinematic fields, and more importantly, U^{ref} becomes also the VID kinematic fields, so that the kinematic fields used in the DDI are affected by experimentally representative systematic and random errors. Hence, this procedure will allow to assess the DDI stress estimations accuracy when using experimental data.

Similarly to what is done in the previous section, Figure 8.18a shows the stress relative error for the selected mechanical states in function of the Von-Mises norm of the plastic strain. The red line in the figure depicts the quadratic fit for all the data with a plastic strain above 0.01, while the grey area represents one standard deviation of the error made by the fit. This shows that, *in fine* the Cordin-based DDI is accurate to $12.6\,\% \pm 13.3\,\%$. Moreover, Figure 8.18b shows the DDI relative error in the space I_1 versus $\|\boldsymbol{\sigma}\|_{VM}$. This figure shows that the introduction of noise in the kinematic fields mainly affects the stress estimations for low values of stress ($\leq 200\,\text{MPa}$, *i.e.* for low values of strains) and for compression states. Indeed, when the sample is under uniaxial tension and for stresses above 200 MPa, the errors stay in the same level as the one estimated previously ($\leq 10\,\%$).

Moreover, in the same manner as in the previous section, Figure. 8.19a shows 10 stress-strain curves obtained for different averaged strain-rates. Figure. 8.18b then shows the relative stress errors at $||\varepsilon_p||_{VM} = 0.002$ and 0.05 for these strain-rates. The circles depict the FE solution using model B, while the stars depict the DDI solution. In this figure, it can be observed that the curves obtained for both the FE solution and the DDI solution follow the same trends. The relative errors obtained for the DDI in this case are lower than $10\,\%$.

To summarize, by using kinematic fields from VID, one can assess the experimental accuracy that can be obtained using the Data-Driven Identification method for our sample geometry, loading conditions and camera. The DDI leads to stress estimations with a relative error of about $12.6\,\% \pm 13.3\,\%$. However, it is able to recover the initial yield stresses and hardening modulus with an accuracy of $5\,\%$ for different strain-rates. Furthermore, the inverse identification is most accurate for mechanical states under uniaxial tension, which represent most of the mechanical states using the chosen geometry.

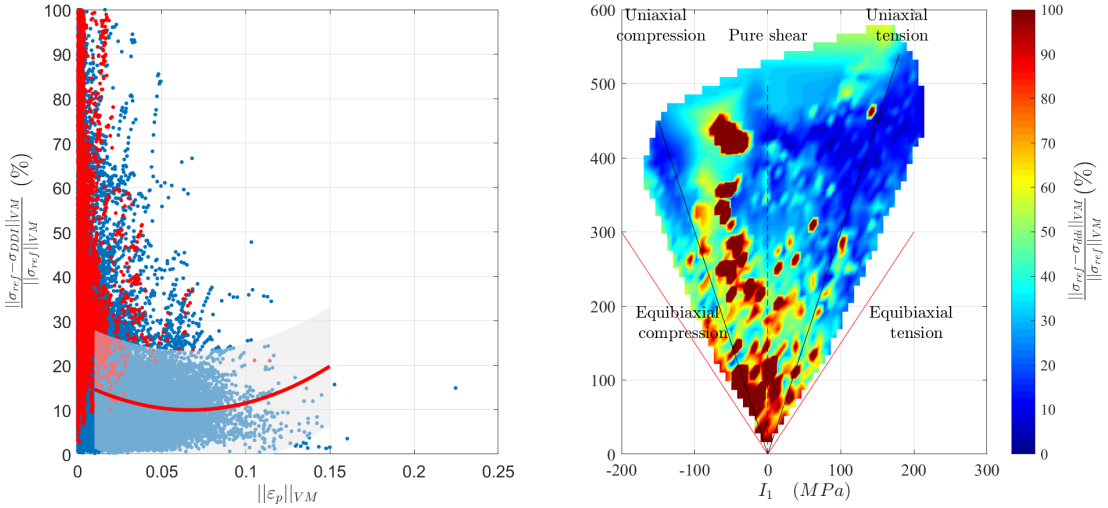

(a) Relative error of the stress estimation in function of $||\varepsilon_p||_{VM}$,

(b) Cartography of the relative error in $(I_1, \|\boldsymbol{\sigma}\|_{VM})$,

Figure 8.18: Estimation of the DDI accuracy when using realistic kinematic data (with noise). The relative error of the stress in function of $||\varepsilon_p||_{VM}$ is plotted, as well as its cartography in the stress invariant space.

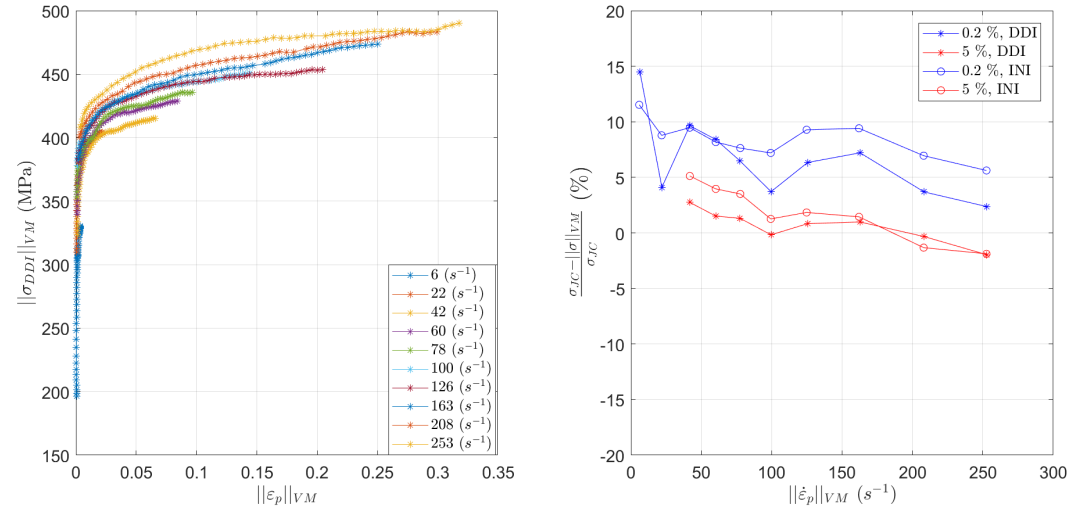

(a) Stress-strain curves for different averaged strain-rates obtained in one experiment,

(b) Relative stress error evolution with the strain-rate, computed at different strains, using the DDI solution or FE solution,

Figure 8.19: Assessment of the DDI impact on stress-strain curves for different averaged strain-rates, using data with noise from VID.

8.5 Conclusion

In this chapter, the Data-Driven Identification algorithm problem formulation is presented. The resolution strategy implemented to solve this problem is also presented. To assess the ability of the proposed method to retrieve stress fields accurately, a numerical

test case is first investigated. The main conclusions are as follows:

- The parameters of the DDI method play an important role in the stress reconstruction. The analysis performed on the numerical test case lead to the selection of these parameters.
- The numerical test case illustrates the ability of the proposed methodology to retrieve the material behaviour despite the use of a wrong set of constitutive parameters as initialization. It showed in particular that the algorithm is able to retrieve the material's strain-rate dependency accurately.
- The accuracy of the stress field estimations is $5.4\,\% \pm 3.7\,\%$ (relative error). Note that these values are lower bound since the kinematic fields used for the numerical test case are noisefree. Using the results from Virtual Image Deformation, the impact of noise on the stress estimation can be assessed. An accuracy of $12.6\,\% \pm 13.3\,\%$ is obtained on the stress estimation. At last, using the DDI Data to perform identification leads to relative errors lower than $10\,\%$.

Experimental application to the XES characterization campaign

The DDI algorithm has been presented and then applied to a numerical test case in the previous Chapter. In addition, the level of uncertainty related to strain level, strain-rate and loading scenario in the test sample have been estimated. Now the proposed method will be applied to the data obtained during the XES characterization campaign that is presented in Part II. The performance of the proposed methodology will be discussed as well as the intrinsic limitations of the method, of the material as well as the geometry chosen.

9.1 Methodology

The experimental procedure for the DDI is very similar to the one presented in Fig. 8.1. In this case, the experimental data replace the one obtained from the first simulation of the numerical test case. Hence, the reference displacement will become the one obtained through the use of DIC during the experiment. The load that will be used to rescale the load profile is the one captured by the load cell during the dynamic tensile test adjusted following the method presented in Section 7.2.

The DDI requires two FE simulations to be performed, the material model chosen for the initialization is the Johnson-Cook model and the parameters used are the one identified on the raw data from ONERA (*i.e.* the model A from the numerical test case). The DDI parameters that will be used for this procedure are the one defined previously, they are recalled in Tab. 9.1.

Criterion on $(\mathcal{S}^j)_j$	5×10^{-3}
Criterion on $(\underline{\mathbf{d}\boldsymbol{\sigma}}_e^j)_{j,e}$	5×10^{-3}
r^*	50
E_o	210 GPa
ν_o	0.29
Number of images	50
Outliers criteria	40 % of r^*
	$\pm$ 1 std of $\|\|\|_r$

Table 9.1: Parameters of the DDI procedure for the experimental application.

The choice of the selection criterion leads to the disregarding of 28.5 % of the mechanical states and 26.5 % of the material states. Similarly to what is done in the previous section, Figure 9.1 depicts the selected elements cartography with in colour their selection frequency. Similarly to the numerical test case, the most disregarded elements are located near the hole and notches. In addition, some elements in the bands are disregarded too when approaching the end of the test. This can be explained by the same reasons as for the numerical tests case: these elements are associated to small cluster near the end of the experiment when they reach high strain and strain-rate values, and hence are disregarded for these specific time steps.

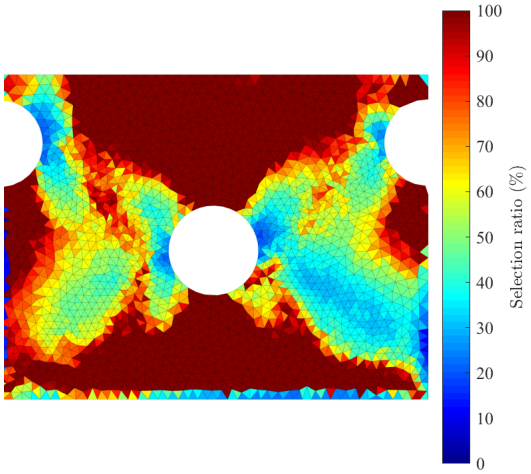

Figure 9.1: Cartography of the selected elements and their frequency.

9.2 DDI results and discussions

Once the DDI algorithm applied, the mechanical and material states are available. From these states the Von-Mises norm of the stresses can be obtained. Figure 9.2 depicts the spatial cartographies of respectively the plastic strains, the Von-Mises stresses as well as the Von-Mises norm of the stress correction performed by the method for the three different time steps. The plastic strains are obtained using Hooke law, plane stress, the plastic incompressibility and the small strain assumption. The elastic properties are identified from the reference data for the XES steel. The cartography of the Von-Mises stresses of the last image (Fig. 9.2f) shows that, as expected, the notches and the central hole create stress concentration bands. In these bands the Von-Mises stresses reach about 500 MPa. In addition, in the secondary bands, the stress is about 400 MPa. Furthermore, Fig. 9.2i shows that the DDI deviates from the initial guess the most around the notches and the holes, with substantial corrections since they reach up to 200 MPa. However, since these corrections concern elements of the mesh near a hole, these number should be taken with precaution. Indeed, it stands for reason that the experimental kinematic fields are less

accurate in these regions, which may in turn have an impact on the stress retrieved with the DDI. In addition, it can be noted that the DDI also applies correction in the upper and lower region of the central hole, similarly to the numerical test case, where the sample is under compression.

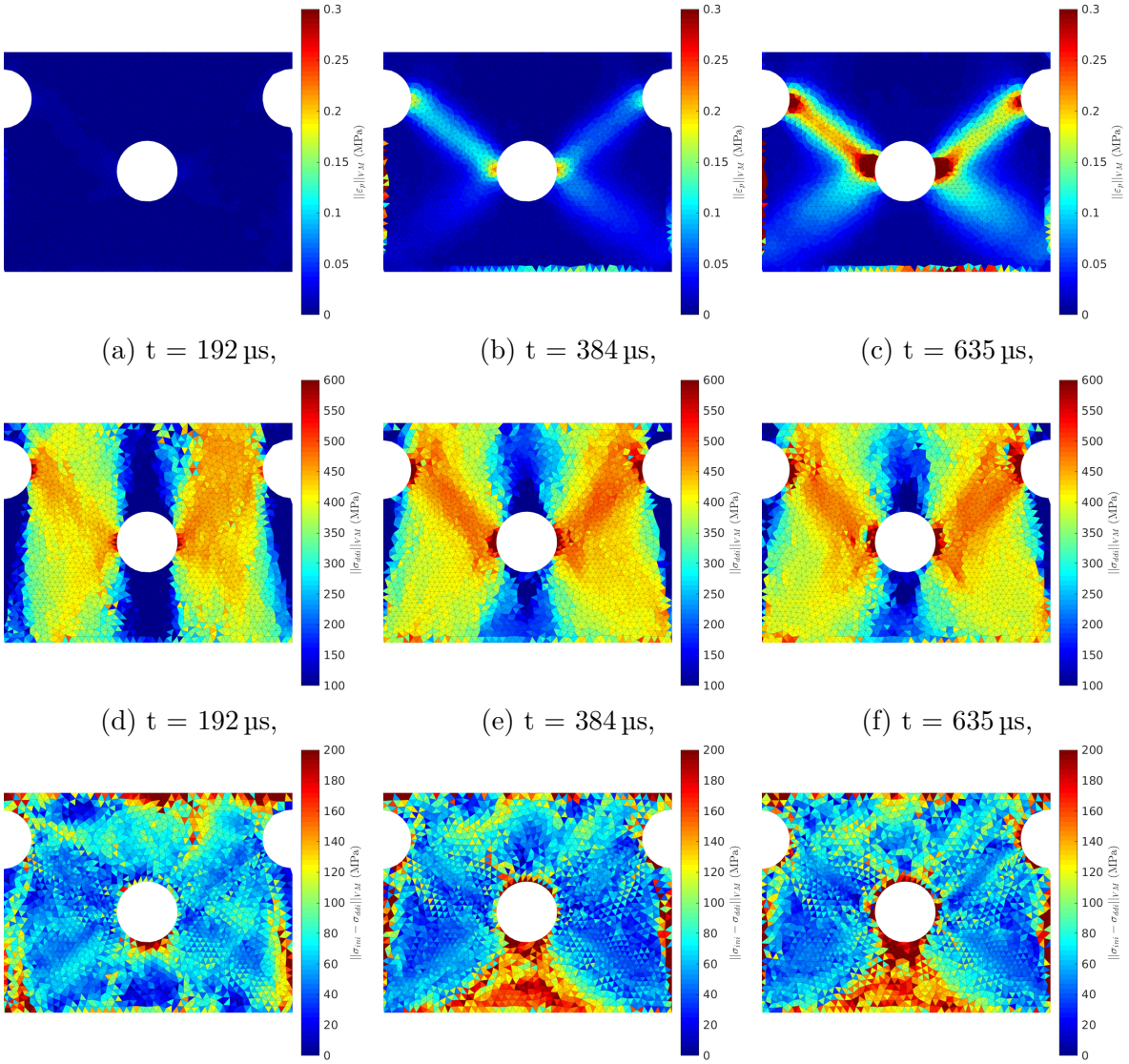

(a) t = 192 µs, (b) t = 384 µs, (c) t = 635 µs,

(d) t = 192 µs, (e) t = 384 µs, (f) t = 635 µs,

(g) t = 192 µs, (h) t = 384 µs, (i) t = 635 µs,

Figure 9.2: Cartographies of the plastic strains, stresses and their corrections performed by the DDI, for three different time steps.

Let us recall that the experiment was designed to provide different loading paths of the material and wide spectra of strain and strain-rates during a single test. Hence, Figure 9.3 enables the verification of these specifications. Fig. 9.3a depicts the stress distribution in the space $(I_1, \|\boldsymbol{\sigma}\|_{VM})$ for the selected mechanical states. It follows that this figure is an indicator of the stress triaxiality that occurs during the experiment. This figure shows that the sample is mainly under an uniaxial tensile state. However, some compression and shear states are reached within the specimen. In addition, Fig. 9.3b shows that the

strain and strain-rate spectra mainly seen by the specimen are [0 – 0.21] and [0 s^{-1} – 500 s^{-1}]. Nevertheless, some regions of the sample reach higher strain and higher strain rate values. Fig. 9.3a and Fig. 9.3b can be compared to the same figures obtained for the simulation performed in Part. II. These figures are recalled in Fig. 9.3c and 9.3d. The stress distribution obtained experimentally is consistent with the prevision of the simulations: we retrieve the fact that the sample is mainly under uniaxial tension, with some shear. However, the compressive and shear states predicted by the simulations are less represented than predicted. An explanation can be that the data presented in these figures are only from the selected elements. Hence, the selection criteria used may disregard the elements that are undergoing shear or compression. Moreover, the comparison with the strain and strain-rate distributions clearly highlights the fact that the criteria lead to a truncation of the spectra investigated. Nevertheless, the strain and strain-rate range obtained experimentally is consistent with the most occurring strains and strain-rates predicted by the simulations. In order to associate these states to a region in the sample, several elements located at different region of interest of the sample are selected (see Fig. 9.4c). The loading paths of these elements are depicted in the previous figures considered[1]. As it can be expected, the region above and below the hole (and by extension the notches) are under a compressive state. Moreover, as expected the elements in the band are mainly in an uniaxial tensile state. Fig. 9.4b clearly highlights that the different region of the bands are under different but quasi-constant strain-rates. This further justifies the specimen geometry since it clearly demonstrates that at least the results of uniaxial tensile tests performed at different strain-rates can be retrieved.

In the previous section (Section 8.3.3.3), the relevance of the material states is demonstrated. Indeed, these points best fit the behaviour of the material. Figure 9.5a depicts projection of the material states. The black and red line are the raw data from previous characterization of the XES steel performed at ONERA. These figures show that the spreading of the material states is more important on the experimental data than on the numerical test case. Let us also note that even after the selection of the clusters, some material states with singular behaviours are remaining. However, most of the material states remaining are still representative of the behaviour of the material. Indeed, the behaviour of the material at 70 s^{-1} from previous characterization is for instance well captured by the DDI method, in the same range of strain-rate (see the colour). This also confirms the fact that the material considered in this study, known to be strain-rate dependent, has a dependency which fades at about 100 s^{-1}. Indeed, the stress response variation from 100 s^{-1} to 500 s^{-1} is more packed than from 1 s^{-1} to 70 s^{-1}. Moreover, similarly to Fig. 8.19a, Figure 9.5b shows 10 stress-strain curves obtained for different averaged strain-rates, and the reference data are depicted by the dashed lines. The grey area around the

1. Note that the dots depicting the loading paths of the considered spatial elements were not "filtered": *i.e.* some dots may represent mechanical states that are discarded using the two selection criteria.

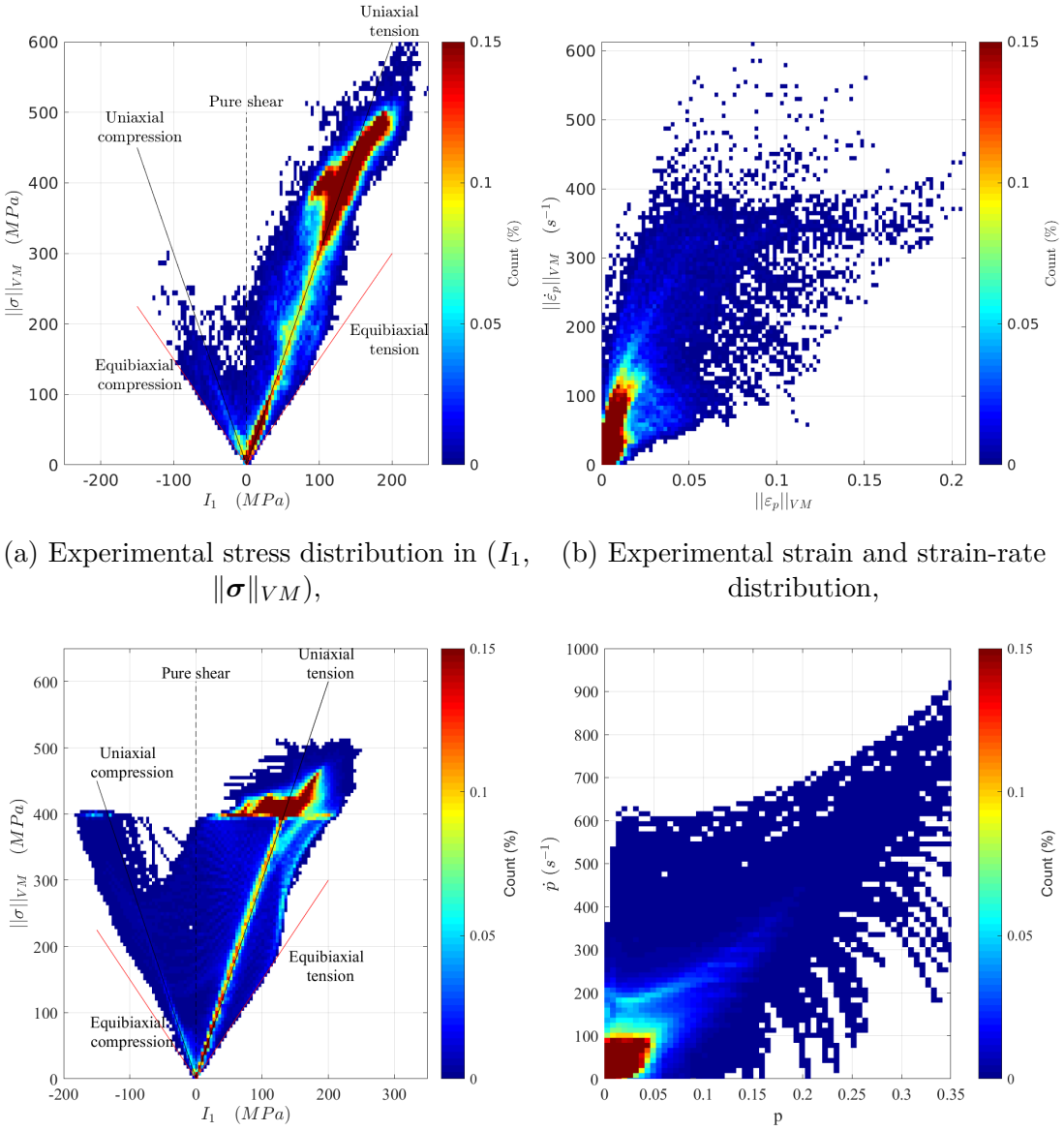

(a) Experimental stress distribution in (I_1, $\|\boldsymbol{\sigma}\|_{VM}$),

(b) Experimental strain and strain-rate distribution,

(c) FE stress distribution in (I_1, $\|\boldsymbol{\sigma}\|_{VM}$) from Chapter 6,

(d) FE strain and strain-rate distribution from Chapter 6,

Figure 9.3: Comparison between the stress distribution, strain and strain-rate distributions during the experiment and the ones predicted in Chapter 6.

dashed line represent a relative uncertainty of ± 10 %. This figure shows that the data obtained for an average strain-rate of 69 s^{-1} fit remarkably well the reference data at 70 s^{-1}. Nevertheless, when taking into account the uncertainty on the stress estimation from Section 8.4, the data from 41 s^{-1} to 194 s^{-1} are also in line with the reference data. In particular, the initial yield stresses as well as the hardening modulus obtained at these strain-rates are in line with the reference data. The figure also allows to confirm the fact that the strain-rate dependency fades off around 100 s^{-1}, and also confirms a softening of the material response for strains below 0.05 (see Fig. 9.6a). Furthermore, this figure can be compared to the stress-strain curves obtained in the literature [Haugou *et al.*, 2006],

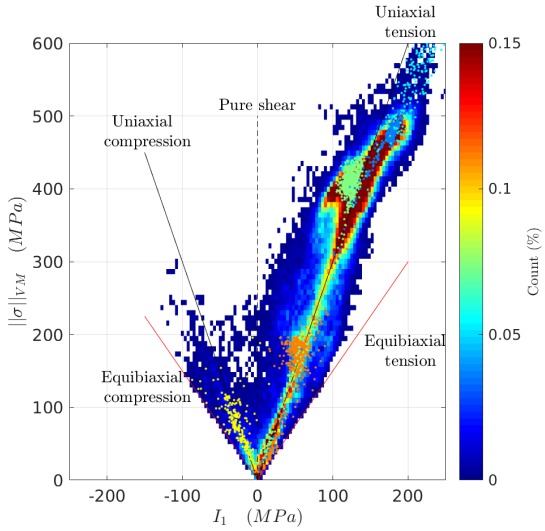

(a) Stress distribution with the loading path of selected elements,

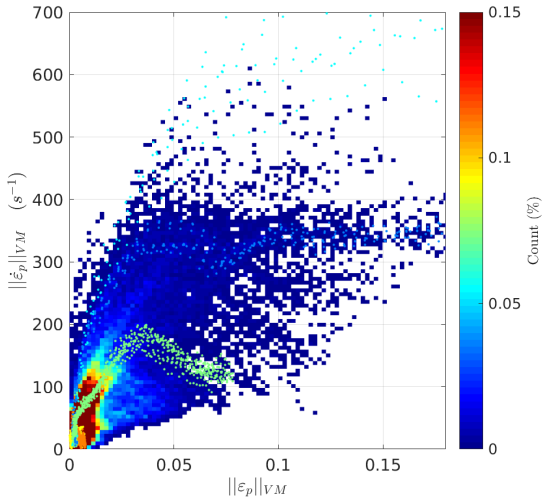

(b) Strain and strain-rate distribution with the loading path of selected elements,

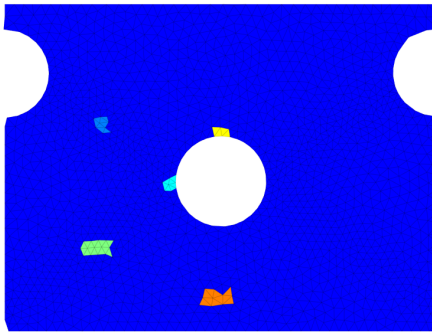

(c) DDI mesh and localization of the selected elements,

Figure 9.4: Stress distribution, strain and strain-rate distributions during the experiment for the selected mechanical states. The loading paths of a few selected elements are superimposed on these distributions.

that are recalled in Figure 9.6. While the DDI stress estimations are in line with our reference data from [Markiewicz *et al.*, 2016], they differ slightly from the ones in Fig. 9.6a. Indeed, while we observe (using DDI) a saturation of the yield stress and hardening at about $160\,\mathrm{s}^{-1}$ with a stress peak near 500 MPa, data obtained from [Haugou *et al.*, 2006] at $200\,\mathrm{s}^{-1}$, $360\,\mathrm{s}^{-1}$ and $440\,\mathrm{s}^{-1}$ show an increase of the peak stress up to 600 MPa followed by a massive softening. Nevertheless, Fig. 9.6b highlights the difficulty to have consistent results with different experimental apparatus at high strain-rates. Indeed, by using different techniques, the stress obtained at a plastic strain of 0.1 at a strain-rate of $500\,\mathrm{s}^{-1}$ has an uncertainty of about 50 MPa which represent a relative error of about 10 %. Regarding Figure 9.6b, one sees that our DDI results are closer to data obtained on SHPB or using the special apparatus designed by Haugou [Haugou *et al.*, 2006]. While the question of the reproducibility of the data using different experimental apparatus remains open, Fig-

ure 9.5b shows that DDI and a dedicated sample geometry allows to accurately capture, with a single apparatus, consistent elasto-plastic data from$30\,\mathrm{s}^{-1}$ to about $300\,\mathrm{s}^{-1}$.

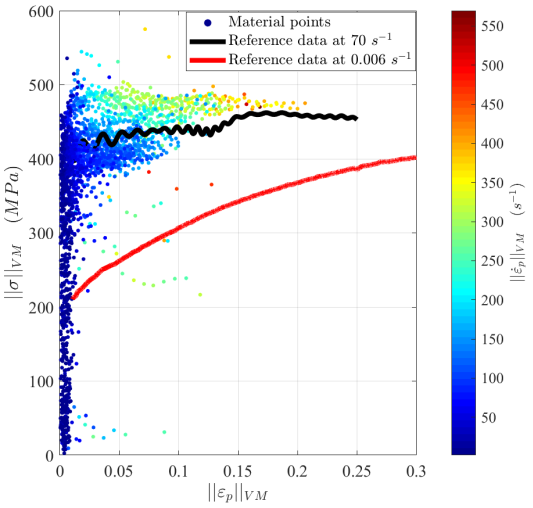

(a) Material states in $(\|\boldsymbol{\varepsilon}_p\|_{VM}, \|\boldsymbol{\sigma}\|_{VM})$. The colour of the markers denote the strain-rates, while the lines denote the reference data from ONERA,

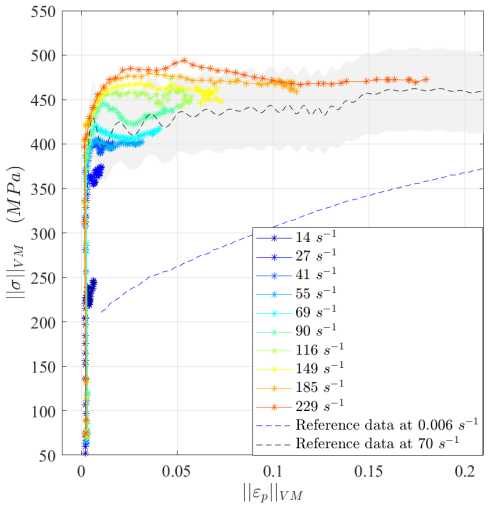

(b) Stress-strain curves for different averaged strain-rates extracted from the selected material states during one experiment,

Figure 9.5: Material states in the space$(\|\boldsymbol{\varepsilon}_p\|_{VM}, \|\boldsymbol{\sigma}\|_{VM})$ as well as stress-strain curves for different averaged strain-rates obtained during one experiment.

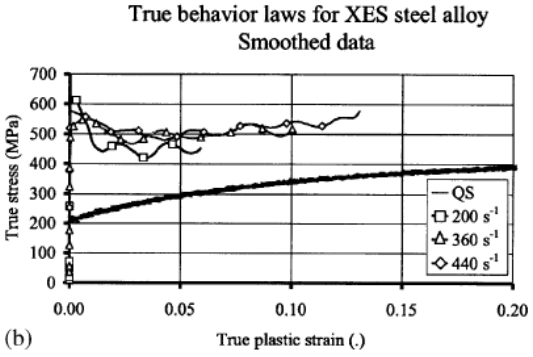

(a) Stress-strain curves obtained for the XES for different strain-rates from [Haugou *et al.*, 2006],

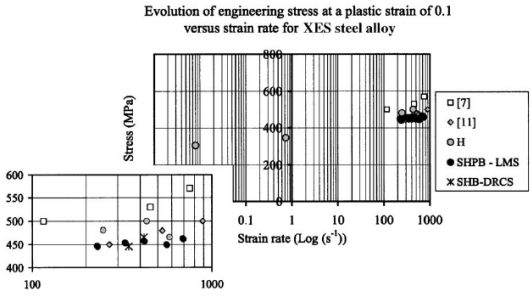

(b) Evolution of the stress at a plastic strain of 0.1 in function of the strain-rate using different techniques, from [Haugou *et al.*, 2006],

Figure 9.6: XES characterization data from [Haugou *et al.*, 2006] and comparison of the results obtained using different experimental techniques.

The material states obtained using this DDI method can also be compared to the stresses predicted by the modified Krupkowsky model that better fits the non-linear strain-rate dependency of the XES steel than the Johnson-Cook model. Since neither the material states nor the direct estimation of Krupkowsky stress from experimental

strains and strain-rates will verify the equilibrium, the comparison can be considered as fair. Hence, Figure 9.7 displays three cartographies of the difference between the stresses predicted by Krupkowsky and the material states: the first one is in the $(\|\boldsymbol{\varepsilon}_p\|_{VM}, \|\dot{\boldsymbol{\varepsilon}}_p\|_{VM})$ space with marker to denote the position of the material states. The second one depicts the discrepancy but in the stress invariant space while the last one is the spatial cartography of the discrepancy. Since the modified Krupkowsky model describes the plastic flow, it is not able to predict stresses in elasticity. Hence, the discrepancy cartography in the stress invariant space only holds meaning in plasticity. This is why this cartography is truncated for values of stresses higher than $200\,\mathrm{MPa}$[2]. It can be observed on the first cartography that the stress discrepancies are mainly higher than $10\,\%$ in two zones: for low values of strain combined with high values of strain-rates and for a specific horizontal band at a strain-rate of about $250\,\mathrm{s}^{-1}$. As it was shown earlier with Figure. 9.4, the first zone is mainly experienced by the elements near the hole (*e.g.* the light blue points), and thus the strain-rates and stress values have to be taken with precautions. In addition, this zone is also associated with few clusters of data, which also explains the significant discrepancy. Indeed, Fig. 9.7a clearly highlights the influence of the cluster distribution on the discrepancy: the more data is available in a region, the lower the discrepancy is. However, no clear explanations was found to explain the second zone of significant error located around $250\,\mathrm{s}^{-1}$. Indeed, this zone is described by several material points as illustrated by Fig. 9.7a. Let us note that apart from the two regions described, the discrepancies remain within the accuracy interval observed for states subjected to uniaxial tension in Section 8.4 which further comforts the relevance of the DDI stress estimations. Moreover, the spatial cartography shows that the discrepancies are mainly located near the notches and the central hole: where the stresses are estimated less accurately using the chosen geometry. At last, the cartography of the difference between the prediction using the modified Krupkowsky model and the DDI results in the stress invariant space is in quite good agreement with the one obtained in Section 8.4. Indeed, this figure shows that the DDI method is able to match the predictions from the constitutive model when the material is under uniaxial tension, within a relative discrepancy of about $10\,\%$. All these results comfort the fact that the modified Krupkowsky model, even calibrated over 3 uniaxial curves, is able to extrapolate well at higher strain-rates and when we slightly deviate from its validity loading configuration domain.

Furthermore, the material states obtained with the DDI can be used in a more conventional way to identify constitutive parameters. Parameters are identified using the material states (without the outliers) obtained in this work. Since these states do not

2. *Nota Bene*: a criterion based on the plastic strain (*e.g.* a threshold at 0.005) would have been more pertinent. However, in our case, some edge effects would remain and thus add non relevant information in the figure.

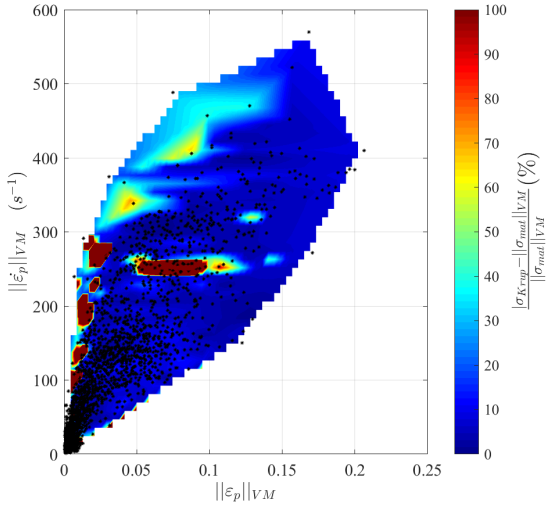

(a) Cartography of the relative error in $(\|\boldsymbol{\varepsilon}_p\|_{VM}, \|\dot{\boldsymbol{\varepsilon}}_p\|_{VM})$, with the cluster distribution superimposed,

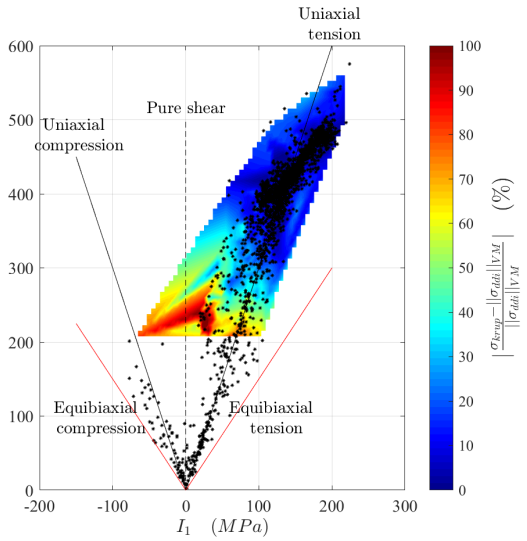

(b) Cartography of the relative error in the stress invariant space using material states,

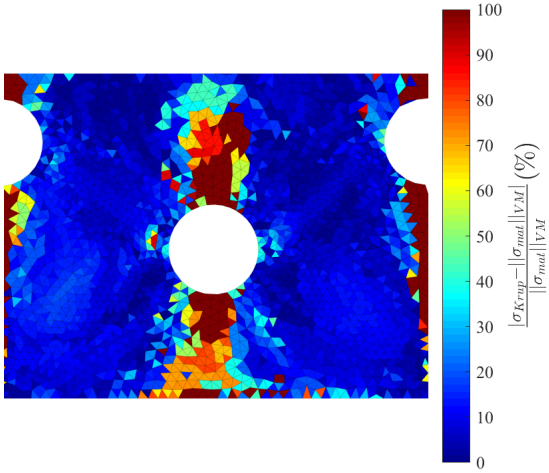

(c) Spatial cartography of the discrepancy between the prediction and the material states at the last image,

Figure 9.7: Comparison between the stress predictions using the modified Krupkowsky model and the material states from the DDI.

contain quasi-static data, the quasi-static data from ONERA is also taken into account, in order to ensure that the parameters identified characterize the material from quasi-statics to high strain-rates. The identification is performed for strains higher than 0.01. The parameters obtained are presented in Tab. 9.2, which also recall the parameters identified in Section 6.2.2.2. As in Section 6.2.2.2, strong variations are observed in particular for exponent c. In addition, ε_0, $\dot{\varepsilon}_0$ and b, which capture the strain-rate dependency, also differ significantly from the reference parameters ($\geq 40\,\%$). Nevertheless, by checking the discrepancies between reference data from ONERA and the modified Krupkowsky model based on the updated parameters using DDI stresses (see Fig 9.8), one observes that the

reference data are capture within 6–7 % of relative error for the quasi-static response and the one at $70\,s^{-1}$. In addition, the data are capture within 10 % for the intermediate response ($0.67\,s^{-1}$). This indicates that the model has a weak sensitivity to its parameters, and also that its 7 parameters can be recovered from only 2 tests: a quasi-static one, and a heterogeneous and high strain-rates one.

Parameters	K (MPa)	ε_0	n	$\dot{\varepsilon}_0$ (s^{-1})	a	b	c
Section 6.2.2.2	544.5	0.032	0.259	0.06	0.0002	0.328	0.0002
This work + QS data	532.0	0.0133	0.2373	0.1391	0.0002	0.4639	0.0038
Relative variation (%)	2.3 %	58.5 %	8.4 %	−131.8 %	0 %	−41.4 %	−1800 %

Table 9.2: Comparison of the modified Krupkowsky model parameters identified using data from ONERA or from this work combined with quasi-static data from ONERA.

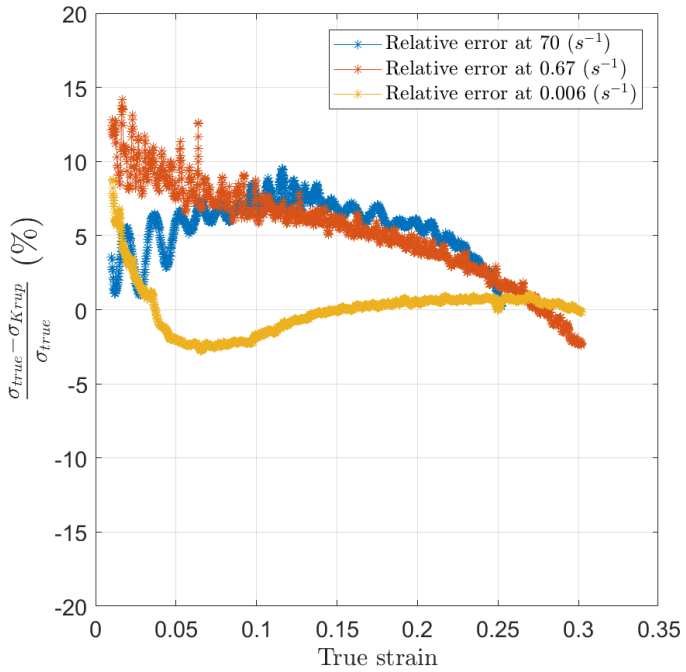

Figure 9.8: Relative errors between the reference data and the fit using the identified parameters.

To summarize, the DDI method has been applied to the experimental data obtained in Part. II. The stress have been reconstructed. The stress distribution confirms that the sample is mainly under uniaxial tension during the experiment, but some regions are under compression and shear (the region above and below the hole and notches for instance). The strain and strain-rate spectra that the sample is submitted to are [0 – 0.21] and [$0\,s^{-1}$ – $500\,s^{-1}$]. Furthermore, the DDI algorithm is able to retrieve the behaviour identified during previous characterization campaigns. In particular, using the material states and

data from a simple quasi-static test, constitutive parameters can be identified for the modified Krupkowsky model, which allow to retrieve the behaviour with a relative error below 10 % for strain-rates from $0.01\,s^{-1}$ to a few hundreds of s^{-1}. At last but not least, based on the accuracy assessment performed in the previous section and a comparison with the predictions of the modified Krupkowsky model, this model's stress predictions can be considered with confidence even when extrapolated for higher strain-rates than the ones used to calibrate it.

9.3 Towards energy balance

One way to study localization phenomena is through energy balance considerations. Following the seminal work of Taylor and Quinney [Taylor and Quinney, 1934], a lot of effort has been put into the study of materials through energy considerations [Chrysochoos *et al.*, 1989, Oliferuk *et al.*, 2004, Berthel, 2007, Seghir, 2012]. Nevertheless, the realization of energy balances for localization phenomena such as adiabatic shear bands remains a challenge. While the realization of full local energy balances falls out of the scope of this PhD work, an estimation of the energy released and stored in the experiment will be performed through the computation of the Taylor-Quinney ratio using experimental data. This ratio was first introduced in [Taylor and Quinney, 1934], and was estimated to be constant and about 90 % for metals. The determination of this ratio is important to understand the thermomechanical behaviour of materials. Hence, efforts have been put in the study of the Taylor-Quinney ratio. In particular, recent works demonstrated that this ratio often considered as constant, for simplicity's sake, varies with the plastic strain [Rittel, 1999, Macdougall, 2000, Vazquez-Fernandez *et al.*, 2019]. Furthermore, by studying several metals, Knysh and his co-authors [Knysh and Korkolis, 2015] showed that this ratio can vary from 0.3 to 0.8, which is lower than the traditionally used value of 0.9. Moreover, in [Rittel *et al.*, 2017] the dependency of this ratio to the loading mode has been evidenced for several metals.

The principal difficulty of the cited works lies in obtaining stresses. In these works, in order to easily retrieve the stresses, the tests conducted are statically determined. In this work, with both the stress fields, the temperature fields and the plastic strains available for heterogeneous tests, a local estimation of the Taylor-Quinney ratio at high strain-rates can be obtained. Let us recall that the experiments realized in this work are adiabatic (see Appendix A). In addition, neglecting thermoelastic effects, that could not be retrieved experimentally anyway, the differential Taylor-Quinney ratio can be approximated by $\frac{\rho C \dot{T}}{||\sigma_{DDI}||_{VM}||\dot{\varepsilon}_p||_{VM}}$ [Vazquez-Fernandez *et al.*, 2019]. In the present case, $||\sigma_{DDI}||_{VM}$ is obtained by computing the Von-Mises norm of the mechanical stresses.

9.3.1 Accuracy of the Taylor-Quinney ratio estimation

Similarly to what is done in Section 8.4, let us begin by assessing the accuracy of the Taylor-Quinney ratio estimation using the data obtained in the mentioned section. Indeed, since the data come from FE simulations, the searched ratio is known and equal to 0.9. The DDI gives access to the stress fields and the plastic strains. In addition, the temperatures from the reference FE simulation will be used. In order to introduce temperature uncertainties similar to the one obtained experimentally, a random gaussian noise with a standard deviation of 300 mK (in line with the one found in Chapter 4) is added. Then, exactly like for the experimental temperatures, a Savitzky-Golay filtering kernel of order 2 with a window of 23 frames is used. Hence, the temperatures obtained can be considered representative of the experimental ones.

Figures 9.9a and 9.10b depict respectively the cartographies of $\rho C\dot{T}$ and $||\boldsymbol{\sigma}_{DDI}||_{VM}||\dot{\varepsilon}_p||_{VM}$ at t = 793 µs. These figures show that both quantities match quite well. Values range from 0 in elastic regions up to 450 W/mm^3 within localization bands. Considering that the Taylor-Quinney coefficient cannot be estimated properly in near zero domains, the elements which values are below 50 W/mm^3 are not taken into account before computing the coefficient. By doing so, a cartography of β can be obtained, it is shown in Fig. 9.9c. In this figure, we retrieve the fact that the Taylor-Quinney coefficient can mainly be accurately estimated in the localization bands. Furthermore, the values obtained in these zones are quite homogeneous. Moreover, Figure 9.9d depicts an estimation of the average differential Taylor-Quinney ratio within one of the main localization band versus $||\varepsilon_p||_{VM}$. For strains below 0.005 (depicted by the red area), the coefficient is higher than 0.95. The coefficient decreases until it reaches a minimum for strains at 0.05. Then it slightly increases until it reaches a plateau. The average value of the identified ratio is 0.79 (depicted by the red line). The systematic and random errors, defined respectively as the average and the standard deviation of the difference between the computed values and 0.9, can then be computed. Hence, it follows that the Taylor-Quinney ratio can be estimated for strains higher than 0.005, with an accuracy of -0.11 ± 0.04. Despite the systematic error being quite important, the uncertainty (or random error) is acceptable.

9.3.2 Experimental estimation of the Taylor-Quinney coefficient

After the accuracy investigation performed previously, the experimental data is used to estimate the Taylor-Quinney coefficient. Similarly to what was done previously, Figures 9.10a and 9.10b depict respectively the cartographies of $\rho C\dot{T}$ and $||\boldsymbol{\sigma}_{DDI}||_{VM}||\dot{\varepsilon}_p||_{VM}$ at t = 645.3 µs. As previously, these figures show that both quantities match quite well, keeping in mind that they were both obtained independently. As previously, by using a threshold at 50 W/mm^3, the cartography of β at the last time step can be obtained (see Fig. 9.10c). This figure shows that, experimentally, it is more difficult to estimate the co-

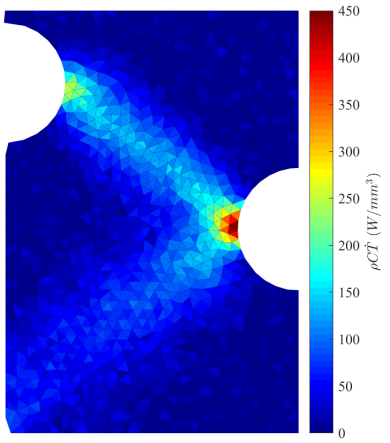

(a) Cartography of $\rho C\dot{T}$ at t = 793 µs,

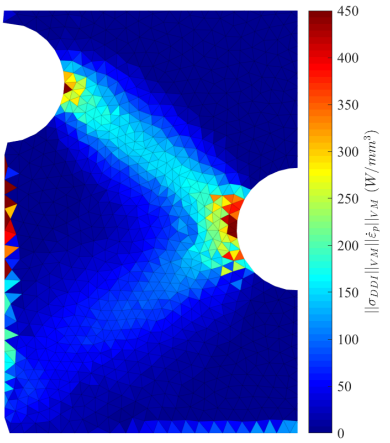

(b) Cartography of $||\boldsymbol{\sigma} DDI||_{VM}||\dot{\varepsilon}_p||_{VM}$ at t = 793 µs,

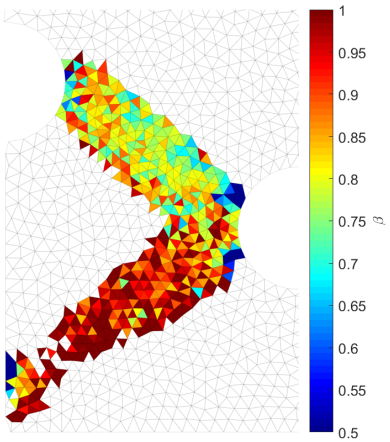

(c) Cartography of β at t = 793 µs,

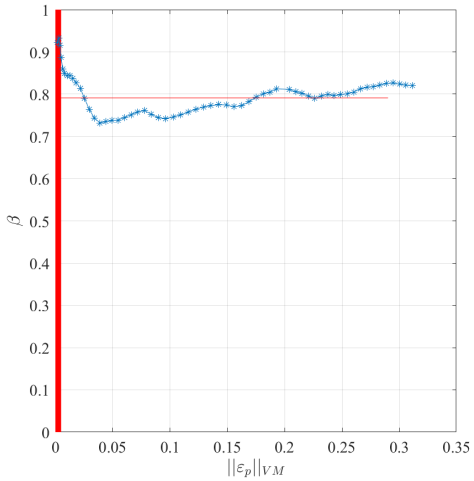

(d) β versus $||\varepsilon_p||_{VM}$,

Figure 9.9: Cartographies of the components of the Taylor-Quinney coefficient as well as cartography of β at the last time step. The evolution of the average coefficient in a localization band is then plotted versus $||\varepsilon_p||_{VM}$. These figures are obtained using data from Section 8.4.

efficient in the secondary localization band. Furthermore, the values are less homogeneous than what was obtained previously. Figure 9.10d depicts an estimation of the average differential Taylor-Quinney ratio within one of the main localization band versus $||\varepsilon_p||_{VM}$. The grey area denotes the random error estimated previously, while the red area denotes the interval of strains between 0 and 0.005. In the last section, it was shown that the coefficient is, in average, underestimated by 0.11 Furthermore, a maximum error of 0.15 is obtained for strains of about 0.03. Hence, based on this figure, the Taylor-Quinney ratio should be close to 0.6 for high strains. This value is in line with values obtained for Stable 316 steel [Vazquez-Fernandez *et al.*, 2019]. In addition, it follows the ratio increase for

strains between 0.03 and 0.2 can be partly explained by the errors observed in Fig. 9.9d. Nevertheless, this does not question the fact that the coefficient increases with the plastic deformation since it is well above the estimated errors from Fig. 9.9d. The evolution of the coefficient that is obtained here is similar to what can be found in the literature [Oliferuk *et al.*, 2004].

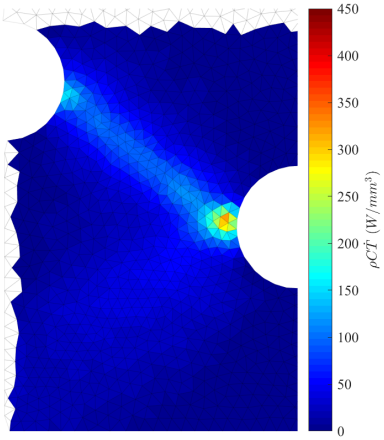

(a) Cartography of $\rho C\dot{T}$ at t = 645.3 µs,

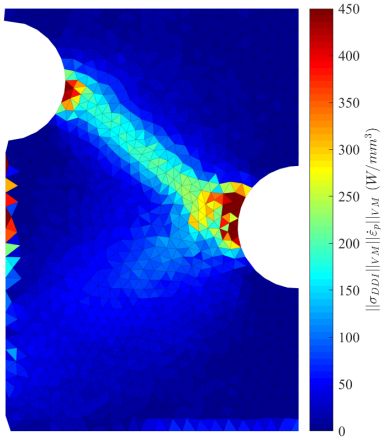

(b) Cartography of $||\boldsymbol{\sigma} DDI||_{VM}||\dot{\varepsilon}_p||_{VM}$ at t = 645.3 µs,

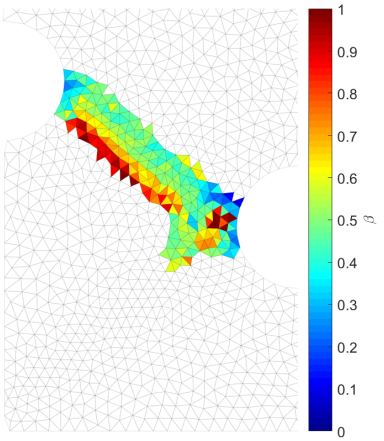

(c) Cartography of β at t = 645.3 µs,

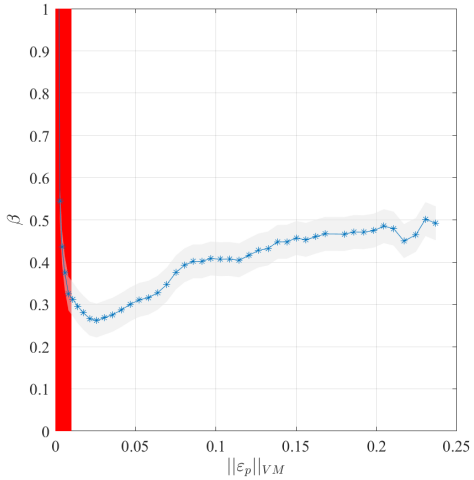

(d) β versus $||\varepsilon_p||_{VM}$,

Figure 9.10: Cartography of the Taylor-Quinney coefficient at the last time step. The evolution of the average coefficient in a localization band is then plotted versus $||\varepsilon_p||_{VM}$.

9.4 Outstandings

9.4.1 Experimental limitations

Specimen geometry and loading This work illustrates the difficulty to cover large spectra of strain, strain-rate, temperature and stress state during a single experiment at high strain-rate.

Indeed, in this work high strain-rate experiments were performed using a heterogeneous geometry submitted to a dynamic tensile test. This kind of experiment allows the sample to undergo wide spectra of strain and strain-rate. However, both quantities remain heavily related: high strain-rates for low values of strains or high strains for low strain-rates are not achievable. Moreover, the stress states that the sample undergoes is mainly uniaxial tension. Furthermore, the temperature is proportional to the plastic strain. As a result, only a small variety of the (strain, strain-rate, temperature, triaxiality) space is explored. Notice that other configurations also suffer from limitations. During impact tests [Fletcher and Pierron, 2018], transient phenomena occur. Hence, complex interactions occur during these experiments which potentially lead to a large spectrum of triaxiality explored. However, during these experiments the strains and temperatures remain low. In addition, ultrasonic excitation of material [Seghir *et al.*, 2019] allow to explore a large spectrum of temperatures. Nevertheless, the approach remains 1D and the strain and strain-rate spectra relatively limited.

Material The XES steel used in this study has a strong strain-rate dependency for strain-rates up to $100\,\mathrm{s}^{-1}$. For strain-rates higher than this value, its dependency saturates. As a result, since the experiment leads to strain-rates higher than the threshold, the experiment mainly confirms observations made for lower strain-rates (at $70\,\mathrm{s}^{-1}$ for example for reference data available at ONERA). It would have been very interesting to take advantage of this dependency to investigate the ability of the DDI method to extrapolate beyond lower strain-rate data.

9.4.2 Methodological limitations

Choice of p_e As presented in Section 8.2, the weight p_e that appears in DDI minimization problem has been set to 1 for each element. This implies that each element have the same weight in this problem, regardless of its localization and its size. However, it has been shown in Section 8.3 that some spatio-temporal elements lead to higher stress uncertainty than others. In this work, this has been tackled by disregarding such elements during a post-treatment procedure. Hence, even though these elements are not taken into account in the analysis, they still have an influence on results. Indeed, for example during the resolution of the material problem (Section 8.2.1.3) these elements will tend to pull

the barycentres (material states) away from low stress uncertainty elements.

A more elegant route that is under investigation would be to attribute a weight *pe* varying continuously from 0 to 1 for each spatio-temporal element considering their stress uncertainty obtained with a numerical test case. This strategy will thus naturally give less weight to elements leading to high stress uncertainties in the DDI strategy. Thus, the stress estimations obtained should be more robust and more accurate. In a way, such an approach would be very similar to some VFM versions where virtual fields are automatically selected to filter-out noise (optimized Virtual Fields). Here, the complexity and non-linearity of the problem does not allow to have an analytical solution, but the use of a numerical twin can produce such a filter.

Implementation of the boundary conditions In the presented study, the boundary conditions were defined as follows:

- $F^j_{mes} = h \sum_{k \in \partial F} \mathbf{f}^j_k$ on the upper edge of the considered mesh,
- $\mathbf{f}^j_k = \mathbf{0}$ in the volume,
- The other boundaries are considered as free edges, including the central hole.

In their work Dalémat and her co-authors [Dalémat *et al.*, 2021] investigated the impact of the choice of the boundary conditions on the DDI solution. They principally focused on the choice of the condition to impose on holes located within the specimen geometry. This is especially relevant when dealing with experimental results. Indeed, for the case of DIC for example, the mesh may not be perfect around the hole and thus may not be perfectly in accordance with the specimen's geometry. Using FE simulations they generated a reference solution and compared the results of the DDI on the mesh with missing nodes near the hole, using different conditions:

- Considering that the nodes of the hole are on a free edge
- Imposing a zero net force on the nodes of the hole.

The authors demonstrated that the second condition lead to errors similar to the reference one where there are no missing nodes (Fig. 9.11). Furthermore, by considering the Von-Mises stresses, they showed that the stresses were overestimated when free edge conditions were considered. Similar conclusions have been obtained on image-based inertial impact test in [Lukić *et al.*, 2020]. The finding from [Dalémat *et al.*, 2021] is summarized in Figure 9.12.

As a result, the use of these recommendations would likely enhance the experimental results presented in Section 8.3.

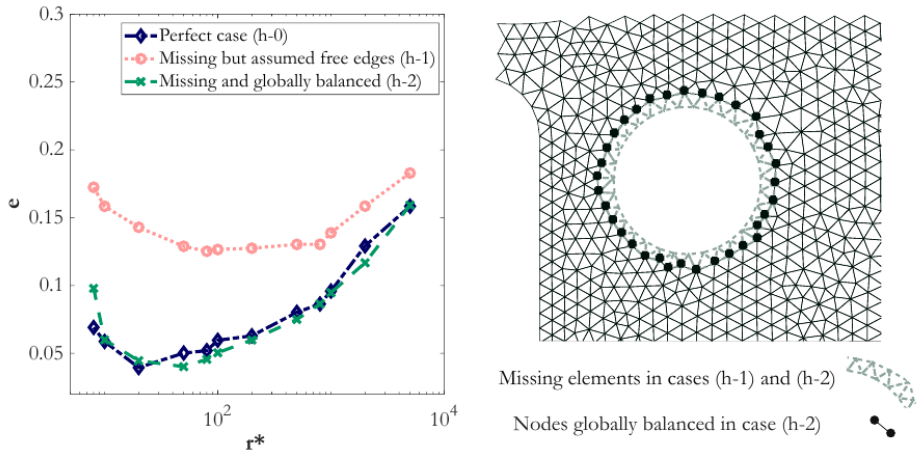

Figure 8: Influence of preprocessing choice for the hole edge definition on the error as a function of r^* for a given C, for the cases of an imperfectly defined edge close to the hole (with (h-1) the assumption of free edge, (h-2) the global balance condition) and of a perfectly defined edge (h-0) (left subfigure). Nodes/elements used in the calculations (right subfigure).

Figure 9.11: Figure from [Dalémat *et al.*, 2021].

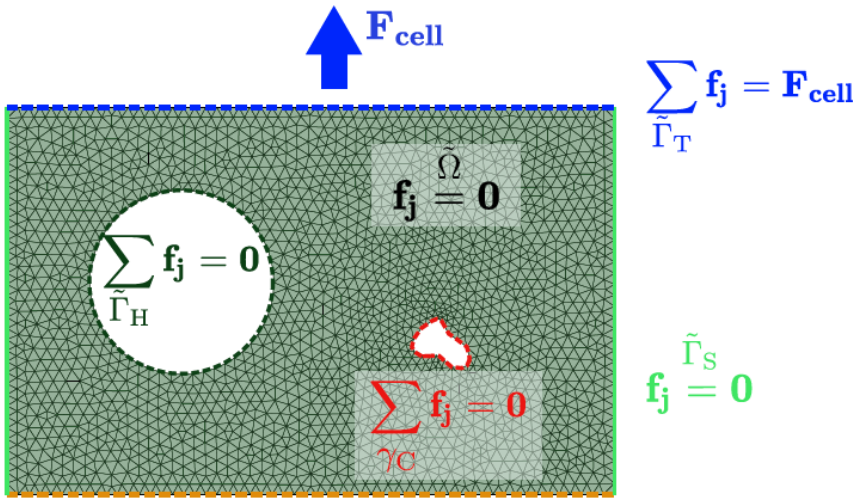

Figure 11: Summary of the proper preprocessing choice to deal with three particular boundaries (top boundary with a global force information, *cluster* of missing data and imperfectly defined edges close to a hole).

Figure 9.12: Figure from [Dalémat *et al.*, 2021]. In this figure, r^* stands for the ratio between the number of mechanical states and the number of material states, while e denotes the relative error between the stress fields identified by the DDI and the reference one.

Addition of the temperature By lack of time, in the proposed algorithm the temperature has not been included. However, the addition of the temperature fields in the methodology would be transparent.

The temperature fields have to be normalized in order to be homogeneous to the other

input data. This can be achieved by considering for instance (from heat equation):

$$\underline{T} = \frac{\rho C_{cal}}{T_o} T, \tag{9.1}$$

where ρ is the material's density, C_{cal} its specific heat and T_o a reference temperature. Then, the DDI norm can be redefined in order to add an argument:

$$\|(\underline{A}, \underline{B}, \underline{C})\|_r^2 = (\underline{A} : \underline{A} + \underline{B} : \underline{B} + \underline{C} : \underline{C}). \tag{9.2}$$

Then, as the constitutive space became $(\underline{\boldsymbol{\varepsilon}}_e^j, \underline{\boldsymbol{\varepsilon}}_e^{j-1}, \underline{\boldsymbol{\sigma}}_e^j, \underline{\boldsymbol{\sigma}}_e^{j-1}, \underline{T}_e^j)_{e,j\in[2,N_t]}$ the cost function becomes:

$$\begin{aligned}\Psi = \sum_{j=2}^{N_t} \sum_{e=1}^{N_e} &\|\boldsymbol{\varepsilon}_e^j - \mathcal{S}_e^j \boldsymbol{\varepsilon}^*, \bar{\boldsymbol{\sigma}}_e^j + \mathbf{d}\boldsymbol{\sigma}_e^j - \mathcal{S}_e^j \boldsymbol{\sigma}^*, \underline{T}_e^j\|_{\mathbb{C}}^2 \\ &+ \|\boldsymbol{\varepsilon}_e^{j-1} - \mathcal{S}_e^j \boldsymbol{\varepsilon}^{**}, \bar{\boldsymbol{\sigma}}_e^{j-1} + \mathbf{d}\boldsymbol{\sigma}_e^{j-1} - \mathcal{S}_e^j \boldsymbol{\sigma}^{**}, \underline{T}_e^j\|_{\mathbb{C}}^2.\end{aligned} \tag{9.3}$$

Since the equations used to compute the stress correction, the selection matrices and to update the material states remain the same, the problem is solved in the exact same manner as what is presented in Section 8.2.

Let us note however, that since in the experiment conducted in this work the temperature is proportional to the plastic strain in the sample, the addition of the temperature is not expected to significantly improve the results of the method. It would add, in a sense, a dimension collinear to the plastic strain. In order for the addition of temperature to be relevant, the experiment has to create points which reach the same strain and strain-rates with different temperatures. Thus, the temperature would be necessary to reconstruct accurately the stresses. This could be obtained by adding a local heating source in the experiment for instance or mixing different tests done at different external temperature using an oven for example.

9.5 Conclusion

In this chapter, the DDI methodology is applied to the experimental data obtained in Part. II. The main conclusions are as follows:

- The application of the proposed method to the experimental data allows estimating stress fields. The material behaviour captured by the material states are consistent with the data obtained at ONERA during previous experimental campaigns. In the presented study, the stress are retrieved with confidence for strains and strain-rates in the range of $[0.01 - 0.21]$ and $[10\,\mathrm{s}^{-1} - 500\,\mathrm{s}^{-1}]$.

- By combining the data from this work and data from a simple quasi-static test, constitutive parameters can be identified. These parameters are able to correctly retrieve the behaviour of the material over several strain-rates decades, with a relative error that remains below $7\,\%$.

- The comparison with the constitutive model classically used for this material shows that discrepancies are mainly located in the hole and notches vicinity. It also highlights the necessity of having loading paths as rich as possible: the DDI is consistent with the constitutive model for strain and strain-rate spectra where a lot of data is available.

- At last but not least, all the thermomechanical quantities needed to estimate the Taylor-Quinney coefficient are now available. The accuracy of this estimation is first assessed using numerical data. It is found that for low strains, the estimation is not reliable. Nevertheless, for strains higher than 0.005, the coefficient can be estimated with an accuracy of -0.11 ± 0.04. The coefficient β can thus be estimated using the experimental temperatures and strain-rates as well as the stresses from the DDI. The evolution of this coefficient as well as its values are in line with what is can be found for mild steels.

Chapter 10

Conclusions

The recent development of Data-Driven Identification approaches applied to mechanics [Leygue *et al.*, 2018, Leygue *et al.*, 2019] opened the way to the consideration of non-parametric characterization of materials *via* heterogeneous fields' observations. Besides, the recent developments in both ultra-high speed imaging and high speed thermography enable coupled measurements with high spatio-temporal resolutions during high strain-rate experiments [Seidt *et al.*, 2017]. As a result, this work focuses on the characterization of metals during a "one-shot" high strain-rate experiment leading to heterogeneous fields. By taking advantage of the high spatio-temporal resolution of the IR and visible light cameras available, a database of thermomechanical points is constituted experimentally. This database is then used to challenge an extension of the Data-Driven Identification to time-dependent material developed in [Langlois *et al.*, 2022].

The contributions of this work are the following:

- A dedicated calibration methodology for a multi-sensor rotating mirror ultra-high speed camera is proposed. Using Zernike polynomials the complex distortions induced by the optical apparatus of such a camera are modelled and corrected. The proposed methodology achieves an accuracy of 0.5 ± 0.2 pixels for the displacements and $100\,\mu m/m \pm 2\,mm/m$ for the strains. In addition, a calibration procedure for a high speed infrared camera is implemented. This procedure achieves an accuracy of $100\,mK \pm 300\,mK$ for very low integration times ($5\,\mu s$ to $25\,\mu s$). These calibration procedures and metrological assessments thus enable the measurement of kinematic and temperature fields with high spatio-temporal sampling during an experiment.

- To produce high strains and high strain-rates as well as heterogeneous mechanical fields, a central hole and two notches are introduced in the dynamic tensile test specimen's geometry. The influence of some geometrical parameters are investigated through FE simulations. Then, using virtually deformed synthetic images, the measurability of the induced mechanical fields is assessed. Finally, experimental dynamic tensile test applied to notched specimens with holes of a XES steel are conducted. Both temperature and kinematic fields are retrieved using a high speed IR camera and an ultra-high speed camera.

- The DDI method for time-dependent materials proposed by [Langlois *et al.*, 2022] is challenged by two tests. The first test is a numerical test case where the reference

solution is known. This test allowed to investigate the method's parameters sensitivity. Furthermore, it demonstrates the ability of this non-parametric characterization method to recover the reference solution, in particular the strain-rate dependency. Then, the proposed non-parametric characterization method is applied to the experimental data acquired during a dynamic tensile test. It leads to estimation of stress for strains and strain-rates in the range of $[0.01 - 0.21]$ and $[0\,\mathrm{s}^{-1} - 500\,\mathrm{s}^{-1}]$. Finally, the stress fields, temperature fields and plastic strain ones are used to get an estimation of the Taylor-Quinney coefficient in a localization band deforming at several hundreds of s^{-1}.

The dedicated calibration methodology for a multi-sensor rotating mirror camera is, to the author's knowledge, the first one to properly tackle the deconvolution of the distortions induced by such a camera. As such, this is but the first brick toward the lasting use of such an imaging technology for displacement measurements. Moreover, the experimental application of the non-parametric characterization methods is a very recent research subject and still under development. Thus, the work proposed is of seminal nature and is to be considered as a convincing proof of concept. As a result, several prospects can be considered:

- It would be interesting to continue the work initiated on the Cordin-580.
  - In the short-term, it is primordial to correct the sensors' sharpness. Since the light reaches each sensor with different angles, the camera induces blurring depending on their positions. However, as each sensor also has its own focusing system, their sharpness can be optimized manually one by one. This improvement could lead to the use of finer DIC meshes and thus better performances.
  - For the moment the use of such a camera implies to run calibration shots before the experiment. This possibly introduces significant costs, as for speeds higher than 750 kfps helium is used. Furthermore, this also leads to long camera run times at very high speed which reduces the mirror-bearing lifetime. Hence, it would be interesting to be able to create a global model of the camera's distortions once and for all. This could reduce the number of calibration shot to only one, in order to take into account the change of the scene. However, this requires to properly model the influence of the mirror speed on the distortions, as well as the addition of helium for ultra-high speed ($>$ 1 Mfps).
- Concerning the Data-Driven Identification several prospects can be considered.
  - First, in a very-short term, the addition of temperature has to be implemented. Using numerical test cases it should be verified that its introduction does not

significantly influence the final result in the actual configuration. Furthermore, by adding a heat source locally in FE simulations, the interest of the introduction of the temperature could be assessed. Indeed, for metals, high temperature often soften the material. As a result, the heat source could potentially lead to the existence of points that share the same strain, strain-rate but different temperatures and stresses. Hence, the introduction of temperature in the constitutive space becomes essential for the DDI to correctly estimate the stresses.

- For the moment, the weight p_e that appears in DDI minimization problem has been set to 1 for each element. This implies that each element has the same weight in this problem, regardless of its localization and its size, and more importantly its sensitivity for the stress estimation. A more elegant route that is under investigation would be to attribute a weight p_e varying continuously from 0 to 1 for each spatio-temporal element considering their stress uncertainties obtained with a numerical test case. This strategy will thus naturally give less weight to elements leading to high stress uncertainties in the DDI strategy.
- At last but not least, the proposed method should be extended to dynamics. This has already been proposed for Data-Driven Computational Mechanics [Kirchdoerfer and Ortiz, 2018]: it simply consists in the addition of the acceleration term in the equilibrium equation of the method. This addition would broaden the application range of the Data-Driven Identification method.

- Finally, particular care should be given to experimental design. Indeed, when using a single actuator at room temperature, obtaining wide spectra of strain and strain-rate is possible. However, this comes at the cost of having a temperature that is nearly proportional to the plastic strain as well as a sample that is mainly in an uniaxial tension state. As a result, attention should be given to design experiments that lead to wide spectra of strain and strain-rate, different and complex stress states as well as a wide range of temperature that is not always proportional to the plastic strain. These experiments would lead the scientific community one step further toward “one-shot” experiments for material characterization.

BIBLIOGRAPHY

[Archer *et al.*, 2020] Archer, T., Berny, M., Beauchêne, P., and Hild, F. (2020). Creep behavior identification of an environmental barrier coating using full-field measurements. Journal of the European Ceramic Society, 40(15):5704–5718.

[Arruda *et al.*, 1995] Arruda, E. M., Boyce, M. C., and Jayachandran, R. (1995). Effects of strain rate, temperature and thermomechanical coupling on the finite strain deformation of glassy polymers. Mechanics of Materials, 19(2-3):193–212.

[Avril *et al.*, 2008] Avril, S., Bonnet, M., Bretelle, A.-S., Grédiac, M., Hild, F., Ienny, P., Latourte, F., Lemosse, D., Pagano, S., Pagnacco, E., and Pierron, F. (2008). Overview of identification methods of mechanical parameters based on full-field measurements. Experimental Mechanics, 48(4):381–402.

[Badaloni *et al.*, 2015] Badaloni, M., Rossi, M., Chiappini, G., Lava, P., and Debruyne, D. (2015). Impact of experimental uncertainties on the identification of mechanical material properties using DIC. Experimental Mechanics, 55(8):1411–1426.

[Barroqueiro *et al.*, 2020] Barroqueiro, B., Andrade-Campos, A., de Oliveira, J. D., and Valente, R. (2020). Design of mechanical heterogeneous specimens using topology optimization. International Journal of Mechanical Sciences, 181:105764.

[Berthel, 2007] Berthel, B. (2007). Mesures thermographiques de champs de dissipation accompagnant la fatigue à grand nombre de cycles des aciers. PhD thesis, Montpellier II.

[Besnard *et al.*, 2006] Besnard, G., Hild, F., and Roux, S. (2006). "Finite-Element" displacement fields analysis from digital images: Application to Portevin–Le Châtelier bands. Exp Mech, 46(6):789–803.

[Bäker, 2006] Bäker, M. (2006). Finite element simulation of high-speed cutting forces. Journal of Materials Processing Technology, 176(1-3):117–126.

[Bodelot, 2008] Bodelot, L. (2008). Étude couplée des champs cinématiques et thermiques à l'échelle de la microstructure des matériaux métalliques. PhD thesis, Université des Sciences et Technologies de Lille I.

[Bodelot *et al.*, 2011] Bodelot, L., Charkaluk, E., Sabatier, L., and Dufrénoy, P. (2011). Experimental study of heterogeneities in strain and temperature fields at the mi-

crostructural level of polycrystalline metals through fully-coupled full-field measurements by Digital Image Correlation and Infrared Thermography. Mechanics of Materials, 43(11):654–670.

[Bossuyt, 2013] Bossuyt, S. (2013). Optimized patterns for Digital Image Correlation. In Jin, H., Sciammarella, C., Furlong, C., and Yoshida, S., editors, Imaging Methods for Novel Materials and Challenging Applications, Volume 3, pages 239–248. Springer New York, New York, NY.

[Bouda *et al.*, 2019] Bouda, P., Langrand, B., Notta-Cuvier, D., Markiewicz, E., and Pierron, F. (2019). A computational approach to design new tests for viscoplasticity characterization at high strain-rates. Computanional Mechanics, 64(6):1639–1654.

[Cameron and Tasan, 2021] Cameron, B. C. and Tasan, C. (2021). Full-field stress computation from measured deformation fields: A hyperbolic formulation. Journal of the Mechanics and Physics of Solids, 147:104186.

[Chamoin *et al.*, 2020] Chamoin, L., Jailin, C., Diaz, M., and Quesada, L. (2020). Coupling between topology optimization and Digital Image Correlation for the design of specimen dedicated to selected material parameters identification. International Journal of Solids and Structures, 193-194:270–286.

[Cherouat *et al.*, 2018] Cherouat, A., Borouchaki, H., and Jie, Z. (2018). Simulation of sheet metal forming processes using a fully rheological-damage constitutive model coupling and a specific 3D remeshing method. Metals, 8(12):991.

[Chrysochoos *et al.*, 2010] Chrysochoos, A., Huon, V., Jourdan, F., Muracciole, J.-M., Peyroux, R., and Wattrisse, B. (2010). Use of full-field Digital Image Correlation and Infrared Thermography measurements for the thermomechanical analysis of material behaviour. Strain, 46(1):117–130.

[Chrysochoos *et al.*, 1989] Chrysochoos, A., Maisonneuve, O., Martin, G., Caumon, H., and Chezeaux, J. (1989). Plastic and dissipated work and stored energy. Nuclear Engineering and Design, 114(3):323–333.

[Chu *et al.*, 1985] Chu, T. C., Ranson, W. F., and Sutton, M. A. (1985). Applications of Digital Image Correlation techniques to experimental mechanics. Experimental Mechanics, 25(3):232–244.

[Cottin *et al.*, 1984] Cottin, N., Felgenhauer, H. P., and Natke, H. G. (1984). On the parameter identification of elastomechanical systems using input and output residuals. Ingenieur Archiv, 54(5):378–387.

[Dalemat, 2019] Dalemat, M. (2019). Une expérimentation réussie pour l'identification de la réponse mécanique sans loi de comportement : Approche Data-Driven appliquée aux membranes élastomères. Phd thesis, École Centrale de Nantes.

[Dalémat *et al.*, 2021] Dalémat, M., Coret, M., Leygue, A., and Verron, E. (2021). Robustness of the Data-Driven Identification algorithm with incomplete input data. working paper or preprint.

[Dalémat *et al.*, 2019] Dalémat, M., Coret, M., Leygue, A., and Verron, E. (2019). Measuring stress field without constitutive equation. Mechanics of Materials, 136:103087.

[Dar *et al.*, 2014] Dar, U. A., Zhang, W. H., and Xu, Y. J. (2014). Numerical implementation of strain rate dependent thermo viscoelastic constitutive relation to simulate the mechanical behavior of PMMA. International Journal of Mechanics and Material Design, 10(1):93–107.

[De and Masilamani, 2013] De, K. and Masilamani, V. (2013). Image sharpness measure for blurred images in frequency domain. Procedia Engineering, 64:149–158.

[Eggersmann *et al.*, 2019] Eggersmann, R., Kirchdoerfer, T., Reese, S., Stainier, L., and Ortiz, M. (2019). Model-free Data-Driven inelasticity. Computer Methods in Applied Mechanics and Engineering, 350:81–99.

[El Bartali *et al.*, 2008] El Bartali, A., Aubin, V., and Degallaix, S. (2008). Fatigue damage analysis in a duplex stainless steel by Digital Image Correlation technique. Fatigue & Fracture of Engineering Materials & Structures, 31(2):137–151.

[Fletcher and Pierron, 2018] Fletcher, L. and Pierron, F. (2018). An image-based inertial impact (IBII) test for tungsten carbide cermets. Journal of Dynamic Behavior of Materials, 4(4):481–504.

[Fletcher and Pierron, 2020] Fletcher, L. and Pierron, F. (2020). The image-based inertial release (IBIR) test: A new high strain rate test for stiffness strain-rate sensitivity identification. Experimental Mechanics, 60(4):493–508.

[Fletcher *et al.*, 2019] Fletcher, L., Van-Blitterswyk, J., and Pierron, F. (2019). A novel image-based inertial impact test (IBII) for the transverse properties of composites at high strain rates. Journal of Dynamic Behavior of Materials, 5(1):65–92.

[Forquin and Lukić, 2018] Forquin, P. and Lukić, B. (2018). On the processing of spalling experiments. Part I: Identification of the dynamic tensile strength of concrete. Journal of Dynamic Behavior of Materials, 4(1):34–55.

[Fourest *et al.*, 2020] Fourest, T., Bouda, P., Fletcher, L. C., Notta-Cuvier, D., Markiewicz, E., Pierron, F., and Langrand, B. (2020). Image-based inertial impact test for characterisation of strain rate dependency of Ti6Al4V titanium alloy. Experimental Mechanics, 60(2):235–248.

[Gama *et al.*, 2004] Gama, B. A., Lopatnikov, S. L., and Gillespie, J. W. (2004). Hopkinson bar experimental technique: A critical review. Applied Mechanics Reviews, 57(4):223–250.

[Gao and Zhang, 2010] Gao, C. and Zhang, L. (2010). A constitutive model for dynamic plasticity of FCC metals. Materials Science and Engineering: A, 527(13-14):3138–3143.

[Gao *et al.*, 2015] Gao, G., Huang, S., Xia, K., and Li, Z. (2015). Application of Digital Image Correlation (DIC) in dynamic notched semi-circular bend (NSCB) tests. Experimental Mechanics, 55(1):95–104.

[Gary, 2000] Gary, G. (2000). Étude expérimentale du comportement dynamique des matériaux. Mécanique & Industries, 1(1):15–26.

[Gary and Nowacki, 1994] Gary, G. and Nowacki, W. K. (1994). Essai de cisaillement plan appliqué à des tôles minces. Journal de Physique IV, 04(C8):C8–65–C8–70.

[Giton *et al.*, 2006] Giton, M., Caro-Bretelle, A. S., and Ienny, P. (2006). Hyperelastic behaviour identification by a forward problem resolution: Application to a tear test of a silicone-rubber. Strain, 42(4).

[Gray III, 2000] Gray III, G. T. (2000). Classic split-hopkinson pressure bar testing. In Mechanical Testing and Evaluation, volume 8, pages 462–476. ASM International.

[Grédiac *et al.*, 2008] Grédiac, M., Pierron, F., Avril, S., and Toussaint, E. (2008). The Virtual Fields Method for extracting constitutive parameters from full-field measurements: A review. Strain, 42(4):233–253.

[Grédiac *et al.*, 2016] Grédiac, M., Sur, F., and Blaysat, B. (2016). The grid method for in-plane displacement and strain measurement: A review and analysis: The grid method. Strain, 52(3):205–243.

[Grédiac *et al.*, 2002] Grédiac, M., Toussaint, E., and Pierron, F. (2002). Special virtual fields for the direct determination of material parameters with the virtual fields method. 1—Principle and definition. International Journal of Solids and Structures, 39(10):2691–2705.

[Grediac, 1989] Grediac, M. (1989). Principe des travaux virtuels et identification. Comptes rendus de l'Académie des sciences. Série 2, Mécanique, Physique, Chimie, Sciences de l'univers, Sciences de la Terre.

[Guzmán *et al.*, 2009] Guzmán, R., Meléndez, J., Aranda, J. M., Essa, Y. E., López, F., and Pérez-Castellanos, J. L. (2009). Measurement of temperature increment in compressive quasi-static and dynamic tests using Infrared Thermography. Strain, 45(2):179–189.

[Haboussa *et al.*, 2011] Haboussa, D., Grégoire, D., Elguedj, T., Maigre, H., and Combescure, A. (2011). X-FEM analysis of the effects of holes or other cracks on dynamic crack propagations. International Journal for Numerical Methods in Engineering, 86(4-5):618–636.

[Haugou *et al.*, 2006] Haugou, G., Markiewicz, E., and Fabis, J. (2006). On the use of the non direct tensile loading on a classical split Hopkinson bar apparatus dedicated to sheet metal specimen characterisation. International Journal of Impact Engineering, 32(5):778–798.

[Herb *et al.*, 2019] Herb, V., Berny, M., Lacombe, B., and Hild, F. (2019). Developpement d'un algorithme de FEMU-TU pour l'identification de propriétés thermomécaniques d'un CMC à hautes températures à partir de mesures de champs. In 21ème Journées Nationales sur les Composites.

[HGH-Infrared, nd] HGH-Infrared (n.d.). Blackbody's datasheet. `https://hgh-infrared.com/wp-content/uploads/2020/12/DCN1000N_H-EN_HGH.pdf`. Last accessed 13 May 2019.

[Hild and Roux, 2012] Hild, F. and Roux, S. (2012). Comparison of local and global approaches to Digital Image Correlation. Experimental Mechanics, 52(9):1503–1519.

[Honorat *et al.*, 2005] Honorat, V., Moreau, S., Muracciole, J.-M., Wattrisse, B., and Chrysochoos, A. (2005). Calorimetric analysis of polymer behaviour using a pixel calibration of an IRFPA camera. Quantitative InfraRed Thermography Journal, 2(2):153–171.

[Hor *et al.*, 2013] Hor, A., Morel, F., Lebrun, J.-L., and Germain, G. (2013). Modelling, identification and application of phenomenological constitutive laws over a large strain rate and temperature range. Mechanics of Materials, 64:91–110.

[Jajam and Tippur, 2011] Jajam, K. and Tippur, H. (2011). An experimental investigation of dynamic crack growth past a stiff inclusion. Engineering Fracture Mechanics, 78(6):1289–1305.

[Johnson and Cook, 1983] Johnson, G. and Cook, W. (1983). A constitutive model and data for metals subjected to large strains, high strain rates and high temperatures. In Proceedings of the 7th International Symposium on Ballistics, volume 21, pages 541–547, The Hague, The Netherlands.

[Jones *et al.*, 2018] Jones, E., Carroll, J., Karlson, K., Kramer, S., Lehoucq, R., Reu, P., and Turner, D. (2018). Parameter covariance and non-uniqueness in material model calibration using the Virtual Fields Method. Computational Materials Science, 152:268–290.

[Kajberg and Wikman, 2007] Kajberg, J. and Wikman, B. (2007). Viscoplastic parameter estimation by high strain-rate experiments and inverse modelling – Speckle measurements and high-speed photography. International Journal of Solids and Structures, 44(1):145–164.

[Kalthoff, 1988] Kalthoff, J. F. (1988). Shadow optical analysis of dynamic shear fracture. Optical Engineering, 27(10):835 – 840 – 6.

[Kang and Huh, 2000] Kang, W. J. and Huh, H. (2000). Crash analysis of auto-body structures considering the strain-rate hardening effect. Technical report, SAE Technical Paper.

[Khan and Liang, 1999] Khan, A. S. and Liang, R. (1999). Behaviors of three BCC metal over a wide range of strain rates and temperatures: Experiments and modeling. International Journal of Plasticity, 15(10):1089–1109.

[Kirchdoerfer and Ortiz, 2016] Kirchdoerfer, T. and Ortiz, M. (2016). Data-Driven computational mechanics. Computer Methods in Applied Mechanics and Engineering, 304:81–101.

[Kirchdoerfer and Ortiz, 2017] Kirchdoerfer, T. and Ortiz, M. (2017). Data Driven computing with noisy material data sets. Computer Methods in Applied Mechanics and Engineering, 326:622–641.

[Kirchdoerfer and Ortiz, 2018] Kirchdoerfer, T. and Ortiz, M. (2018). Data-Driven computing in dynamics. International Journal for Numerical Methods in Engineering, 113(11):1697–1710.

[Kirkpatrick *et al.*, 2007] Kirkpatrick, S. J., Duncan, D. D., Wang, R. K., and Hinds, M. T. (2007). Quantitative temporal speckle contrast imaging for tissue mechanics. Journal of the Optical Society of America A, 24(12):3728.

[Kirugulige *et al.*, 2007] Kirugulige, M. S., Tippur, H. V., and Denney, T. S. (2007). Measurement of transient deformations using Digital Image Correlation method and high-speed photography: Application to dynamic fracture. Applied Optics, 46(22):5083.

[Klepaczko and Chiem, 1986] Klepaczko, J. and Chiem, C. (1986). On rate sensitivity of F.C.C. metals, instantaneous rate sensitivity and rate sensitivity of strain hardening. Journal of the Mechanics and Physics of Solids, 34(1):29–54.

[Klepaczko *et al.*, 1999] Klepaczko, J. R., Nguyen, H. V., and Nowacki, W. K. (1999). Quasi-static and dynamic shearing of sheet metals. European Journal of Mechanics - A/Solids, 18(2):271–289.

[Knysh and Korkolis, 2015] Knysh, P. and Korkolis, Y. P. (2015). Determination of the fraction of plastic work converted into heat in metals. Mechanics of Materials, 86:71–80.

[Koohbor *et al.*, 2016] Koohbor, B., Kidane, A., Lu, W.-Y., and Sutton, M. A. (2016). Investigation of the dynamic stress–strain response of compressible polymeric foam using a non-parametric analysis. International Journal of Impact Engineering, 91:170–182.

[Lakshminarayanan and Fleck, 2011] Lakshminarayanan, V. and Fleck, A. (2011). Zernike polynomials: A guide. Journal of Modern Optics, 58(7):545–561.

[Langlois *et al.*, 2022] Langlois, R., Coret, M., and Réthoré, J. (2022). Non-parametric stress field estimation for history dependent materials: Application to ductile material exhibiting Piobert–Lüders localization bands. Strain, page 30. under review.

[Langrand and Combescure, 2004] Langrand, B. and Combescure, A. (2004). Non-linear and failure behaviour of spotwelds: A "global" finite element and experiments in pure and mixed modes I/II. International Journal of Solids and Structures, 41(24-25):6631–6646.

[Langrand and Markiewicz, 2010] Langrand, B. and Markiewicz, E. (2010). Strain-rate dependence in spot welds: Non-linear behaviour and failure in pure and combined modes I/II. International Journal of Impact Engineering, 37(7):792–805.

[Le Louëdec *et al.*, 2015] Le Louëdec, G., Pierron, F., Sutton, M. A., Siviour, C., and Reynolds, A. P. (2015). Identification of the dynamic properties of Al 5456 FSW welds using the Virtual Fields Method. Journal of Dynamic Behavior of Materials, 1(2):176–190.

[LeBlanc and Lassila, 1996] LeBlanc, M. and Lassila, D. (1996). A hybrid technique for compression testing at intermediate strain rates. Experimental Techniques, 20(5):21–24.

[Lee *et al.*, 2012] Lee, D., Tippur, H., and Bogert, P. (2012). Dynamic fracture of graphite/epoxy composites stiffened by buffer strips: An experimental study. Composite Structures, 94(12):3538–3545.

[Leygue *et al.*, 2018] Leygue, A., Coret, M., Réthoré, J., Stainier, L., and Verron, E. (2018). Data-based derivation of material response. Computer Methods in Applied Mechanics and Engineering, 331:184–196.

[Leygue *et al.*, 2019] Leygue, A., Seghir, R., Réthoré, J., Coret, M., Verron, E., and Stainier, L. (2019). Non-parametric material state field extraction from full field measurements. Computational Mechanics, 64(2):501–509.

[Liu, 2021] Liu, C. (2021). Nonuniform stress field determination based on deformation measurement. Journal of Applied Mechanics, 88(7):071005.

[Lukić *et al.*, 2020] Lukić, B., Saletti, D., and Forquin, P. (2020). Validation of the photomechanical spalling test in the case of non-linear dynamic response: Application to a granite rock. Strain, 56(6):e12363.

[Macdougall, 2000] Macdougall, D. (2000). Determination of the plastic work converted to heat using radiometry. Experimental Mechanics, 40(3):298–306.

[MacQueen *et al.*, 1967] MacQueen, J. *et al.* (1967). Some methods for classification and analysis of multivariate observations. In Proceedings of the fifth Berkeley symposium on mathematical statistics and probability, volume 1, pages 281–297. Oakland, CA, USA.

[Malchow *et al.*, 2019] Malchow, P., Ravindran, S., and Kidane, A. (2019). Localized microstructural deformation behavior of dynamically deformed pure magnesium. In Alor-Hernández, G., Sánchez-Cervantes, J. L., Rodríguez-González, A., and Valencia-García, R., editors, Current Trends in Semantic Web Technologies: Theory and Practice, volume 815, pages 225–228. Springer International Publishing, Cham.

[Marcotte *et al.*, 2013] Marcotte, F., Tremblay, P., and Farley, V. (2013). Infrared camera NUC and calibration: Comparison of advanced methods. In Holst, G. C. and Krapels, K. A., editors, Infrared Imaging Systems: Design, Analysis, Modeling, and Testing XXIV, page 870603, Baltimore, Maryland, USA. International Society for Optics and Photonics.

[Marek *et al.*, 2017] Marek, A., Davis, F. M., and Pierron, F. (2017). Sensitivity-based virtual fields for the non-linear Virtual Fields Method. Computational mechanics, 60(3):409–431.

[Markiewicz *et al.*, 2016] Markiewicz, E., Langrand, B., Leconte, N., Fabis, J., and Dupuy, T. (2016). A methodology for the viscoplastic behaviour characterisation of spot-weld heat affected materials. Journal of Materials Processing Technology, 238:169–180.

[Maynadier *et al.*, 2012] Maynadier, A., Poncelet, M., Lavernhe-Taillard, K., and Roux, S. (2012). One-shot measurement of thermal and kinematic fields: InfraRed Image Correlation (IRIC). Experimental Mechanics, 52(3):241–255.

[Moulart *et al.*, 2011] Moulart, R., Pierron, F., Hallet, S., and Wisnom, M. (2011). Full-field strain measurement and identification of composites moduli at high strain rate with the Virtual Fields Method. Experimental Mechanics, 51:509–536.

[Oliferuk *et al.*, 2004] Oliferuk, W., Maj, M., and Raniecki, B. (2004). Experimental analysis of energy storage rate components during tensile deformation of polycrystals. Materials Science and Engineering: A, 374(1-2):77–81.

[Orteu *et al.*, 2008] Orteu, J.-J., Rotrou, Y., Sentenac, T., and Robert, L. (2008). An innovative method for 3-D shape, strain and temperature full-field measurement using a single type of camera: Principle and preliminary results. Experimental Mechanics, 48(2):163–179.

[Pan *et al.*, 2009] Pan, B., Qian, K., Xie, H., and Asundi, A. (2009). Two-dimensional Digital Image Correlation for in-plane displacement and strain measurement: A review. Measurement Science and Technology, 20(6):062001.

[Peirs *et al.*, 2011] Peirs, J., Verleysen, P., Van Paepegem, W., and Degrieck, J. (2011). Determining the stress–strain behaviour at large strains from high strain rate tensile and shear experiments. International Journal of Impact Engineering, 38(5):406–415.

[Pierron *et al.*, 2011a] Pierron, F., Cheriguene, R., Forquin, P., Moulart, R., Rossi, M., and Sutton, M. (2011a). Performances and limitations of three ultra high-speed imaging cameras for full-field deformation measurements. Applied Mechanics and Materials, 70:81–86.

[Pierron and Fletcher, 2019] Pierron, F. and Fletcher, L. (2019). Generalized stress–strain curves for IBII tests on isotropic and orthotropic materials. Journal of Dynamic Behavior of Materials, 5(2):180–193.

[Pierron and Grédiac, 2012] Pierron, F. and Grédiac, M. (2012). The Virtual Fields Method. Springer New York, New York, NY.

[Pierron *et al.*, 2011b] Pierron, F., Sutton, M. A., and Tiwari, V. (2011b). Ultra high speed DIC and Virtual Fields Method analysis of a three point bending impact test on an aluminium bar. Experimental Mechanics, 51(4):537–563.

[Pierron *et al.*, 2014] Pierron, F., Zhu, H., and Siviour, C. (2014). Beyond Hopkinson's bar. Philosophical Transactions of the Royal Society A: Mathematical, Physical and Engineering Sciences, 372(2023):20130195–20130195.

[Platzer *et al.*, 2021] Platzer, A., Leygue, A., Stainier, L., and Ortiz, M. (2021). Finite element solver for Data-Driven finite strain elasticity. Computer Methods in Applied Mechanics and Engineering, 379:113756.

[Poggio *et al.*, 1988] Poggio, T., Voorhees, H., and Yuille, A. (1988). A regularized solution to edge detection. Journal of Complexity, 4(2):106–123.

[Priadi *et al.*, 1991] Priadi, D., Levaillant, C., Penazzi, L., Di Pasquale, E., and Aita, S. (1991). Introduction of strain rate effects in constitutive equations suitable for sheet metal stamping applications. In MECAMAT 91, page 1991.

[Products, nd] Products, S. Q. (n.d.). Technical specification for Xenon short arc lamps. `https://www.sqpuv.com/PDFs/TechnicalSpecificationGuide.pdf`. Accessed: 2021-11-10.

[Rastogi, 2000] Rastogi, P. K., editor (2000). Photomechanics. Number v. 77 in Topics in applied physics. Springer, Berlin ; New York.

[Ravi-Chandar *et al.*, 1999] Ravi-Chandar, K., Lu, J., Yang, B., and Zhu, Z. (1999). Failure mode transitions in polymers under high strain rate loading. International Journal of Fracture, page 40.

[Réthoré, 2018] Réthoré, J. (2018). Ufreckles, doi:10.5281/zenodo.1433776.

[Reu and Nissen, 2014] Reu, P. L. and Nissen, M. R. (2014). The evolution of high and ultra-high speed imaging from qualitative to quantitative. Technical report, Sandia National Lab.(SNL-NM), Albuquerque, NM (United States).

[Rittel, 1999] Rittel, D. (1999). On the conversion of plastic work to heat during high strain rate deformation of glassy polymers. Mechanics of Materials, 31(2):131–139.

[Rittel *et al.*, 2017] Rittel, D., Zhang, L., and Osovski, S. (2017). The dependence of the Taylor–Quinney coefficient on the dynamic loading mode. Journal of the Mechanics and Physics of Solids, 107:96–114.

[Rodriguez and Filisko, 1986] Rodriguez, E. L. and Filisko, F. E. (1986). Temperature changes in poly(methyl methacrylate) and high-density polyethylene during rapid compressive deformation. Polymer Engineering & Science, 26(15):1060–1065.

[Rose and Menzel, 2021] Rose, L. and Menzel, A. (2021). Identification of thermal material parameters for thermo-mechanically coupled material models: Verification and model dependency. Meccanica, 56:393–416.

[Rossi *et al.*, 2016] Rossi, M., Badaloni, M., Lava, P., Debruyne, D., and Pierron, F. (2016). A procedure for specimen optimization applied to material testing in plasticity with the Virtual Fields Method. In AIP Conference Proceedings, page 200016. AIP Publishing LLC.

[Rossi *et al.*, 2015] Rossi, M., Lava, P., Pierron, F., Debruyne, D., and Sasso, M. (2015). Effect of DIC spatial resolution, noise and interpolation error on identification results with the VFM identification. Strain, 51(3):206–222.

[Roux and Hild, 2020] Roux, S. and Hild, F. (2020). Optimal procedure for the identification of constitutive parameters from experimentally measured displacement fields. International Journal of Solids and Structures, 184:14–23.

[Rubino *et al.*, 2019] Rubino, V., Rosakis, A., and Lapusta, N. (2019). Full-field ultrahigh-speed quantification of dynamic shear ruptures using Digital Image Correlation. Experimental Mechanics, pages 1–32.

[Samaca Martinez *et al.*, 2015] Samaca Martinez, J., Toussaint, E., Balandraud, X., Le Cam, J.-B., and Berghezan, D. (2015). Heat and strain measurements at the crack tip of filled rubber under cyclic loadings using full-field techniques. Mechanics of Materials, 81:62–71.

[Schreier *et al.*, 2009] Schreier, H., Orteu, J.-J., and Sutton, M. A. (2009). Image correlation for shape, motion and deformation measurements. Springer US.

[Seghir, 2012] Seghir, R. (2012). Experimental and numerical investigation of thermomechanical couplings and energy balance in metallic polycrystals. PhD thesis, Ecole Centrale de Lille.

[Seghir and Pierron, 2018] Seghir, R. and Pierron, F. (2018). A novel image-based ultrasonic test to map material mechanical properties at high strain-rates. Experimental Mechanics, 58(2):183–206.

[Seghir *et al.*, 2019] Seghir, R., Pierron, F., and Fletcher, L. (2019). Image-based stress field reconstruction in complex media. In Baldi, A., Quinn, S., Balandraud, X., Dulieu-Barton, J. M., and Bossuyt, S., editors, Residual Stress, Thermomechanics & Infrared Imaging, Hybrid Techniques and Inverse Problems, Volume 7, pages 101–104. Springer International Publishing, Cham.

[Seghir *et al.*, 2013] Seghir, R., Witz, J.-F., Bodelot, L., Charkaluk, E., and Dufrénoy, P. (2013). An improved lagrangian thermography procedure for the quantification of the temperature fields within polycrystals. Quantitative InfraRed Thermography Journal, 10(1):74–95.

[Seidt *et al.*, 2017] Seidt, J., Kuokkala, V.-T., Smith, J., and Gilat, A. (2017). Synchronous full-field strain and temperature measurement in tensile tests at low, intermediate and high strain rates. Experimental Mechanics, 57(2):219–229.

[Song *et al.*, 2016] Song, L., Zhou, Z., Wang, X., Zhao, X., and Elson, D. S. (2016). Simulation of speckle patterns with pre-defined correlation distributions. Biomedical Optics Express, 7(3):798.

[Stainier *et al.*, 2019] Stainier, L., Leygue, A., and Ortiz, M. (2019). Model-free Data-Driven methods in mechanics: material data identification and solvers. Computational Mechanics, 64(2):381–393.

[Sun *et al.*, 2005] Sun, Y., Pang, J. H. L., Wong, C. K., and Su, F. (2005). Finite element formulation for a Digital Image Correlation method. Applied Optics, 44(34):7357.

[Sutton *et al.*, 1983] Sutton, M., Wolters, W., Peters, W., Ranson, W., and McNeill, S. (1983). Determination of displacements using an improved digital correlation method. Image and Vision Computing, 1(3):133–139.

[Tayeb *et al.*, 2021] Tayeb, A., Le Cam, J. B., Grédiac, M., Toussaint, E., Robin, E., Balandraud, X., and Canévet, F. (2021). Identifying hyperelastic constitutive parameters with sensitivity-based virtual fields. Strain, 57(6):e12397.

[Taylor and Quinney, 1934] Taylor, G. I. and Quinney, H. (1934). The latent energy remaining in a metal after cold working. Proceedings of the Royal Society of London. Series A, Containing Papers of a Mathematical and Physical Character, 143(849):307–326.

[Thibos *et al.*, 2002] Thibos, L. N., Applegate, R. A., Schwiegerling, J. T., and Webb, R. (2002). Standards for reporting the optical aberrations of eyes. Journal of Refractive Surgery, 18:9.

[Tiwari *et al.*, 2007] Tiwari, V., Sutton, M. A., and McNeill, S. R. (2007). Assessment of high speed imaging systems for 2D and 3D deformation measurements: Methodology development and validation. Experimental Mechanics, 47(4):561–579.

[Toussaint *et al.*, 2012] Toussaint, E., Balandraud, X., Le Cam, J.-B., and Grédiac, M. (2012). Combining displacement, strain, temperature and heat source fields to investigate the thermomechanical response of an elastomeric specimen subjected to large deformations. Polymer Testing, 31(7):916–925.

[Tremblay *et al.*, 2010] Tremblay, P., Belhumeur, L., Chamberland, M., Villemaire, A., Dubois, P., Marcotte, F., Belzile, C., Farley, V., and Lagueux, P. (2010). Pixel-wise real-time advanced calibration method for thermal infrared cameras. In Holst, G. C. and Krapels, K. A., editors, Infrared Imaging Systems: Design, Analysis, Modeling, and Testing XXI, page 766212, Orlando, Florida. International Society for Optics and Photonics.

[Vazquez-Fernandez *et al.*, 2019] Vazquez-Fernandez, N. I., Soares, G. C., Smith, J. L., Seidt, J. D., Isakov, M., Gilat, A., Kuokkala, V. T., and Hokka, M. (2019). Adiabatic heating of austenitic stainless steels at different strain rates. Journal of Dynamic Behavior of Materials, 5(3):221–229.

[Verleysen and Peirs, 2017] Verleysen, P. and Peirs, J. (2017). Quasi-static and high strain rate fracture behaviour of Ti6Al4V. International Journal of Impact Engineering, 108:370–388.

[Vinel *et al.*, 2021] Vinel, A., Seghir, R., Berthe, J., Portemont, G., and Réthoré, J. (2021). Metrological assessment of multi-sensor camera technology for spatially-resolved ultra-high-speed imaging of transient high strain-rate deformation processes. Strain, 57(4):e12381.

[Wang *et al.*, 2016a] Wang, P., Pierron, F., Rossi, M., Lava, P., and Thomsen, O. (2016a). Optimised experimental characterisation of polymeric foam material using DIC and the Virtual Fields Method. Strain, 52(1):59–79.

[Wang *et al.*, 2016b] Wang, X., Witz, J.-F., El Bartali, A., and Jiang, C. (2016b). Infrared thermography coupled with Digital Image Correlation in studying plastic deformation on the mesoscale level. Optics and Lasers in Engineering, 86:264–274.

[Witz *et al.*, 2017a] Witz, J.-F., Lecomte-Grosbras, P., Morch, A., Martel, C., Lesaffre, F., and Brieu, M. (2017a). Digital Image Correlation for large strain. In International Digital Imaging Correlation Society, pages 163–167. Springer.

[Witz *et al.*, 2017b] Witz, J.-F., Réthoré, J., and Hosdez, J. (2017b). Regularization techniques for finite element DIC. In International Digital Imaging Correlation Society, pages 137–140. Springer.

[Wu *et al.*, 2004] Wu, H., Ma, G., and Xia, Y. (2004). Experimental study of tensile properties of PMMA at intermediate strain rate. Materials Letters, 58(29):3681–3685.

[Yee and Takemori, 1982] Yee, A. F. and Takemori, M. T. (1982). Dynamic bulk and shear relaxation in glassy polymers. I. Experimental techniques and results on PMMA. journal of Polymer Science: Polymer Physics Edition, 20(2):205–224.

Appendix A

About the adiabatic and quasi-static state of the experiments

In this Appendix, the adiabatic and quasi-static state of the heterogeneous experiment conducted in this PhD work will be discussed.

A.1 Quasi-static state of the experiment

Figure A.1 shows a cartography of the axial acceleration at t = 468.22 µs, it is obtained by differentiating twice in time the filtered displacement using a simple centred difference scheme. It shows that the acceleration is about 4000 m s^{-2} in most of the sample. Note that this value may be underestimated due to the low temporal resolution used for this test (in one interframe, $\approx$ 15 µs, the wave in the sample travels approximately the ROI observed, $\approx$ 48 cm). The acceleration reaches 10 000 m s^{-2} near the holes and the notches in absolute value. This is two to three order of magnitude lower than the acceleration estimated in the inertial impact test. Furthermore, the quasi-static state of the experiment can be further justified by looking at the ratio between the kinematic density energy and the strain density energy. This ratio can be written as $\frac{\rho v^2}{E\varepsilon^2}$, with ρ the density of the material, E its Young modulus, v a particle velocity and ε strains. Hence, by considering $v = 5\,\mathrm{m\,s^{-1}}$ and $\varepsilon = 0.01$ one get an upper bound of this ratio's possible value during the experiment. Using $E = 210\,\mathrm{GPa}$ and $\rho = 7405\,\mathrm{kg\,m^{-3}}$, the ratio obtained is in the order of magnitude of 1×10^{-2}. Hence, this demonstrates that the experiment can be considered as quasi-static and validate the assumptions done in the simulation performed in Chapter 6.

A.2 Adiabatic state of the experiment

The temperature can be used to demonstrate that the experiment conducted in this work can be considered as adiabatic. As a rule of thumb, isothermal to adiabatic transition can be found by looking at Fourier's ratio $\frac{\lambda\tau}{\rho C L^2}$ where λ is the thermal conductivity, ρ is the density, C the specific heat, τ and L respectively a characteristic time and length. This

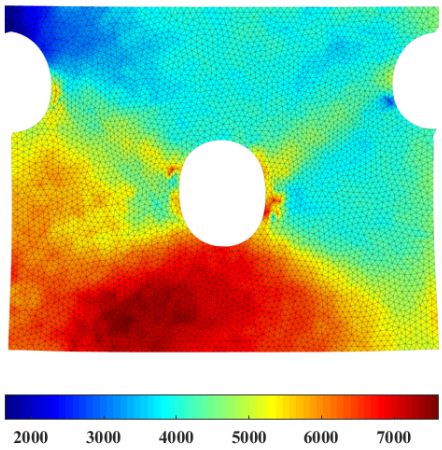

Figure A.1: Cartography of the axial acceleration at t = 468.22 µs (in $\mathrm{m\,s^{-2}}$).

simplified relationship is obtained from heat equation in adiabatic conditions, without any heat sources and when neglecting thermoelastic effects. Since the Cordin's frame rate is 68 kfps, τ is given the value $\frac{1}{68000}$ s. In the present case, the bands are about 7 elements wide, that is to say about 2 mm wide. As a result, using $\lambda = 50\,\mathrm{W\,m^{-1}\,K^{-1}}$, $\rho = 7405\,\mathrm{kg\,m^{-3}}$, $C = 500\,\mathrm{J\,K^{-1}\,kg^{-1}}$ and $L = 2\,\mathrm{mm}$, one finds a ratio of approximately 5×10^{-5}. Hence, there is a difference of several orders of magnitude between the heat production from the term $\rho C\dot{T}$ and the conduction term $\lambda\frac{\partial^2 T}{\partial^2 x}$. Furthermore, even when considering $L = 290\,\mu\mathrm{m}$ (which is the size of an element in the bands), the Fourier ratio obtained is of approximately 2×10^{-3}. Thus, the experiment can be considered as adiabatic.

Standard sample geometry

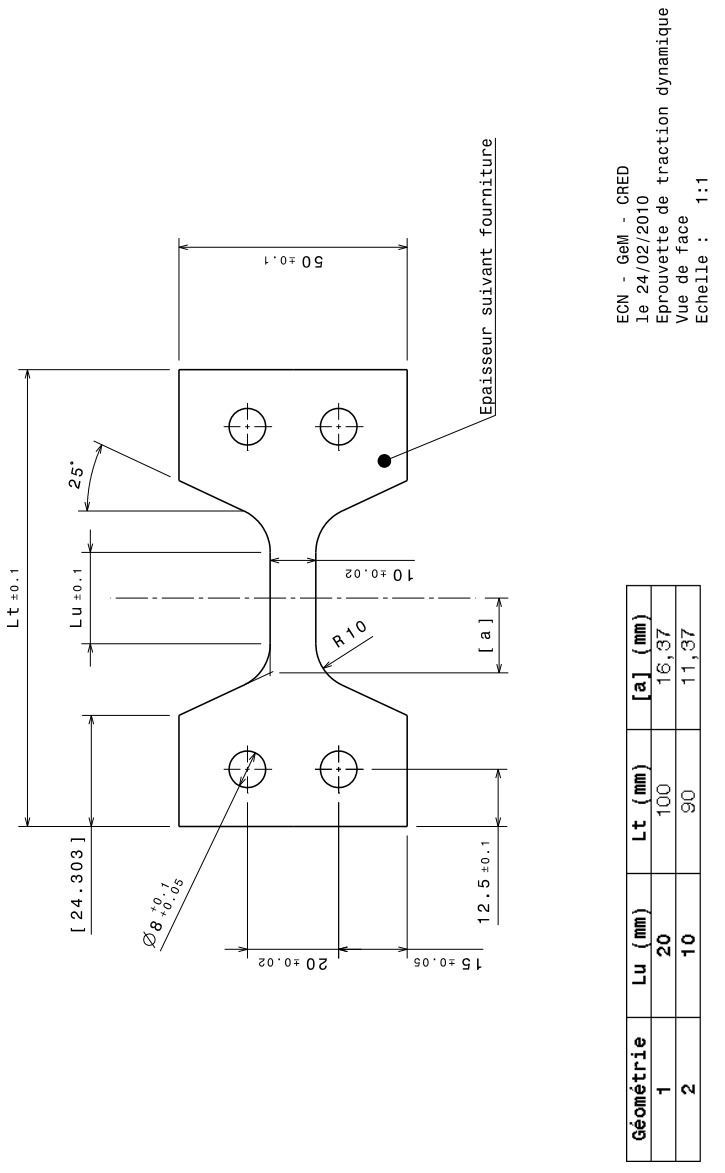

Géométrie	Lu (mm)	Lt (mm)	[a] (mm)
1	20	100	16,37
2	10	90	11,37

Figure B.1: Design of the standard sample geometry used with the MTS-819.

Design of the sample geometry used in this PhD thesis

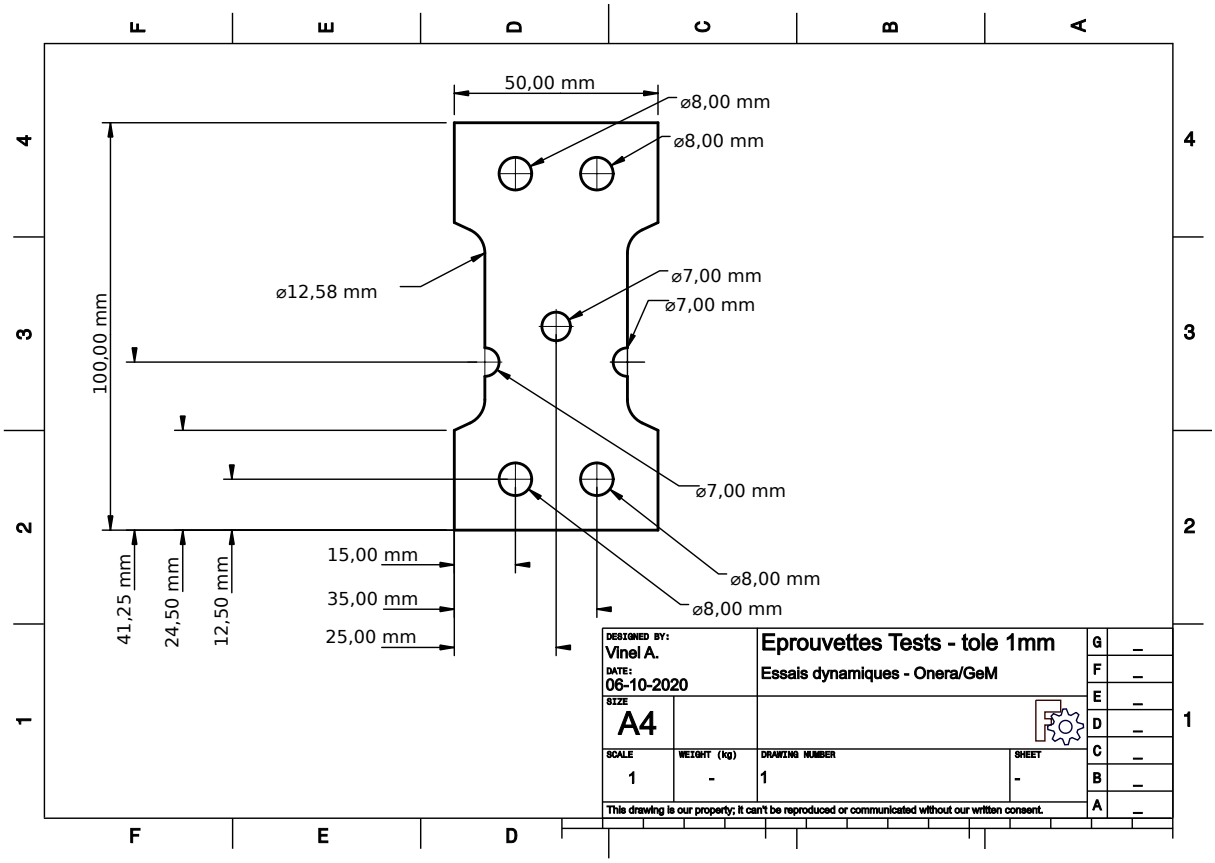

Figure C.1: Design of the sample geometry used to characterize a XES steel.

Appendix D

Data from an additional test on the XES steel – 1

In this Appendix, the different fields obtained during a test, not presented in Chapters 7 and 8, are given.

D.1 Kinematic and temperature fields

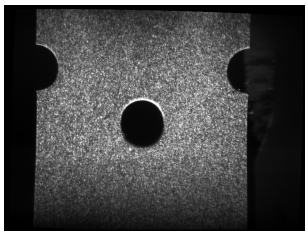

(a) Undistorted image,

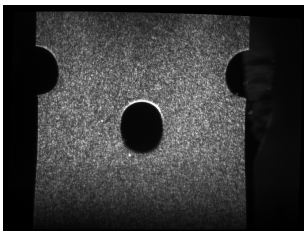

(b) Undistorted image,

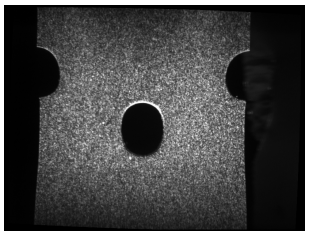

(c) Undistorted image,

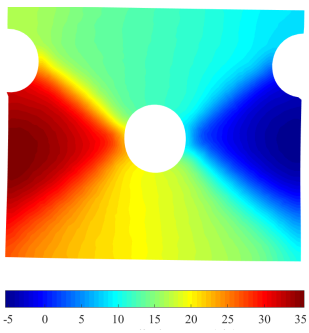

(d) U_x (pix), t = 258.9 µs,

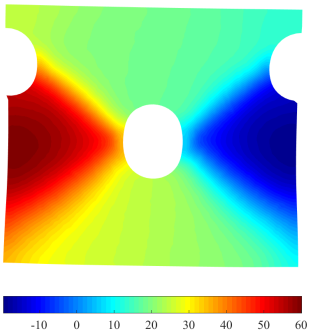

(e) U_x (pix), t = 465.4 µs,

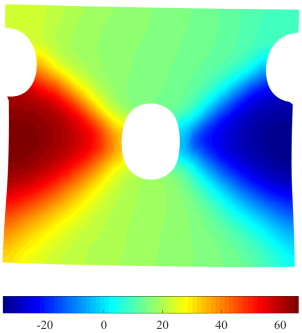

(f) U_x (pix), t = 583.4 µs,

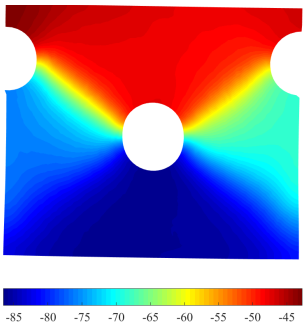

(g) U_y (pix), t = 258.9 µs,

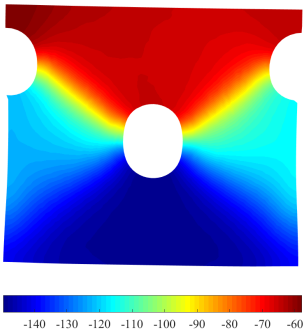

(h) U_y (pix), t = 465.4 µs,

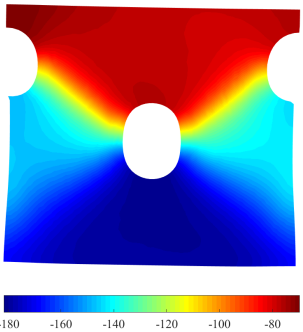

(i) U_y (pix), t = 583.4 µs,

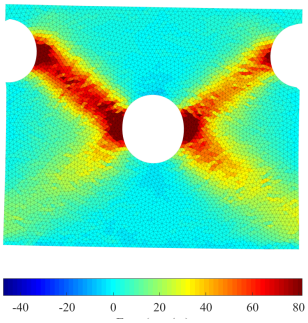

(j) Axial strain (m/m), t = 258.9 µs,

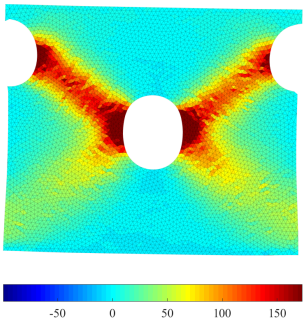

(k) Axial strain (m/m), t = 465.4 µs,

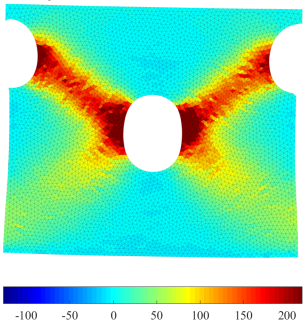

(l) Axial strain (m/m), t = 583.4 µs,

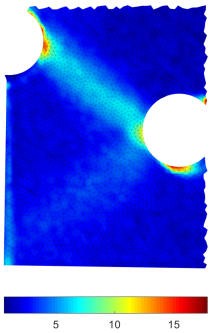

(m) T-To (°C) at t =258.9 µs,

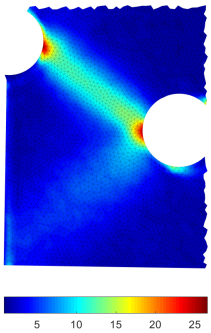

(n) T-To (°C) at t =465.4 µs,

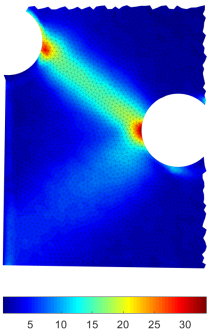

(o) T-To (°C) at t =583.4 µs,

Figure D.1: Undistorted images, displacement fields and strain fields obtained during a dynamic tensile test, for different time steps.

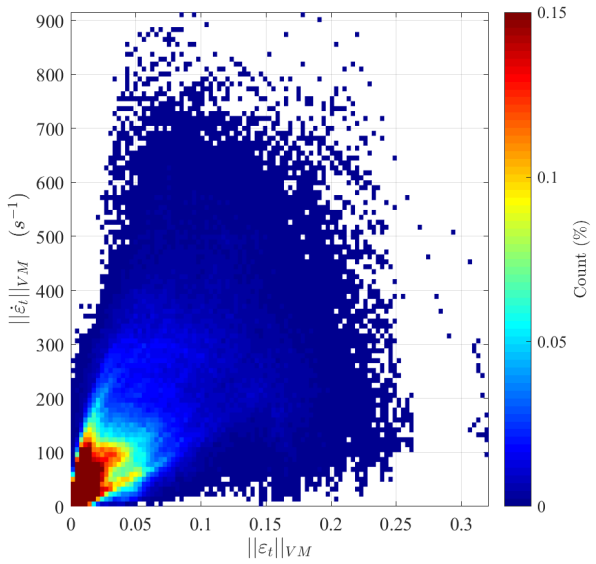

Figure D.2: Von-Mises norm of the strain vs Von-Mises norm of the strain-rates distribution obtained during the experiment, prior to crack initiation. The colour corresponds to a 2D histogram plot. The count per bin is normalized by the number of element in the ROI multiplied by the number of time steps. The stress states that were never experienced by the sample remain white.

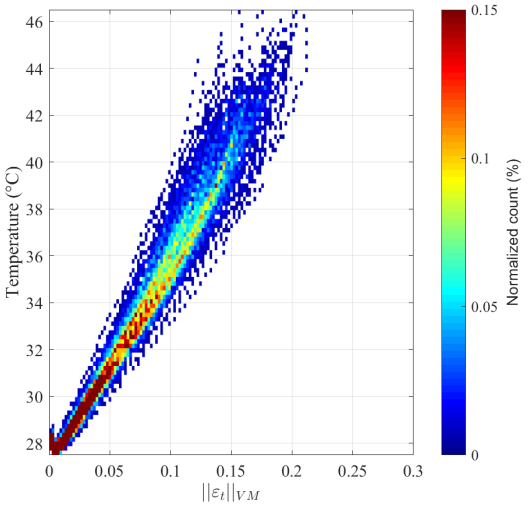

Figure D.3: Temperature vs Von-Mises norm of the total strain distribution for elements in the main localization band before crack initiation.

D.2 DDI Results

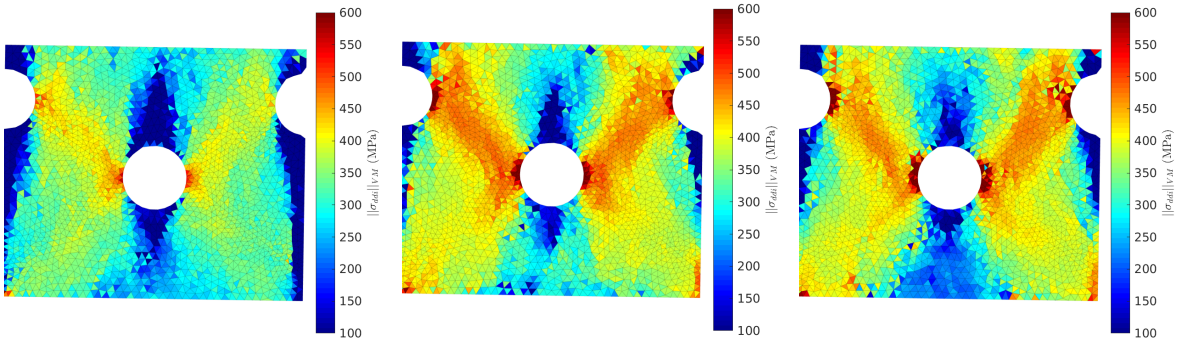

(a) t = 37.7 µs, (b) t = 347.4 µs, (c) t = 642.4 µs,

Figure D.4: Cartographies of the stresses, for three different time steps.

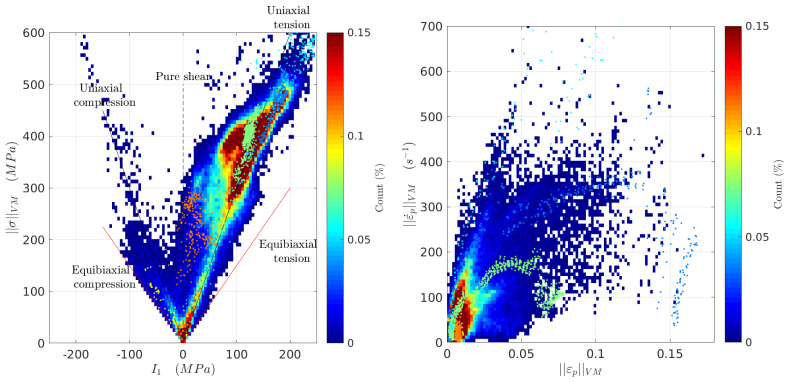

(a) Stress distribution with the loading path of selected elements,

(b) Strain and strain-rate distribution with the loading path of selected elements,

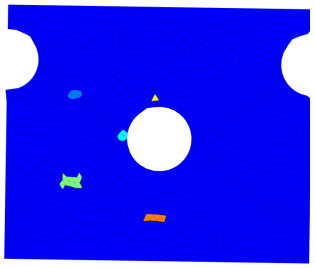

(c) DDI mesh and localization of the selected elements,

Figure D.5: Stress distribution, strain and strain-rate distributions during the experiment. The loading paths of a few selected elements are superimposed on these distributions.

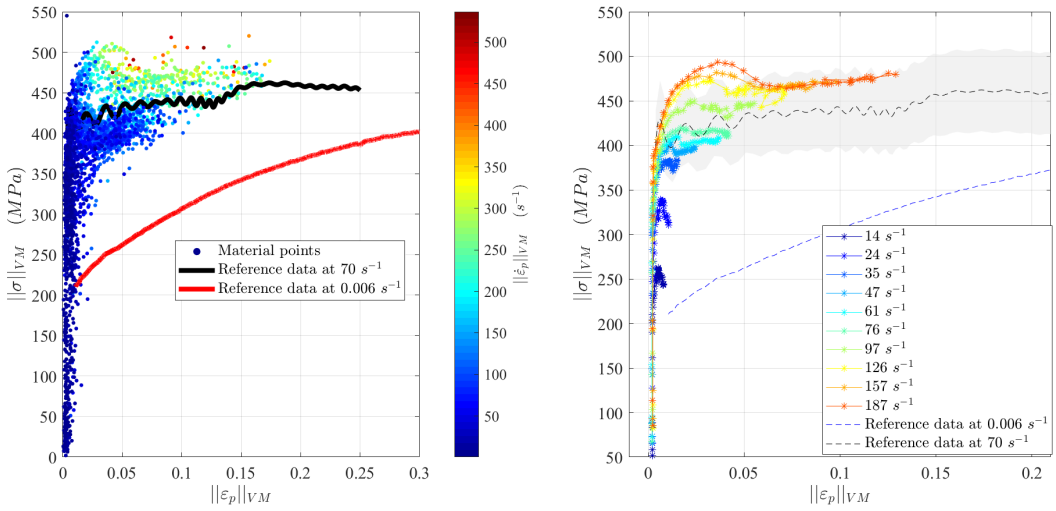

(a) Material states in ($\|\boldsymbol{\varepsilon}_p\|_{VM}$, $\|\boldsymbol{\sigma}\|_{VM}$). The colour of the markers denote the strain-rates, while the lines denote the reference data from ONERA,

(b) Stress-strain curves for different averaged strain-rates extracted from the selected mechanical states during one experiment,

Figure D.6: Material states in the space($\|\boldsymbol{\varepsilon}_p\|_{VM}$, $\|\boldsymbol{\sigma}\|_{VM}$) as well as stress-strain curves for different averaged strain-rates obtained during one experiment.

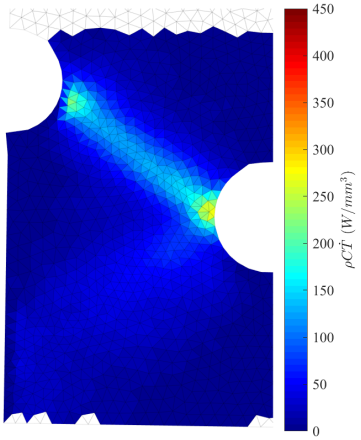

(a) Cartography of $\rho C\dot{T}$,

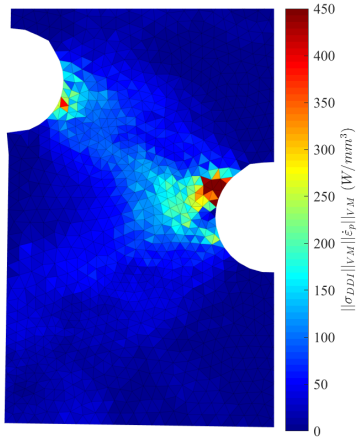

(b) Cartography of $||\boldsymbol{\sigma} DDI||_{VM}||\dot{\varepsilon}_p||_{VM}$,

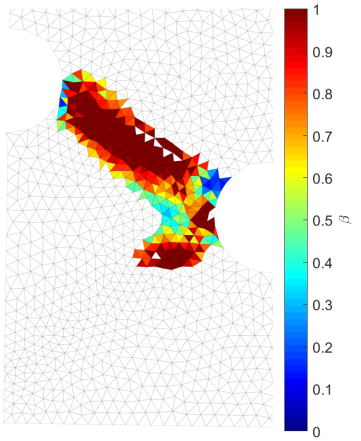

(c) Cartography of β,

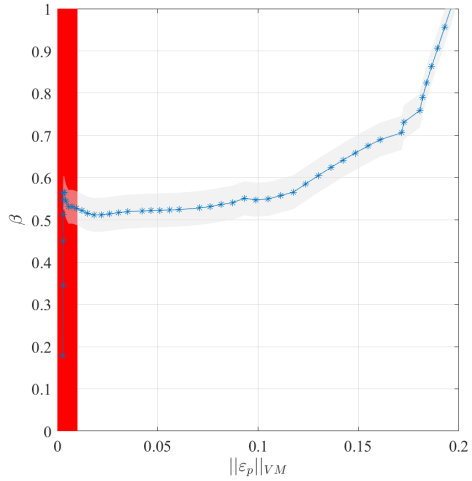

(d) β versus $||\varepsilon_p||_{VM}$,

Figure D.7: Cartography of the Taylor-Quinney coefficient at the last time step. The evolution of the average coefficient in a localization band is then plotted versus $||\varepsilon_p||_{VM}$.

Appendix E

Data from an additional test on the XES steel – 2

In this Appendix, the different fields obtained during a test, not presented in Chapters 7 and 8, are given.

E.1 Kinematic and temperature fields

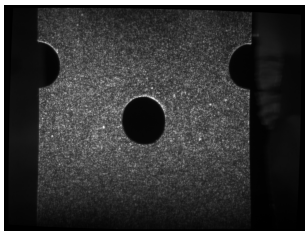

(a) Undistorted image,

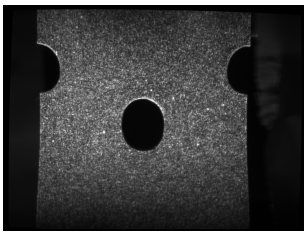

(b) Undistorted image,

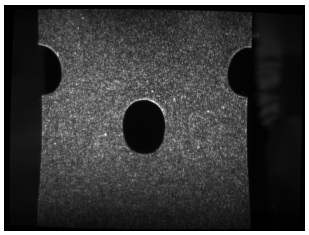

(c) Undistorted image,

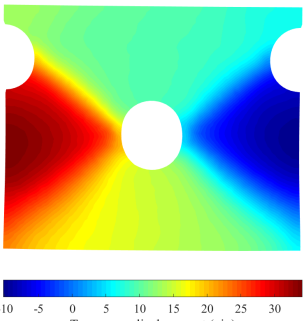

(d) U_x (pix), t = 291.3 µs,

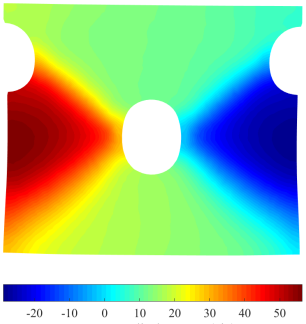

(e) U_x (pix), t = 511.7 µs,

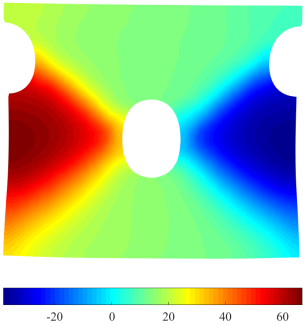

(f) U_x (pix), t = 629.2 µs,

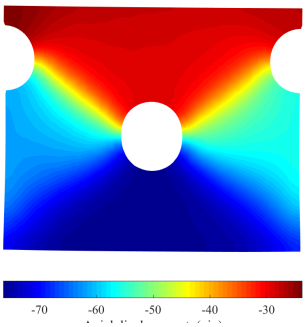

(g) U_y (pix), t = 291.3 µs,

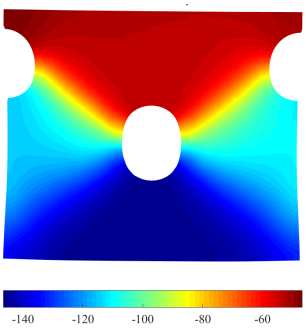

(h) U_y (pix), t = 511.7 µs,

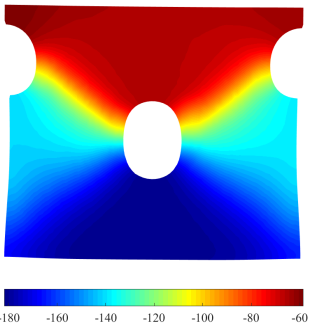

(i) U_y (pix), t = 629.2 µs,

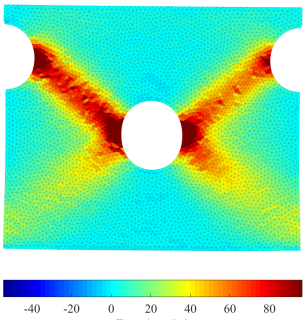

(j) Axial strain (m/m), t = 291.3 µs,

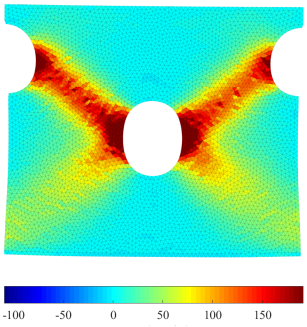

(k) Axial strain (m/m), t = 511.7 µs,

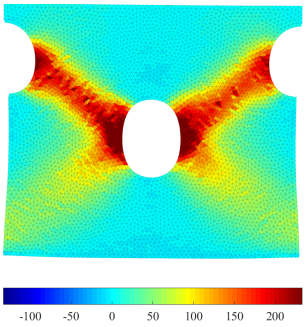

(l) Axial strain (m/m), t = 629.2 µs,

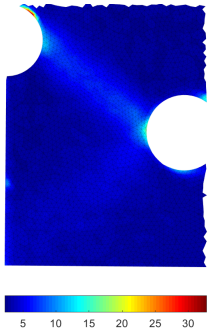

(m) T-To (°C) at t =291.3 µs,

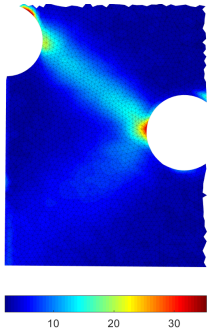

(n) T-To (°C) at t =511.7 µs,

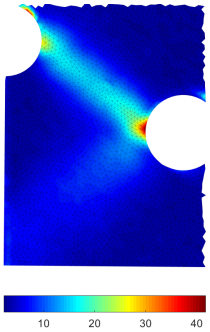

(o) T-To (°C) at t =629.2 µs,

Figure E.1: Undistorted images, displacement fields and strain fields obtained during a dynamic tensile test, for different time steps.

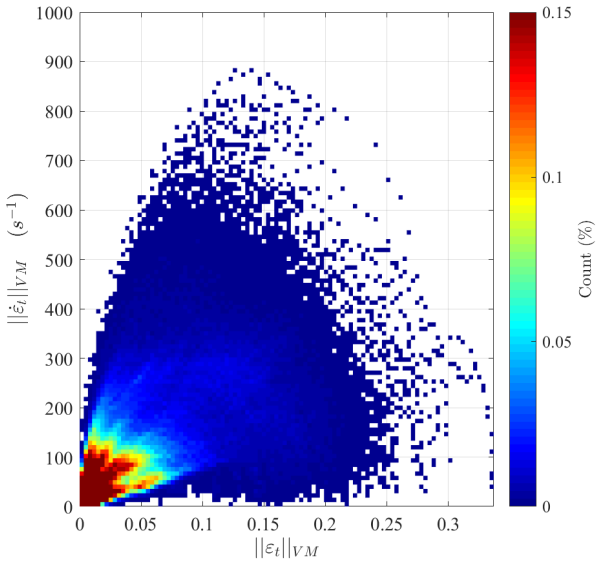

Figure E.2: Von-Mises norm of the strain vs Von-Mises norm of the strain-rates distribution obtained during the experiment, prior to crack initiation. The colour corresponds to a 2D histogram plot. The count per bin is normalized by the number of element in the ROI multiplied by the number of time steps. The stress states that were never experienced by the sample remain white.

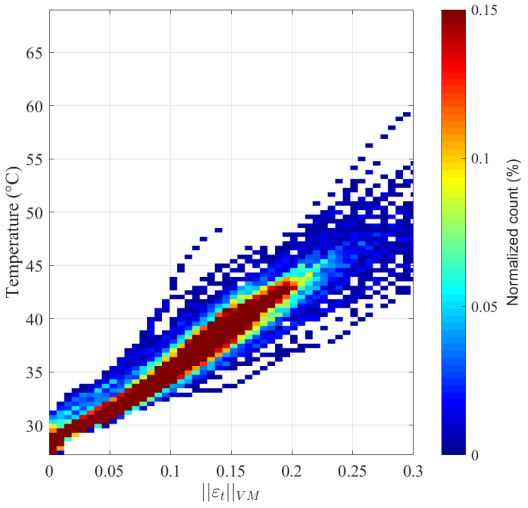

Figure E.3: Temperature vs Von-Mises norm of the total strain distribution for elements in the main localization band before crack initiation.

E.2 DDI Results

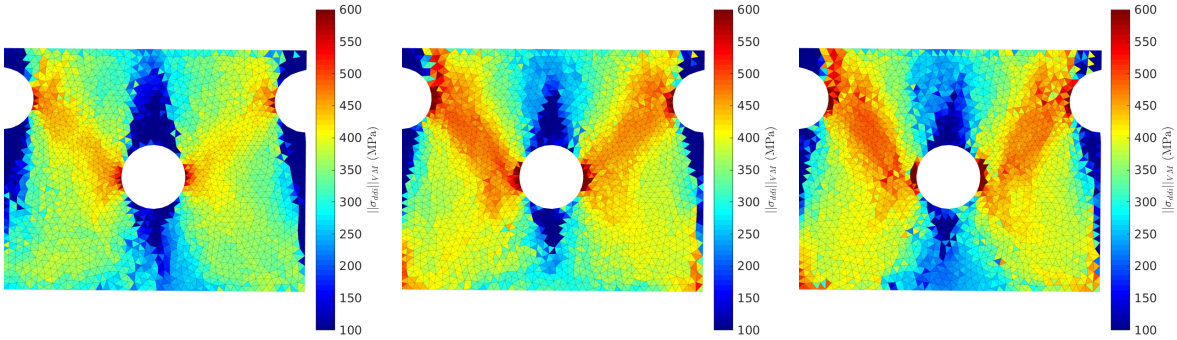

(a) t = 85.5 µs, (b) t = 394.1 µs, (c) t = 688.0 µs,

Figure E.4: Cartographies of the stresses, for three different time steps.

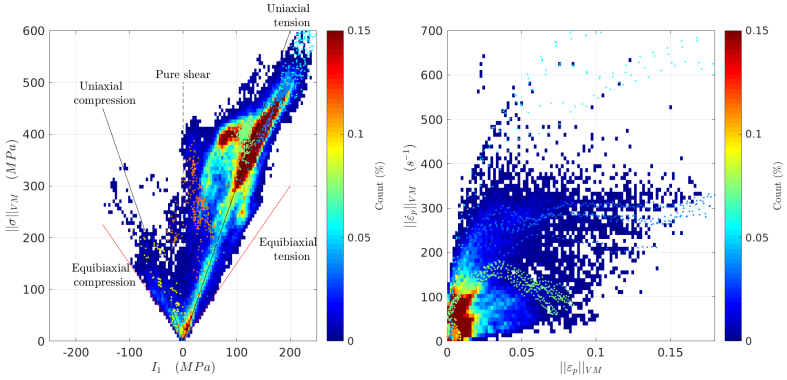

(a) Stress distribution with the loading path of selected elements,

(b) Strain and strain-rate distribution with the loading path of selected elements,

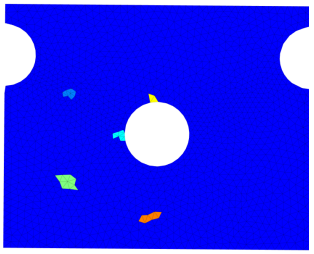

(c) DDI mesh and localization of the selected elements,

Figure E.5: Stress distribution, strain and strain-rate distributions during the experiment. The loading paths of a few selected elements are superimposed on these distributions.

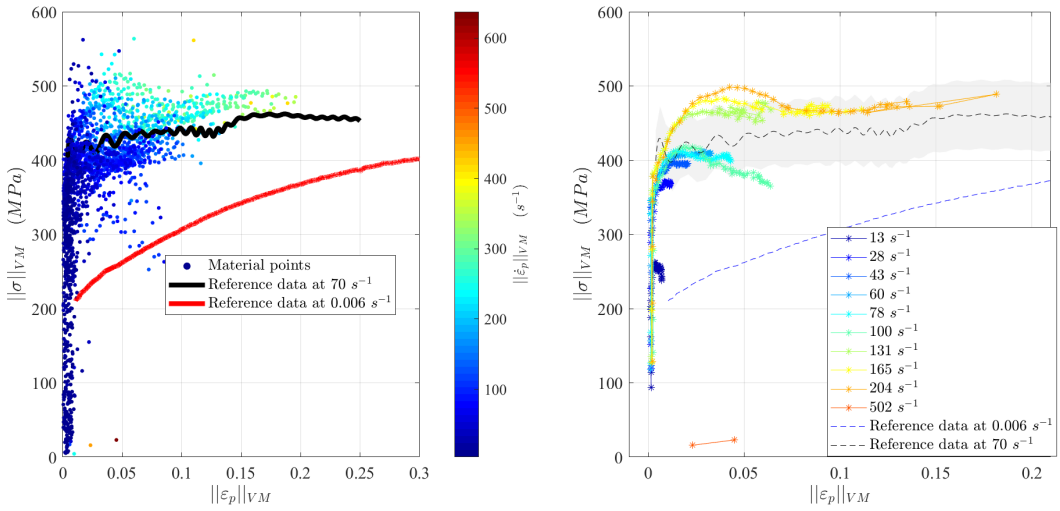

(a) Material states in ($\|\boldsymbol{\varepsilon}_p\|_{VM}$, $\|\boldsymbol{\sigma}\|_{VM}$). The colour of the markers denote the strain-rates, while the lines denote the reference data from ONERA,

(b) Stress-strain curves for different averaged strain-rates extracted from the selected mechanical states during one experiment,

Figure E.6: Material states in the space($\|\boldsymbol{\varepsilon}_p\|_{VM}$, $\|\boldsymbol{\sigma}\|_{VM}$) as well as stress-strain curves for different averaged strain-rates obtained during one experiment.

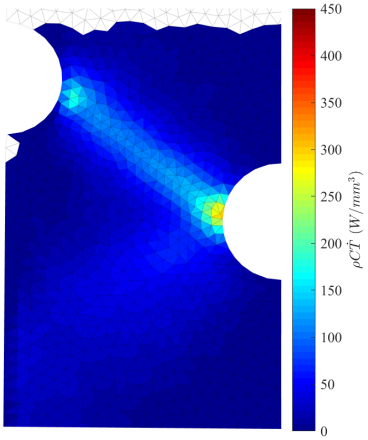

(a) Cartography of $\rho C\dot{T}$,

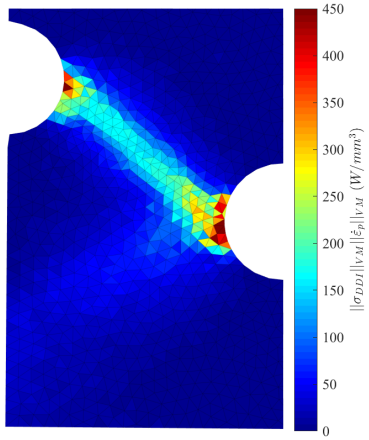

(b) Cartography of $||\boldsymbol{\sigma} DDI||_{VM}||\dot{\varepsilon}_p||_{VM}$,

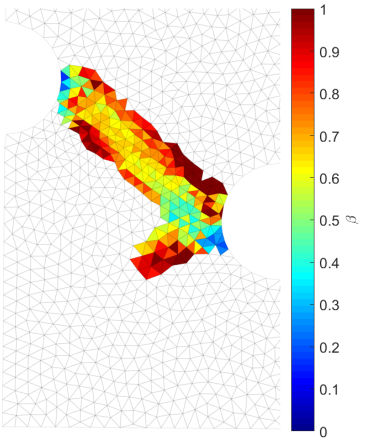

(c) Cartography of β,

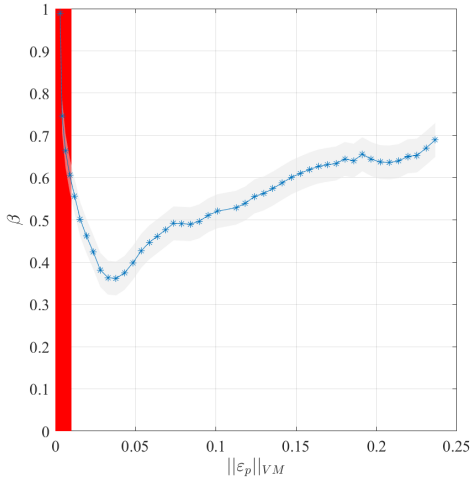

(d) β versus $||\varepsilon_p||_{VM}$,

Figure E.7: Cartography of the Taylor-Quinney coefficient at the last time step. The evolution of the average coefficient in a localization band is then plotted versus $||\varepsilon_p||_{VM}$.

DOCTORAT BRETAGNE LOIRE / SCIENCES POUR L'INGENIEUR

CENTRALE NANTES

Titre : Caractérisation thermomécanique du comportement dynamique des métaux via mesures de champs ultra-rapides

Mot clés : Imagerie ultra-rapide ; Corrélation d'Images Numériques ; Thermographie Lagrangienne ; Grandes vitesses de déformation ; Méthodes Data-Driven

Résumé : À ce jour, les moyens experimentaux et d'analyses permettant de caractériser le comportement visco-thermo-mécanique de matériaux soumis à des chargements extrêmes et complexes sont limités. Dans ce contexte, cette thèse propose de développer une stratégie originale alliant essais hétérogènes, mesure de champs ultra-rapide et reconstruction non-paramétrique de champs de contrainte.

Les travaux de cette thèse reposent sur l'utilisation conjointe d'une caméra ultra-rapide (Cordin-580) et d'une caméra rapide infrarouge (Telops M3K), qui présentent à ce jour les meilleurs résolutions spatio-temporelles sur le marché, pour capturer les champs thermomécaniques au cours d'essais hétérogènes. Pour ce faire, des méthodes spécifiques sont développées afin d'évaluer avec une grande résolution spatiale les déformations (incertitude de $2\,\mathrm{m}\varepsilon$) et les températures (incertitude de $0.3\,°\mathrm{C}$) pour de grandes vitesses d'aquisition. Une campagne experimentale permettant de couvrir de larges gammes de déformation, vitesse de déformation, température ainsi que triaxialité en un seul essai, tout en s'assurant de leur mesurabilité est ensuite dimensionnée.

Au final, l'essai proposé est analysé avec une méthode originale de reconstruction des champs de contrainte qui permet de caractériser en un seul essai la réponse visco-plastique d'un acier sur une plage de vitesse allant de $10\,\mathrm{s}^{-1}$ à $500\,\mathrm{s}^{-1}$ avec des incertitudes de $10\,\%$, tout en offrant des régimes de chargements qui sondent en partie la réponse au cisaillement et à la compression. L'évaluation conjointe de la température et des contraintes permet *in fine* l'évaluation locale de l'énergie qui permettra, à terme, d'établir en une poignée d'essai des modèles thermomecaniquement fondés.

Title: Characterization of the thermomechanical behaviour of metals for high strain-rates, using ultra-high speed imaging cameras

Keywords: Ultra-High Speed imaging; Digital Image Correlation; Lagrangian Thermography; High strain-rates; Data-Driven methods

Abstract: To this date, the experimental and analytical strategies allowing to characterize the visco-thermomechanical behaviour of materials subjected to extreme and complex loadings are limited. In this context, this thesis proposes to develop an innovative strategy combining heterogeneous tests, full-field measurements at ultra-high speed and a non-parametric stress field reconstruction method.

The work of this thesis relies on the joint use of an ultra-high speed camera (Cordin-580) and a high speed infrared camera (Telops M3K), which present to date the best spatio-temporal resolutions of the market, to capture the thermomechanical fields during a heterogeneous test. To do so, dedicated methods allowing to measure with a high spatial sampling strains (uncertainty of $2\,\mathrm{m}\varepsilon$) and temperatures (uncertainty of $0.3\,°\mathrm{C}$) for high acquisition speeds are developed. An experimental campaign allowing to cover large ranges of strain, strain-rate, temperature and triaxiality in a single test, while ensuring their measurability is then designed.

Finally, the proposed test is analysed with an original method of stress field reconstruction which allows to characterize in a single test the visco-plastic response of a steel over a range of strain-rate from $10\,\mathrm{s}^{-1}$ to $500\,\mathrm{s}^{-1}$ with uncertainties of $10\,\%$, while providing loading paths that partially cover the shear and compression response. The combined evaluation of temperature and stress fields allow the local evaluation of energy, which will likely allow in the near future thermodynamically based models to be established using a reduced number of tests.